UNIVERSITY OF SOUTHAMPTON

Active Galactic Nuclei at High Angular Resolution: An Interferometric Study into the Dusty Hearts of AGN

by

James Henry Leftley

A thesis submitted in partial fulfilment for the
degree of Doctor of Philosophy

in the
Faculty of Engineering and Physical Sciences
Department of Physics and Astronomy

June 2020

UNIVERSITY OF SOUTHAMPTON

ABSTRACT

FACULTY OF ENGINEERING AND PHYSICAL SCIENCES
DEPARTMENT OF PHYSICS AND ASTRONOMY

Doctor of Philosophy

by James Henry Leftley

Infra-Red (IR) interferometry of local Active Galactic Nuclei (AGN) has revealed a warm ($\sim$300K-400K) polar dust structure that cannot be trivially explained by the putative dust torus of the unified model. The polar dust led to the development of the disk+wind scenario which comprises of a hot ($\sim$1000K) compact equatorial dust disk and a polar dust wind.

The goal of this work is to use IR interferometry to test if the polar dust wind is ubiquitous in AGN and how it is created. Ultimately, I will attempt to determine if the disk+wind model is a good description of AGN.

Here I present MIDI observations of ESO 323-G77, a Seyfert galaxy hosting a Type 1 AGN, and prove that it hosts a polar dust structure consistent with a dusty wind suggesting the wind is ubiquitous. I proceed to study ESO 323-G77 in the near-IR with GRAVITY and find structure on the scale of the hot dust disk from the disk+wind model. Further investigating the link between the MIDI observed structure and Eddington ratio reveals that the winds are likely to be driven by radiation pressure. Finally I analyse ALMA observations of NGC 3783, a well studied galaxy that hosts a Seyfert Type 1 AGN, and constrain a CO(3-2) molecular gas disk that agrees with the material reservoir disk of the disk+wind model.

The observations studied in this thesis preferentially support the radiation pressure driven polar wind and disk model over the classic dusty torus model. The confirmation of the new model sets the stage for future high resolution studies into AGN physics and AGN driven galactic feedback mechanisms.

Contents

Nomenclature xvii

Declaration of Authorship xix

Acknowledgements xx

1 Introduction 1
- 1.1 Seyfert Galaxies . . . 1
- 1.2 The Central Engine . . . 3
  - 1.2.1 Eddington Limit . . . 5
  - 1.2.2 The accretion disk . . . 5
- 1.3 Polarised Broad Lines in NGC 1068 . . . 5
- 1.4 The Dusty Torus . . . 6
- 1.5 The Spectral Energy Distribution of a Seyfert Nucleus . . . 6
- 1.6 The Clumpy Torus . . . 9
- 1.7 Dusty Tori and Interferometry . . . 9
  - 1.7.1 The polar dust . . . 10
  - 1.7.2 The hot dust . . . 11
  - 1.7.3 The molecular gas . . . 12
- 1.8 Motivation and Outline of this Work . . . 13

2 Interferometry: An Overview 15
- 2.1 The Two Telescope Case . . . 15
  - 2.1.1 Young's double slit experiment with a monochromatic point source . . . 16
  - 2.1.2 A step towards realism: the extended polychromatic source . . . 20
  - 2.1.3 Real world measurements . . . 22
  - 2.1.4 Visibilities of simple models . . . 23
  - 2.1.5 The *uv* plane . . . 25
- 2.2 The Three Plus Telescope Case . . . 26
  - 2.2.1 Closure phase . . . 27

3 Observations and Data Reduction 29
- 3.1 MIDI . . . 29
  - 3.1.1 Observations . . . 30
  - 3.1.2 Reduction . . . 32
    - 3.1.2.1 Data sorting . . . 32
    - 3.1.2.2 Calibration . . . 34
    - 3.1.2.3 Quality Control . . . 35

3.1.2.4 Visibility determination . . . 36
3.1.2.5 No-Track Mode . . . 36
3.2 AMBER . . . 39
3.2.1 Observations . . . 39
3.2.2 Reduction . . . 39
3.2.2.1 The AO problem with AMBER . . . 40
3.3 GRAVITY . . . 42
3.3.1 Observations . . . 42
3.3.2 AO correction for faint objects . . . 44
3.3.3 Reduction . . . 44
3.3.3.1 Visibility determination . . . 45
3.3.4 Closure phase determination . . . 48
3.4 VISIR . . . 49
3.5 ISAAC and NACO . . . 49
3.6 ALMA . . . 50

4 The Mid-IR Interferometric Study of ESO 323-G77 53
4.1 Introduction . . . 53
4.1.1 ESO 323-G77 . . . 53
4.1.2 MIDI modelling . . . 54
4.2 Observations . . . 54
4.2.1 Interferometric observations . . . 55
4.2.2 Interferometric data reduction . . . 57
4.2.3 VISIR data . . . 58
4.2.4 Finding the system axis . . . 59
4.3 Results . . . 60
4.3.1 Morphology and variability from single-dish observations . . . 60
4.3.2 Interferometric observations . . . 61
4.3.2.1 Dust morphology from interferometric observations . . . 61
4.4 Modelling . . . 62
4.4.1 Geometric model . . . 62
4.4.1.1 MCMC Bayesian modelling . . . 64
4.4.2 Influence of the *uv* plane . . . 66
4.4.3 Geometric modelling results . . . 67
4.4.4 CAT3D-WIND radiative transfer modelling . . . 70
4.5 Discussion . . . 74
4.5.1 Comparison of the results . . . 74
4.5.2 An evolution of the dust distribution with Eddington ratio? . . . 76
4.6 Chapter Summary . . . 77

5 The Near-IR Interferometric Study of ESO 323-G77 79
5.1 Observations and Reduction . . . 79
5.2 Observational Results and Discussion . . . 81
5.3 Modelling . . . 83
5.4 Modelling Results and Discussion . . . 86

6 New Evidence for Radiative Pressure Driving 91

6.1 Introduction . . . 91
6.1.1 Radiation pressure . . . 91
6.2 Eddington Ratio . . . 92
6.3 Observations and Reduction . . . 93
6.3.1 MIDI . . . 93
6.3.1.1 Non-detections . . . 94
6.3.2 VISIR . . . 94
6.3.3 SEDs . . . 98
6.3.3.1 Spitzer . . . 98
6.4 Modelling . . . 98
6.4.1 SED modelling . . . 99
6.5 Results . . . 100
6.5.1 General results . . . 100
6.5.2 Results for individual objects . . . 100
6.5.3 SED visibility fractions . . . 102
6.5.4 Results on the correlation between extended flux fraction and Eddington ratio . . . 102
6.6 Discussion . . . 105
6.6.1 The evolution of dust distribution with Eddington ratio . . . 105
6.6.2 MATISSE candidates . . . 109
6.7 Chapter Summary . . . 110

7 The cold gas in NGC 3783 **111**
7.1 Observations and Reduction . . . 113
7.2 Results . . . 114
7.2.1 A molecular inflow? . . . 118
7.2.2 The HCN emission . . . 120
7.3 Chapter Conclusions and Summary . . . 120

8 Conclusions **123**
8.1 The Polar Dust of ESO 323-G77 and its Implications . . . 123
8.2 The Sublimation Radius of ESO 323-G77 . . . 124
8.3 Does the Distribution of Dust Depend on Radiation Pressure? . . . 125
8.4 The Missing Dust . . . 126
8.5 The Molecular Disk of NGC 3783 . . . 127
8.6 The General Structure of AGN Dust . . . 127

A Figures **129**

B Tables **143**

List of Figures

1.1 An example of a Type 1 and Type 2 AGN spectrum. This figure was adapted from https://pages.astronomy.ua.edu/keel/agn/ courtesy of Bill Keel (Keel, 1983). 2
1.2 A cross section diagram of the layout of the unified model of AGN. The corona is depicted in grey around the accretion disk, all other components are as labelled. Sizes are not to scale. 7
1.3 An example SED of an unobscured (Type 1) AGN in black and the components that comprise the SED as labelled. The black line is the sum of the coloured component lines. Figure from Hickox and Alexander (2018). 8
1.4 A cross section diagram of the layout of the dusty wind model of AGN. The corona is depicted in grey around the accretion disk, all other components are as labelled. Sizes are not to scale. 12

2.1 A graphical representation of Young's double slit/pinhole experiment. 16
2.2 A diagram illustrating a simplified layout of the optical light path of a two telescope interferometer. In grey is a movable mirror that can adjust the length of d_2 The two paths are fed into the instrument. 17
2.3 A representation of a Michelson-Morley interferometer, the arrows depict the light path. 18
2.4 A representation of a Michelson type detector, the arrows depict the light path. . 19
2.5 Left: The circle depicts Earth and each line depicts two telescopes on the surface at four intervals as it rotates. Right: The plot depicts the change in location of the telescopes, observing a fixed source, on the *uv* plane at each location as the Earth rotates. For example, X_1 corresponds to location 1, at a time later the telescopes move to location 2 and, therefore, X_2. 26
2.6 This figure shows a diagram of the phase introduced by the atmosphere to each telescope in the three telescope case. 27

3.1 A simplified diagram of the MIDI instrument. The blue line is the uninterfered beam from telescope 1, the red line is the uninterfered beam from telescope 2, the green line and purple line are the interfered beams. 30
3.2 The flowchart of how a night of MIDI data are reduced and calibrated. 33
3.3 An example of the detector image and the fitted mask. The photometry on the left is a cross section from the detector image on the right. These images are produced using plotting scripts from https://www.blackholes.de/downloads.html. 34
3.4 An example of a waterfall plot displaying the OPD of the delay line in green and the fringe in black for a bright calibrator. Any flagged frames show the OPD in light green. 35
3.5 Here I show the normalised difference between adjacent tracked and no track observations for 7 calibrators. I plot 2 different OPD ranges for 2 wavelengths and for each pair I plot the average value and standard deviation of the points. . 37

3.6 Both plots depict the uncalibrated spectrum of HD 220954 when reduced with differing OPD ranges. The red lines denote the tracked calibrator and the blue lines denotes the no track. The lower plot is normalised by the Tracked OPD range 0-20 spectrum. 38
3.7 The flowchart for the AMBER++ reduction method 41
3.8 The calibrated visibility squared of red calibrators, as seen with AMBER, against mean wave front error of the baseline. Original plot created by Dr. Makoto Kishimoto (priv. comm.) 43
3.9 A flowchart representation of the steps taken to reduce GRAVITY data 46
3.10 This plot depicts the visibility squared of the calibrators (red) and science object (purple) against the average Strehl ratio of the two telescopes that comprise the relevant baseline. This plot is with default pipeline frame selection. 47
3.11 This plot depicts the visibility squared of the calibrators (red) and science object (purple) against the average Strehl ratio of the two telescopes that comprise the relevant baseline. This plot is with 3% flux cut frame selection. 48
3.12 The flowchart for the reduction of an ISAAC and NACO observation 51

4.1 An HST image of ESO 323-G77 observed as part of HST programme 5479. . . 55
4.2 The *uv* coverage for ESO 323-G77. The individual points are colour coded according to their correlated flux in the 11.8 μm bin, $F_{\mathrm{corr}}(11.8\,\mu\mathrm{m})$. 57
4.3 The highest and lowest correlated fluxes measured by MIDI. The VISIR spectrum is also shown for comparison. 58
4.4 Image of the 500.7 nm [O III] emission line for ESO 323-G77 using data from S7 (Thomas et al., 2017). North and East are given in the plot. The red line is the mean value found for the elongation direction of the geometric model in this chapter and the blue line is the polar axis implied by the polarisation direction (Schmid et al., 2003). The shaded regions are the 1σ errors on the measurements. The axes are distance from the centre of the AGN. 59
4.5 $V(11.8\,\mu\mathrm{m})$ observations binned into three groups based on PA and fitted with a Gaussian and a constant. The singular red point was given the same constant as the other two fits. 62
4.6 False colour image of the geometric model. The blue, green, and red channels are the average geometric model fits for 8.6 μm and 9 μm, 10.2 μm, and 10.6 μm, and 11.8 μm and 12.2 μm respectively. Each channel is plotted individually below the main panel. The models fluxes are plotted with logarithmic colour scaling. Overplotted is the 66% light radius at 11.8 μm for four different position angles, fitted with an ellipse (dashed line). Also indicated is the mean position angle of the major axis of the geometrical model and its uncertainty in red (c.f. Figure 4.7 and 4.8) and the system axis in blue. 63
4.7 Probability with which an object with position angle, PA, of $\mathrm{PA_{in}}$ is modelled with a PA between 146° and 169°. This gives the uncertainty of the fitted PA of ESO 323-G77 at the 68% and 95% confidence intervals as 12° and 24° respectively. This does not include objects with an axis ratio, ϵ, of 1. 67
4.8 Position angle, PA, of the major axis of the geometric model for each wavelength bin. The orange line is the weighted average value. 68
4.9 Unresolved source fraction, p_f, of the geometric model for each wavelength bin. The orange line is the weighted line of best fit. 69
4.10 Major axis FWHM, Θ_y, of the geometric model for each wavelength bin. The orange line is the weighted line of best fit. 69

4.11 Axis ratio, ϵ, of the geometric model for each wavelength bin. The orange line is the weighted average. 70
4.12 The $V(11.8\,\mu\text{m})$ of each observation against its baseline. The data points are coloured by PA from the Gaussian major axis of the geometric model in real space. The fitted geometric model is overplotted for different PAs. The value at 0 m base length is the VISIR observation at $11.8 \pm 0.2\,\mu$m and its errors are a systematic offset for all the *uv* points. 72
4.13 Figure originally from Leftley et al. (2018) with permission. High-resolution SED of ESO 323-G77. The filled circles represent observed photometry from the near-IR and mid-IR, while the red line shows the VISIR spectrum. The data have been corrected for Galactic extinction of $A_V = 1.2$. The light-grey lines show *CAT3D-WIND* model SEDs that are consistent with the 95% confidence interval of the best fit (solid dark-grey line; see text for details). The dashed black line shows the SED of the model that is used to reproduce the MIDI interferometry in Figure 4.14. 73
4.14 Figure originally from Leftley et al. (2018) with permission. Radial visibility versus baseline as observed (filled circles) and modelled with *CAT3D-WIND* (solid lines) model at $12\,\mu$m for ESO 323-G77. The colours represent position angle with respect to 155°, the major axis of the geometric model. 74

5.1 The GRAVITY *uv* plane for ESO 323-G77. 80
5.2 The visibility squared observations, at $2.15\,\mu$m, are in red. In purple is the best fit model to the observations with $1\,\sigma$ error and in orange is the reverberation mapped radius with $1\,\sigma$ error. I only show visibility squared from 0.5 to 1 for clarity. 82
5.3 The closure phase for the $2.15\,\mu$m, $2.26\,\mu$m, and $2.34\,\mu$m wavelength bins are plotted in purple against baseline length in Mλ. The red depicts the best fitting model at sampled at the same *uv* locations. 86
5.4 The three point source best fit model to the GRAVITY observations convolved with the beam size. The colourbar represents normalised flux in log scale. The beam is given in white and the crosses denote the point source locations. 87
5.5 The visibility squared for the $2.15\,\mu$m, $2.26\,\mu$m, and $2.34\,\mu$m wavelength bins are plotted in purple against triangle perimeter in Mλ. The red depicts the best fitting model at sampled at the same *uv* locations. 88
5.6 The $2.2\,\mu$m prediction of the visibility made by the *CAT3D-WIND* model created in Chapter 4. 89

6.1 The comparison between the spectrophotometry from VISIR (in red) and MIDI (in light blue). Note that the VISIR spectra of NGC 7213 and NGC 2110 have been re-scaled as described in Section 6.3.2. 96
6.2 The subplots show, from left to right, the *uv* plane, the visibility measurements and best model fit, the SED, and the geometric model unresolved source fraction vs. extended component FWHM PDF. Each row shows the result for one object. In the *uv* plane, the purple points represent observations of high enough quality to be used directly in the analysis, the orange points are the excluded observations. The visibility plot depicts the visibility of each "good" observation vs. baseline length with the best fit geometric model overlaid. The SED contains data from ISAAC (pale orange), VISIR (purple), and Spitzer (grey). 103
6.2 Cont. 104

6.3 The of ratio extended source flux to unresolved source flux for Type 2 objects compared to their Eddington ratio. The purple points are the objects discussed in this chapter, the orange point is NGC 1052 from Fernández-Ontiveros et al. (2019). The red line overlaid is the linear best fit, with 1σ errors, to the purple points and the grey dashed line is the same but includes the orange point. 106
6.4 Flux ratio against Eddington ratio for all objects, including NGC 1052. 107
6.5 Flux ratio against distance for all objects, including NGC 1052. 107
6.6 Flux ratio against X-ray luminosity for all objects, including NGC 1052. 108
6.7 The fraction of flux interior to each radius, as a function of $r-r_i$, where r is the distance from the AGN engine, and r_i is the interior surface of the 'torus', for various Eddington ratios $\eta_{\rm Edd}$. 109
6.8 This plot shows the correlation from Figure 6.3 with the model from Figure 6.7 overlaid for different $r-r_i$. 110

7.1 This figure is taken with permission from Hönig (2019). It depicts the dusty wind model and which component is traced by which molecular line or wavelength. 112
7.2 An HST image of NGC 3783 using the WFC3/UVIS detector. The data were downloaded from the HST Legacy Archive and was observed as part of the HST proposal 11661. 113
7.3 Average continuum subtracted HCN line flux density between 350.97 GHz, 351.02 GHz. The FWHM beam size is in white. The white dotted line on the colourbar is the 3σ level 116
7.4 Average continuum subtracted CO line flux density over 100 MHz centred on the amplitude of the line. The FWHM beam size is in solid white. For comparison, the region of HCN emission is the white circle and the 3σ flux limit is the dotted white line in the colourbar. 117
7.5 A velocity map of NGC 3783's CO line produced from band 7 data. Positive velocity is moving away from the observer. The purple line is the cut made to produce the PV diagram in Figure 7.6 118
7.6 A PV diagram of NGC 3783's CO line along the purple line in Figure 7.5. The purple points are the velocity of the CO line as determined by a Gaussian fit. Positive velocity is moving away from the observer. 119
7.7 Figure from Williamson et al. (2020). A PV diagram created using a slit across the equator of a hydrodynamic disk+wind model inclined at 80°. The PV diagram is produced for a variety of line transitions. Each row contains a model with a different optical thickness. The details of the models can be found in the paper. 119

A.1 Corner plot (Foreman-Mackey, 2016) of the Probability Density Function (PDF) of each parameter, the fitted Fourier space visibility distribution, and the reconstructed brightness distribution for the 8.2 μm geometric model fit. 130
A.2 The same as figure A.1 for the 8.6 μm geometric model fit. 131
A.3 The corner plot for the 9.0 μm geometric model fit and the model result displayed in both Fourier and real space. 132
A.4 Same as figure A.1, but for the 9.4 μm geometric model fit. 133
A.5 The same as figure A.1 for the 9.8 μm geometric model fit. 134
A.6 The same as figure A.1 for the 10.2 μm geometric model fit. 135
A.7 Same as figure A.1, but for the 10.6 μm geometric model fit. 136

A.8 The same as figure A.1 for the 11 μm geometric model fit. 137
A.9 The same as figure A.1 for the 11.4 μm geometric model fit. 138
A.10 Same as figure A.1, but for the 11.8 μm geometric model fit. 139
A.11 The same as figure A.1 for the 12.2 μm geometric model fit. 140
A.12 The same as figure A.1 for the 12.6 μm geometric model fit. 141
A.13 Same as figure A.1, but for the 13 μm geometric model fit. 142

List of Tables

4.1 Table of MIDI observations of ESO 323-G77. (a) Data previously used in Kishimoto et al. (2011b), Burtscher et al. (2013), and López-Gonzaga et al. (2016); (b) Unpublished data. 56

4.2 VISIR photometry of ESO 323-G77. *a*) Large uncertainties due to strong background variations from clouds. 60

4.3 Results of model fitting for each wavelength bin. p_f is the unresolved source fraction, ϵ is the ratio of the major axis to minor axis, Θ_y is the major axis FWHM, θ is the angle from north to east of the Θ_y component of the Gaussian and f is the fractional amount for which the variance is underestimated by the likelihood function if the errors were assumed correct (Foreman-Mackey et al., 2013). 71

4.4 Results of the best fit *CAT3D-WIND* model. N_0 is the average number of clouds in the line of sight in the equatorial region, a_d is the radial power-law index for the disk αr^{a_d}, where r is in units of the sublimation radius, a_w is the radial power-law index of the dust clouds in the polar wind, h is a unitless disk height scaling factor, θ_w is the opening angle of the polar wind, θ_σ is the angular width of the polar wind, $f_{\rm wd}$ is the wind to disk ratio, and inc is the inclination. 71

5.1 The GRAVITY observations used in this chapter and their integration time. . . 81

5.2 The size of the hot dust in ESO 323-G77 from a thin ring model fit to the visibility squared and the hot dust size from reverberation mapping (Boulderstone et al., in prep). The average is the mean of the visibility sizes. 83

5.3 The bounds for each free parameter of the point source model. 84

5.4 The bounds for each free parameter of the radially symmetric Gaussian model. A_f is the relative amplitude flux. 85

5.5 The bounds for each free parameter of the elongated symmetric Gaussian model. A_f is the relative amplitude flux, $\rm FWHM_{major}$ is the FWHM of the major axis, and ϵ is the axis ratio. 85

5.6 The modelling result for the combination of the 2.15 μm, 2.26 μm, and 2.34 μm wavelength bins. *This component was fixed. 88

6.1 VISIR photometry. Column descriptions: (2): Dates of the individual epochs during which always both filters, PAH1 and PAH2_2 were observed; (3) and (4): nuclear flux densities at 8.6 μm and 12 μm estimated from the filters PAH1 and PAH2_2, respectively through Gaussian fit photometry. The quoted uncertainties are dominated by the systematic uncertainties on the calibrator flux in all cases which is $\leq$ 10%; (5) and (6): the smallest FWHM values in the PAH1 and PAH2_2 filters, respectively, of all the epochs from Gaussian fitting. The major and minor axis are averaged. Values marked by a * are taken from the VISIR image collection of Asmus et al. (2014) if they provide better estimates than the new data. Fairall 49 is completely taken from the latter work and is listed here for convenience. 97
6.2 Spitzer/IRS observations used in SEDs. 98
6.3 Modelling results. Θ is the FWHM of the extended Gaussian, p_f is the unresolved source fraction, and Θ_{up} is the upper limit of the FWHM estimated from the single-dish FWHM of the nucleus (Asmus et al., 2014, http://dc.g-vo.org/sasmirala) 100

7.1 ALMA observations used in this work, $\delta\Theta_{\rm res}$ id the angular resolution, FoV is the maximum recoverable scale, $\delta\omega$ is the frequency resolution, and Int is the integration time. 114
7.2 The four spectral windows for each ALMA observation. 114

B.1 Summary table of AGN featured in this work 144
B.1 The Luminosities and black hole masses used in this work. a) Reference for given AGN activity type: α) Véron-Cetty and Véron (2006), β) Osterbrock and Martel (1993), γ) Krimm et al. (2013), δ) Panessa and Bassani (2002), ϵ) Bennert et al. (2006), ζ) Veron-Cetty and Veron (1998); b) Hubble Distances (CMB) from NED; c) Total 12 μm Luminosity values derived fluxes provided by Asmus et al. (2014); d) Absorption corrected X-ray Luminosity derived from Asmus et al. (2015); e) Reference for black hole mass: 1) Gu et al. (2006), 2) Lodato and Bertin (2003), 3) Onken and Peterson (2002), 4) Greenhill et al. (2003), 5) Makarov et al. (2014), 6) Cid Fernandes et al. (2004), 7) Vestergaard and Peterson (2006), 8) Wang and Zhang (2007), 9) Garcia-Rissmann et al. (2005), 10) Peterson et al. (2004), 11) Denney et al. (2006), 12) Cappellari et al. (2009), 13) Wang and Zhang (2007), 14) Koss et al. (2017) ,15) Ho et al. (2009); f) N_H values from Asmus et al. (2015); g) extended component flux; h) unresolved source flux; i) Reference for extended and unresolved fluxes: Lo) López-Gonzaga et al. (2016), Bu Burtscher et al. (2013), Th) This work, Le) Leftley et al. (2018), F8) Fernández-Ontiveros et al. (2018), F9) Fernández-Ontiveros et al. (2019) 145
B.2 List of MIDI Observations 146
B.2 a) Due to short coherence time (<4ms), b) high atmospheric dust, c) clouds, d) high wind (pointing limited) 149
B.3 List of ISAAC Observations 150

Nomenclature

ADU - Arbitrary Detector Units
AGN - Active Galactic Nuclei
ALMA - Atacama Large Millimeter Array
AMBER - Astronomical Multi-BEam combineR
AO - Adaptive Optics
AT - Auxiliary Telescope
BIC - Bayesian Information Criteria
BL - Baseline Length
BLR - Broad Line Region
CAL - CALibrator
Dec - Declination
DFFA - Dual-Field oFf-Axis mode
DFNA - Dual-Field oN-Axis mode
DIT - Detector Integration Time
ELT - Extremely Large Telescope
ERIS - Enhanced Resolution Imager and Spectrograph
ESO - European Southern Observatory
FWHM - Full Width Half Maximum
HR - High Resolution
HST - Hubble Space Telescope
IR - Infra-Red
ISAAC - Infrared Spectrometer And Array Camera
LINER - Low-Ionisation Nuclear Emission-line Region galaxies
LoS - Line of Sight
LR - Low Resolution
MACAO - Multi-Application Curvature Adaptive Optics
MATISSE - Multi AperTure mid-Infrared SpectroScopic Experiment
MCMC - Markov chain Monte Carlo
METIS - Mid-infrared ELT Imager and Spectrograph
MIDI - MID-infrared Interferometer
MR - Medium Resolution
NACO - NAOS-CONICA

NAOS - Nasmyth Adaptive Optics System
NLR - Narrow Line Region
OPD - Optical Path Delay
P2VM - Pixel to Visibility Matrix
PA - Position Angle
PSF - Point Spread Function
QSO - Quasi-Stellar Object
RA - Right Ascension
RCAL - Red CALibrator
SCI - SCIence
SED - Spectral Energy Distribution
SF - Structure Function
SFM - Single-Field Mode
SVD - Stellar Velocity Distribution
UT - Unit Telescope
UV - UltraViolet
VISIR - VLT Imager and Spectrometer for mid-IR
VLT(I) - Very Large Telescope (Interferometer)
WCS - World Coordinate System
WFE - Wave Front Error

Declaration of Authorship

I, James H. Leftley, declare that this thesis titled, 'Active Galactic Nuclei at High Angular Resolution: An Interferometric Study into the Dusty Hearts of AGN' and the work presented in it are my own. I confirm that:

- This work was done wholly or mainly while in candidature for a research degree at this University.
- Where any part of this thesis has previously been submitted for a degree or any other qualification at this University or any other institution, this has been clearly stated.
- Where I have consulted the published work of others, this is always clearly attributed.
- Where I have quoted from the work of others, the source is always given. With the exception of such quotations, this thesis is entirely my own work.
- I have acknowledged all main sources of help.
- Where the thesis is based on work done by myself jointly with others, I have made clear exactly what was done by others and what I have contributed myself.

Signed:

_____

Date:

_____

Acknowledgements

I want to give a special thanks Sebastian Hönig and Konrad Tristram for their patience and for providing me with the many unique opportunities I have been given. Without their interest, dedication, and enthusiasm for my work I would have never accomplished what I have and enjoyed my time as much as I did. I especially want to thank them for encouraging me to undertake, and supporting me through, two years in Chile where I met amazing people and engaged many once in a lifetime experiences. I will be forever grateful for the impact they have had.

Furthermore, I would like to thank Poshak Gandhi for being my second supervisor and providing a lot of assistance with my work. The help was invaluable and the advice was always appreciated.

A special thanks goes to Daniel Asmus for so much time and effort spent providing me with data, proofing my work, and even prepping for interviews. Doubly so for proof reading this thesis multiple times during an especially busy period with no obligation.

A further thanks goes to Makoto Kishimoto who played a large role in my research and took it upon himself to host me in Japan for two weeks to personally tutor me in AMBER.

A thanks in advance goes to Leonard Burtscher and Christian Knigge who still agreed to read my thesis and perform my defence by video chat after a global pandemic closed the universities.

I would not have made it to the end of this PhD without the great support of my friends and family. Despite the physical distances between us at times, you never failed to be there.

Finally, my biggest thank you goes to Charlotte whose love and support has meant the world to me and who caught many typos and linguistic errors in this thesis (including a very hidden "the the").

Chapter 1

Introduction

The first Active Galactic Nuclei (AGN) ever discovered was found by Fath (1909), they described an emission line galaxy that contained diffuse nuclear emission of narrow lines. The discovered galaxy was NGC 1068 which has since become an archetype for AGN. It was not long before more AGN were discovered, although they were not known to be related to each other until over 30 years later. Seyfert (1943) identified that the galaxies that hosted these AGN could be grouped into a single class of objects and as such they were named Seyfert Galaxies.

1.1 Seyfert Galaxies

Since their initial discovery, there have been a variety of different phenomenological features discovered that are present in some AGN and not others. AGN have been separated into several classes based on these features. The most populated classes of AGN are Seyfert galaxy nuclei and a class called quasars or QSOs (Quasi-Stellar Objects). Quasars got their name from the fact that they look like stars in the optical (Schmidt, 1969). What made quasars different to Seyfert AGN is that, at the time of discovery, they did not appear to have an associated host galaxy. Quasars have since been found to have host galaxies (Kristian, 1973); however, quasars are so bright that the host galaxy is dim by comparison. The class name still remains in use with the definition of a quasar changed to be based on its luminosity. Hickox and Alexander (2018) give the luminosity cutoff between Seyfert galaxy AGN and quasars as 10^{45} erg s^{-1} or $\sim 3 \times 10^{11}$ L$_{\odot}$. In this work, the AGN I will focus on are the ones hosted by Seyfert galaxies. Seyfert galaxies are typically normal, clearly visible, and usually spiral galaxies but their nuclear regions display abnormally high levels of emission by comparison. The emission from Seyfert galaxy nuclei rivals the output of the entire host galaxy ($\sim 10^{11}$ L$_{\odot}$) from a much smaller region; this was the original morphological definition of these objects put forward by Seyfert (1943).

Instead of a morphological definition, Seyfert galaxies are now identified by their spectrum which contains highly ionised emission lines (Keel, 1983). In the optical wavelength range,

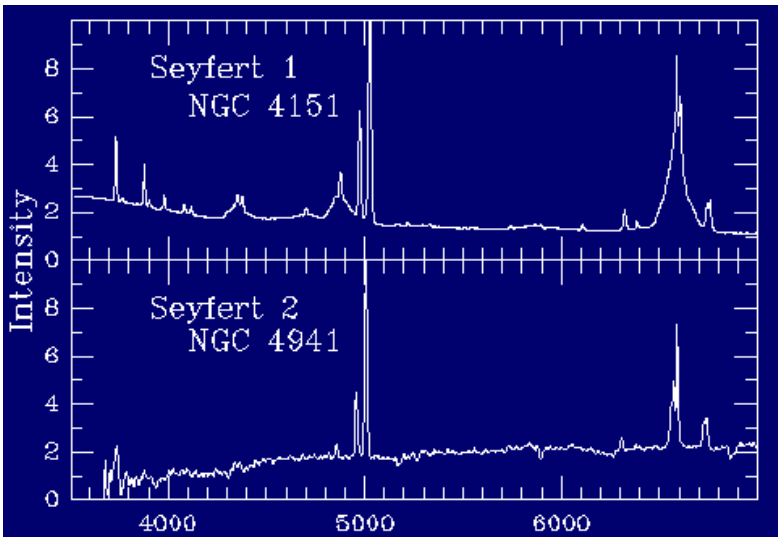

FIGURE 1.1: An example of a Type 1 and Type 2 AGN spectrum. This figure was adapted from https://pages.astronomy.ua.edu/keel/agn/ courtesy of Bill Keel (Keel, 1983).

Seyfert AGN contain a mix of forbidden and permitted lines with a narrow equivalent width. The "narrow lines" imply a gas velocity of $\leqslant 1000\,\mathrm{km\,s^{-1}}$ (Hickox and Alexander, 2018). An example of a spectrum containing narrow lines can be found in the bottom panel of Figure 1.1. With modern telescopes, the narrow line emission has been spatially resolved and appears to be in the form of two outflowing, oppositely orientated cones (e.g. Durré and Mould, 2018).

In the optical spectra of some Seyfert AGN there is a second set of broader permitted, but not forbidden, lines that overlap the narrow ones. An example of a spectrum containing narrow and broad lines can be found in the top panel of Figure 1.1. The "broad lines" have a width indicative of velocities $\geqslant 1000\,\mathrm{kms^{-1}}$ (Hickox and Alexander, 2018). The high velocities of the broad lines imply that they arise from a region that is hotter than the region the narrow lines originate from and this region is always unresolved to single dish imaging; although, it was spectro-astrometrically resolved by IR interferometry in a recent breakthrough (GRAVITY Collaboration et al., 2018b). The broad line emission region must also be denser than the narrow line emission region to explain the lack of forbidden lines, which are collisionally suppressed (Hickox and Alexander, 2018). Khachikian and Weedman (1974) used the presence of these broad, spatially unresolved lines to separate Seyferts into two categories. Type 1, where both narrow and broad lines are present, and Type 2, where only the narrow lines are present.

Intermediate type galaxies were first defined in Osterbrock (1981) by Dr. Donald E. Osterbrock. They range between 1 and 2 and are defined by the relative strength of the broad and narrow components of the Hβ emission line. The scheme was later refined to a more rigid definition by Winkler (1992). The types were distinguished by the Hβ to [O III] 500.7 nm ratio (F(486.1)/F(500.7)). They set hard limits for each type as follows:

Type 1: F(486.1)/F(500.7)>5.0

Type 1.2: 2.0<F(486.1)/F(500.7)<5.0

Type 1.5: 0.333<F(486.1)/F(500.7)<2.0

Type 1.8: F(486.1)/F(500.7)<0.333 and broad component visible in Hα and Hβ.

Type 1.9: Broad component visible in Hα but not Hβ.

Type 2.0: No broad component visible.

Where F(λ) is the flux of the emission line at that wavelength. Two additional classifications were added by Veron-Cetty and Veron (1998):

Type 1h: Broad hydrogen recombination lines (Hα, Hβ, etc) lines visible in polarised optical light but not in unpolarised.

Type 1i: Broad hydrogen recombination lines (Hα, Hβ, etc) lines visible in infrared light and not optical.

Another class of AGN are called narrow-line Type 1 (Osterbrock and Pogge, 1985). These are Type 1 AGN that exhibit evidence of a broad line region, however the emission lines are relatively narrow when compared to other Type 1 AGN. They are defined as:

Type 1n : FWHM(Hβ)$\leqslant$ 2000 kms^{-1} and F(486.1)/F(500.7)<3.0

Finally, there are a low nuclear luminosity class of AGN called LINERs. LINER is an acronym for Low-Ionisation Nuclear Emission-line Region galaxies (Heckman, 1980). I denote a LINER using the definitions from Heckman (1980) and Véron-Cetty and Véron (2003) using the [O I] 630 nm, [O II] 372.7 nm, and [O III] 500.7 nm lines:

Type 3: F(372.7)/F(500.7)$\geqslant$ 1.0, F(500.7)/F(630)$\leqslant$ 3.0, and no broad Balmer lines present.

Type 3b: F(372.7)/F(500.7)$\geqslant$ 1.0, F(500.7)/F(630)$\leqslant$ 3.0, and broad Balmer lines present.

Type 3h: F(372.7)/F(500.7)$\geqslant$ 1.0, F(500.7)/F(630)$\leqslant$ 3.0, and broad Balmer lines are present in polarised light but not in unpolarised.

1.2 The Central Engine

The presence of ionised emission lines presented one of the early clues as to the "fuel" of these Seyfert nuclei and AGN in general (Woltjer, 1959). At the time of discovery, the narrow line emission was spatially unresolved. With the resolution available, the emission must have been on scales of less than 100 pc. It was known that these lines have an order of magnitude velocity dispersion of 10^3 km s^{-1}.

Equating gravitational and centripetal force gives the mass required to keep material with velocity v gravitationally bound at a radial distance r:

$$M \approx v^2 r/\mathrm{G} \tag{1.1}$$

Where M is the mass required and G is the gravitational constant. Therefore, solving Equation 1.1 for the mass required to keep the narrow line emitting material gravitationally bound, at the upper limit of the radial distance, gives an upper limit for the central mass of $10^{10}\,\mathrm{M}_\odot$. Because the emission lines are characteristic of low density gas, the lower limit for the mass can estimated. The density limit of the gas infers a minimum volume and, therefore, a minimum orbital radius leading to the lowest mass required to gravitationally bind the material. From Equation 6.15 of Peterson (1997), using their maximum electron density of $10^6\,\mathrm{cm}^{-1}$, an Hβ line luminosity of 10^{41} erg/s, and a fill factor of 1 gives a radius of 0.19 pc. The minimum radius translates to a lower limit of $\sim 10^7\,\mathrm{M}_\odot$. While a very crude argument made under the assumption that the emitting material is gravitationally bound, this suggests that either a significant amount of the mass of a Seyfert galaxy is contained in just the central 10's of parsecs or the emission region must be very compact.

Another clue about the nature of the central engine comes from the AGN's enormous energy output. There are few processes that could fit the entire emission of a galaxy containing billions of stars into a region comparable to the size of the Oort cloud. For a typical Seyfert nucleus luminosity of $\sim 10^{11}\,\mathrm{L}_\odot$, or $\sim 10^{37}$ W, converting mass directly to energy would require $0.002\eta^{-1}\,\mathrm{M}_\odot\mathrm{y}^{-1}$ where η is the mass conversion efficiency and $0 < \eta \leqslant 1$. The accretion rate ($\dot{m}$) required to maintain a luminosity L is found using:

$$\begin{aligned} \mathrm{E} &= \eta m c^2 \\ &\text{or} \\ \mathrm{L} &= \eta \dot{m} c^2; \end{aligned} \tag{1.2}$$

where E is energy, m is mass, and c is the speed of light. For nuclear fusion, $\eta \approx 10^{-3}$ which would give a mass requirement of $2\,\mathrm{M}_\odot\mathrm{y}^{-1}$. Considering approximately 1 in 100 galaxies host an AGN and the universe is $\sim 10^{10}$ y old, an argument can be made that the "on time" for an AGN is at least 10^8 y (Woltjer, 1959). The on time argument is made under the assumption that all galaxies have AGN but they are off in some. If you assume that only some galaxies have AGN, inactive or otherwise, then the on time must be longer. A longer on time means that each AGN would require more mass, from either the host or itself, than is available so the AGN cannot be powered by fusion. Furthermore, the efficiency of nuclear fusion would not allow the liberation of enough energy from the small inferred volume. The issues are only exacerbated when considering that there are AGN, like quasars, that typically have 100 times higher luminosity. Only accretion onto a compact object can provide the efficiency required (Salpeter, 1964). The compact object is generally accepted to be a supermassive black hole. Krolik (1999) give the efficiency of accretion onto a black hole from $\eta = 0.06$ up to $\eta = 0.42$ if

the black hole is spinning rapidly, however, $\eta = 0.1$ is generally considered a good estimate (e.g. Frank et al., 1992). Accretion still requires $\sim 0.02\,M_{\odot}y^{-1}$ but it is viable.

1.2.1 Eddington Limit

If the central engine is powered by accretion then the maximum Luminosity the accreting object can achieve can be inferred. The radiation liberated from the accretion process can interact with the accreting matter, creating an outward pressure. If the radiation pressure exceeds the inward force of gravity then accretion cannot take place. This Luminosity is called the Eddington Luminosity and it is derived in Section 6.2. The Eddington Luminosity is defined as:

$$L_{\mathrm{Edd}} \quad = \quad 1.26x10^{31}\frac{M_{\mathrm{bh}}}{M_{\odot}}\,\mathrm{W}, \tag{1.3}$$

where M_{bh} is black hole mass. By substituting the Eddington Luminosity into Equation 1.2 the Eddington Limit can be found. This is the maximum rate an object can accrete and it only depends on the mass of the accreting black hole. This assumes that the object accretes spherically and emits radiation isotropically which is not necessarily the case.

1.2.2 The accretion disk

Accretion converts gravitational potential energy into thermal energy. As a particle descends down a potential well, it imparts the converted energy to the surrounding matter. The thermal energy is then radiated away, producing the intense radiation that is seen in AGN. The accreting matter takes the form of a disk. A disk is formed because the incoming matter has angular momentum. If every particle has angular momentum, collisions and other momentum transfer mechanisms will cause all opposing angular momentum vectors to cancel. The final stable state of the accreting material is the net momentum of the initial material. If the net angular momentum of the incoming material is non-zero, the net angular momentum must be in a single plane, i.e. a disk. This accretion geometry is what allows some AGN to exceed the Eddington limit.

1.3 Polarised Broad Lines in NGC 1068

Because the optical lines are present in both types of AGN, the argument for accretion power applies to both types. In both types, the thermal emission from the AGN ionises diffuse gas which produces the narrow line emission. Only in Type 1s is there a set of broad ionised lines from a second denser and hotter gas component. The broad lines remained a distinction between the two types until NGC 1068 was observed in polarised optical light (Antonucci and Miller, 1985). NGC 1068 was considered a Type 2 and did not show broad lines in its optical spectra.

However, when observed with optical spectropolarimitry, broad lines were seen in polarised optical light. The discovery of a Type 1h lent itself to the idea that the broad line emission was not intrinsically absent in Type 2 AGN but obscured. Furthermore, the obscuration was not present at every angle from the central engine. The broad line emission could be seen in polarised light because it is reflected by material that has an unobscured view of the central engine and the light is polarised upon reflection. The reflected component is too dim to be seen in the unpolarised light but can be seen when only the polarised emission is considered.

Therefore, Type 1 and Type 2 (and Type 1h) AGN could be explained by the same model. They both have an accretion disk, narrow line emission from a Narrow Line Region (NLR), broad line emission from a Broad Line Region (BLR), and an angular dependant obscuring medium. The type an AGN appears to be is dictated by the angle at which it is viewed. The single model which explains both Type 1 and Type 2 AGN as an orientation effect is known a the unification scheme.

1.4 The Dusty Torus

In the unified model Antonucci and Miller (1985); Antonucci (1993) present, dusty gas surrounds the equator of the central engine at $\sim$ 1 pc and it is responsible for reprocessing radiation from the central engine into the IR by thermal emission. The obscuring dusty material takes the form of an equatorial dusty torus. It should be noted that the dusty torus is thought to actually be mostly gas by mass.

The toroidal obscuring material can explain the difference between a Type 1 and a Type 2 AGN. An AGN looks like a Type 2 when it is orientated such that our Line of Sight (LoS) to the central engine, and BLR, is blocked by the dusty torus, i.e. "edge on". The same AGN appears as a Type 1 when it is less inclined and the LoS to the central engine is over the torus rim and the central region is unobscured, i.e. "face on". The NLR is much larger than the dust torus so it is unobscured in both cases. A diagram of the unified model is in Figure 1.2. However, this model is not complete and there are still some observations it struggles to explain such as "true Type 2s" which do not appear to show any hidden broad lines in the same manner NGC 1068 (Bianchi et al., 2012).

1.5 The Spectral Energy Distribution of a Seyfert Nucleus

The accretion disk is expected to emit thermally and the addition of the dusty torus introduces a second thermally emitting component that is on a larger spatial scale than the accretion disk and therefore cooler. These AGN components should be apparent in its Spectral Energy Distribution (SED). The SED of an unobscured (i.e. Type 1) AGN is presented as the black line in Figure 1.3.

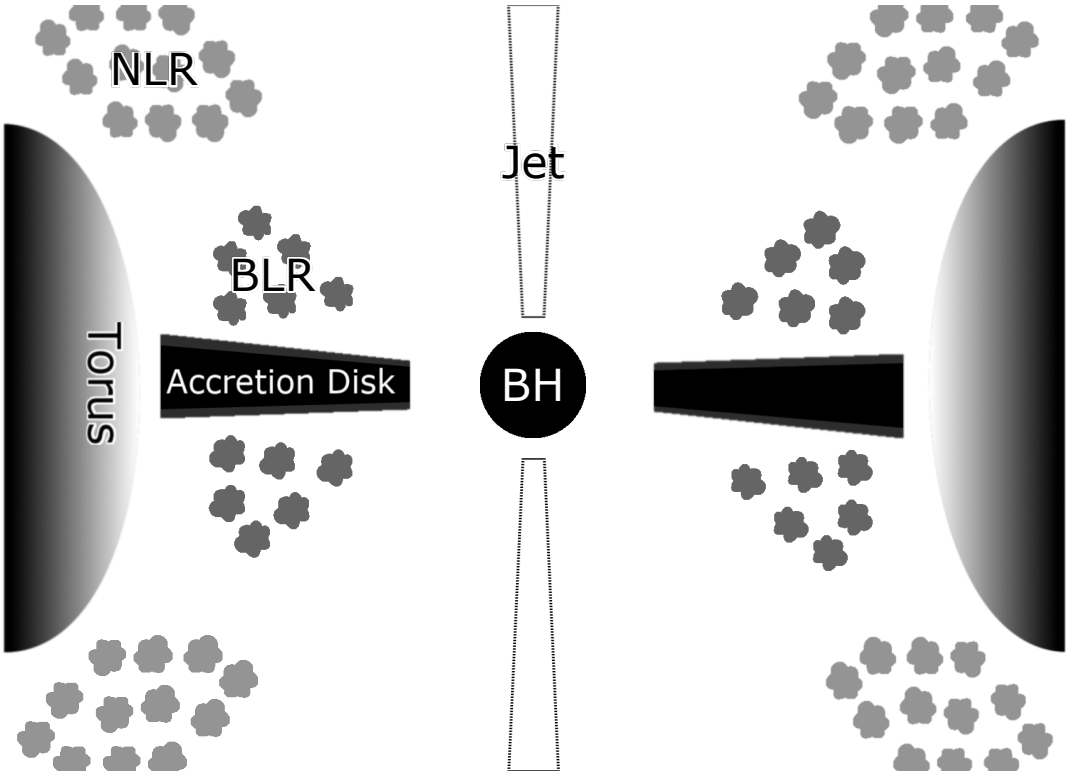

FIGURE 1.2: A cross section diagram of the layout of the unified model of AGN. The corona is depicted in grey around the accretion disk, all other components are as labelled. Sizes are not to scale.

Overall, the spectrum of an AGN is broadly flat in terms of νF_ν; however, the SED shows several peaks and features present at multiple wavelengths.

I will start with the central engine. The accretion disk is expected to be highly ionised and at a temperature of 10^4 K to 10^5 K. A black body at 10^4 K to 10^5 K is expected to emit primarily in the optical/UV spectrum (Peterson, 1997). In Figure 1.3, the blue line is what is expected for the accretion disk thermal emission (Hickox and Alexander, 2018). In the optical, it is shown that the accretion disk is indeed a good explanation of the AGN continuum emission. Furthermore, the optical/UV flux in an AGN will vary over time. The timescale of the variation ranges from hours to weeks which, due to the finite speed of light, suggests that the emitting component is on subparsec spatial scales (Tristram, 2007; Hickox and Alexander, 2018). The suggested spatial size is consistent with the expected size of the accretion disk from theory.

The next component is the dusty torus. In the IR, there is a clear "bump" that is distinct from the accretion disk emission. The feature is consistent with thermal emission from a material with a lower temperature than the accretion disk. The IR bump has a very consistent Wien cutoff at 1 μm between observed objects. The Wien cutoff changes with temperature so a constant cutoff suggests that the component has a similar temperature in all objects. The cutoff can be explained by ~ 1500 K dust emission; at ~ 1500 K graphite grains sublimate (Barvainis, 1987). With a centrally heated object, the distance the dust must be from the engine to survive is given in Barvainis (1987). The limitation on the dust temperature explains the consistent Wien cutoff.

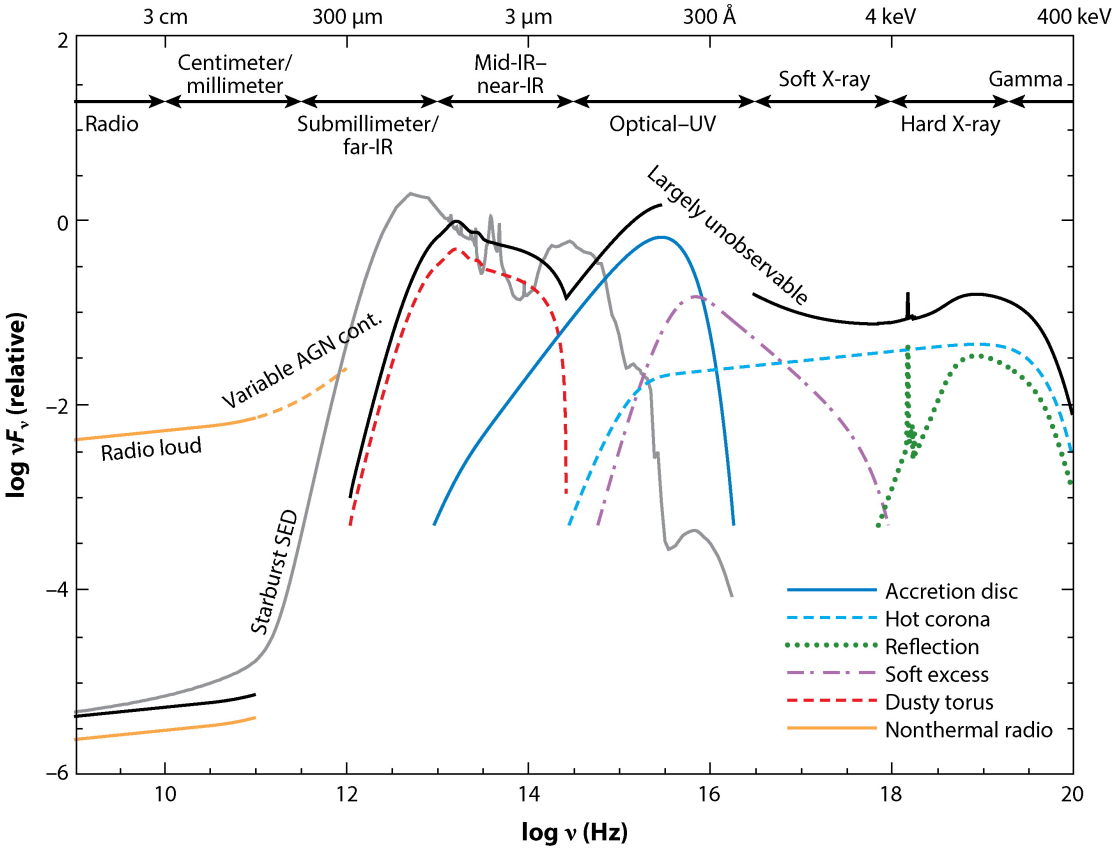

Hickox RC, Alexander DM. 2018.
Annu. Rev. Astron. Astrophys. 56:625–71

FIGURE 1.3: An example SED of an unobscured (Type 1) AGN in black and the components that comprise the SED as labelled. The black line is the sum of the coloured component lines. Figure from Hickox and Alexander (2018).

The dusty torus is consistent with the observed IR SED and it is shown in Figure 1.3 as the red dashed line.

In the X-ray, the SED stops being consistent with thermal emission from either the accretion disk or dusty torus. In the $1-10$ keV photon energy range, the emission often shows variations on very short time scales (days to weeks). The short timescales suggest the X-ray emission is from a small region $<<1$ pc, i.e. inside the torus. The $1-10$ keV range can be explained by a power-law caused by inverse Compton scattering (Liang and Thompson, 1979). The inverse Compton scattering is thought to happen in a hot corona around the accretion disk giving it the size necessary to explain the short timescale variation. Between 10 and 30 keV there is an X-ray bump caused by reflection of the coronal X-ray emission off the accretion disk (George and Fabian, 1991). At lower energies of <1 keV there is a "soft excess" (Arnaud et al., 1985) possibly caused by warm Comptonization of accretion disk emission.

Finally, there is clear non-thermal emission at radio wavelengths. In some AGN there is significant radio emission while in others there is not. At any given optical luminosity, there are

10 times fewer radio loud object than quiet (Wilson and Colbert, 1995). The radio SED in radio loud objects is a power-law that is consistent with synchrotron emission. The synchrotron emission is produced by relativistic electrons moving in a two-sided jet from the polar direction (the direction perpendicular to the plane of the disk). The jet can be on spatial scales that are resolvable by radio telescopes (see Marschern, 2010, for details of AGN jets). When radio loud AGN are observed by radio telescopes, there are two main components that both emit by synchrotron. An unresolved core and an extended structure. The extended structure is caused by the aforementioned jet that can extend out to Mpc distances and the unresolved source is on a scale less than 0.01 pc. In this work, I primarily deal with radio quite AGN. Radio quiet objects do not have the strong jet that is present in the loud objects. In these objects the jet is either not present or very weak. The jet base can be bright enough to dominate emission at shorter wavelengths, particularly in louder objects. For example, jet contribution in the IR was shown in Centaurus A, a radio-loud "Type 2" (Meisenheimer et al., 2007).

1.6 The Clumpy Torus

The unified model is very successful at explaining the different AGN phenomena in terms of a single model. The cornerstone of the model is the angular dependant obscuring material thought to be in the form of an equatorial torus. Originally, the dusty torus used the most basic satisfactory description of the dust distribution which was a torus with a smooth internal structure. The smooth dust model explains the obscuration but fails to explain how the thickness of such a structure would be supported against collapsing into a disk due to self-gravity. Making the torus "clumpy", i.e. composed of a distribution of clouds, requires less support, for example by radiation pressure (Pier and Krolik, 1992b). It is supposedly easier to support a clumpy torus because the radiation pressure drives the random motion of the clouds giving a thickness. Radiation pressure is the momentum imparted on a particle from a flux of photons. In AGN astrophysics the observable measuring radiation pressure is the Eddington ratio. Eddington ratio is the ratio of the luminosity of an AGN compared to the luminosity at which radiation pressure on a free falling particle equals the force on the particle from gravity. For example, an Eddington ratio of > 1 outweighs gravity and blows away the accreting material.

Observational evidence of the clumpy nature of the torus was found in the X-rays. The obscuration experienced by the emitted X-rays as they pass through the torus sometimes shows rapid variation. The clumpiness can explain the rapid change in the effective amount of obscuration seen in some AGN (Risaliti et al., 2005).

1.7 Dusty Tori and Interferometry

The dusty torus is an important component in AGN physics; however, it was not until relatively recently in the timescale of AGN science, almost 100 years since the first AGN was discovered,

that instrumentation capable of resolving the thermal emission of the dusty torus became available. The reason for the difficulty in observing the torus is that the torus is predicted to be on very small angular scales. Even in the most nearby Seyfert galaxies, the 1-10 pc predicted size (Pier and Krolik, 1992a, 1993) translates to 10s of milliarcseconds (mas) and the bulk of the dust emits in the mid-IR. Taking the Rayleigh criterion of single dish telescopes, $\zeta = 1.22\frac{\lambda}{D}$ where D is the telescope diameter and λ is the wavelength, a dish size of 8.2 m, as available at the Very Large Telescope (VLT), has a maximum resolution of 307 mas at 10 μm. To resolve dusty tori, a larger telescope is required.

Until the completion of telescopes such as the 30 m class Extremely Large Telescopes (ELTs) or larger (Cirasuolo, 2019), these large apertures have to instead be simulated through the use of long baseline interferometry. Instruments such as the Keck interferometer (Colavita et al., 2013) and the VLTI (VLT Interferometer Beckers et al., 1990) have successfully been used for the parsec scale study of AGN (e.g Swain et al., 2003; Tristram, 2007; Raban et al., 2009; Kishimoto et al., 2011b; Hönig et al., 2012, 2013; Burtscher et al., 2013; Tristram et al., 2014; Hönig et al., 2014; López-Gonzaga et al., 2016). While the Keck interferometer managed to partially resolve eight AGN (Kishimoto et al., 2011a) in the near-IR, the VLTI was the first interferometer that allowed the direct study of the angular dependent geometry of the dust distribution in Seyfert nuclei on the parsec scale. VLTI/MIDI (MID Infrared inteferometer, Leinert et al., 2003) was used to observe position angle (PA), defined as the angle on sky from North through East, dependent structure in the mid-IR and VLTI/AMBER (Astronomical Multi-BEam combineR, Petrov et al., 2007) observed near-IR structure. These two instruments on the VLTI opened the gates for AGN IR Interferometry.

1.7.1 The polar dust

The first Seyfert AGN to show angular dependent dust structure was the AGN hosted by the Circinus galaxy, hereafter referred to as Circinus, followed by NGC 424 (Tristram et al., 2007; Hönig et al., 2012). Circinus initially was thought to show a toroidal structure as predicted by the unification scheme, however, NGC 424 showed dust emission in the polar region. Later on, in Tristram et al. (2014), Circinus was also found to host a polar dust structure, responsible for 80% of the mid-IR emission, as well as an equatorial dust disk.

Type 2 AGN in modelling can show a weak polar extension when using the torus model (e.g. Schartmann et al., 2005, 2008) but do typically show equatorial extensions. Hönig et al. (2012) reported that the polar extension could be explained by an optically thin dusty wind along the poles which may be launched from a hot dusty torus that is on a scale smaller than the classical warm dusty torus. The wind would form a hollow cone-like structure around the NLR and replace the warm torus as the source of thermal mid-IR emission. The new hot torus provides the reservoir of material for the accretion disk and the obscuration required for the unification scheme.

In the polar wind model, the wind connects the smallest scales around the central engines with the larger scale host galaxies; it is also capable of explaining the apparent near isotropy of the mid-infrared emission inferred in large AGN samples (e.g Gandhi et al., 2009; Asmus et al., 2015), all observations of Circinus (Stalevski et al., 2017; Vollmer et al., 2018; Stalevski et al., 2019), and the larger scale polar dust seen more recently in Asmus et al. (2016). The hot torus would then dominate the near-IR instead of the mid-IR. Later papers proceeded to report polar dust structures in NGC 3783 (Hönig et al., 2013), NGC 1068 (López-Gonzaga et al., 2014), and NGC 5506 (López-Gonzaga et al., 2016). MCG-5-23-16 and NGC 4507 were shown to have enough observations to constrain an extension however they did not show significant elongation in any direction (López-Gonzaga et al., 2016).

The discovery of a polar extension in the Type 1 AGN hosted by NGC 3783 and the absence of equatorial extended AGN favours the polar dust model over the torus model. A Type 1, unlike the Type 2s, cannot show a polar extension in the torus model without a warped accretion disk structure. In a Type 2 the directly illuminated inside edge of the torus is obscured, but if the torus is inclined slightly a portion of the inner edge may be unobscured in the polar direction leading to a polar extension. In a Type 1 the illuminated inside edge of the torus would be completely unobscured to the observer and prevent the weak polar extension possible in Type 2s; therefore, a polar extension in the torus model could only be explained by a warped disk preferentially illuminating the inner edge of the dust torus in the polar direction by chance (Hönig, 2019). Motivated by the new evidence, the disk+wind model was developed (Hönig et al., 2012). A radiative transfer model of the disk+wind scenario, called *CAT3D-WIND*, was later developed (Hönig and Kishimoto, 2017). In the disk+wind model, a disk with a scale height replaces the hot dust torus and serves the same function. The *CAT3D-WIND* model is a radiative transfer model that can be used to create model SEDs as well as model interferometric observations. A diagram of the dusty wind scenario can be found in Figure 1.4. In the disk+wind model the wind is driven by radiation pressure. Because emission from a disk is anisotropic, greater radiation pressure is applied to dust in the polar direction allowing it to be driven without destroying the hot dust disk (Hönig and Kishimoto, 2017; Williamson et al., 2019).

1.7.2 The hot dust

The source of obscuration in the disk+wind scenario is from a hot dust disk and the launch region of the dusty wind which primarily emits in the near-IR. This makes the near-IR an important regime to test the disk+wind model. So far, AGN have been less studied with near-IR interferometry than with mid-IR interferometry. Weigelt et al. (2012) studied NGC 3783 using AMBER; they report a hot, 1400K, thin dust ring fit. Further observations have revealed a geometrically thin disk is responsible for the hot dust emission. Kishimoto et al. (2009, 2011a) reported that near-IR interferometry was likely tracing the sublimation radius of the AGN using Keck observations which agrees with the discovered thin ring/disk. Furthermore, a recent breakthrough observation of NGC 1068 with GRAVITY produced an image of the hot dust which could be

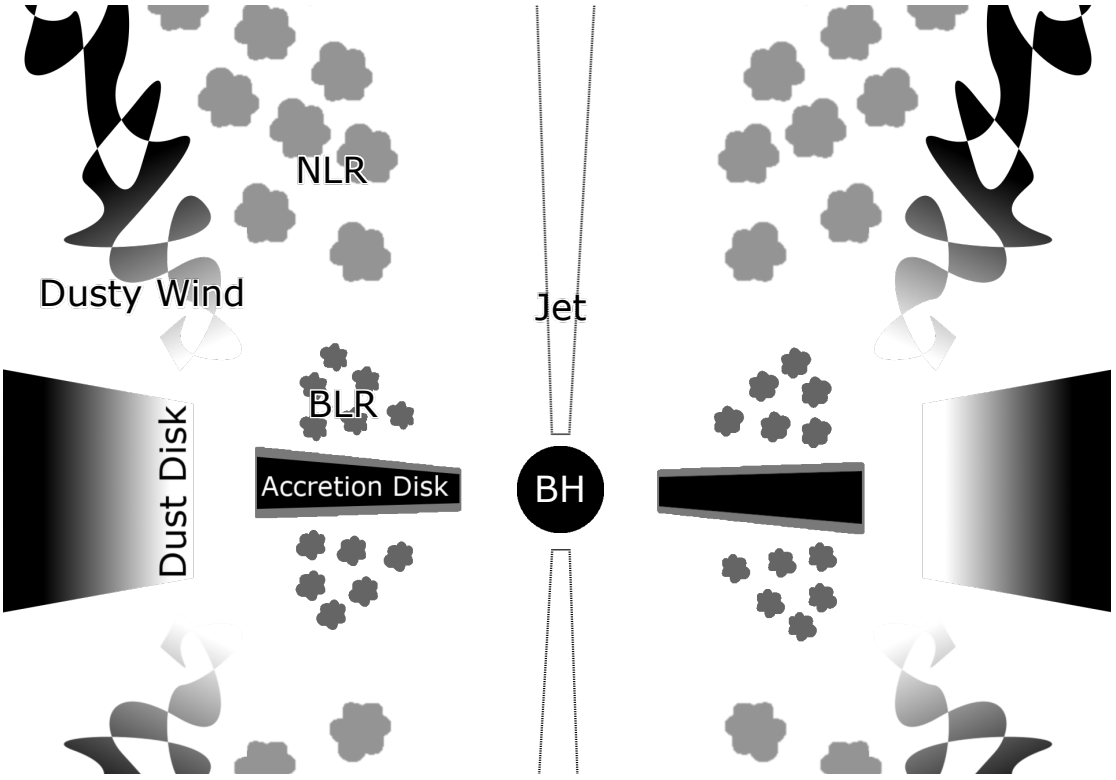

FIGURE 1.4: A cross section diagram of the layout of the dusty wind model of AGN. The corona is depicted in grey around the accretion disk, all other components are as labelled. Sizes are not to scale.

explained by a thick clumpy hot dust ring/disk (Gravity Collaboration et al., 2020). The disk component can be explained in the disk+wind model as the hot dust disk, thought to be responsible for the bulk of the near-IR emission. However, the ring like emission can also be explained in the classic torus model as the expected sublimation radius inside the torus. Further study of the near-IR dust distribution is needed to distinguish the two.

1.7.3 The molecular gas

The main focus of this work is the dust in AGN which is best observed with IR continuum emission. However, where there is dust there is gas and in astronomy it is common practice to use molecular lines such as CO to trace dense gas (e.g. García-Burillo et al., 2014). ALMA (Atacama Large Millimetre/submillimetre Array) provides high angular resolution images, at mm wavelengths, which can have a resolution up to 20 mas depending on the antenna configuration and observation frequency chosen. The angular resolution is approaching the predicted spatial scales of the putative tori. While it is difficult to say exactly which dust will be traced by which gases, the molecular lines allow for the acquisition of something that cannot be found with continuum measurement: kinematics. Kinematics give a whole new layer of information about the structure of an object. Continuum can show the distribution of an emitter but kinematics can tell if it is inflowing, outflowing, or in orbit. However, molecular gas lines only give the kinematics

of the molecular gas directly and the dust kinematics can only be inferred from this. Recent observations of AGN have shown that the molecular gas forms disks and outflows (e.g. Gallimore et al., 2016; Combes et al., 2019).

1.8 Motivation and Outline of this Work

The polar dust models are in direct contention with the torus model that is still prevalent in the field of AGN (Hönig and Kishimoto, 2017; Hönig, 2019). One of the points of contention is the polar extensions in the mid-IR (e.g. López-Gonzaga et al., 2016). With the current sample of polar extended objects, it can be argued that the observations are consistent with the torus model; this is because the six studied Type 2 AGN can be explained by illumination effects of the inner edge of the dusty torus and there is only one Type 1 in the sample (Schartmann et al., 2005, 2008). The single Type 1 can then be attributed to a chance illumination of the torus by a warped accretion disk in such a way that it appears polar extended. Warped disks are known to exist (e.g. Tristram et al., 2014) and they could cause parts of the inner torus edge to appear brighter than others. Furthermore, in the near-IR the current observations are consistent with both models.

In this work, my aim is to thoroughly test the distribution of dusty material and molecular gas. By utilising high angular resolution interferometry I will attempt to test which, if either, model is the better descriptor of the AGN dust structure. A study into more AGN with MIDI will allow me to distinguish between the polar dust and torus models in the mid-IR. Furthermore, a larger sample could allow for a study of changes in dust distribution with driving mechanisms which should be present in the dusty wind model. A study of high resolution near-IR observations may allow for the geometry of the hot dust to be constrained and, if the polar dust model is correct, the launch region of the dusty wind could also be constrained.

Chapter 2 gives a detailed overview of the theory behind interferometry. Chapter 3 provides the details behind the reduction of the observations used in this work. Chapter 4 is the complete study of ESO 323-G77 in the mid-IR using MIDI. In Chapter 5, I study ESO 323-G77 in the near-IR using GRAVITY and attempt to gain insight into the geometry of the hot dust. In Chapter 6, I delve into the relationship between radiation pressure and the distribution of dust in AGN. Chapter 7 is a look into the central molecular gas emission in NGC 3783 and here I attempt to create a working understanding of the kinematics and geometry. Finally, in Chapter 8 I summarise this work and draw my final conclusions.

Chapter 2

Interferometry: An Overview

Long baseline IR interferometry has proven to be an effective way to resolve IR thermal emission on the small angular scales of the putative dusty torus. MIDI is a two telescope mid-IR beam combiner that can use any Unit Telescope (UT) or Auxiliary Telescope (AT) pair at the VLTI. AMBER is a three telescope near-IR beam combiner capable of using three UT's or AT's. AMBER and MIDI have successfully been utilised to resolve the dusty structure in AGN. However, MIDI was decommissioned in 2015 and AMBER was decommissioned after the 2018 observing period (P101). Both instruments have a successor, MIDI was replaced with MATISSE (The Multi AperTure mid-Infrared SpectroScopic Experiment, Lopez et al., 2014) and AMBER was replaced with GRAVITY (GRAVITY Collaboration et al., 2017). Both of these new instruments can simultaneously use 4 UT's or AT's. Both instruments are already in use at the VLTI and promise to expand the pool of feasible AGN thanks to their fainter limiting magnitudes and the reduced observation time required per AGN.

I make use of MIDI, AMBER, and GRAVITY in this work. I also analyse observations from ALMA. All these instruments are interferometers. Therefore, in this chapter I will explore the fundamentals of interferometry for different numbers of telescopes before exploring the instrumentation and observational data in proceeding chapters.

2.1 The Two Telescope Case

An interferometer is an instrument that receives light from multiple telescopes and coherently combines it. The simplest form of interferometer is that of two telescopes. In the two telescope case the interferometer can be likened to Young's double pinhole experiment (Young, 1804) or, in the case of MIDI, the Michelson-Morley interferometer (Michelson and Morley, 1887). The pinholes of Young's experiment (see Figure 2.1) are the telescopes and the screen is the instrument, e.g. MIDI. The following derivation for the two telescope case was originally performed in the work of Tristram (2007). Much of the derivation itself is adapted from this work.

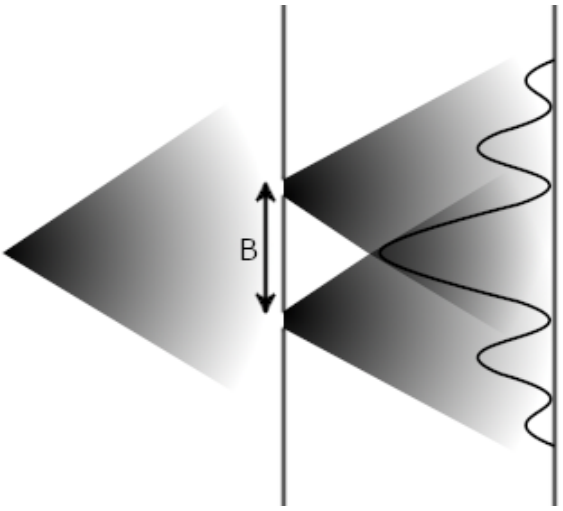

FIGURE 2.1: A graphical representation of Young's double slit/pinhole experiment.

2.1.1 Young's double slit experiment with a monochromatic point source

Let us define the position of two telescopes T_1 and T_2 as $\vec{x}_1$ and $\vec{x}_2$, The baseline vector $\vec{B}$ is defined as the difference between these vectors, $\vec{B} = \vec{x}_2 - \vec{x}_1$ with the baseline length of the setup $B = |\vec{B}|$ denoting the distance between the two telescopes. Each telescope is directed towards the target source S. The source is placed at an infinite distance, and the direction of the source with respect to the centre of the baseline is represented by the unit vector $\vec{s}$. As a first approximation, I will assume the source is point like and monochromatic. Therefore, the light that arrives at each telescope can be defined as

$$\begin{aligned} \vec{E}_1 &= \vec{E}_{1,0} e^{i\vec{k}\vec{x}_1 - i\omega t} \\ \vec{E}_2 &= \vec{E}_{2,0} e^{i\vec{k}\vec{x}_2 - i\omega t}, \end{aligned} \tag{2.1}$$

where the angular frequency $\omega = 2\pi\nu$ and the wave vector $\vec{k} = -2\pi\vec{s}/\lambda = -k\vec{s}$. Substituting $\vec{B} = \vec{x}_2 - \vec{x}_1$ gives

$$\vec{E}_2 = \vec{E}_{2,0} e^{i\vec{k}\vec{x}_1 + i\vec{k}\vec{B} - i\omega t} \tag{2.2}$$

The common phase component of $i\vec{k}\vec{x}_1$ can be omitted from each wave (Equation 2.3). The phase difference between each wave at the telescopes, therefore, only depends on $\vec{sB}$, i.e. the difference in optical path length of the two telescopes.

$$\begin{aligned} \vec{E}_1 &= \vec{E}_{1,0} e^{-i\omega t} \\ \vec{E}_2 &= \vec{E}_{2,0} e^{i\vec{k}\vec{B} - i\omega t} \end{aligned} \tag{2.3}$$

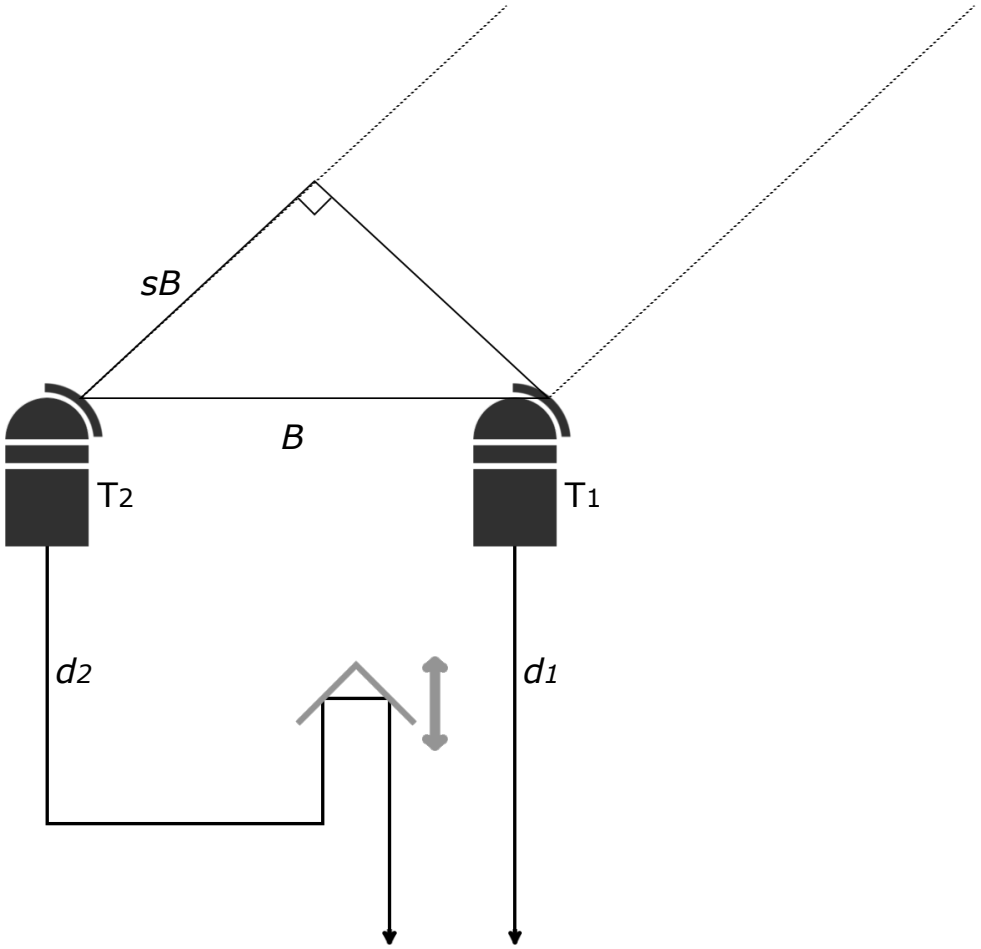

FIGURE 2.2: A diagram illustrating a simplified layout of the optical light path of a two telescope interferometer. In grey is a movable mirror that can adjust the length of d_2 The two paths are fed into the instrument.

Equation 2.3 is the form the light waves take upon arrival at the telescopes. On their way to the instrument detector, the waves propagate down two separate light paths with length d_1 and d_2 (Figure 2.2). After propagating down each path, the two waves take the form

$$\begin{aligned} \vec{E}_1 &= \vec{E}_{1,0} e^{ikd_1} e^{-i\omega t} \\ \vec{E}_2 &= \vec{E}_{2,0} e^{ikd_2} e^{i\vec{k}\vec{B} - i\omega t} \end{aligned} \tag{2.4}$$

Equation 2.4 may be what arrives at the detector, however, the detector measures the time averaged intensity, I, defined as $|\vec{E}|^2$ where $\vec{E} = \vec{E}_1 + \vec{E}_2$. Using Equation 2.4 to calculate I gives

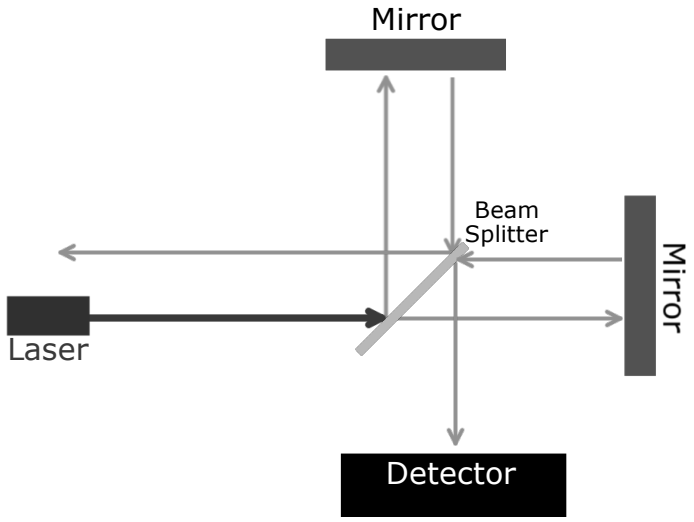

FIGURE 2.3: A representation of a Michelson-Morley interferometer, the arrows depict the light path.

$$\begin{aligned} I &= (\vec{E_1}+\vec{E_2})\cdot(\vec{E_1^*}+\vec{E_2^*}) \\ &= \vec{E_{1,0}^2}+\vec{E_{2,0}^2}+\vec{E}_{1,0}\vec{E}_{2,0}e^{ikd_1}e^{-ikd_2}e^{-i\vec{k}\vec{B}}+\vec{E}_{1,0}\vec{E}_{2,0}e^{ikd_2}e^{i\vec{k}\vec{B}}e^{-ikd_1} \\ &= I_1+I_2+\sqrt{I_1I_2}e^{ik(d_1-d_2+\vec{sB})}+\sqrt{I_1I_2}e^{-ik(d_1-d_2+\vec{sB})} \end{aligned} \tag{2.5}$$

By convention the total optical path difference (OPD) of $d_1-d_2+\vec{sB}$ is defined as δ. To simplify the equation further the relation $2\cos\theta = e^{i\theta}+e^{-i\theta}$ is used. Unfortunately, because real world systems are non-ideal $I_{1,0} \neq I_{2,0}$. The inequality could be due to differences in optical transmission or light collection area for example. Therefore, each telescope is assigned an efficiency η such that $I_x = \eta_x I_s$ where I_s is the source intensity. So equation 2.5 becomes

$$I = I_s(\eta_1+\eta_2+2\sqrt{\eta_1\eta_2}\cos k\delta) \tag{2.6}$$

Equation 2.6 is what would be measured by an interferometer if the combination of the beams took place on the detector. Detector plane interference is known as a Fizeau type interferometer. However, as mentioned previously for the case of MIDI, the interferometer is a Michelson type which bears a resemblance to the famous Michelson-Morley experiment (Figure 2.3). The key difference is that the beam combination happens in the pupil plane. After the light enters the telescopes and travels down the optical paths, it is not fed onto a detector but into a beam combiner, which is a half silvered mirror. There the beams are made coplanar and then fed onto the detector (Figure 2.4). Therefore, it is the interference at the beam combiner that is important.

Upon interaction with the light, the beam combiner transmits a fractional amount t of the time averaged intensity and reflects r. When the electromagnetic wave is reflected it gains a phase

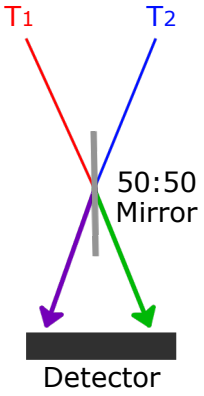

FIGURE 2.4: A representation of a Michelson type detector, the arrows depict the light path.

shift of $e^{i\frac{\pi}{2}}$. After combination each wave takes the form

$$\begin{aligned} \vec{E_1'} &= \sqrt{t}\vec{E_1} + \sqrt{r}\vec{E_2}e^{i\frac{\pi}{2}} \\ \vec{E_2'} &= \sqrt{t}\vec{E_2} + \sqrt{r}\vec{E_1}e^{i\frac{\pi}{2}} \end{aligned} \tag{2.7}$$

Repeating Equation 2.5 for each of these separate interfered waves yields

$$\begin{aligned} I_1' &= (\sqrt{t}\vec{E_1} + \sqrt{r}\vec{E_2}e^{i\frac{\pi}{2}}) \cdot (\sqrt{t}\vec{E_1^*} + \sqrt{r}\vec{E_2^*}e^{-i\frac{\pi}{2}}) \\ &= t\vec{E}_{1,0}^2 + r\vec{E}_{2,0}^2 + \sqrt{t}\vec{E}_{1,0}\sqrt{r}\vec{E}_{2,0}e^{ikd_1}e^{-ikd_2}e^{-i\vec{k}\vec{B}}e^{-i\frac{\pi}{2}} + \sqrt{t}\vec{E}_{1,0}\sqrt{r}\vec{E}_{2,0}e^{ikd_2}e^{i\vec{k}\vec{B}}e^{-ikd_1}e^{i\frac{\pi}{2}} \\ &= tI_1 + rI_2 + \sqrt{tI_1rI_2}e^{ik\delta}e^{-i\frac{\pi}{2}} + \sqrt{tI_1rI_2}e^{-ik\delta}e^{i\frac{\pi}{2}} \\ &= tI_1 + rI_2 + \sqrt{tI_1rI_2}(e^{i(k\delta-\frac{\pi}{2})} + e^{-i(k\delta-\frac{\pi}{2})}) \\ &= tI_1 + rI_2 + 2\sqrt{tI_1rI_2}(\cos(k\delta - \frac{\pi}{2})) \\ I_1' &= tI_1 + rI_2 + 2\sqrt{tI_1rI_2}\sin k\delta \end{aligned} \tag{2.8}$$

and

$$\begin{aligned} I_2' &= (\sqrt{t}\vec{E_2} + \sqrt{r}\vec{E_1}e^{i\frac{\pi}{2}}) \cdot (\sqrt{t}\vec{E_2^*} + \sqrt{r}\vec{E_1^*}e^{-i\frac{\pi}{2}}) \\ &= r\vec{E}_{1,0}^2 + t\vec{E}_{2,0}^2 + \sqrt{r}\vec{E}_{1,0}\sqrt{t}\vec{E}_{2,0}e^{-ikd_1}e^{ikd_2}e^{i\vec{k}\vec{B}}e^{-i\frac{\pi}{2}} + \sqrt{r}\vec{E}_{1,0}\sqrt{t}\vec{E}_{2,0}e^{-ikd_2}e^{-i\vec{k}\vec{B}}e^{ikd_1}e^{i\frac{\pi}{2}} \\ &= rI_1 + tI_2 + \sqrt{rI_1tI_2}e^{ik\delta}e^{i\frac{\pi}{2}} + \sqrt{rI_1tI_2}e^{-ik\delta}e^{-i\frac{\pi}{2}} \\ &= rI_1 + tI_2 + \sqrt{rI_1tI_2}(e^{i(k\delta+\frac{\pi}{2})} + e^{-i(k\delta+\frac{\pi}{2})}) \\ &= rI_1 + tI_2 + 2\sqrt{rI_1tI_2}(\cos(k\delta + \frac{\pi}{2})) \\ I_2' &= rI_1 + tI_2 - 2\sqrt{rI_1tI_2}(\sin k\delta) \end{aligned} \tag{2.9}$$

These beams have opposite phase and therefore can be subtracted to extract the interferometric component:

$$\begin{aligned} I &= I_1' - I_2' \\ &= tI_1 + rI_2 + 2\sqrt{tI_1 rI_2}\sin k\delta - rI_1 - tI_2 + 2\sqrt{rI_1 tI_2}(\sin k\delta) \\ &= (t-r)I_1 + (r-t)I_2 + 4\sqrt{tI_1 rI_2}\sin k\delta \\ &= (t-r)(I_1 - I_2) + 4\sqrt{trI_1 I_2}\sin k\delta \end{aligned} \tag{2.10}$$

$$I = I_s[(t-r)(\eta_1 - \eta_2) + 4\sqrt{tr\eta_1\eta_2}\sin k\delta]$$

For an ideal beam splitter, $t = r = 0.5$ and for an ideal telescope $\eta = 1$. Therefore the first term cancels and the intensity simplifies to

$$I = 2I_s \sin k\delta. \tag{2.11}$$

Therefore, in an ideal case, Equation 2.11 is what is expected for a monochromatic point source.

2.1.2 A step towards realism: the extended polychromatic source

Real sources are not monochromatic. Therefore, the next step is to repeat the derivation for a polychromatic point source. A polychromatic source has a source intensity I_s that has a dependence on k. The telescope and instrument also have a finite passband and, therefore, η_1, η_2, r, and t also depend on k.

Light at different wavelengths are mutually uncorrelated which allows for the polychromatic case to be treated as the sum of monochromatic sources with different k. To simplify things, I will only consider the interferometric contribution.

$$I = 4\int I_s(k)\sqrt{t(k)r(k)\eta_1(k)\eta_2(k)}\sin k\delta \, \mathrm{d}k \tag{2.12}$$

Extended sources can be treated in much the same way. An extended source can be interpreted as a collection of incoherent point sources with different pointings. Therefore, I integrate over $\vec{s}$:

$$\begin{aligned} I &= 4\sqrt{tr\eta_1\eta_2}\int I_s(\vec{s})\sin(k(d_1-d_2+\vec{sB}))\,\mathrm{d}\vec{s} \\ &= \frac{2\sqrt{tr\eta_1\eta_2}}{i}\left[\int I_s(\vec{s})e^{ik(d_1-d_2+\vec{sB})}\,\mathrm{d}\vec{s} - \int I_s(\vec{s})e^{-ik(d_1-d_2+\vec{sB})}\,\mathrm{d}\vec{s}\right] \\ &= \frac{2\sqrt{tr\eta_1\eta_2}}{i}\left[e^{ik(d_1-d_2)}\int I_s(\vec{s})e^{ik\vec{sB}}\,\mathrm{d}\vec{s} - e^{-ik(d_1-d_2)}\int I_s(\vec{s})e^{-ik\vec{sB}}\,\mathrm{d}\vec{s}\right] \end{aligned} \tag{2.13}$$

A Fourier transform is defined as

$$\mathcal{F}\{g(t)\} = G(f) = \int_{-\infty}^{\infty} g(t)e^{-2\pi ift}\,\mathrm{d}t \tag{2.14}$$

and because $k = 2\pi/\lambda$, in Equation 2.13 each integral can be defined as the Fourier transform of $I_s(\vec{s})$.

$$\mathcal{V}(\vec{B}/\lambda) = \int I_s(\vec{s})e^{-2\pi i\vec{sB}/\lambda}\,\mathrm{d}\vec{s} \tag{2.15}$$

$\mathcal{V}(\vec{B}/\lambda)$ is known as the complex visibility. The complex visibility is complex and can instead be written as an absolute and phase component

$$\mathcal{V}(\vec{B}/\lambda) = \tilde{I}(\vec{B}/\lambda)e^{i\phi(\vec{B}/\lambda)} \tag{2.16}$$

The Fourier transform of a real function is Hermitian, i.e., $\mathcal{V}(-\vec{B}/\lambda) = \mathcal{V}^*(\vec{B}/\lambda)$. Therefore, if the two telescopes are swapped only the phase changes sign. When considering the interferometric data, generally the normalised visibility is used. The normalised visibility, in most cases, can be thought of as how resolved an object is to the interferometer; it is the coherently summed flux of a source compared to the total flux. The normalised visibility is defined as

$$V(\vec{B}/\lambda) = \frac{|\mathcal{V}(\vec{B}/\lambda)|}{|\mathcal{V}(\vec{0})|} = \frac{\tilde{I}(\vec{B}/\lambda)}{\tilde{I}(\vec{0})} \tag{2.17}$$

However,

$$\begin{aligned} \tilde{I}(\vec{0}) &= |\mathcal{V}(\vec{0})| = \left|\int I_s(\vec{s})e^{-2\pi i0}\,\mathrm{d}\vec{s}\right| \\ &= I_s \end{aligned} \tag{2.18}$$

Therefore, Equation 2.13 can be rewritten as

$$\begin{aligned} I &= \frac{2\sqrt{tr\eta_1\eta_2}}{i}\left[e^{ik(d_1-d_2)}\mathcal{V}(\vec{B}/\lambda)-e^{-ik(d_1-d_2)}\mathcal{V}(-\vec{B}/\lambda)\right] \\ &= \frac{2\sqrt{tr\eta_1\eta_2}}{i}\left[e^{ik(d_1-d_2)}\tilde{I}(\vec{B}/\lambda)e^{i\phi(\vec{B}/\lambda)}-e^{-ik(d_1-d_2)}\tilde{I}(\vec{B}/\lambda)e^{-i\phi(\vec{B}/\lambda)}\right] \\ &= 4\tilde{I}(\vec{B}/\lambda)\sqrt{tr\eta_1\eta_2}\sin\left(k(d_1-d_2)+\phi(\vec{B}/\lambda)\right) \\ I &= 4V(\vec{B}/\lambda)I_s\sqrt{tr\eta_1\eta_2}\sin\left(k(d_1-d_2)+\phi(\vec{B}/\lambda)\right) \end{aligned} \tag{2.19}$$

The visibility can then be determined from the detector intensity. If the amplitude of the intensity on the detector is measured, the sine component becomes 1 and the visibility becomes

$$V(\vec{B}/\lambda) = \frac{I_A}{4I_s\sqrt{tr\eta_1\eta_2}}. \tag{2.20}$$

2.1.3 Real world measurements

Equation 2.20 gives the visibility, $V(\vec{B}/\lambda)$, which is what is usually measured in IR interferometry; or in MIDI's case, the correlated flux $\tilde{I}(\vec{B}/\lambda)$ is measured and used to calculate the visibility. However, if the visibility was determined for every value of $\vec{B}$ it would not be possible to reconstruct an image of the source. Because an interferometer sees the Fourier transform of the intensity distribution, to truly reconstruct the source the complex visibility ($\mathcal{V}(\vec{B}/\lambda)$) would be needed. As can be seen from Equation 2.16, image reconstruction would require the visibility and the phase.

In a perfect system the phase could be determined for each baseline. However, in reality the atmosphere complicates the phase determination by introducing an unknown and fluctuating phase component. The phase can be corrected with a phase reference which is an object that has a known phase. The reference would have to be observed in simultaneity as the atmosphere fluctuates rapidly. The atmospheric component of the phase can be determined by taking the difference between the observed phase and the known phase. Observing a reference is not always possible, therefore, for the two telescope case I will not explicitly use the phase in modelling.

The phase is responsible for the small scale detail and any offset in the photocentre. The phase carries significant information but it does not mean the visibility by itself is useless. The visibility contains information about large scale fluctuations in brightness distributions and, with relatively few observations, simplistic source structures such as disks and Gaussians can thus be inferred. This is useful because many sources in astronomy have overarching geometry that can be explained by these simple models.

2.1.4 Visibilities of simple models

Here I will explore the two simple models that are frequently used in this work, a point source and a Gaussian.

The point source can be represented by a 2D Dirac delta function. In the two telescope case, the interferometer is only sensitive in the direction of the baseline. Therefore, only the brightness distribution projected onto the axis parallel to the baseline is measured. The problem then becomes 1D. To calculate the projected brightness distribution, I integrate over the component perpendicular to the baseline. I define m as parallel to the baseline and n as perpendicular.

Therefore,

$$\begin{aligned} I(u) &= I_0 \int \delta(m-m_0)\delta(n-n_0)\mathrm{d}n \\ &= I_0\delta(m-m_0) \end{aligned} \tag{2.21}$$

As was discovered in Section 2.1.2, $\mathcal{V}(m)$ is the Fourier transform of $I(m)$. As described by Equation 2.15,

$$\begin{aligned} \mathcal{V}(B/\lambda) &= I_0 \int_{-\infty}^{\infty} \delta(m-m_0)e^{-2\pi imB/\lambda}\,\mathrm{d}m \\ &= I_0 e^{-2\pi m_0 iB/\lambda} \end{aligned} \tag{2.22}$$

The normalised visibility from Equation 2.17 is then

$$\begin{aligned} V(B/\lambda) &= |e^{-2\pi m_0 iB/\lambda}| \\ &= 1 \end{aligned} \tag{2.23}$$

The normalised visibility of a point source is a constant. For a true point source, no baseline length will change the visibility. Of course, in the real world there are no true point sources and structure will eventually be resolved with a large enough separation of telescopes. However, many objects are adequately described by a point source with the current limitations of baseline length hence its inclusion in this work.

For the Gaussian I will again start with the projected 1D case. The projection of an elliptical 2D Gaussian of arbitrary major and minor axis σ is again a Gaussian. Therefore $I(m)$ can be described as

$$I(m) = I_0 e^{-\frac{m^2}{2\sigma^2}} \tag{2.24}$$

Then, again, the Fourier transform gives the visibility.

$$\mathcal{V}(B/\lambda) = I_0 \int_{-\infty}^{\infty} e^{-\frac{m^2}{2\sigma^2}} e^{-2\pi i m B/\lambda} \, \mathrm{d}m \tag{2.25}$$

It is easier to write the exponential introduced by the Fourier transform as its sine and cosine components.

$$\begin{aligned} \mathcal{V}(B/\lambda) &= I_0 \int_{-\infty}^{\infty} e^{-\frac{m^2}{2\sigma^2}} [\cos(2\pi m B/\lambda) - i \sin(2\pi m B/\lambda)] \, \mathrm{d}m \\ &= I_0 \int_{-\infty}^{\infty} e^{-\frac{m^2}{2\sigma^2}} \cos(2\pi m B/\lambda) \, \mathrm{d}m - \int_{-\infty}^{\infty} i e^{-\frac{m^2}{2\sigma^2}} \sin(2\pi m B/\lambda) \, \mathrm{d}m \end{aligned} \tag{2.26}$$

The separated integrals can be evaluated separately. The sine integral is odd and evaluates to zero, the cosine integral is given by Abramowitz and Stegun (1970) and evaluates as follows:

$$\mathcal{V}(B/\lambda) = I_0 \sqrt{2\sigma^2 \pi} e^{-2\pi^2 \sigma^2 (B/\lambda)^2}. \tag{2.27}$$

The normalised visibility is then

$$V(B/\lambda) = e^{-2(\pi \sigma B/\lambda)^2}. \tag{2.28}$$

Equation 2.28 is the generic result for one observation of a two telescope interferometer. However, unlike the point source the geometry will change with the orientation of the source relative to the baseline if the major and minor axis are not equal. Therefore, I redefine m and n as an orthogonal arbitrary set of axis. Classically, the axis are orientated along the cardinal directions where m is east and n is north. The 2D Gaussian equation, where the Gaussian's major and minor axis coincide with m and n, is then

$$I(m,n) = I_0 e^{-\frac{n^2}{2\sigma_n^2}} e^{-\frac{m^2}{2\sigma_m^2}} \tag{2.29}$$

Because Equation 2.29 is just the product of two Gaussians, the 2D Fourier transform is of the same form as the 1D case.

$$V(u,v) \quad = \quad e^{-2(\pi\sigma_m u)^2} e^{-2(\pi\sigma_n v)^2}. \tag{2.30}$$

Where u and v are parallel to m and n and $B/\lambda = \sqrt{u^2+v^2}$. To find the generalisation of Equation 2.30 to a 2D Gaussian that has a major axis at an angle θ from n, the axis rotation matrix can be applied. The axis rotation can be applied in Fourier space such that

$$\begin{bmatrix} \cos\theta & -\sin\theta \\ \sin\theta & \cos\theta \end{bmatrix} \cdot \begin{bmatrix} u \\ v \end{bmatrix} \quad = \quad \begin{bmatrix} u\cos\theta - v\sin\theta \\ u\sin\theta + v\cos\theta \end{bmatrix} \tag{2.31}$$

I define u' as $u\cos\theta - v\sin\theta$ and v' as $u\sin\theta + v\cos\theta$. Equation 2.30 becomes

$$V(u,v) \quad = \quad e^{-2(\pi\sigma_n)^2(\frac{u'^2}{\epsilon^2}+v'^2)} \tag{2.32}$$

where ϵ is the axis ratio of the Gaussian, i.e. $\epsilon = \sigma_n/\sigma_m$.

The Gaussian source case highlights a commonly encountered observation effect in inteferometry. Because interferometers usually have a shortest baseline length that is much greater than the individual telescope dish size, it is possible to have a case where an unresolved object in single dish imaging is over-resolved to the interferometer. Being over-resolved means that the object is on a larger scale than the interferometer can see. The visibility from an over-resolved Gaussian is ~ 0 and it is not possible to determine the structure responsible for the drop in visibility without additional shorter baselines.

2.1.5 The *uv* plane

When comparing multiple observations with differing $\vec{B}$, a common reference frame is required. In the previous section I introduced the coordinates u and v where u is parallel to East and v is parallel to North. The coordinate system is commonly referred to as the *uv* plane. When an observation is taken with a vector $\vec{B}$, a point in the *uv* plane is sampled. By sampling enough points the original image can be reconstructed.

To cover enough of the *uv* plane with a small number of telescopes, the separation of the telescopes and their PA must be changed. In the real world filling the *uv* plane is problematic as the telescopes are usually immobile, as in the case of the UTs at the VLTI, or can only be moved to a number of specific locations, as in the case of the ATs.

The only way the distance between the telescopes at a set PA can be modified is to change the observing wavelength. However, you may not observe the same structures in an object

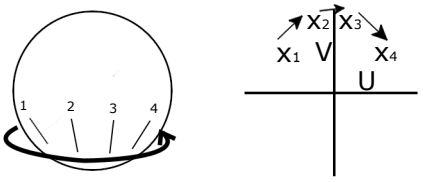

FIGURE 2.5: Left: The circle depicts Earth and each line depicts two telescopes on the surface at four intervals as it rotates. Right: The plot depicts the change in location of the telescopes, observing a fixed source, on the *uv* plane at each location as the Earth rotates. For example, X_1 corresponds to location 1, at a time later the telescopes move to location 2 and, therefore, X_2.

at a different wavelength so caution must be applied. Conversely, the PA of the telescopes is something that can be changed without changing the geolocations of the telescopes.

It is possible to take advantage of the Earth's rotation. Because it is the projected baseline that is important, as the Earth rotates it changes the relative position of the telescopes on sky (Figure 2.5). Using the Earth's rotation, more of the *uv* plane can be sampled than would otherwise be possible using fixed telescopes. The path the telescopes trace out on the *uv* plane as the Earth rotates is known as a *uv* track. This allows greater constraint in modelling the *uv* plane or, in some cases, the use of image reconstruction.

2.2 The Three Plus Telescope Case

Accommodating for an extra telescope is not as complicated as it may initially appear. Where as the two telescope case offered one distinct baseline, three telescopes offer three distinct telescope pairs and therefore three baselines. These three baselines can be treated independently for visibility determination and differential phase. This continues with the addition of more telescopes at the rate of $N_b = \frac{N_t^2 - N_t}{2}$ where N_b is the number of baselines and N_t is the number of telescopes.

In some IR interferometers, the light for each baseline is interfered separately. This leads to the unfortunate need to split the light from each telescope into parts. In the ideal case, the fractional amount of light from each telescope that is sent to each baseline is $(N_t - 1)^{-1}$.

There are a number of reasons that more than two telescopes would be used. One reason is time. Each observation of the source, and associated calibrators, takes time. MIDI, for example, can spend many hours per source trying to fill the *uv* plane one *uv* point at a time. Three telescopes give three baselines, and therefore, three *uv* points per observation. This allows the *uv* plane to be filled at a greater rate. The second reason relates to phase determination using something called the closure phase.

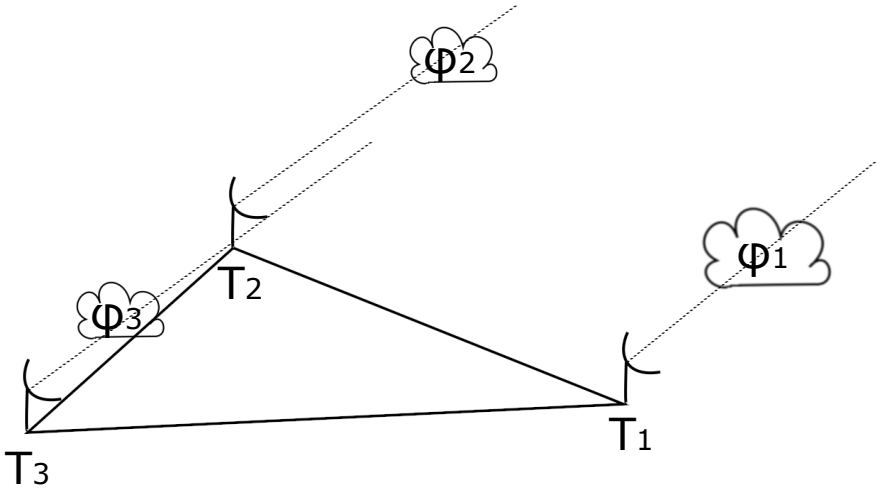

FIGURE 2.6: This figure shows a diagram of the phase introduced by the atmosphere to each telescope in the three telescope case.

2.2.1 Closure phase

As was mentioned in Section 2.1.3, the atmosphere introduces a dynamic phase component that is difficult to remove from the source phase. One solution is calculating the closure phase.

The closure phase is simply the summation of the phases from three baselines, observed in simultaneity, that share three telescopes. For a generic source morphology, a pair of telescopes, labelled T_1 and T_2, will measure a phase Φ_{12}. This will be the composite of the source phase as seen by that baseline, ϕ_{12}, and the atmospheric phase component of each telescope, $\varphi_1 - \varphi_2$ (Figure 2.6).

In the case of three telescopes, the phase of each baseline can be written in a similar manner.

$$\begin{aligned} \Phi_{12} &= \phi_{12} + \varphi_1 - \varphi_2 \\ \Phi_{23} &= \phi_{23} + \varphi_2 - \varphi_3 \\ \Phi_{31} &= \phi_{31} + \varphi_3 - \varphi_1 \end{aligned} \tag{2.33}$$

Therefore the summation of these phases yields

$$\begin{aligned} \Phi_{12} + \Phi_{23} + \Phi_{31} &= \phi_{12} + \phi_{23} + \phi_{31} + \varphi_1 - \varphi_1 + \varphi_2 - \varphi_2 + \varphi_3 - \varphi_3 \\ &= \phi_{12} + \phi_{23} + \phi_{31}. \end{aligned} \tag{2.34}$$

The final product of the summation contains no atmospheric component. The three source phase components cannot be disentangled and, therefore, this phase does not allow for image

reconstruction. It does, however, provide an invaluable constraint when modelling by providing a second modellable observable quantity that is sensitive to source asymmetries.

The closure phase can also be calculated using a quantity called the bispectrum. The bispectrum is defined as the product of the complex visibility of each baseline.

$$\begin{aligned} \mathcal{B}_{123} &= \mathcal{V}_{12}\mathcal{V}_{23}\mathcal{V}_{13}^{*} \\ &= \mathcal{V}_{12}\mathcal{V}_{23}\mathcal{V}_{31} \end{aligned} \tag{2.35}$$

The closure phase is then the angle of the bispectrum:

$$\phi_{123} = \arctan\left(Im(\mathcal{B}_{123})/Re(\mathcal{B}_{123})\right) \tag{2.36}$$

Chapter 3

Observations and Data Reduction

In this chapter I will describe the observations strategy and reduction process for the main instruments used in Chapters 4, 6, 5, and 7. Any deviation from these reduction methods and the details of the observations for each chapter can be found in the chapter itself.

3.1 MIDI

MIDI (Leinert et al., 2003) is a two beam Michelson-type interferometer that operates in the N band (7.5 μm to 14.5 μm) at the VLTI. The two incoming beams from the telescopes, upon reaching the instrument, first encounter a beam splitter. The beam splitter splits each beam into two and sends one beam to the interferometer and one to the detector to be used for photometry (Figure 3.1). In the case of faint observations and of this work, the beam splitter is removed and 100% of the light is interfered; known as HIGH_SENSE mode. HIGH_SENSE mode is often used for faint targets. In HIGH_SENSE mode the photometry is observed separately. The two beams destined for the interferometer are then passed through the opposite faces of a half silvered mirror. The mirror produces two pupil plane interfered beams which have opposite phase. The beams are fed onto the detector and read separately. In front of the detector a filter, prism, or grism can be placed which intersects both the interfered beams and the photometry beams. The prism and grism spectrally disperse the beams with an R of 30 and 230 respectively. The interfered beams can then be subtracted from each other to calculate the interferometric component as in Equation 2.10.

MIDI has been decommissioned and all observations in this work were archival and not planned nor executed by me. Therefore, I will not discuss the observation strategy for MIDI here.

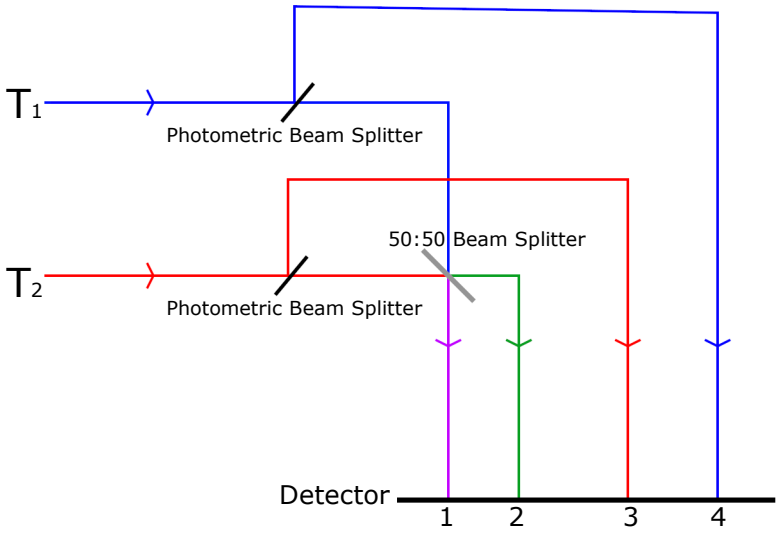

FIGURE 3.1: A simplified diagram of the MIDI instrument. The blue line is the uninterfered beam from telescope 1, the red line is the uninterfered beam from telescope 2, the green line and purple line are the interfered beams.

3.1.1 Observations

MIDI observations of an object are split into multiple stages which serve particular roles in the observation, these files are further split into parts for storage reasons which constitute separate files on the archive. Acquisition images are sometimes observed to check if the beams overlap properly. Fringe search is used to find the zero OPD position by making observations while methodically changing the OPD. Fringe track uses piezo controlled mirrors to oscillate the OPD over a set range and scan the fringe, in the offset tracked mode it adjusts the OPD to keep a consistent average distance of 40 μm from the fringe while oscillating. If the fringe is too dim, no-track mode can be used in which the average OPD is set and not changed throughout the observation although the piezo scanning still takes place. By rapidly scanning the fringe, MIDI can distinguish the instrumental and atmospheric delay during reduction allowing for their removal. Finally, the photometry for each telescope is recorded.

One of the biggest problems of IR inteferometry is the atmosphere. I mentioned previously that the atmosphere introduces a rapidly varying phase component, i.e., it changes the OPD between the two telescopes. The atmospheric change is a problem for observations because of a quantity called the coherence length. It is a consequence of Equation 2.12 that may not be immediately clear. By integrating over the N band and making the assumption that $\eta_x(k)$ is constant in the N band and 0 elsewhere, I get

$$I = 4\int_{k_0-\Delta k/2}^{k_0+\Delta k/2} I_s(k)\sqrt{t(k_0)r(k_0)\eta_1(k_0)\eta_2(k_0)}\sin k\delta\,\mathrm{d}k. \tag{3.1}$$

If I take a simple constant source intensity of $I_s(k)$=I_{k_0} the integral simplifies to

$$I = 4I_{k_0}\sqrt{t(k_0)r(k_0)\eta_1(k_0)\eta_2(k_0)}\int_{k_0-\Delta k/2}^{k_0+\Delta k/2}\sin k\delta\,\mathrm{d}k. \tag{3.2}$$

The integral solves to

$$\begin{aligned} I &= \int_{k_0-\Delta k/2}^{k_0+\Delta k/2}\sin k\delta\,\mathrm{d}k \\ &= \left[-\frac{\cos k\delta}{\delta}\right]_{k_0+\Delta k/2}^{k_0+\Delta k/2} \\ &= \delta^{-1}\left(\cos(k_0\delta-\delta\Delta k/2)-\cos(k_0\delta+\delta\Delta k/2)\right) \\ &= 2\delta^{-1}\sin(k_0\delta)\sin(\delta\Delta k/2) \\ &= \Delta k\sin(k_0\delta)\,\mathrm{sinc}(\delta\Delta k/2). \end{aligned} \tag{3.3}$$

The sinc function introduces a stipulation, it becomes small if $|\delta\Delta k/2| > \pi$. If $k = -2\pi/\lambda$ then $\mathrm{d}k = 2\pi\lambda^{-2}\mathrm{d}\lambda$. Therefore, the sinc function becomes small if $\lambda_0^2/\Delta\lambda \lesssim \delta$. The derived quantity is the coherence length and it is the change in path required for the fringes to be lost. For the N band the coherence length is approximately 22 μm. If the beams are spectrally dispersed with the prism, R= $\lambda_0/\Delta\lambda = 30$ which makes the coherence length a larger $R\lambda_0 \approx 0.3$ mm. If the atmosphere moves the delay line more than the coherence length while integrating then the fringes will be lost and the measured intensity, and therefore the visibility, will be erroneously lowered. There are two ways to combat the loss: make the integration shorter than the time it takes for the atmospheric OPD to change significantly or compensate for the change by moving the delay line. MIDI does the former. MIDI takes multiple observations with very short integration times which are called frames. In MIDI's tracking mode, the fringe tracker can then use the previously observed frames to adjust the OPD for the next frame.

For my reduction, the fringes and photometry are needed. In a standard observation, a fringe track is immediately followed by photometry although this is not necessary. Burtscher et al. (2012) recommend that the photometry is skipped and the science and calibrator object's fringe tracks are observed in sequence. Therefore, some observations do not have photometry immediately following the fringe track. All observations I reduced used the prism for spectral dispersion.

3.1.2 Reduction

For the reduction of MIDI data, I used an IDL program called EWS 2.0 from MIA+EWS 2.0 (Jaffe, 2004) with the addition of scripts from https://www.blackholes.de/downloads.html. These additional scripts were created by Dr. Konrad Tristram. While MIDI is a complex piece of machinery and the data produced is large and difficult to handle properly, the reduction pipeline is extremely powerful and makes the user side of the reduction process relatively straight forward. Here I will go over my reduction of the MIDI data, for a detailed overview of the theory and practice behind the reduction I direct you to read Chapter 3 of Tristram (2007) and Burtscher et al. (2012) for a description of the pipeline and Chapter 2 of this work for the theory.

3.1.2.1 Data sorting

First, to maximise signal to noise, all observations within 30 minutes were combined into a single observation. Grouping observations is highly recommended for faint sources by López-Gonzaga et al. (2016). They state that if an object is unresolved to a single dish telescope of size D then two *uv* points that have a separation of $\lesssim$D should not vary significantly and can be averaged. On the longest baseline the maximum distance you can move in 30 minutes on, say, ESO 323-G77, which features heavily in this work, is $\sim$ 14 m. The observations I present in this work are less separated than 14 m and it can be shown that all the objects in this work are unresolved or barely resolved to an 8.2 m telescope from Asmus et al. (2014). Therefore, I can average observations of less than 30 minute separation; the best way to average observations without making assumptions about error propagation is to treat them as one discontinuous observation during reduction. It is important to note that when combining files only observations of the same modes should be combined. No-track and tracked mode, for example, should be kept separate as well as prism and grism modes.

MIDI observations are split into three file groups, the photometry from the two telescopes and the interferometric data from the baseline. The observation files are often individually split into multiple pieces of 100 MB, due to their large size, on the ESO archive. Therefore, file combination is a part of the pipeline making it quite straight forward. When using the function midi_redset to perform the reduction, a single observation is defined as three strings where each string is sequence of space separated file locations. The three strings are for the first telescope's photometry, defined as A open, the second telescope's, defined as B open, and the inteferometric file, defined as AB open. Furthermore, midi_redset performs reduction for a list of observations allowing the reduction of an entire night at once. The full flowchart of how a night is reduced can be found in Figure 3.2.

The masks mentioned in Figure 3.2 are used to remove erroneous signal from detector pixels outside the location of the source signal when determining the correlated flux. An example of the fitted mask can be seen in Figure 3.3.

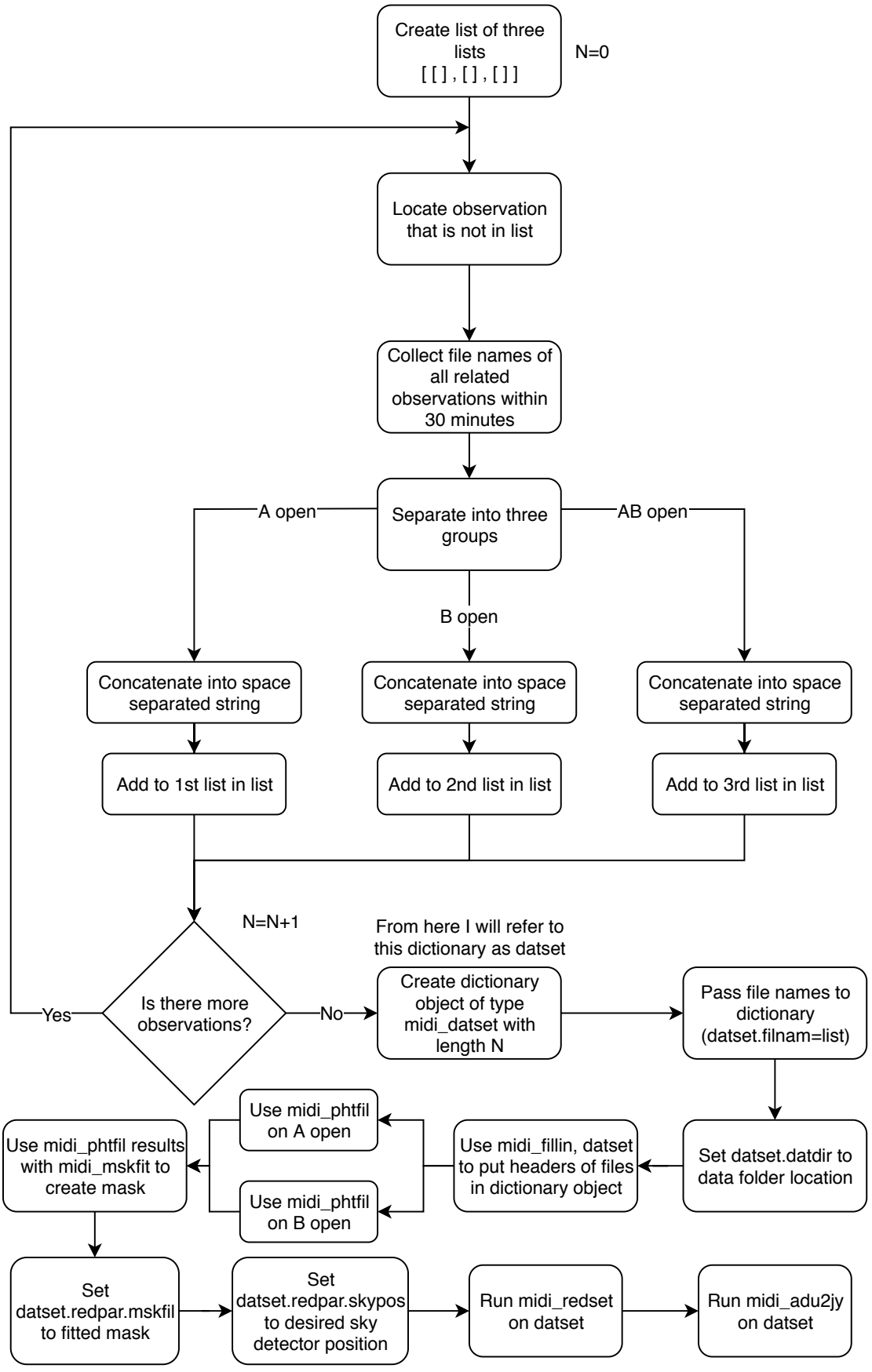

FIGURE 3.2: The flowchart of how a night of MIDI data are reduced and calibrated.

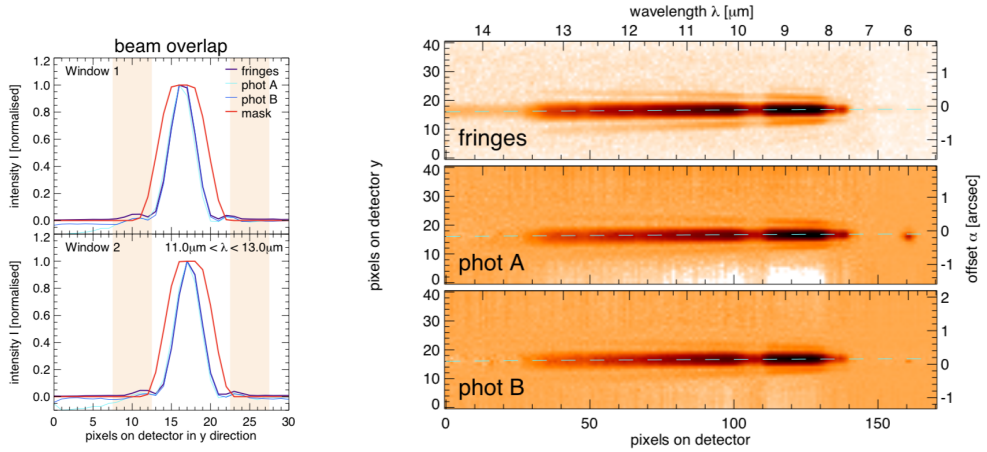

FIGURE 3.3: An example of the detector image and the fitted mask. The photometry on the left is a cross section from the detector image on the right. These images are produced using plotting scripts from https://www.blackholes.de/downloads.html.

3.1.2.2 Calibration

I perform the reduction in the same manner for science and calibrator objects. The reduction will produce an uncalibrated single-dish spectrophotometry and an uncalibrated correlated flux. To calibrate the science observations a calibrator that meets three basic requirements is needed. First, as a general rule for both quantities, the calibrator must be observed in the same mode as the science target.

Second, to calibrate the spectrophotometry, an object of known flux is needed. I divide the expected spectrum by the observed spectrum to get the conversion factor in Flux/ADU of each wavelength bin, where ADU stands for Arbitrary Detector Units. The uncalibrated science spectrum is multiplied by the conversion factor to receive the calibrated flux. Thankfully, there are a couple of catalogues of standard stars which match the second criteria (e.g. Cohen et al., 1999).

Third, to calibrate the correlated flux, an object of known correlated flux is needed. The correlated flux standard is more difficult than the spectrophotometric standard because you must know the objects geometry, as seen by the interferometer. The simplest solution is to use a point source. A point source, for example an unresolved star, has a known normalised visibility of 1. Therefore, from Equation 2.17, correlated flux = single-dish flux and the target's correlated flux can be calibrated in a similar manner to the spectrophotometry. Conveniently, many standard stars are unresolved to MIDI making the selection process simpler. www.jmmc.fr provide tools to help select good calibrators or to check if particular calibrators are known to be unsuitable.

By default, the standard star chosen was the closest one observed in time. However, all calibrators were reduced for the night, not just those relevant to the object of interest. For each of the calibrators, I calculate the ADU/Jy value and plotted it against time. What the plot shows is how the night changed in atmospheric quality. On a perfect night, the conversion factor would remain constant but changes in the atmosphere cause it to fluctuate. The fluctuation is a source of error

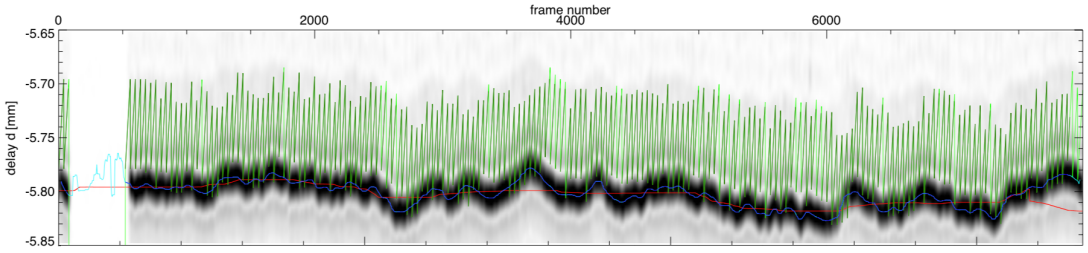

FIGURE 3.4: An example of a waterfall plot displaying the OPD of the delay line in green and the fringe in black for a bright calibrator. Any flagged frames show the OPD in light green.

while calibrating and it is why it is important for the calibrator to be taken close to the science target in time. If the ADU/Jy value changes significantly, greater than $\sim 10\%$ in the time frame between the calibrator and science, the interpolated ADU/Jy value between a calibrator either side of the target object should be taken instead when calibrating. A significant fluctuation did not occur for any of the observations in this work, however, there is still some variation which should be taken into account. In cases where there is more than four calibrators on a night, it is possible to create a structure function (SF).

An SF essentially quantifies how much a variable changes in x, on average, for a change in y where x and y are arbitrary. For my case, y is time and x is Jy/ADU. A SF is calculated by taking the absolute difference in two points in both x (dx) and y (dy), then repeating this for every non-degenerate pairing. By plotting dx and dy against each other, it is possible to extract the expected amount of change in x from a given change in y. For low numbers of data points it is necessary to model the SF. A SF is flat if the changes are random and it shows structure if they are not. In my case the SF would linearly increase to a point then decrease, the separation between the calibrator and the target was on the linearly increasing section which meant I could fit it with a straight line and calculate the expected change in Jy/ADU with time. The SF derived variance was then added in quadrature to the statistical error from EWS.

3.1.2.3 Quality Control

Once the reduction is complete, a quality control was performed by hand. First, by plotting the detector intensity against detector position in the direction perpendicular to the wavelength dispersion. The detector intensity is averaged over a chosen wavelength range and normalised for clarity. I check if the assigned sky bands include any non-sky emission. If so they must be moved and the reduction re-performed. I check the sky bands at 12 μm with a bin width of $\pm 1\,\mu$m. The mask should also contain all the source emission. Figure 3.3 shows the sky bands correctly placed and the mask correctly fitted for calibrator HD 10052.

The fringe tracking and flagging must also be checked by plotting the waterfall plot and the OPD position (Figure 3.4). A waterfall plot is a common plot in interferometry and is essentially the reduced group delay for each frame stacked in order of observation time. In offset tracking mode, the OPD, the green line in Figure 3.4, should follow the fringe, shown as the black line,

while scanning. Any fringes where the OPD strays more than 0.1 mm from the fringe should be flagged, shown as the light green.

Finally, I check the uncalibrated and calibrated correlated flux. The uncalibrated correlated flux should show a strong atmospheric absorption feature at 9.8 μm which should be removed in the calibrated. The atmospheric component can sometimes be under or over-subtracted and result in erroneous features in the resulting spectrum. It is also indicative that the calibrator may not have been suitable because the atmosphere has varied too much between the calibrator and the science. More commonly in my observations, however, was the feature lacking in the uncalibrated spectrum. The lack of the feature in the uncalibrated spectrum means that something is causing the suppression of detected emission and the observation may not be reliable. The suppression can be from the source being to faint for the instrument, poor atmospheric conditions, bad sky subtraction, and/or a bad mask. If the cause is poor reduction, the reduction should be reperformed.

3.1.2.4 Visibility determination

Following the reduction and calibration steps gives the correlated flux and the MIDI photometry. For bright objects, these can be used to calculate the visibility by Equation 2.17. However, the photometry becomes unreliable for relatively dim objects, as compared to galactic sources, such as AGN due to very high residuals after background subtraction. Tristram (2007) gives the reason behind the residuals as contamination by emission from the tunnels which house the VLTI delay lines. The contamination causes the MIDI photometry to have large uncertainties. Therefore, I make a substitution for the MIDI photometry to calculate the visibility.

Instead I use spectrophotometry from VISIR. VISIR can perform single-dish spectrophotometry at the VLT using UT3 in the N-band, the same band as MIDI. It is important to keep in mind that the aperture used for extraction of the VISIR data must be comparable to the mask used to extract the MIDI data to minimise differential flux losses. AGN are also variable so the VISIR spectrophotometry should be taken close enough in time to the MIDI observations to minimise the effect. Therefore, it is prudent to compare the MIDI photometry to the VISIR photometry when used. Because photometry is usually taken with multiple observations, it is possible to compare the VISIR spectrophotometry to the average MIDI to compensate for some of the unreliability of the MIDI spectrophotometry.

3.1.2.5 No-Track Mode

The no-track mode on MIDI, used by many of the observations in Chapter 6, can cause the measured correlated flux to be artificially reduced if the object fringe strays too far from the set delay position due to the coherence length. To prevent losses, EWS only selects those frames where the fringes are within 100 μm of the set delay position. The OPD limit is standard for all modes

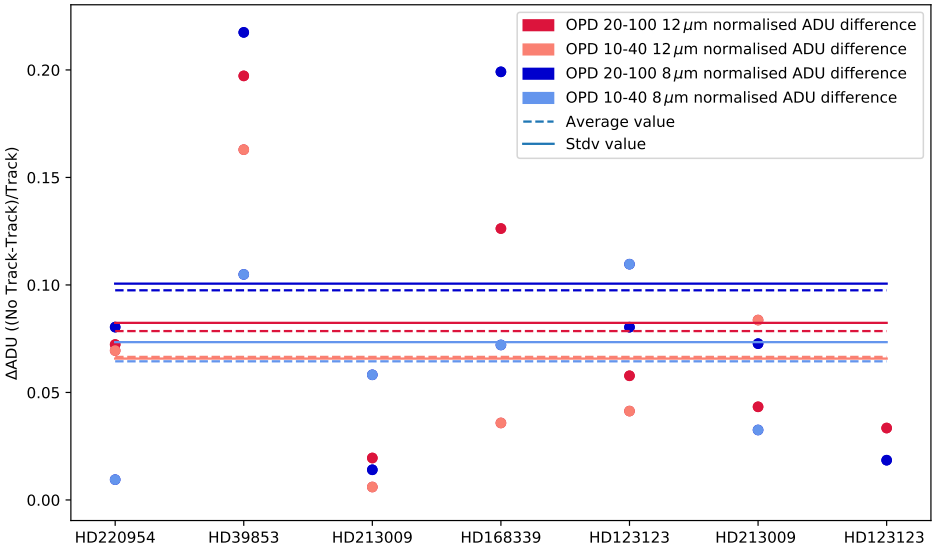

FIGURE 3.5: Here I show the normalised difference between adjacent tracked and no track observations for 7 calibrators. I plot 2 different OPD ranges for 2 wavelengths and for each pair I plot the average value and standard deviation of the points.

offered by MIDI. To check for any systematic differences between tracked and non tracked objects I compared the normalised difference in ADU of calibrators that have adjacent non tracked and tracked observations. Figure 3.5 shows the objects used as well as the normalised ADU differences at 8 μm and 12 μm.

I find that the no-track calibrators normally have a lower correlated flux. Furthermore, when I separated the results by the amount of time the fringe spends close to the piezo delay position, I find that observations that spend most of their time near this position have higher fluxes, closer to that of the tracked calibrators, when compared to those that spent very little time near the piezo delay position. However, there is less difference between calibrators which have a moderate amount of frames, $\approx 50\%$, recorded close to zero OPD, and those which only have a few frames recorded close to zero OPD.

The discrepancy between tracked and no-track sources could be caused by the difference in average OPD, the distance between the group delay fringe peak and the piezo delay line position, between tracked and no-track sources. A tracked object is normally, on average, 40 μm away from the piezo delay. However, a no-track object can spend a significant amount of time close to the 100 μm limit. So, even with the limit, the difference may be significant. To test if the average OPD difference is the cause, I set the acceptable OPD range to be more strict. By choosing OPD ranges smaller than the piezo scanning range I should remove the average OPD effect at the expense of the number of frames that can be used to calculate the correlated flux. I split the standard OPD range into 20 μm blocks, setting minimum OPD, minOPD, and maximum OPD, maxOPD, in EWS to [0,20,40,60,80] and [20,40,60,80,100] respectively. I compared the

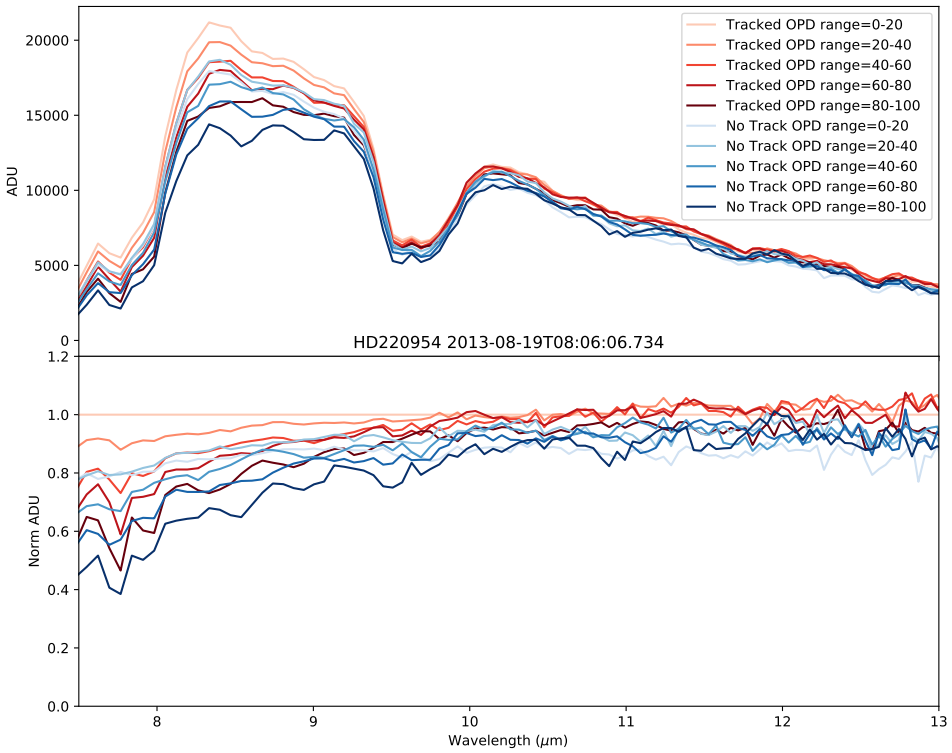

FIGURE 3.6: Both plots depict the uncalibrated spectrum of HD 220954 when reduced with differing OPD ranges. The red lines denote the tracked calibrator and the blue lines denotes the no track. The lower plot is normalised by the Tracked OPD range 0-20 spectrum.

uncalibrated correlated flux of the tracked and no-track calibrators for each range. I find that the uncalibrated correlated flux decreases with increasing OPD as expected. However, I also find that even for the narrow OPD ranges the correlated fluxes obtained in tracked and no-track mode do not agree. The difference in correlated fluxes for the two modes shows no consistency or further structure between objects (example for one object in Figure 3.6). Therefore, I cannot correct for the difference when reducing and calibrating objects taken with the no-track mode.

Because the conversion factor loosely depends on the average OPD I will still have these correlation losses if I calibrate no-track science with no-track calibrators. Therefore, I include an additional 8% uncertainty on the correlated flux of all no-track observations at 12 μm. The error was derived from the scatter of the conversion factor differences between the comparable tracked and no-track calibrators and can be seen in Figure 3.5. I also show the mean difference for two different OPD ranges, the standard range of 20 μm–100 μm and a more restricted range of 10 μm–40 μm to demonstrate that this offers no significant reduction in the error at either wavelength.

3.2 AMBER

AMBER (Petrov et al., 2007) is not actively used in this work, it was intended to be used for a near-IR study of ESO 323-G77, among other AGN. Unfortunately, AMBER suffered from visibility loss on faint objects that resulted in the data being unreliable. GRAVITY, which is used in this work, operates under similar principles on the same telescopes and understanding the problems encountered by AMBER gives insight on how to avoid the same problems with GRAVITY.

3.2.1 Observations

AMBER observations were made and reduced using a mode called AMBER++ (Millour, private communication). AMBER++ is a special mode for particularly faint objects that, under normal operations, AMBER could not track. AMBER took multiple consecutive short observations, like MIDI, and live reduced them to find the group fringe. By plotting the fringe, much like in Figure 3.4, the OPD can be adjusted to keep the fringe close to zero OPD. For faint objects, the fringe is lost in the noise and it is untracked. However, the human eye is very good at pattern recognition. AMBER++ allows the observer to adjust the OPD manually during the observation in an attempt to keep the fringe centred. In AMBER, the photometry is recorded simultaneously.

A single frame DIT in the AMBER++ mode was on the order of 50-200ms depending on seeing conditions with a total observation time of 5 minutes for one dim object. Because these observations are done in visitor mode, these exact numbers will depend on the observer and conditions.

3.2.2 Reduction

AMBER reduction is handled by the amdlib software (Millour et al., 2004) which is complimented by the amdlibPipeline yorick package (Millour et al., 2008) utilised in AMBER++. AMBER uses the Pixel to Visibility Matrix (P2VM) method to extract complex visibilities directly. Unlike the other interferometers in this work, each of the baselines are not separated onto different detectors. The setup can be more likened to the Young's double slit than the Michelson type. The three beams are combined on one detector which results in three overlapped interference patterns. AMBER uses an artificial coherent source of known complex visibility to create the P2VM which characterises the stable imperfections of the optical path. The P2VM quantifies the linear relationship between the pixels and the complex visibility effectively by modelling the detector interferogram (interferometric pattern).

I used the amdlibPipeline package to reduce the data, choosing to extract the visibility squared for 50 frame chunks of the manually tracked fringe. First amdlib is run which takes care of the initial reduction. It takes the raw detector data and removes the bad pixels and background. The

P2VM is then applied to calculate the raw visibility and the raw photometry is extracted. The raw visibility is bias subtracted and the pipeline returns the uncalibrated visibility per frame.

Upon the return of the uncalibrated visibility, the amdlibPipeline takes over. The returned visibility squared still requires calibration from a calibrator object but first the coherence loss from the non-zero OPD has to be removed. There are two forms of OPD movement loss: jitter and slow fringe drift. The jitter is OPD changes on a time scale shorter than the integration time of a frame and the slow OPD drift is the OPD change on timescales larger than a single frame. The slow OPD drift can be solved by letting the OPD change during the observation. The general rule when observing is to try and keep the OPD within $40-50\,\mu$m of the fringe position but otherwise not to move the OPD too much. By not adjusting the OPD, the fringe is allowed to deviate from the OPD zero and from this the visibility squared can be compared to the OPD. The raw visibility squared against OPD can be approximated by a Gaussian (Millour et al., 2004) and the amplitude of the Gaussian is the true visibility squared. Jitter is corrected by assuming the OPD shift between two frames is the sole source of the jitter. The OPD shift is found for each pair of frames and compared to their visibility squared. By working out how the visibility squared changes with the jitter between frames, the jitter is then corrected for.

After the correction, the corrected files are passed back to the amdlib script where the frames are averaged into the selected 50 frame blocks and the final uncalibrated squared visibility is found. From the remaining bins I checked for any remaining structure with OPD. If so I took the peak of a fitted Gaussian and determined the visibility squared, otherwise the average visibility squared is taken (reduction flowchart in Figure 3.7).

I performed the reduction for science and calibrator objects. For AMBER, because the complex visibility is the extracted product, I do not need to know the total flux of the calibrator. I just need its visibility which is 1 for a point source. Under normal circumstances, the ratio of the visibilities from the science and calibrator gives the calibrated science visibilities. However the visibilities determined for relatively faint objects such as AGN have a large scatter.

3.2.2.1 The AO problem with AMBER

I have mentioned before that the atmosphere is a big limiting factor in IR interferometry. The fluctuations in the atmosphere move the OPD, causing flux loss, and introduce a phase factor making phases difficult to determine. However, there is another problem that is not unique to inteferometry; the atmosphere will distort and smear an image at a ground based observatory. The observed distortion fluctuates with the observing conditions. The distortion is often quantified in the observables: seeing or Strehl ratio. The seeing is defined normally as the FWHM of a point spread function, which is what a point source appears as after atmospheric distortion, and the Strehl ratio is the ratio between the peak intensity obtainable if the system were diffraction limited and the observed peak intensity. The atmospheric smearing effectively makes a point source appear extended to an interferometer and therefore causes visibility loss. The VLTI

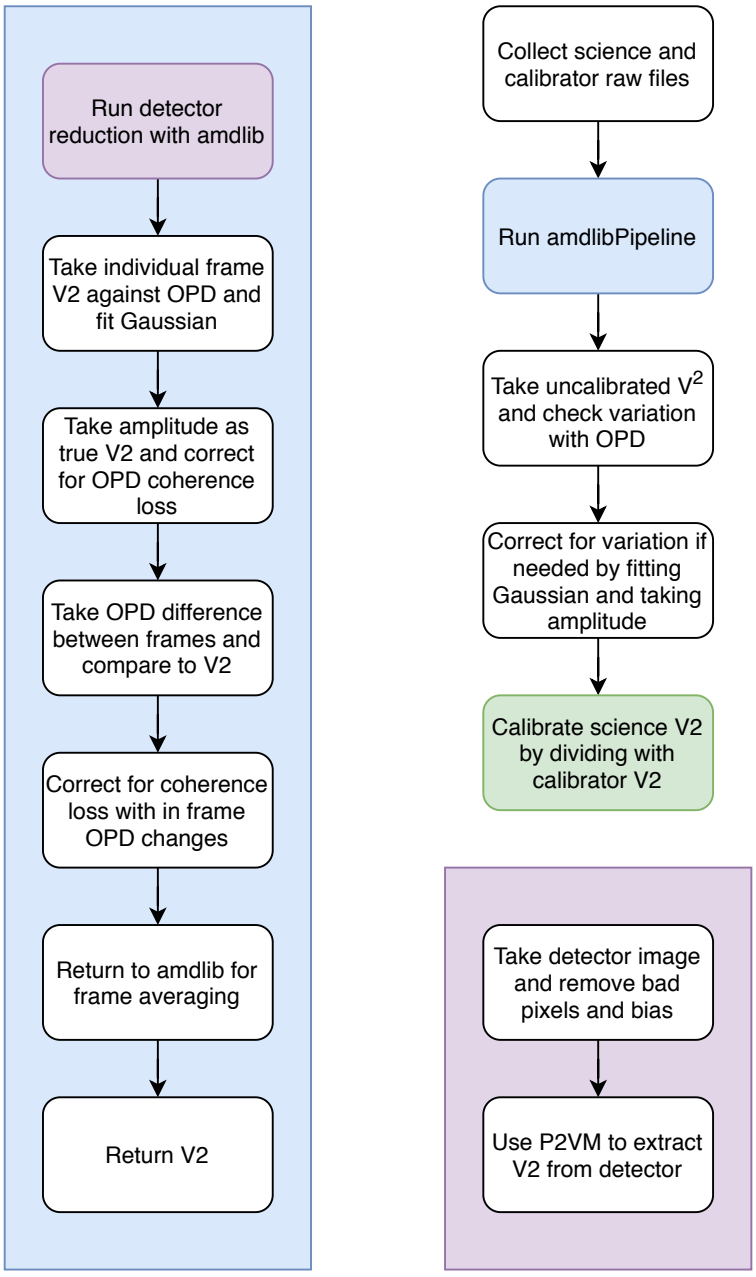

FIGURE 3.7: The flowchart for the AMBER++ reduction method

tries to fight the effect with an Adaptive Optics (AO) system that deforms a mirror in the light path of the telescopes to counteract the oncoming deformed wavefront and get back the original undistorted image.

An AO system uses a bright point source to determine the image deformation due to atmospheric turbulence. The VLTI specific AO is MACAO (Multi-Application Curvature Adaptive Optics, Arsenault et al., 2003). MACAO reads the incoming wave front and deforms a mirror in the light path to correct the atmospheric distortion by assuming it is looking at a point source. The corrected wave front is then fed into the VLTI. The correction is an issue for AGN because if there is no bright star nearby with which to use off-axis AO then the AGN itself must be

used. The problem with using an AGN is AGN are relatively dim to MACAO and therefore the correction is often poor. To correct for the poor AO, a red calibrator, which is a star that is unresolved and of a similar V and R band magnitude to the AGN, is sometimes observed. The dim nature of the red calibrator should mean that MACAO performs the same with the calibrator as the AGN and I can correct for the coherent flux loss which manifests as a lower visibility than would otherwise be measured.

I tried to quantify the AO loss using some observables, primarily the Wave Front Error (WFE). The WFE is provided by ESO and relates to the performance of the AO system. There is a trend to be found between the calibrated visibility squared and the WFE (Figure 3.8), unfortunately, the relationship is not trivial and, with the calibrators taken before the decommissioning of AMBER, the range of WFE that most AGN occupy was not observed. When correcting the loss with the limited range of WFE I had access to, the science visibility squared was too scattered to draw any conclusions from. The main conclusion that can be drawn from the red calibrators is that the AO systems effect on the visibility is real and must be considered when observing the absolute visibility of faint targets. The second result is that, despite the complexity of the problem, the red calibrators were still effective in the individual case. The structure seen in the red calibrators was seen in the science observations with the same WFE. Therefore, while the loss cannot yet be modelled, a calibrator taken close in time with the same MACAO performance can be used to correct it. The main issue with AMBER was that the red calibrators were not dim enough to MACAO to mimic the performance of some of the AGN. The non-trivial relationship between WFE and visibility squared meant that it could not be modelled and extrapolated to higher WFE and more red calibrators were needed at higher WFE to match the AGN.

3.3 GRAVITY

GRAVITY is the last IR interferometric instrument used in this work. Some of the reduction was done with tools provided by ESO and some with custom made scripts. I will detail the reduction process here.

3.3.1 Observations

As a relatively new piece of equipment, GRAVITY observations are difficult to perform correctly because every case is different. GRAVITY was designed with a very specific purpose which it has already achieved, to test the theory of relativity by observing the passing of a star close to the galactic centre (GRAVITY Collaboration et al., 2018a). It is perhaps the scientific focus that makes observation setup a challenge.

First, to understand how to best set up the instrument I must explain how it functions. As with both IR interferometers so far, GRAVITY has to compensate for the coherence length. Where as MIDI and AMBER solved the coherence length problem by taking short exposures,

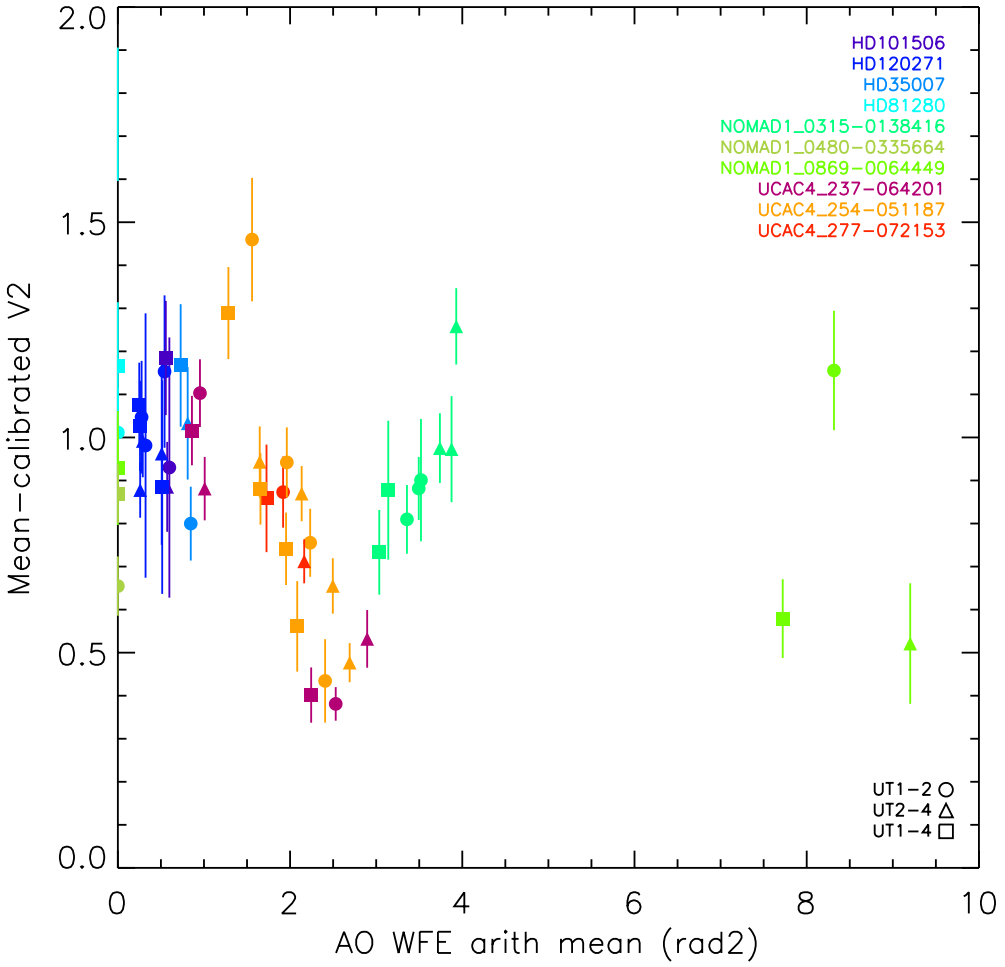

FIGURE 3.8: The calibrated visibility squared of red calibrators, as seen with AMBER, against mean wave front error of the baseline. Original plot created by Dr. Makoto Kishimoto (priv. comm.)

GRAVITY tries to actively fight the atmospheric change. How it achieves the correction is actually not that different from the previous solutions. GRAVITY has two separate channels which are illuminated simultaneously. One channel is the science channel which has the ability to perform low (R$\sim$ 20), mid (R$\sim$ 500), and high (R$\sim$ 4000) spectral resolution measurements. The second channel is the fringe tracker which only observes in low resolution. The fringe tracker channel provides low resolution measurements for short, ms, integration times. The fringe tracker data are live reduced and atmospheric OPD change is calculated and compensated for by changing the delay line OPD. The method is not dissimilar to how MIDI tracks the fringe over long periods of time, although the method for determining the atmospheric OPD change is necessarily different. The exact method behind the fringe tracking can be found in Lacour et al. (2019). The difference then lies in the science channel. By using the fringe tracker to adjust the OPD the science channel can integrate over long, $\sim$ 10 s periods of time without coherence loss, allowing for much dimmer sources to be observed. The dual channel functionality is important to consider when planning an observation.

GRAVITY offers three setups, Single-Field Mode (SFM), Dual-Field oFf-Axis mode (DFFA), and Dual-Field oN-Axis mode (DFNA). SFM uses the object of interest as the fringe tracker and science object. 50% of the light is given to the fringe tracker and 50% to the science channel per baseline. DFFA requires a second object near the target at a distance between 0.27 arcseconds and 2 arcseconds for the UTs. 100% of the offset object's light is given to the fringe tracker and 100% of the target's light is given to the science channel. The bright source for tracking allows very dim objects to be observed with long integration times. DFNA is used when the offset object is closer than 0.27 arcseconds. Like in SFM, the light is split between the two channels. Each channel then observes the appropriate source. In DFNA mode each channel receives less than half the light due to losses. For the latest technical details see the GRAVITY user manual for the current observing period.

In my case, I observed the AGN in ESO 323-G77. The nucleus of ESO 323-G77 is dim by the standards of the GRAVITY fringe tracker and there is no off-axis bright object with which to perform either dual field mode. When attempted in SFM, 50% of the light was not enough to successfully track. However, the fringe tracker data can be used for more than just tracking. Because I was interested in the continuum more than line emission, I did not require high spectral resolution. The fringe tracker itself provides low spectral resolution (R$\sim$ 20) data, albeit for short integration times, therefore, I did not need the science channel at all. Currently there is no mode which sends 100% of the target light to the fringe tracker so I used DFFA. The offset target for the fringe tracker was set to be ESO 323-G77 and the science target was set to be an arbitrary piece of the sky far enough away. The setup meant that 100% of the target light was sent to the fringe tracker and the science channel observed nothing. When reduction and analysis was performed, the science channel was ignored.

3.3.2 AO correction for faint objects

Normally, an observation with GRAVITY consists of a bright calibrator following the science, known as SCI-CAL. The calibrator should be unresolved to GRAVITY and preferably of known magnitude. The second point is not necessary though, thanks to the P2VM method (Tatulli et al., 2007; Lacour et al., 2019). However, as seen with AMBER, I need to check and correct for AO effects. As such, I take two different red calibrators either side of the AGN to give a range of calibrators with which to test the AO loss. The alternative setup is known as RCAL-SCI-RCAL-CAL.

3.3.3 Reduction

Initially, I make use of the ESOREX pipeline through the python tools provided by the Gravity Consortium to perform the initial reduction. Then I calculate the final visibility and phase from the reduced products manually. The python tools use PYTHON 2.7, for the manual reduction section PYTHON 3.7 was used instead.

First, the pipeline must be setup correctly for the reduction of these objects. Normally, the default setup is enough but for my reduction of a dim object I only want the pipeline to perform the initial reduction and not the final product determination. By default, the pipeline reduces the raw object data and returns a visibility, visibility squared, differential flux, and closure phase. First it performs the reduction and calculates the complex visibility for each frame on each baseline. It then calculates the given quantities from the complex visibility. However, it is possible to get the pipeline to return an intermediary product known as the p2vmred. The p2vmred file returns the complex visibility per frame per wavelength bin as well as meteorology data. To get the p2vmred file, in the configuration file for the gravity_vis recipe of esorex, the –p2vmreduced-file should be set to true. I also set the –reduce-acq-cam to true to get the Strehl value during the observation.

Second, to reduce gravity data, the appropriate data files and calibration files must be present. An observation usually consists of a dark, sky, flat, wave, and P2VM file. Either the dark or sky may be omitted if the science channel data are not of interest. With these files, I then run the gravi_reduce script from the python tools. The flowchart of the reduction process for a single RCAL-SCI-RCAL-CAL observation is available in Figure 3.9.

3.3.3.1 Visibility determination

To determine the visibility and visibility squared (V and V^2 in Figure 3.9) I initially used the default pipeline frame rejection. The pipeline uses a signal to noise cut off of 3 by default. To determine the AO visibility loss, I compared the visibility of all calibrators to the Strehl ratio, calculated from the acquisition camera images. The Strehl ratio was my best proxy for the performance of the AO systems. Also considered was the coherence time, the FWHM of a Gaussian fitted to the object as seen by the acquisition camera, the core width and power index of a Moffat function fitted to the object, and the variance in the central position of the source, i.e. the "jitter", in the acquisition camera over the course of the observation. All these showed the visibility losses from AO performance but it was best classified by the Strehl and the FWHM.

The loss was detected in the calibrators as shown in Figure 3.10. By modelling the loss, I could remove the majority from the science objects but a significant scatter, approximately 0.2 in visibility on the best night, still rendered most of the visibility data useless. Therefore, I derived a separate method for accounting for the loss.

I utilised the individual frame complex visibility and selected frames based on my own criteria. I attempted to use the group delay to select frames, as done in GRAVITY Collaboration (2019), which did provide a significant improvement, however, I found that selecting by geometric flux provided the best correction in my data. Further improvement may possibly be found by enforcing both criteria, however, at the risk of selecting too few frames for a good signal to noise. The frame selection will be explored further in future work.

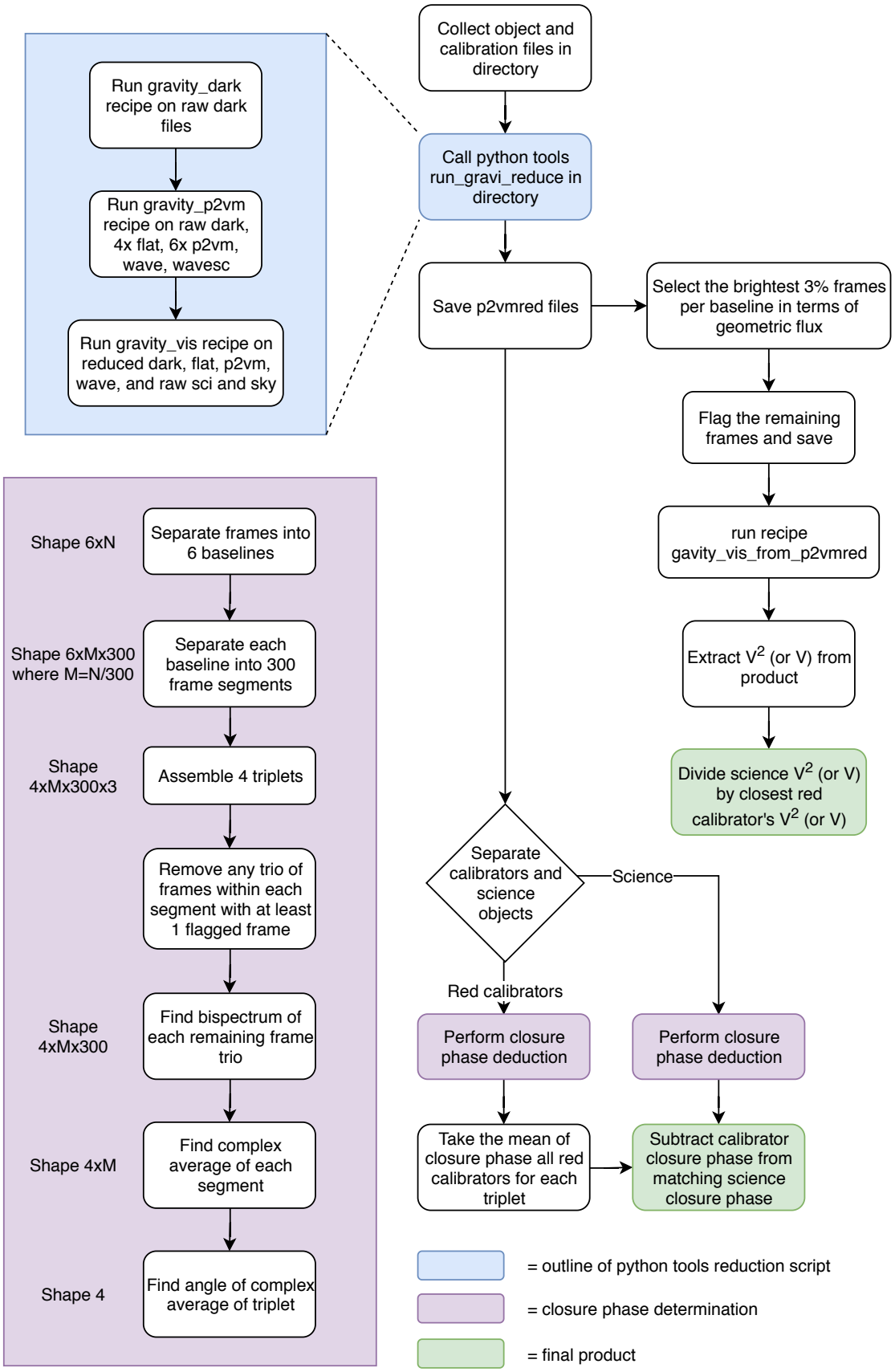

FIGURE 3.9: A flowchart representation of the steps taken to reduce GRAVITY data

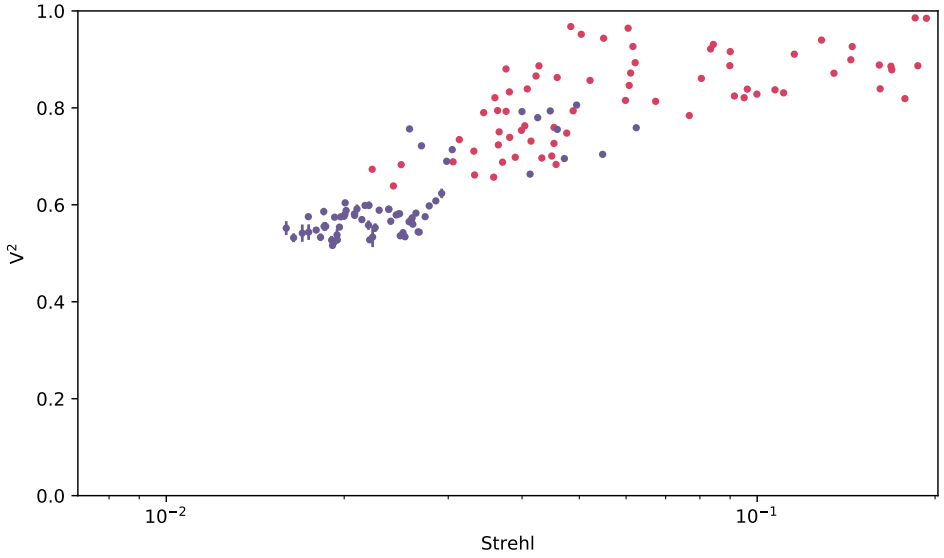

FIGURE 3.10: This plot depicts the visibility squared of the calibrators (red) and science object (purple) against the average Strehl ratio of the two telescopes that comprise the relevant baseline. This plot is with default pipeline frame selection.

For both calibrators and science targets, I selected the 3% brightest frames in geometric flux, not including any frames rejected by the gravity_vis recipe. Figure 3.11 depicts the same as Figure 3.10 with the 3% flux cut; it demonstrates that the science becomes more comparable to the calibrators. 3% was chosen as the cutoff empirically by testing 1% to 10% cutoffs and comparing the results. 3% provided the best trade off between improved data and increased uncertainty. All non-selected frames were then flagged and the visibility and visibility squared were calculated using the GRAVITY python tool run_gravi_reduce_from_p2vmred with the ESOREX recipe gravity_vis_from_p2vmred using the flag –use-existing-rejection=TRUE. The selection removed the majority of the relative AO loss, i.e. the loss between the science and the closest red calibrator. The overall trend between visibility squared and AO still exists after the flux cut but at a lesser gradient. Further correction of the visibility squared using the remaining correlation only increases the scatter. To remove the remaining error, I calibrated the science data with the red calibrators instead of the bright calibrators.

I hypothesise that the reason the AO loss can be removed through a flux cut is because when the AO is performing well more flux is injected into the fibre. Therefore, by selecting the highest geometric fluxes, I select the frames where the AO is performing best or where the atmosphere was least turbulent. The flux cut method is reminiscent of "lucky imaging" sometimes used for ground based photometry (Fried, 1978).

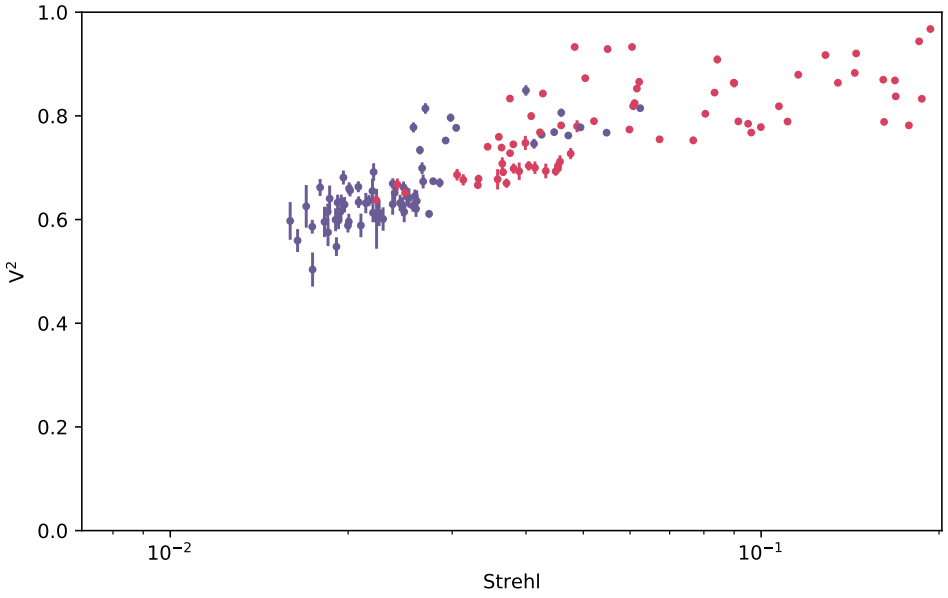

FIGURE 3.11: This plot depicts the visibility squared of the calibrators (red) and science object (purple) against the average Strehl ratio of the two telescopes that comprise the relevant baseline. This plot is with 3% flux cut frame selection.

3.3.4 Closure phase determination

The closure phase is very important to determine accurately. While it is piston-invariant, i.e. not dependent on atmospheric fluctuations, there are still some residual offsets that need correcting after the initial pipeline reduction.

Unlike the visibility, I did not need to discard any frames other than those with a signal to noise of less than 3; this meant that less data was lost and the final observables were less noisy. To calculate the closure phase from a single frame in the p2vmred file, I used a similar manner to the pipeline (See latest GRAVITY pipeline manual). The closure phase of each frame is the angle of the bispectrum, as demonstrated in Equation 2.35, and I follow the method set by the fringe tracker (Lacour et al., 2019). When observing, the fringe tracker data are averaged over 300 frames to perform the tracking. I therefore, split my data into 300 frame segments. In each segment, I only consider a trio of frames if all three are unflagged and I remove any trios that are not. I then calculate the mean bispectrum of the segment. I calculate the final closure phase from the angle of the mean of the bispectrum of every segment in the observation (Equation 3.4) and the standard error from their distribution.

$$\Phi_{ijk} = \arg\left(\frac{1}{n}\sum_{N=0}^{n}\frac{1}{300}\sum_{f=300N}^{299+300N}\Psi_{ijkf}\right). \tag{3.4}$$

Where n is the number of segments, N is the segment, Ψ_{ijk} is the bispectrum of three telescopes, and f is the frame.

I calculate the closure phase for every science and calibrator observation and find that all calibrators have non-zero closure phase. The closure phase of the red calibrators on the same night are approximately equal and the common phases are clearly present in the science. The bright calibrators have a very large phase of $\approx 7^\circ$ on every night. I do not know what causes the phase and more bright calibrators would need to be checked to see if this is instrumental or if this is a bad calibrator. Because multiple red calibrators show the same phase component I can conclude this phase is instrumental. I therefore subtract the mean closure phase of the red calibrators from the science target. The remaining closure phase was taken to be truly from the science object.

3.4 VISIR

The VLT-mounted Imager and Spectrometer for the mid-IR (VISIR; Lagage et al., 2004; Käufl et al., 2015; Kerber et al., 2016) is a single dish imager and spectrograph mounted on the VLT. It can produce spectrophotometric data over the same wavelength range as MIDI and I use VISIR observations as replacement for the poor MIDI spectrophotometry. These data were instrumental to the work in Chapter 4 and 6. The data reduction was not performed by me but instead by Dr. Daniel Asmus. Instead of giving a full reduction here a summary is available in the relevant chapter.

3.5 ISAAC and NACO

The Infrared Spectrometer and Array Camera (ISAAC, Moorwood et al., 1998) is an imager and spectrograph that observes between $1-5\,\mu$m. The Nasmyth Adaptive Optics System (NAOS) Near-Infrared Imager and Spectrograph (CONICA) (shortened to NACO Lenzen et al., 2003; Rousset et al., 2003) can perform AO assisted imaging in the $1-5\,\mu$m range as well as imaging polarimetry, and coronography. I only used the imaging capabilities of both these instruments.

ISAAC was one of the instruments used to create SEDs in Chapter 6. All ISAAC and NACO observations were archival. I did not apply for any of the used observations, the programme IDs are given in the chapter they are used in. The ISAAC data were extracted using the python package PHOTUTILS (Bradley et al., 2019) and ASTROPY (Astropy Collaboration et al., 2013). When creating an SED for an object, I collected all the available ISAAC data in the H, Ks, L, and M bands and any relevant calibrator objects on the same night. The data were reduced and calibrated using a self written script in PYTHON 3.7. The reduction process (see Figure 3.12 for reduction flowchart) differed if the observation was in chopping mode or not. For the L and M band, chopping was used. However, it was not used for the H and Ks bands. Chopping is where the secondary mirror is oscillated between two close positions on the sky that include

the target, observations are made at each visitation. When receiving the raw file from the ESO archive, each field is precombined and the observation received consists of just two images. These images theoretically have the same sky and biases but with the objects in the field moved. If you take the difference between these images you receive an image with the sky and biases removed as well as a positive and negative version of the source. I use PHOTUTILS StarFinder to locate the two sources and I extracted the flux of each of these sources as well as the flux from an annulus around each of the sources. The aperture has a radius of 0.5" and the annulus has an inner and outer radii of 1.8" and 2.5" respectively. I calculated the local background of each source from its associated annuli and removed it from the extracted counts. Finally, by taking half the difference between the two extracted fluxes, the reduced flux can be found.

Images observed in other modes were reduced differently. I first find the closest dark with the same integration time (DIT) and remove it from the image. If there is no dark of the same DIT then I take the two closest darks in time, find the average count of each, and interpolate the average value to the DIT of the observation. I then remove the average dark value from the observation image. Next, I use the PHOTUTILS script mmm_bkg to quantify the remaining background level and subtract it from the image. The subtraction makes source detection easier to perform. For the source detection I use PHOTUTILS IRAFStarFinder. To identify the correct source, I use the WCS (World Coordinate System) information available in the header and the RA and Dec of the object. The counts from an aperture and an annulus, of the same radii as used in the chopping case, around the source was extracted, the background was calculated from the annulus and removed from the source counts.

In both cases, the initial error on the uncalibrated source was derived from the background noise. Each extracted observation was calibrated using the closest standard star in time. The calibrators were reduced with the same method as the target sources. The uncertainty on the calibration was found by reducing all observations of the standard star within 1 hour of the selected calibration observation and finding the standard deviation and average count. The additional error was added in quadrature to the error derived from the background noise. The zero point was calculated for each calibration observation and the average was used as the zero point for the science observation.

NACO was used when ISAAC observations were unavailable and was reduced in the same manner.

3.6 ALMA

The Atacama Large Millimetre/submillimetre Array (ALMA) is different to the IR interferometers discussed in the previous sections. It is a mm interferometer comprised of 66 movable antennae. The large number of antenna makes filling the *uv* plane much more feasible allowing for high quality image reconstruction. ALMA data can be difficult to reduce and requires personalised reduction depending on the observation. Therefore, here I will provide an overview of

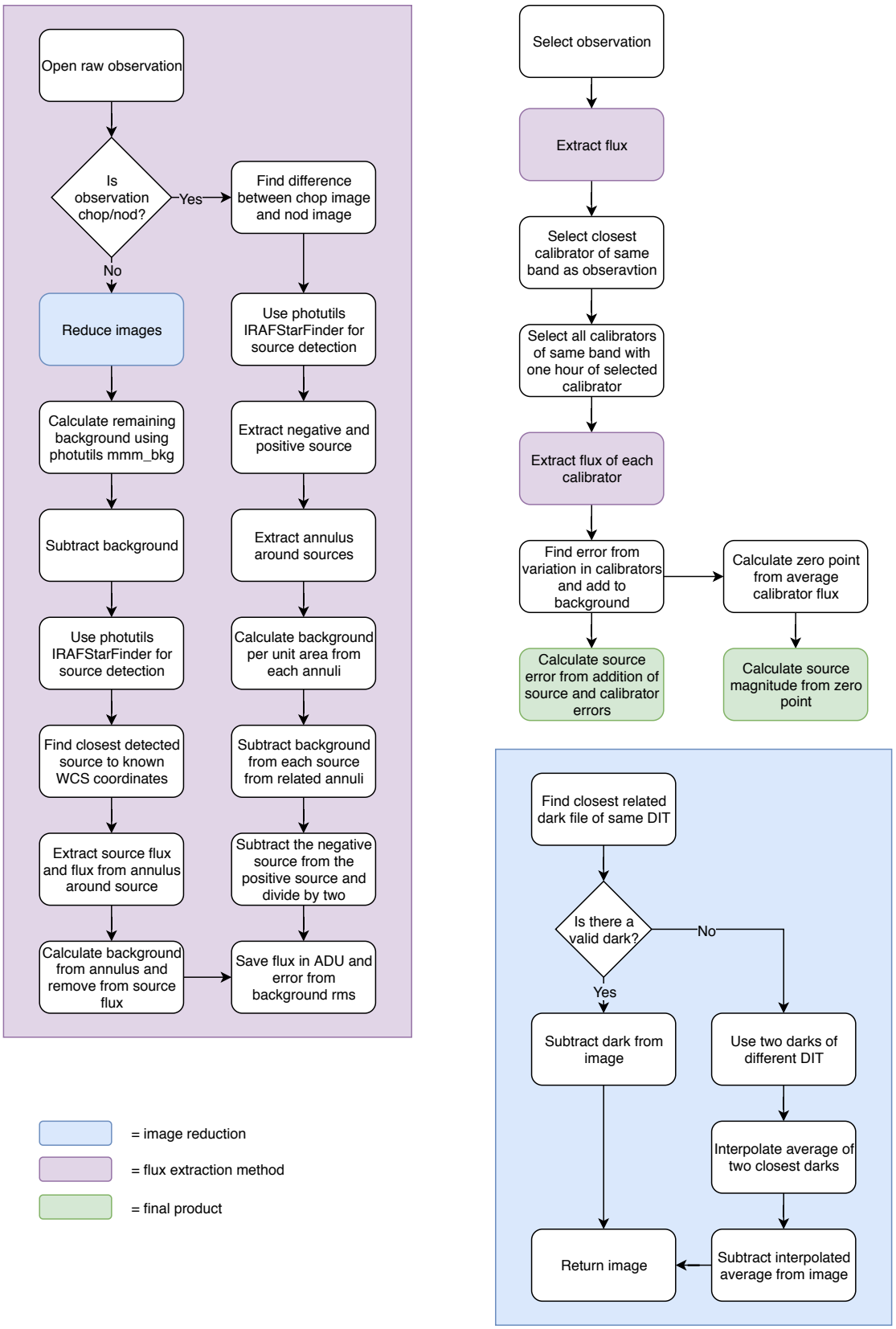

FIGURE 3.12: The flowchart for the reduction of an ISAAC and NACO observation

the reduction method I employed, however, not all the steps provided here will be applicable to every situation. Therefore, caution should be applied when following my methodology.

For data reduction I used CASA (McMullin et al., 2007) with TCLEAN for image cleaning. First, I run the ScriptForPI CASA script provided for each observation, using the version of CASA the script was made in, to reclaim the data products. The pipeline reproduces the calibration and reduction done for the observations. After the initial products are created I switch to CASA 5.4.0-70. Once the reduced products were available I made use of the TCLEAN software in interactive mode to remove artefacts introduced by the distribution of the *uv* points. Having gaps in the *uv* plane introduces structure in the reclaimed image. TCLEAN removes the artificial structure by applying user chosen masks. To perform the image creation, the complex visibility is binned in a grid in the *uv* plane, each complex visibility bin is then multiplied by a weight. The weighting determines the behaviour of the image reconstruction. The weighting chosen was 'natural' which provides the highest sensitivity at the cost of possible widening the PSF. Natural weighting uses the summed $1/\sigma^2$, where σ is the standard deviation of the visibility of the *uv* point, of each *uv* point in the grid section to determine the weight of the section and it is best for low signal to noise lines which is suitable for my science goal. The grid is then fast Fourier transformed to produce a dirty image. The dirty image is essentially the true source image convolved with the beam. The beam is what a point source would look like to the interferometer based on the *uv* plane coverage. The TCLEAN function then attempts to deconvolve the dirty image to recover the true source. It uses the user defined masks to find and remove the residuals from the image. I separately performed the cleaning over all the observations concatenated and the observations individually.

Chapter 4

The Mid-IR Interferometric Study of ESO 323-G77

4.1 Introduction

This chapter is adapted from the published work Leftley et al. (2018). I am lead author of this work and led the reduction, analysis, and interpretation.

4.1.1 ESO 323-G77

ESO 323-G77, shown in Figure 4.1, is a spiral Seyfert galaxy which hosts a Type 1.2 AGN that is an important new target to test the disk+wind model (see Table B.1 for details on ESO 323-G77). Its importance comes from its nature as a Type 1. In a Type 1 it is harder to explain a polar dust extension with a torus model. To explain a polar extension in a Type 1 would require a chance illumination of a region of the inner edge of the torus by a warped disk that happened to be in the polar direction. It is also polar scattered when observing optical polarisation (Schmid et al., 2003). When observing optical polarised light in AGN, there are two main sources of scattering. Equatorial, i.e. scattering off the accretion disk, or polar scattering. Which one of these dominates can give information about the inclination. Low inclination, or face on, sources with a clear view of the accretion disk, i.e. Type 1, normally show equatorial scattering. Because ESO 323-G77 is both a Type 1 and polar scattered, the conclusion drawn by Schmid et al. (2003) is that our LoS is grazing the obscuring material partially obscuring the accretion disk, the polar scattering then comes from dust clouds above the source.

ESO 323-G77 has been studied with mid-IR interferometry before using MIDI. A snap-shot analysis of four observations by Kishimoto et al. (2011b) fitted with a power-law brightness distribution revealed that the radial size of the emission area decreased at shorter wavelengths.

Burtscher et al. (2013) found a significantly smaller radial size of emission based on a Gaussian model with with the same four observations and one more that was deemed not usable in Kishimoto et al. (2011b). López-Gonzaga et al. (2016) performed a more expansive statistical analysis of these data using an elongated Gaussian plus point source model. They found the minor axis Full Width Half Maximum (FWHM) of the Gaussian to be 17 mas with an axis ratio of 1.4 or equivalently an average FWHM of 21 mas or 6.5 pc using an angular scale for ESO 323-G77 of $0.311\,\mathrm{pc\,mas^{-1}}$. When testing the fitted model of ESO 323-G77 it was discovered that the extension was unconstrained in PA. Asmus et al. (2016) reports on an extension along the putative torus mid-plane at subarcsecond spatial resolution based on single-telescope mid-IR images with an error of 27° in PA of the major axis of the extension. However, the subarcsecond extension is on a larger scale than that of the putative dust torus.

4.1.2 MIDI modelling

When previous MIDI observations of AGN were modelled, it was often found that the emission can be interpreted as a combination of two distinct emission components. One component is partially resolved, and often polar extended, whereas the other is unresolved at all baseline lengths available. However, two distinct components is not the only interpretation of the emission, it can also be explained as a single power-law component, e.g. Kishimoto et al. (2011b) and Hönig et al. (2012). In this work, I use the two-component model. The two-component model allows the separation of the extended and unresolved emission and makes this work easily comparable to Burtscher et al. (2013) and López-Gonzaga et al. (2016). In Burtscher et al. (2009) it was found that the unresolved component could be interpreted as hot dust near the sublimation radius.

In this chapter, I present 10 successful MIDI observations in order to pin down the radial and angular-dependent size of the warm dust in ESO 323-G77. In Section 4.2, I describe the observations and data reduction, including new measurements with VISIR. In Section 4.3, I present the findings from the reduced VISIR data as well as an initial interpretation of the MIDI data. In Section 4.4, I model the MIDI data with, firstly, a geometric model and, secondly, the radiative transfer model *CAT3D-WIND*. In Section 4.5, I discuss the results in the context of other measurements.

4.2 Observations

This chapter is based on European Southern Observatory (ESO) observing programmes 083.B-0452, 084.B-0366, 087.B0401, 092.B-0718, 095.B-0376, and 290.B-5113.

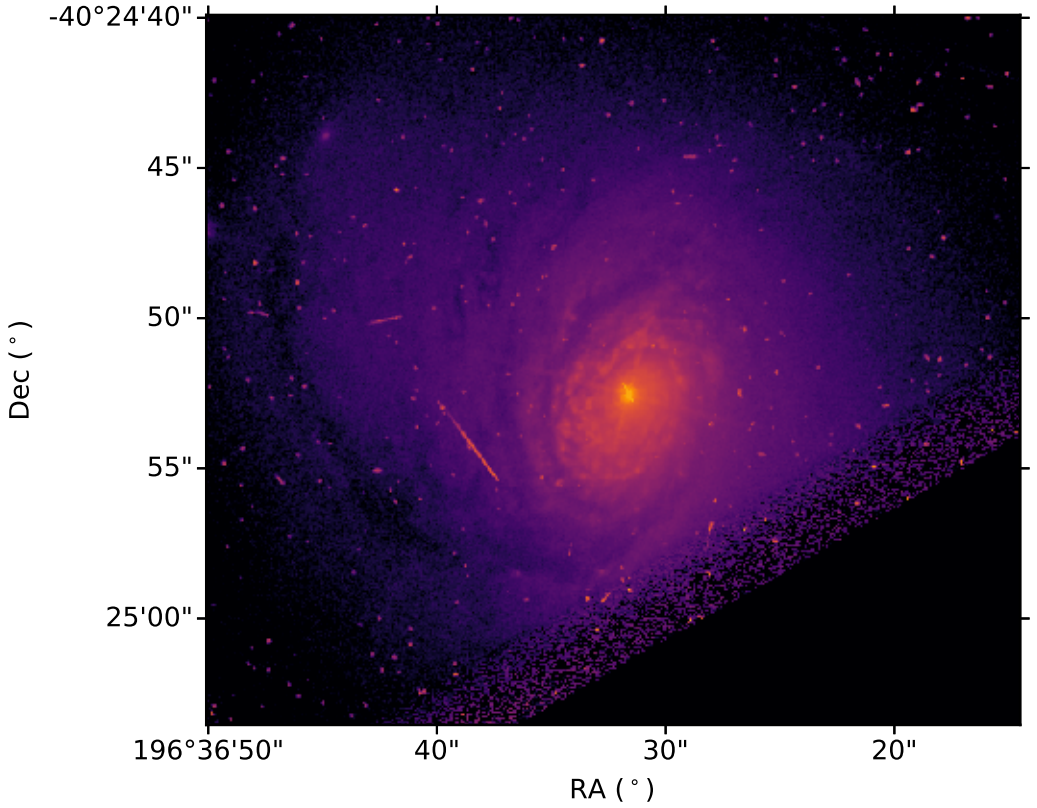

FIGURE 4.1: An HST image of ESO 323-G77 observed as part of HST programme 5479.

4.2.1 Interferometric observations

For all MIDI observations, both those from the previous works and the additional new data, only 8.2 m unit telescope (UT) pairs were used due to the relative faintness of ESO 323-G77. The observations were carried out between 2009 and 2014.

In total, 11 fringe tracks and complimentary single-dish spectra were observed. All observations are listed in Table 4.1. HD112213 was used as the calibrator star except on 2011 April 15, where HD100407 was observed instead. All of the single-dish spectra were supplemented with the high signal to noise VISIR spectrum from Hönig et al. (2010), observed on 2009 May 04, which provides a better reference to determine visibilities and therefore sizes (see Section 4.2.3).

Date	UT	Stations	Proj BL (m)	PA (deg)	Calibrator	Comment	Programme	Note	No. Files
2009 May 08	01:04:03	UT3/UT4	56.8	94.4	HD112213		083.B-0452	a	2
2009 May 10	03:12:36	UT1/UT2	54.1	30.5	HD112213		083.B-0452	a	2
2009 May 10	04:15:43	UT1/UT2	51.8	37.1	HD112213		083.B-0452	a	2
2009 May 11	04:07:36	UT1/UT4	118.4	75.0	HD112213		083.B-0452	a	1
2009 May 12	00:10:57	UT1/UT4	126.9	36.9	HD112213		083.B-0452	a	2
2010 Mar 01	03:15:11	UT1/UT2	56.3	353.2	HD112213		084.B-0366	b	2
2010 Mar 02	04:43:06	UT1/UT3	102.4	11.6	HD112213		084.B-0366	b	2
2010 Mar 02	06:00:16	UT1/UT3	101.8	23.5	HD112213		084.B-0366	b	2
2010 Mar 02	07:50:55	UT1/UT3	97.3	38.5	HD112213	Poor fringe tracking	084.B-0366	b	1
2011 Apr 15	05:02:59	UT2/UT3	44.5	47.7	HD100407		087.B-0401	b	2
2014 Mar 16	06:23:41	UT1/UT3	99.5	34.0	HD112213		092.B-0718	b	2

TABLE 4.1: Table of MIDI observations of ESO 323-G77. (a) Data previously used in Kishimoto et al. (2011b), Burtscher et al. (2013), and López-Gonzaga et al. (2016); (b) Unpublished data.

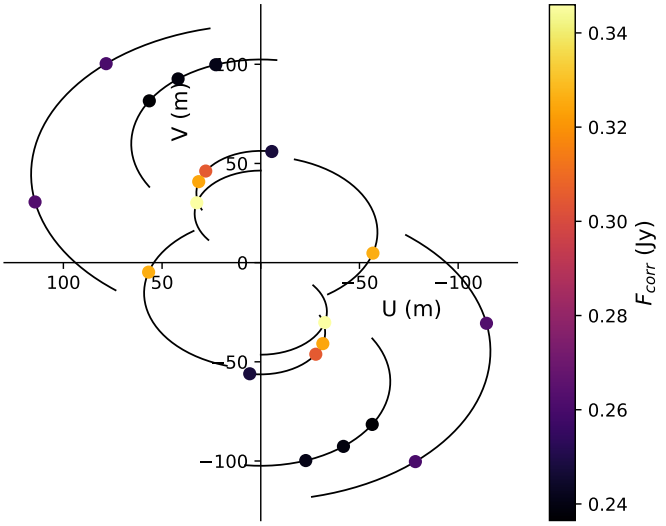

FIGURE 4.2: The *uv* coverage for ESO 323-G77. The individual points are colour coded according to their correlated flux in the 11.8 μm bin, $F_{\rm corr}(11.8\,\mu{\rm m})$.

4.2.2 Interferometric data reduction

The MIDI observations were reduced in accordance with Chapter 3; further analysis of the data was performed using PYTHON 2.7 with the ASTROPY, EMCEE, and OIFITS libraries (Astropy Collaboration et al., 2013; Foreman-Mackey et al., 2013). All observations from previous works were re-reduced in order to obtain a homogeneous data set. The fitted mask widths used increase from 5.0 ± 0.35 pixels (0.42") at 8 μm to 7.7 ± 0.8 pixels (0.65") at 13 μm.

There were 25 attempted fringe tracks on ESO 323-G77 with MIDI in total. One of these had an insufficient signal for fringe tracking due to high wind (see Table 4.1), three on 2009 March 09 have insufficient signal to noise because the fringes could not be tracked properly, and two on 2014 March 16 are non-detections due to extreme atmospheric dust. The remaining 19 observations were sorted into 30 minute groups, combined, and reduced in accordance with López-Gonzaga et al. (2016). I hence obtained 10 independent measurements of $F_{\rm corr}(\lambda)$, as listed in Table 4.1 and shown in Figure 4.2.

By default, the calibrator observed closest in time to the science target was used for the calibration. The SF was used for all observations and its value for the time difference between the science object and its calibrator was added in quadrature to the statistical error provided by EWS. For each night, the SF showed a clear structure consistent with non-random variation, most likely due to variations of the observing conditions.

The uncertainties of the MIDI single-dish spectra were too large to make them usable. Instead, I used the total flux spectrum from Hönig et al. (2010) obtained with VISIR, $F_{\rm VISIR}(\lambda)$, to calculate

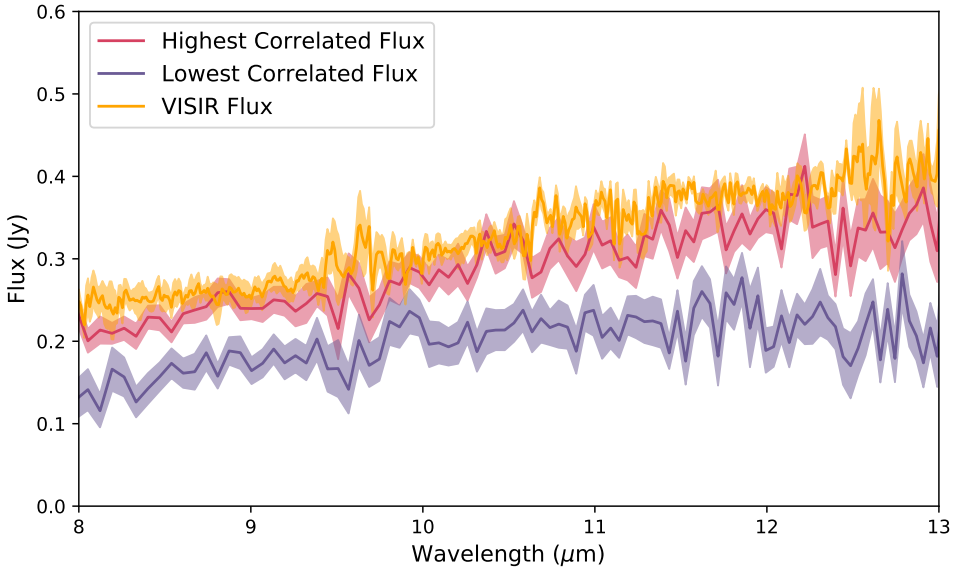

FIGURE 4.3: The highest and lowest correlated fluxes measured by MIDI. The VISIR spectrum is also shown for comparison.

the visibility using: $V(\lambda) = \frac{F_{\rm corr}(\lambda)}{F_{\rm VISIR}(\lambda)}$. Because the VISIR spectrum was extracted by fitting a Gaussian to the PSF with FWHM = 0.4" at 12 μm, the extraction window is similar to the mask used for MIDI, and hence aperture effects should be minimal, considering that the source is essentially unresolved in the mid-IR (see Section 4.3.1). The VISIR spectrophotometry, as well as the highest and lowest $F_{\rm corr}(\lambda)$ values, are plotted in Figure 4.3. I compared the re-reduced data to that of Burtscher et al. (2013) and found that the resulting $F_{\rm corr}(\lambda)$ values are in agreement within errors.

4.2.3 VISIR data

The following section on VISIR data was adapted from Leftley et al. (2018). The context is needed to understand this work so I have included it here. The reduction was performed by Dr. Daniel Asmus.

ESO 323-G77 was observed with the upgraded VISIR as part of programme 095.B-0376 to study mid-IR flux changes in the last 6 years since its previous spectrophotometry with VISIR (Hönig et al., 2010; Asmus et al., 2014). The observations were carried out in standard imaging mode in the PAH1 (8.6 μm) and PAH2_2 (11.88 μm) filters with perpendicular nodding and a chop/nod throw of 8". In total, four epochs were obtained with each filter in service mode between 2015 August and 2016 February with on-source exposure times of 7 and 10 minutes, respectively (see Table 4.2). For flux calibration and point spread function (PSF) reference purposes, the science observations were preceded and followed by a mid-IR standard star from the catalogue from Cohen et al. (1999).

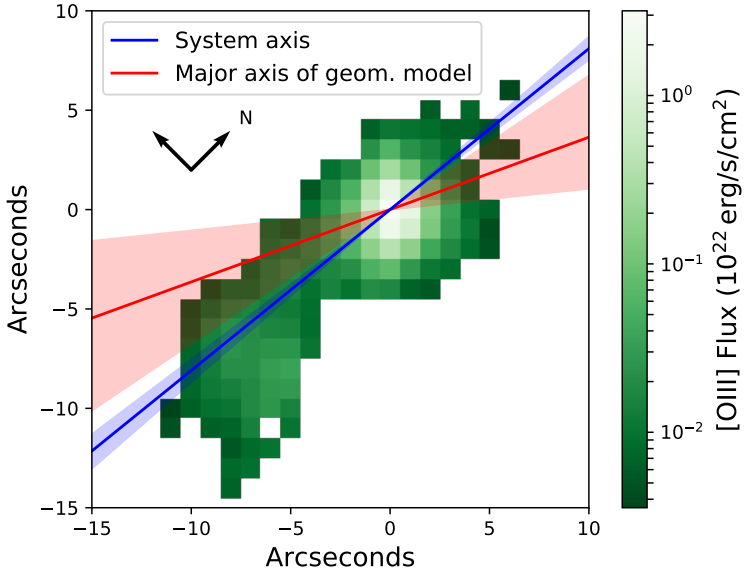

FIGURE 4.4: Image of the 500.7 nm [O III] emission line for ESO 323-G77 using data from S7 (Thomas et al., 2017). North and East are given in the plot. The red line is the mean value found for the elongation direction of the geometric model in this chapter and the blue line is the polar axis implied by the polarisation direction (Schmid et al., 2003). The shaded regions are the 1σ errors on the measurements. The axes are distance from the centre of the AGN.

The data reduction was performed with a custom made PYTHON pipeline, and flux measurements were obtained using the custom developed IDL software package, MIRPHOT (Asmus et al., 2014). The results are displayed in Table 4.2.

4.2.4 Finding the system axis

The system axis in this thesis is the polar axis, i.e. the axis that is perpendicular to the accretion disk, implied by the optical polarisation and the NLR. Mulchaey et al. (1996) presented spatially extended [O III] emission from the NLR of ESO 323-G77. However, in Type 1 Seyfert galaxies the central, unresolved, [O III] emission often drowns out the more extended, lower surface-brightness, NLR emission resulting in poorly constrained extensions. Thus, the authors only note a North−South extension. New data from the S7 survey reveals the [O III] emission in lower spatial resolution but with higher signal to noise (Thomas et al., 2017). The prereduced data products are available at https://datacentral.aao.gov.au/asvo/surveys/s7/. I used the line fitting program KUBEVIZ (Fossati et al., 2016) to perform a single Gaussian and continuum fit to the 500.7 nm and 495.9 nm [O III] lines. The 500.7 nm component is shown in Figure 4.4 with the system axis overplotted. Polarised emission in AGN arises from either an equatorial scattering medium on the scale of the BLR inside the putative torus, or the polar region co-spatial with the innermost NLR. Schmid et al. (2003) measured a polarisation angle of the optical emission of $84° \pm 2°$, this is reaffirmed with near-IR polarisation measurements from Batcheldor et al.

Date	Filter	$\lambda(\mu m)$	Flux (mJy)	Error (mJy)
2009 May 10	ARIII	8.99	300.9	31.6
2010 Mar 10	PAH1	8.59	275.2	31.6
2015 Aug 03[a]	PAH1	8.59	315	54.2
2016 Jan 15	PAH1	8.59	369.1	38.1
2016 Feb 16	PAH1	8.59	340.5	34.5
2016 Feb 28	PAH1	8.59	359.9	36.6
2009 May 10	PAH2_2	11.88	383.4	40.7
2010 Mar 10	PAH2_2	11.88	378.7	40.3
2015 Aug 03[a]	PAH2_2	11.88	695	374
2016 Jan 15	PAH2_2	11.88	440.0	44.7
2016 Feb 16	PAH2_2	11.88	473.4	54.4
2016 Feb 28	PAH2_2	11.88	449.2	45.5

TABLE 4.2: VISIR photometry of ESO 323-G77. *a*) Large uncertainties due to strong background variations from clouds.

(2011). Smith et al. (2004) reports that the polarisation in ESO 323-G77 is dominated by scattering in the polar region. Therefore, the system axis is expected at an angle of approximately $174^\circ \pm 2^\circ$ in agreement with the polar axis inferred from the NLR.

4.3 Results

4.3.1 Morphology and variability from single-dish observations

The previous subarcsecond resolution mid-IR images of ESO 323-G77 from Asmus et al. (2016) indicate that the nucleus may be marginally extended in comparison to the PSF as measured from consecutively observed standard stars with major and minor axis FWHMs of 0.40" and 0.38" at 12 μm. The PA of the major axis is, on average, 95° but with a significant scatter of 27°, so that any elongation remains uncertain. The new data shows the same morphology at 12 μm, while being consistent with an unresolved nucleus at 8.6 μm. The variations in the PSF, as measured from the standard stars before and after, are too large to draw any firmer conclusion on the nuclear mid-IR morphology. Even the average combined PAH1 and PAH2_2 images, with total exposure times of 30 and 40 minutes, respectively, do not reveal any further, faint structures.

Furthermore, the VISIR imaging from Asmus et al. (2014), obtained contemporaneous with the 2009 and 2010 MIDI observations, does not reveal any significant flux changes. From the new measurements obtained between 2015 April and 2016 February, average flux densities of 346 ± 21 mJy and 514 ± 96 mJy were derived for the total nuclear emission, in PAH2_2 and PAH1 respectively, for all epochs combined. There is no sign of evolution during the seven months the observations were obtained. However, these values are 20% higher than the values measured in 2009/2010. Therefore, it is likely that the intrinsic flux of the AGN increased over the last $5-6$ years. Because I use a common VISIR spectrum to find $V(\lambda)$, this could cause $V(\lambda)$ to be overestimated in observations after 2010, especially effecting the 2014 observation.

I therefore compared the 2014 MIDI observation to the two close UT1/UT3 observations from 2010. $F_{\rm corr}(\lambda)$ is lower for the 2014 observation than the two 2010 observations, which would not be expected if it were effected by an *increase* in flux. Furthermore, I compared observations of the same PA with different baseline lengths. Again, the 2014 measurement lies below a Gaussian interpolation of the measurements from 2010. I therefore conclude that the increase in $F_{\rm tot}(\lambda)$ did not lead to a measurable increase of $F_{\rm corr}(\lambda)$ and hence does not significantly impact my results.

4.3.2 Interferometric observations

As mentioned in Section 3.1, EWS provides wavelength differential phases, with the absolute phase information being destroyed by the atmosphere. However, the differential phase spectrum for every observation is flat, at 0°, within 1σ errors. No discernible phase implies that there is no image centre shift in the wavelength range observed. Therefore, I did not include phase information in the fitting beyond making the model's centre invariant in location and the model centrosymmetric.

4.3.2.1 Dust morphology from interferometric observations

As an initial check for structure, I plot $V(\lambda)$ against baseline length in Figure 4.5. $V(11.8\,\mu\text{m})$ never falls below 0.6, which makes the source approximately 60% unresolved. An interesting feature of Figure 4.5 is an apparent levelling off of $V(\lambda)$ for BL > 80 m. The level feature could be interpreted as the source having two distinct components, one of which is partially resolved and the second unresolved and responsible for more than 60% of the flux. The unresolved component must be on a scale smaller than ~5 mas.

To check for any angular dependence, I binned the observations, by PA, into three bins of 60° (Figure 4.5). When considering each bin separately, a clear decrease with baseline length in the green and blue bins can be seen. The remaining red bin contains only one observation; therefore, the decrease for this bin cannot be seen directly. However, it has a visibility of 1 at a baseline length of $0-8.2$ m, from the VISIR single dish imaging, and I make the assumption that the unresolved component does not show any noticeable angular dependence. I assigned each bin a Gaussian and a constant to show the baseline dependent change. All the constants were set to be the same at 0.65. In Figure 4.5 it can be seen that the source is more resolved in the $120°-180°$ bin and less resolved in the $60°-120°$ bin.

With evidence of angular structure, I performed a clearer, model independent, test for angle dependent structure by calculating the 66% light radius ($r_{0.66}$) for the $11.8\,\mu$m data shown in Figure 4.5. I chose 66% of the flux to match the flux value of the singular red point. I separated the observations into four bins at 26°, 41°, 85°, and 174° with 4, 3, 2, and 1 observations in each bin respectively. I then fit a straight line to each bin, except for the 174° bin, which corresponds

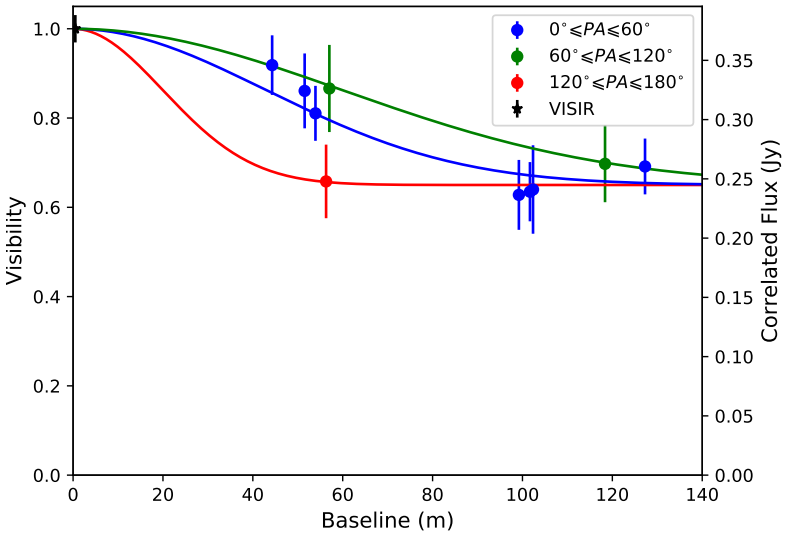

FIGURE 4.5: $V(11.8\,\mu\text{m})$ observations binned into three groups based on PA and fitted with a Gaussian and a constant. The singular red point was given the same constant as the other two fits.

to the lone red point in Figure 4.5, and interpolated each of the other bins to the visibility value of the red point, $V = 0.66$. The interpolation provides the baseline length at which each bin has a visibility value of 0.66. I convert the baseline length to RA and DEC, using $r_{0.66} = \frac{BL}{2\lambda}$, and derive errors for the fitted bins using a Monte Carlo method. The result is the 66% light radius, which is the angular size at which 66% of the flux is contained. To the 66% light radius, I fit an ellipse. The result is plotted in Figure 4.6 with a PA of the major axis of 166° and an axis ratio of 3.1.

4.4 Modelling

4.4.1 Geometric model

Due to the low *uv* coverage and the lack of absolute phase information, it is impossible to reconstruct an image from the data; instead, I have to fit a model. To obtain a first understanding for the geometry of the warm dust in ESO 323-G77, I fit a two component model to the visibility data, similar to the one described in López-Gonzaga et al. (2016). In the geometric model, the unresolved component is represented by a 2D radially symmetric Gaussian with an FWHM of the dust sublimation radius of ESO 323-G77 given in Kishimoto et al. (2011b). The second Gaussian is an elongated 2D Gaussian. The model was analytically converted to Fourier space to produce the final model for fitting. The analytical description of the visibility is given by:

$$V(u,v,\lambda,\Theta_y,\epsilon) = (1-p_f)F_1(u,v,\lambda,\Theta_y,\epsilon)+p_f F_2(u,v,\lambda), \quad (4.1)$$

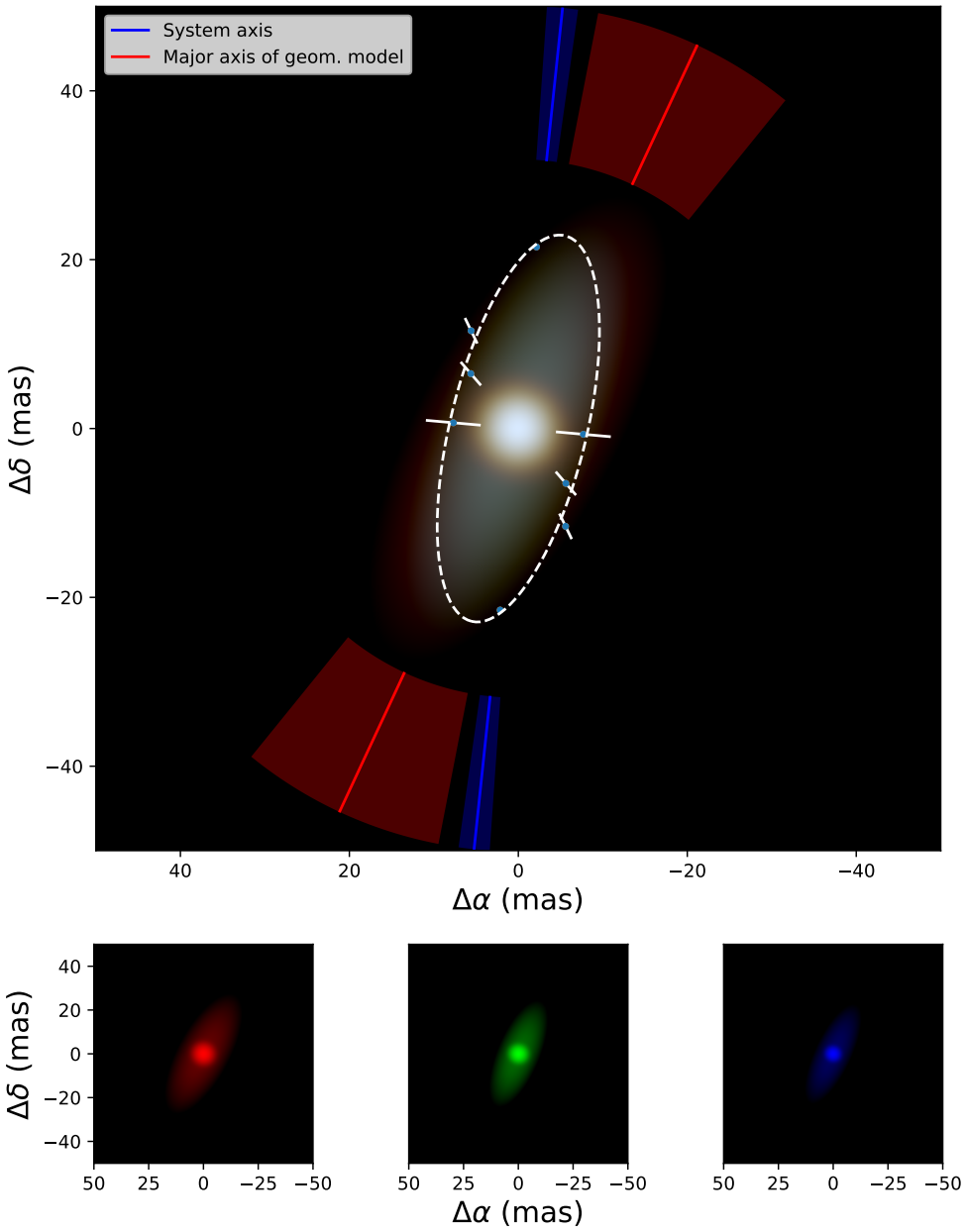

FIGURE 4.6: False colour image of the geometric model. The blue, green, and red channels are the average geometric model fits for 8.6 μm and 9 μm, 10.2 μm, and 10.6 μm, and 11.8 μm and 12.2 μm respectively. Each channel is plotted individually below the main panel. The models fluxes are plotted with logarithmic colour scaling. Overplotted is the 66% light radius at 11.8 μm for four different position angles, fitted with an ellipse (dashed line). Also indicated is the mean position angle of the major axis of the geometrical model and its uncertainty in red (c.f. Figure 4.7 and 4.8) and the system axis in blue.

where

$$\begin{aligned} F_1(u,v,\lambda,\Theta_y,\epsilon) &= \exp\left[-\left(\frac{C\Theta_y}{\lambda}\right)^2\left(\frac{u'^2}{\epsilon^2}+v'^2\right)\right], \\ F_2(u,v,\lambda) &= \exp\left[-\left(\frac{C\Theta_s}{\lambda}\right)^2(u^2+v^2)\right], \end{aligned} \tag{4.2}$$

and

$$\begin{aligned} C &= \frac{\pi^2}{1.296\cdot 10^9\cdot\sqrt{\ln 2}}, \\ v' &= u\sin\theta + v\cos\theta, \\ u' &= u\cos\theta - v\sin\theta, \end{aligned} \tag{4.3}$$

where Θ_y is the FWHM value of the major axis of the elongated Gaussian in mas, ϵ is the major to minor axis ratio of the elongated Gaussian, Θ_s is the expected sublimation radius in mas, λ is the wavelength, and p_f is the unresolved fraction. The constant C comes from the conversion of degrees to mas and the conversion from σ to FWHM with an extra factor of π originating from the Fourier transform.

The $V(\lambda)$ measurements were separated into bins by wavelength with a width of $0.4\,\mu$m and fitted independently of each other. Fitting multiple wavelengths had the advantage of being able to test the models dependence on λ.

4.4.1.1 MCMC Bayesian modelling

The MCMC (Markov Chain Monte Carlo) method of model fitting is used in Chapter 4, 5, and 6 of this work. Here I will give a general overview of MCMC fitting and I will leave any specifics to the chapters in which it is used. EMCEE is a python implementation of Goodman & Weare's Affine Invariant MCMC Ensemble sampler (Goodman and Weare, 2010).

In a general MCMC, you have a collection of walkers. Each of these walkers can be likened to an individual realisation of a standard fitting routine. In a general fitting routine a sample is obtained at a location in parameter space. The goodness of fit for the sample is evaluated and the routine bases where to take the next sample from the previous. Eventually, repetitive sampling leads the routine to the best fitting set of parameters. The given explanation is a gross oversimplification of a fitting routine but it is the basis of how a walker works.

In the Metropolis-Hastings case, which is not used in this work but is a common MCMC implementation in astronomy, a walker initially samples its position in parameter space. It then proposes a new location based on a random probability I will call the movement probability, commonly a normal distribution with a given width centred on the walker. The proposed location is then sampled. The walker is then given a probability of accepting the proposed location

based on the evaluation of the two locations and movement probability for the size of the step needed. If the proposal is accepted the process is repeated at that point, if it is not then the process is repeated from the previous point. The process is done for every walker for a given number of iterations. The difference between the Metropolis-Hastings method and the Goodman & Weare's affine invariant method is that the movement probability is based on the position of the other walkers instead of itself. A walker at position X_1 makes a move by randomly selecting another walker from the ensemble with a position X_2. The location it then proposes (X_p) is given by:

$$X_p = X_2 + Z(X_1 - X_2), \tag{4.4}$$

where Z is a scaling variable (Goodman and Weare, 2010). Z is picked from the distribution g(z)=$z^{-0.5}$ for z between 1/2 and 2. The location is then accepted or refused based on the evaluation of the two locations and Z.

How I evaluate the drawn parameter samples is where the Bayesian component of the fitting comes in. For a sample, I calculate the posterior probability. The posterior is defined by Bayes theorem:

$$p(\alpha|\text{data}) = \frac{p(\text{data}|\alpha) \times p(\alpha)}{p(\text{data})}, \tag{4.5}$$

where α is the model parameters, $p(\alpha|\text{data})$ is the posterior distribution, $p(\text{data}|\alpha)$ is the likelihood function, and $p(\alpha)$ is the prior distribution. The notation here is such that the probability of A occurring given B is denoted by p(A|B). Therefore, the posterior is the probability of a model given the data and by maximising this, the most likely model for the data is found. The denominator can be difficult to evaluate, it is defined as the probability of obtaining the sample of data for every possible model. It is essentially a normalisation that does not depend on α. The shape of the posterior distribution is held in the numerator. Since I am not attempting to calculate the absolute probability value, just the parameter combination for which it is maximised, I do not need the denominator. I only require the likelihood and the prior.

$$p(\alpha|\text{data}) \propto p(\text{data}|\alpha) \times p(\alpha), \tag{4.6}$$

The likelihood is the probability of generating the data given that the model has the parameters α. To find a good descriptor for the likelihood, I invoke the central limit theorem. There are many hidden factors between a source and determining the visibility or phase (atmosphere, imperfect optics, detector noise, etc.) so the central limit theorem says that the probability distribution will tend to Gaussian. Therefore, I use a normal distribution for my likelihood. Furthermore, I assume that the variance in the data is underestimated in the errors by a fractional amount f. It is easier to evaluate the likelihood in log space programmatically so the ln likelihood is:

$$\ln p(\text{data}|\alpha) = -0.5 \sum_{n}^{N} \left[\frac{(y(x_n) - \text{model}(x_n, \alpha))^2}{\sigma_n^2 + f^2 \text{model}(x_n, \alpha)^2} + \ln\left(2\pi\left(\sigma_n^2 + f^2 \text{model}(x_n, \alpha)^2\right)\right) \right], \tag{4.7}$$

for a set of data of length N with values y and positions x. The variance is denoted by σ.

Finally, I need a prior. The prior is the knowledge you have of a system. A true prior requires you to have information about the system with which to predict the probability that a combination of parameters α exists. I cannot predict the prior for my systems without introducing personal bias. Therefore, because of my ignorance of the true distribution of parameters I make an uninformative prior. A flat prior is essentially a top hat function over the possible parameter space. The probability is non-zero, flat and sums to one over the possible range and is zero where it is not possible. There is still some bias introduced when deciding what is possible, however, it can be assumed that, say, an object in an image cannot be smaller than the resolution for example without losing information about the system. Any value smaller than the resolution would have to be treated as an upper limit to the size at the resolution regardless of the fit derived uncertainty.

With the prior and likelihood, I can perform the MCMC analysis. Each walker samples the posterior probability distribution and, once it reaches the maxima, will still vary around the peak. The variation is dictated by the uncertainty in the result as set by the provided information. By taking the median of all the samples of all the walkers after they settle around an answer, I can find the most likely set of parameters. By taking the 16th and 84th quantiles of the distribution of samples for each parameter, I get the $\pm\sigma$ errors assuming the distribution is Gaussian.

The MCMC method may seem like a lot of trouble, but in a sparse data system with possible hidden error it has some advantages. The MCMC method can reduce the bias effect from the under-sampled directions in the *uv* plane. It also has the advantage of providing probability distributions for all fitted parameters, listed in Table 4.3, from the distribution of the samples measured by the walkers. However, it is important to note that using MCMC Bayesian fitting does not necessarily make the fit reliable, the fitting still has to be adequately tested.

4.4.2 Influence of the *uv* plane

To ensure any results produced were uninfluenced by the positions of the *uv* points, I input a wide range of test data. I employed the same method of mock data creation as that in López-Gonzaga et al. (2016). The test data was produced by using the same model as was fitted to the data. I used the *uv* position values from the real data and assigned each a mock visibility from a mock model. Each *uv* point was then randomly offset by Gaussian noise derived from the real error of the original it represented. I then fitted the set of mock data and compared the resulting parameters to the input parameters to test the reliability of the recovered PA, not the viability of the model itself. To make sure there were no degeneracies in the fitting due to poor *uv* coverage, all parameter combinations were tested, removing any degenerate pairings. Taking into account the fit result from Burtscher et al. (2013) and López-Gonzaga et al. (2016), I chose the following parameter space:

$$0.0 \leqslant p_f \leqslant 0.9 \text{ in steps of } 0.1$$

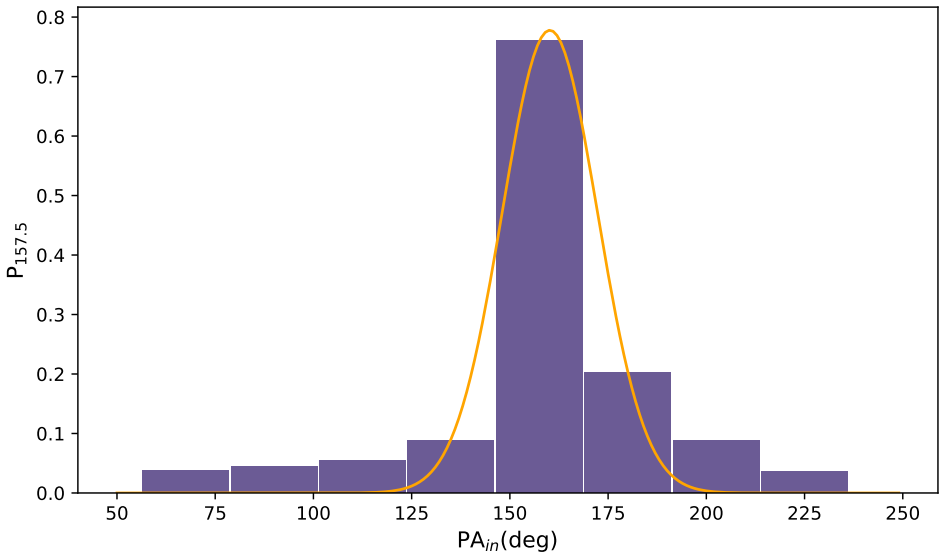

FIGURE 4.7: Probability with which an object with position angle, PA, of PA_{in} is modelled with a PA between 146° and 169°. This gives the uncertainty of the fitted PA of ESO 323-G77 at the 68% and 95% confidence intervals as 12° and 24° respectively. This does not include objects with an axis ratio, ϵ, of 1.

$$1.0 \leqslant \epsilon \leqslant 4.0 \text{ in steps of } 1.0$$

$$11.7 \leqslant \Theta_y \leqslant 49.0 \text{ in steps of } 9.3$$

$$0^\circ.0 \leqslant PA \leqslant 157^\circ.5 \text{ in steps of } 22^\circ.5$$

The test was repeated five times, giving 6300 results; the result for PA is plotted in Figure 4.7. This plot shows the probability that a source with a PA of PA_{in} would be fit by a PA of 157.5° given the distribution of the *uv* plane. If the observations are fitted with a smaller error in PA than recovered with this method, the true uncertainty would still be the one given by this test due to the influence of the *uv* plane distribution. From the test, I derive an uncertainty for the recovered PA of 12° for 68% confidence and 24° for 95% confidence. I conclude that with the new measurements since 2010 the *uv* coverage is now sufficient to constrain any elongation.

4.4.3 Geometric modelling results

The results of the MCMC Bayesian fitting of the interferometric data at each wavelength can be found in Table 4.3. The detailed fit results can be found in Figures A.1–A.13 in the Appendix. I find that the fits at longer wavelength, $\lambda > 10\,\mu$m, are well constrained. At shorter wavelengths, I find that the UT3/UT4 observation dominates, making the fit less constrained.

I plot the model parameters as a function of wavelength in Figures 4.8–4.11, as well as the weighted average or a linear fit to the wavelength dependency. The weights are $1/\sigma^2_{\text{err}}$. This does not account for correlated noise which is present between the fits. The correlated noise comes

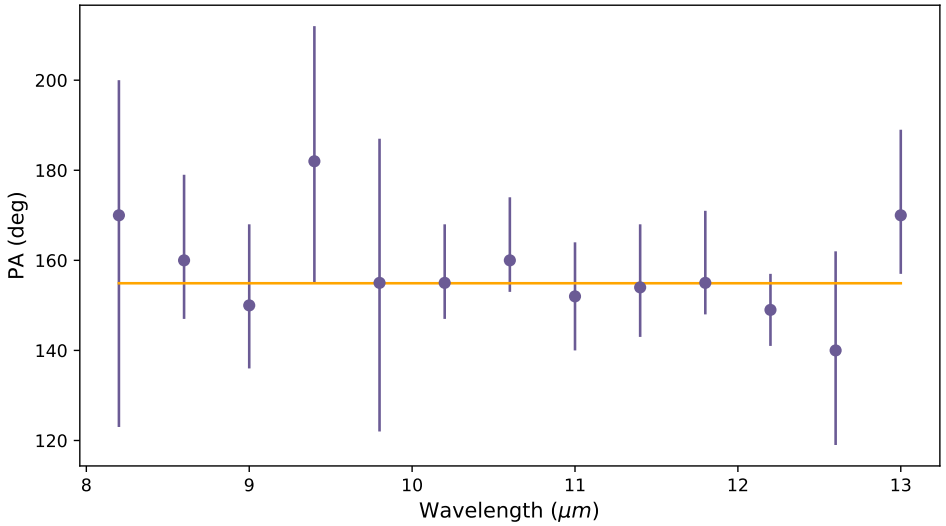

FIGURE 4.8: Position angle, PA, of the major axis of the geometric model for each wavelength bin. The orange line is the weighted average value.

from the visibility which has a common statistical error contribution at every wavelength. Any averaged results given in the text are produced without weighting and the errors are determined from the scatter in the results or from Figure 4.7 in the case of PA.

In Figure 4.8, it can be seen that the PA is fairly well constrained. I find that the PA has an average value of $155^\circ \pm 12^\circ$. Figure 4.8 shows hints of a steady decrease in PA with increasing wavelength; however, there is no statistically significant correlation found, using the Spearman rank, with a p value of 0.45 ± 0.3. At the same time, in Figure 4.9 I find that the unresolved source fraction increases from 62% to 79% for shorter wavelengths. I interpret the increase as greater influence from the hot component at shorter wavelengths. I also find that the major axis is well defined above 10 μm with $\Theta_y = 26.6$ mas at 10.2 μm. The major axis increases with wavelength to $\Theta_y = 32.4$ mas at 13.0 μm (Figure 4.10). Because the longer wavelengths probe cooler dust, I see the major axis increase as evidence for the dust being heated by the central engine. I find $\epsilon(\lambda) = 2.9 \pm 0.3$, without any dependency on wavelength which suggests that the geometry does not change significantly with wavelength, only the total size changes. To highlight any change in geometry with wavelength, I plot an RGB image of the geometric model results in Figure 4.6 together with the 66% light radius. Each channel in the image represents the average of two of the model results: the blue represents the average of the 8.6 μm and 9 μm results; the green represents the average of the 10.2 μm and 10.6 μm results; and the red represents the average of the 11.8 μm and 12.2 μm results. Each channel is convolved with the maximum angular resolution at that wavelength. The two component structure with the strongly elongated extended component can be clearly seen. The above mentioned increase in size of the extended component with wavelength can also be seen: the emission starts bluer in the centre and becomes redder toward the edges of the extended component.

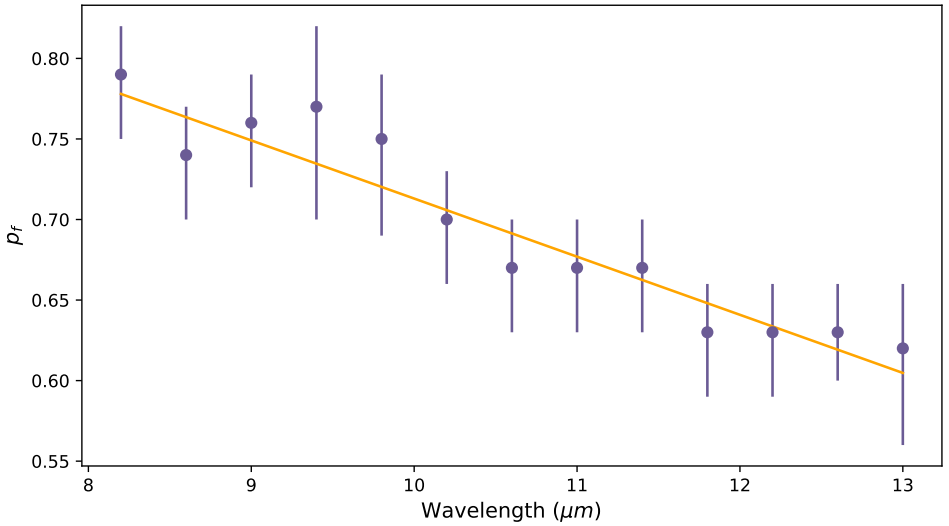

FIGURE 4.9: Unresolved source fraction, p_f, of the geometric model for each wavelength bin. The orange line is the weighted line of best fit.

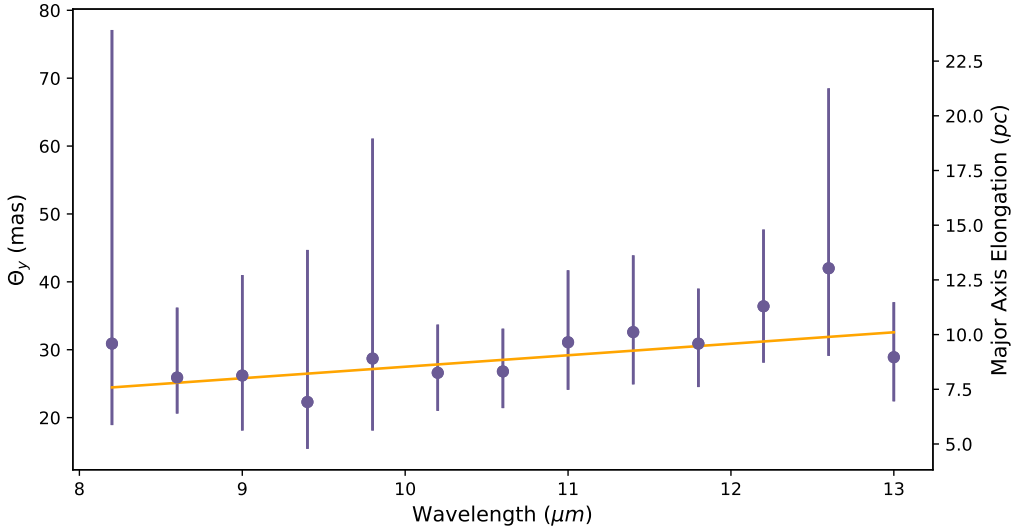

FIGURE 4.10: Major axis FWHM, Θ_y, of the geometric model for each wavelength bin. The orange line is the weighted line of best fit.

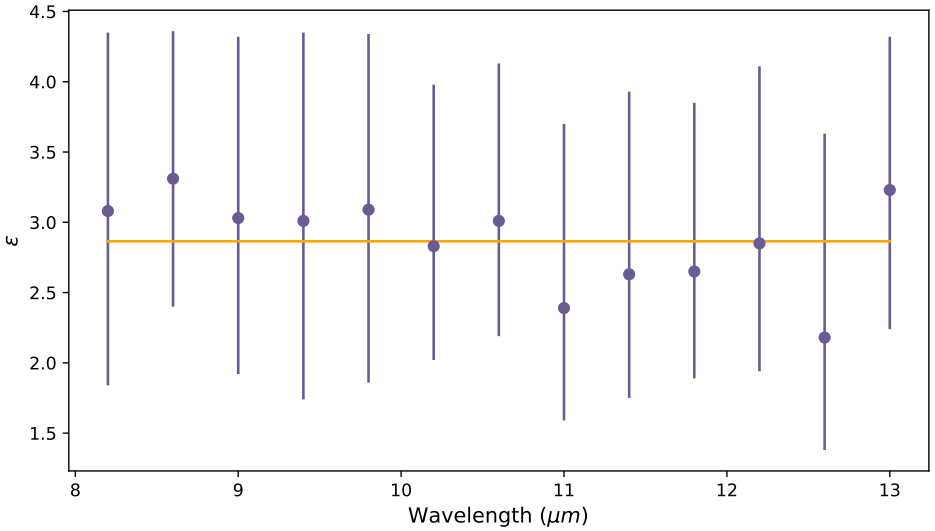

FIGURE 4.11: Axis ratio, ϵ, of the geometric model for each wavelength bin. The orange line is the weighted average.

Figure 4.12 shows the interferometric data at 11.8 μm as a function of baseline length, similar to Figure 4.5, with the geometric model overplotted. The plot suggests that the PA is not constrained solely by the single visibility measurement at BL = 56.3 m and PA = 353°.2 which has a lower visibility than other points at similar baseline lengths (red point in Figure 4.5). To further check the 56.3 m influence, I re-fitted the 11.8 μm data without this observation. I recovered the PA as 158^{+17}_{-9}°, the unresolved fraction as $0.63^{+0.03}_{-0.04}$, ϵ as $2.2^{+1.2}_{-0.7}$, and a Θ_y of $27.8^{+8.6}_{-6.5}$ mas. The result is within errors of the original fit but with greater uncertainty. From the result, I can say the point helped to constrain the model result but is not solely responsible for it. The most sensitive result of the change is the PA. Each observation at the ~55 meter baseline length constrains the direction of the extension. The errors in Figure 4.8 only include the uncertainties found by MCMC fitting and do not include the uncertainty found from the influence of the *uv* plane.

4.4.4 CAT3D-WIND radiative transfer modelling

Radiative transfer models have been used to explain to explain the IR SEDs of AGN by simulating the reprocessed dust emission for a given distribution of dust. Models have previously used the dusty torus to successfully explain the SEDs of Seyfert AGN (Hönig et al., 2010). However, SED fitting provides zeroth order information about the geometry and not information about the true dust distribution. This changed in Hönig and Kishimoto (2017). Instead of just SED fitting, they used the polar dust wind radiative transfer model, *CAT3D-WIND*, and the clumpy dust torus model, *CAT3D*, to simultaneously fit mid-IR interferometry and IR SED of NGC 3783. In the *CAT3D-WIND* model the dust clumps are arranged in a thin disk and a hollow bi-cone, as seen

Wavelength (μm)	p_f	ϵ	Θ_y (mas)	θ (deg)	ln(f)
8.2	$0.79^{0.03}_{0.04}$	$3.08^{1.27}_{1.24}$	$30.9^{46.2}_{12}$	170^{30}_{47}	$-8.9^{4.3}_{4.1}$
8.6	$0.74^{0.03}_{0.04}$	$3.31^{1.05}_{0.91}$	$25.9^{10.3}_{5.3}$	160^{19}_{13}	$-9.8^{4.6}_{3.7}$
9	$0.76^{0.03}_{0.04}$	$3.03^{1.29}_{1.11}$	$26.2^{14.8}_{8.1}$	150^{18}_{14}	$-9^{3.9}_{4.1}$
9.4	$0.77^{0.05}_{0.07}$	$3.01^{1.34}_{1.27}$	$22.3^{22.4}_{6.9}$	182^{30}_{27}	$-10.8^{5}_{3.1}$
9.8	$0.75^{0.04}_{0.06}$	$3.09^{1.25}_{1.23}$	$28.7^{32.4}_{10.6}$	155^{32}_{33}	$-9.3^{4.3}_{3.9}$
10.2	$0.7^{0.03}_{0.04}$	$2.83^{1.15}_{0.81}$	$26.6^{7.1}_{5.6}$	155^{13}_{8}	$-10.5^{4.7}_{3.4}$
10.6	$0.67^{0.03}_{0.04}$	$3.01^{1.12}_{0.82}$	$26.8^{6.3}_{5.4}$	160^{14}_{7}	$-10.8^{4.6}_{3.2}$
11	$0.67^{0.03}_{0.04}$	$2.39^{1.31}_{0.8}$	$31.1^{10.6}_{7}$	152^{12}_{12}	$-9.3^{4}_{3.9}$
11.4	$0.67^{0.03}_{0.04}$	$2.63^{1.3}_{0.88}$	$32.6^{11.3}_{7.7}$	154^{14}_{11}	$-9.6^{4.2}_{3.7}$
11.8	$0.63^{0.03}_{0.04}$	$2.65^{1.2}_{0.76}$	$30.9^{8.1}_{6.4}$	155^{16}_{7}	$-10.6^{4.6}_{3.3}$
12.2	$0.63^{0.03}_{0.04}$	$2.85^{1.26}_{0.91}$	$36.4^{11.3}_{8.3}$	149^{8}_{8}	-9.2^{4}_{4}
12.6	$0.63^{0.03}_{0.03}$	$2.18^{1.45}_{0.8}$	$42^{26.5}_{12.9}$	140^{22}_{21}	$-9.6^{4.3}_{3.7}$
13	$0.62^{0.04}_{0.06}$	$3.23^{1.09}_{0.99}$	$28.9^{8.1}_{6.5}$	170^{19}_{13}	$-10^{4.6}_{3.6}$

TABLE 4.3: Results of model fitting for each wavelength bin. p_f is the unresolved source fraction, ϵ is the ratio of the major axis to minor axis, Θ_y is the major axis FWHM, θ is the angle from north to east of the Θ_y component of the Gaussian and f is the fractional amount for which the variance is underestimated by the likelihood function if the errors were assumed correct (Foreman-Mackey et al., 2013).

in Figure 1.4, instead of a clumpy torus. The data of NGC 3783 could not be reproduced with the more general clumpy dust torus model that *CAT3D-WIND* is based off of.

The same strategy as Hönig and Kishimoto (2017) was incorporated to model the interferometry of ESO 323-G77. First, the high-resolution IR photometry and spectroscopy of ESO 323-G77 was used to find acceptable fits to the SED from the suite of approximately 132,000 *CAT3D-WIND* models. The observed IR SED in comparison to model SEDs is shown in Figure 4.13. VLT/ISAAC fluxes have been extracted from archival ESO data[1] using standard photometric procedures. The VISIR fluxes were presented by Asmus et al. (2014) while the *Spitzer* IRAC and 2MASS photometry was reported by Kishimoto et al. (2011b). The latter paper's Galactic extinction correction of $A_V = 1.2$ mag was utilised. The light-grey lines in Figure 4.13 represent all models within the 95% confidence interval of the best SED fit (solid dark-grey line) according

[1] data acquired as part of programme 290.B-5113, PI D. Asmus

Parameter	N_0	a_d	a_w	h	θ_w	θ_σ	$f_{\rm wd}$	inc
Value	5	−3	−1	0.1	30°	10°	0.6	60°

TABLE 4.4: Results of the best fit *CAT3D-WIND* model. N_0 is the average number of clouds in the line of sight in the equatorial region, a_d is the radial power-law index for the disk $\propto r^{a_d}$, where r is in units of the sublimation radius, a_w is the radial power-law index of the dust clouds in the polar wind, h is a unitless disk height scaling factor, θ_w is the opening angle of the polar wind, θ_σ is the angular width of the polar wind, $f_{\rm wd}$ is the wind to disk ratio, and inc is the inclination.

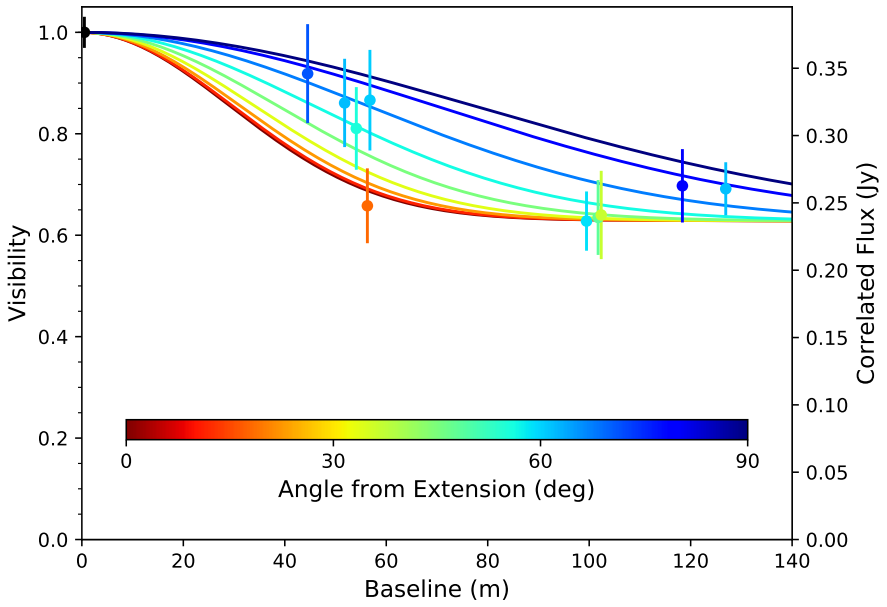

FIGURE 4.12: The $V(11.8\,\mu\text{m})$ of each observation against its baseline. The data points are coloured by PA from the Gaussian major axis of the geometric model in real space. The fitted geometric model is overplotted for different PAs. The value at 0 m base length is the VISIR observation at $11.8 \pm 0.2\,\mu$m and its errors are a systematic offset for all the *uv* points.

to a χ^2 distribution. The SEDs strongly prefer compact disk emission ($a_d = -2.5 \cdots -3$) with a more extended wind component ($-0.5 \leq a_w \leq -1.5$). The scale height, h, of the disk is relatively small, with three-quarter of all models preferring $h = 0.1$ and the remainder $h = 0.2$. Based on the SED alone, the mean number of clouds, N_0, along the line of sight is favoured as being $N_0 = 5$, with only half as many obscuring the AGN when grazing the hollow cone, i.e. $0.25 < f_{\text{wd}} < 0.75$. N_0 is expected to be between 1 and 10 in most AGN because when a cloud model is physically motivated a single cloud has a size and density that equates to a column density of $10^{22} - 10^{23}\,\text{cm}^{-2}$ (e.g. Krolik and Begelman, 1988; Vollmer and Beckert, 2002; Beckert and Duschl, 2004). Considering typical column densities seen in AGN, the order of cloud along the equatorial line of sight comes out as approximately $N_0 \sim 10$. Inclinations of the accepted *CAT3D-WIND* models range from 0° to 60° with a preference for lower inclinations. Finally, the opening angle of the cone is $\theta_w = 30°$ in about 80% of all acceptable models with the remaining at $\theta_w = 45°$. The width of the hollow cone is unconstrained by the SEDs.

Before beginning the computationally expensive task of simulating 3D radiative transfer models, it is prudent to exclude any model which cannot produce good fits for the interferometric data. ESO 323-G77 is highly polar extended, therefore, low inclination models can be excluded because they do not show the required strong angular dependence of visibility. Large opening angles of 45° are also disregarded for the same reason. ESO 323-G77's high unresolved source fraction means radial dust distributions of $a_w = -0.5$ can be disregarded. They generally overestimate the contribution from the wind leading to visibilities that are too low. All remaining

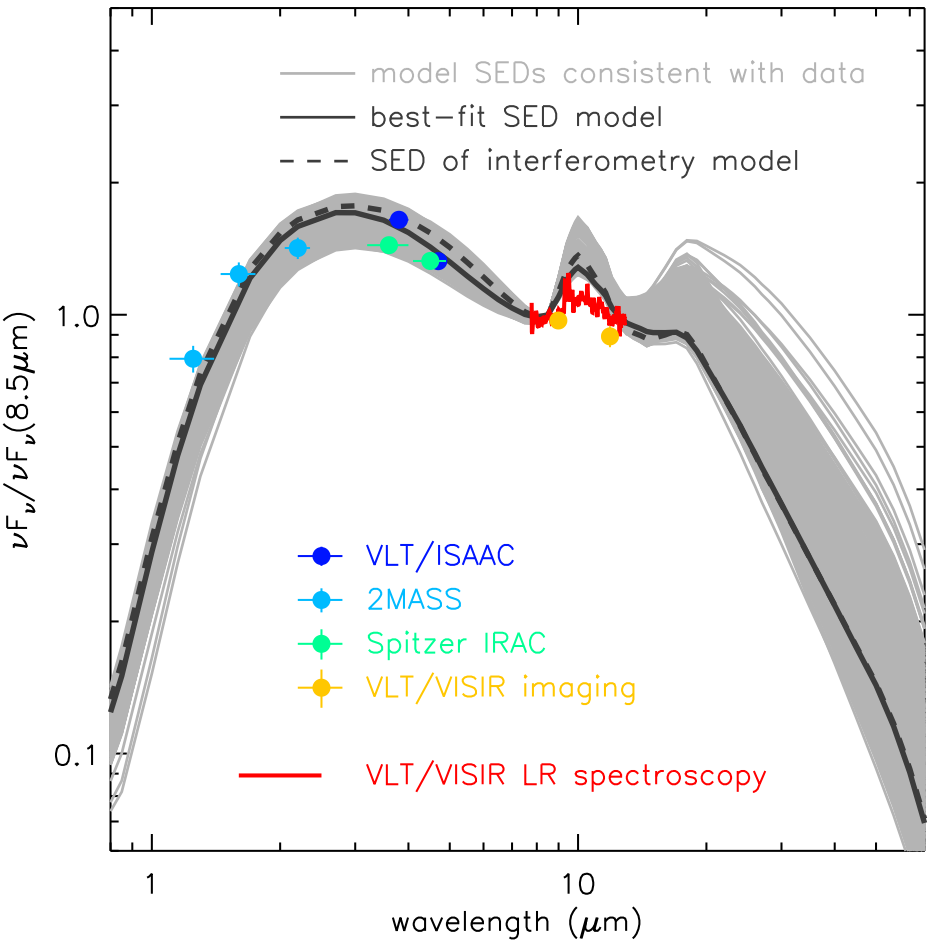

FIGURE 4.13: Figure originally from Leftley et al. (2018) with permission. High-resolution SED of ESO 323-G77. The filled circles represent observed photometry from the near-IR and mid-IR, while the red line shows the VISIR spectrum. The data have been corrected for Galactic extinction of $A_V = 1.2$. The light-grey lines show *CAT3D-WIND* model SEDs that are consistent with the 95% confidence interval of the best fit (solid dark-grey line; see text for details). The dashed black line shows the SED of the model that is used to reproduce the MIDI interferometry in Figure 4.14.

models were then simulated. Reproducing the unresolved source fraction and strong PA dependence well constrained the available parameter space leaving only a few models that can produce satisfactory visibilities. The best fitting model parameters are listed in Table 4.4 and the corresponding visibilities produced by this model are shown in Figure 4.14 along with the observational data. Within the tested parameter space, these values were the only combination to reproduce the SED, visibility, and strong PA dependence. The only parameter that had a major degeneracy was the width of the hollow cone, θ_σ, which produced similar results for 10° and 15°.

Similarly to the *CAT3D-WIND* modelling of NGC 3783 in Hönig and Kishimoto (2017), these new results illustrate the constraining power of interferometric data on the geometry of the dust distribution. SED modelling is restricted to the integrated, zero-dimensional emission, with the

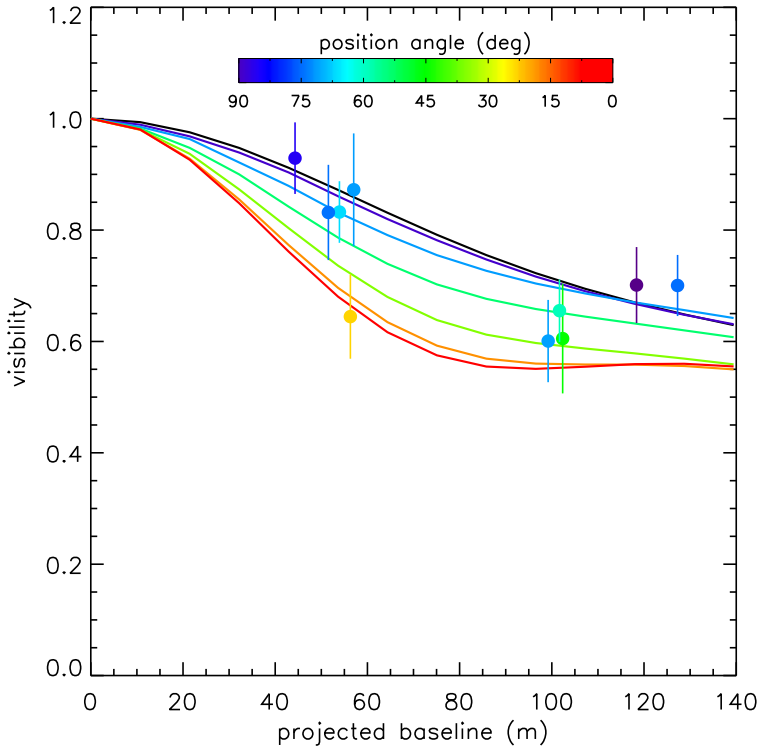

FIGURE 4.14: Figure originally from Leftley et al. (2018) with permission. Radial visibility versus baseline as observed (filled circles) and modelled with *CAT3D-WIND* (solid lines) model at 12 μm for ESO 323-G77. The colours represent position angle with respect to 155°, the major axis of the geometric model.

geometric distribution contributing a highly degenerate flux weighting function. Interferometry provides additional two-dimensional constraints of the flux distribution that reveal features not necessarily captured by a model based only on an SED. Indeed, the SED of ESO 323-G77 has a shape that is covered by classical torus-only models as well as the disk+wind model (see Hönig and Kishimoto, 2017, for a comparison of torus model and disk+wind model SED parameter space). However, the clumpy torus model alone fails to simultaneously fit the SED and the interferometric data. Interferometry revealed the significant polar-elongated mid-IR emission, which can only be reproduced by the disk+wind model.

4.5 Discussion

4.5.1 Comparison of the results

The 500.7 nm [O III] emission from the S7 data is shown in Figure 4.4. I overplotted the PA of the geometric model as a red line and the polar axis derived from the polarisation measurements as a blue line. Although the NLR appears to be bent or obscured 5" from the central region, Figure 4.4 shows that the mid-IR emission in ESO 323-G77 is polar extended.

The constraints on the mid-IR size presented here are consistent with previous observations of ESO 323-G77: Kishimoto et al. (2011b) report a Gaussian FWHM of 24.6 mas $\pm$ 0.8 mas, while I find an average FWHM of 21 mas $\pm$ 2.3 mas at 11.8 μm. Burtscher et al. (2013) perform a two component fit, consisting of a Gaussian and a point source, finding that their point source fraction for ESO 323-G77 is unconstrained. They proceeded to use a 1 component model, consisting of only the radially symmetric Gaussian, and by consequence find an FWHM of only 6.74 mas which is far smaller than my result and the result from Kishimoto et al. (2011b). López-Gonzaga et al. (2016) report a FWHM of 17.3 mas for the minor axis and an ϵ of 1.4 in their Figure A.1 (N. Lopez 2017, private communication). The PA was unconstrained and, therefore, the axis ratio was reduced as well as the major axis size; however, the average sizes can still be compared. The López-Gonzaga et al. (2016) result corresponds to an average size of 21 mas, which agrees with my result within 1σ.

The geometric model reproduces the interferometric data very well (see Figure 4.12), and directly infers the geometry of the source from the data. The *CAT3D-WIND* model, on the other hand, gives a better description of the properties of the AGN beyond geometry as described in Hönig and Kishimoto (2017). The parameters between both the geometric and the radiative transfer models are very comparable. The primary feature constrained by the *CAT3D-WIND* model is the average distribution and density of the dust clumps, which is much more concentrated toward the disk than for other AGN (see, e.g. Hönig and Kishimoto, 2017). The clump distribution is essential in understanding the luminosity distribution to make predictions for what would be observed in other wavelengths. Since the model was generated using the SED, it did not relate to the interferometric data directly, instead the observed interferometric data narrowed down the possible *CAT3D-WIND* models that fit the SED. Future observations in other wavelengths could further narrow down the possible models. It should be noted that none of the *CAT3D-WIND* models reproduced the 10 μm silicate feature, this is not unexpected because the silicate feature is very sensitive to the actual dust composition. The global opacities are not super sensitive to the exact details of the dust composition and do not significantly effect the dust clump distribution.

The *CAT3D-WIND* model can be used to predict the size and shape of the *hot* dust emission. Based on the best fit model, I expect a hot dust disk with an inclination of 60° and a major axis FWHM, if approximated by a Gaussian, of about 0.3 pc ($\approx$ 1 mas). The hot dust can be observed with near-IR interferometry in the *K*-band, e.g. with VLTI/GRAVITY, and corresponds to a visibility of 0.8 on a 130 m baseline (UT1/UT4) oriented along the system plane at PA=65°. In the direction of the outflow (i.e. along the system axis), I would expect a higher visibility of 0.93 at the same baseline length. The implied radius of the *K*-band emission from the model of 0.15 pc is a factor of 2.3 larger than the model sublimation radius of $\sim$0.065 pc inferred independently from the SED fitting and the visibility scaling. The discrepancy is expected since interferometry measures an average size of the brightness distribution rather than the smallest emission radius (Kishimoto et al., 2007, 2011a). Reverberation mapping, on the other hand, is more sensitive to the smallest scales of the brightness distribution. When observed over time,

the near-IR emission is shown to vary in flux. The near-IR variation approximately mirrors the UV/optical emission variations but at a lag of tens to hundreds of days. Because the near-IR emission is caused by dust that cannot exist too close to the central engine, a lag is expected. It takes time for light to travel the distance between the engine and the dust. The dust emission only reacts to the change in flux from the central engine once the light travels the gap between the two components. The distance between the two components is simply $d = ct$ where d is the distance, c is the speed of light, and t is the travel time (e.g. Clavel et al., 1989; Glass, 1992). The method of measuring the absolute radial size of the dust component in AGN through the lag time is reverberation mapping. Indeed, reverberation mapping of ESO 323-G77 shows a lag between the optical and near-IR emission of about 89 days or 0.075 pc, fully consistent with the inference from the presented *CAT3D-WIND* model (B. Boulderstone et al. 2020, in preparation).

López-Gonzaga et al. (2016) report seven objects with a sufficient *uv* coverage to constrain an extension. Of these objects, six are Type 2 Seyferts and one is a Type 1 Seyfert (NGC3783), making ESO 323-G77 only the second Type 1 Seyfert with sufficient *uv* coverage to constrain an extension. The detection of a second polar extended Type 1 is in strong support of the disk+wind model because polar extensions in Type 2s can also be explained by the standard torus model due to self-shielding effects or anisotropic illumination (Hönig et al., 2012); however, polar extended Type 1 AGN cannot easily be explained by such models.

In fact, López-Gonzaga et al. (2016) find that the PA of all the objects that show an extension is approximately 20° away from the system axis. I also find the offset for ESO 323-G77. The disk+wind model explains the offset as an edge brightening effect of the hollow cone.

4.5.2 An evolution of the dust distribution with Eddington ratio?

The observations and modelling have revealed highly elongated mid-IR dust emission in ESO 323-G77 with a much higher elongation than those found in previous work (Hönig et al., 2012; López-Gonzaga et al., 2016). Furthermore, ESO 323-G77 is the first clear example of an AGN dominated by unresolved emission in the mid-infrared that, at the same time, has a detected polar extension.

From the full IR SED and the strong unresolved source-wavelength anti-correlation revealed by the geometric modelling, I interpret the dominant unresolved source as the Rayleigh-Jeans tail of the hot dust emission originating from the inner region of the disk close to the sublimation radius. These results indicate strong similarities of ESO 323-G77 with the compact emission seen in two quasars (Kishimoto et al., 2011b). Given that ESO 323-G77 is considered to have a higher Eddington ratio than typical Seyferts (relatively narrow Hydrogen emission lines in the optical), similar to quasars, the result hints at evolution of the geometric dust distribution around an AGN with Eddington ratio. The evolution would take the form of more dust in the disk at higher Eddington ratios possibly caused by the larger reservoir of dust being able to provide more fuel to the AGN which would cause the higher Eddington ratio. Indeed, such a

scenario is consistent with radiation pressure shaping the mass distribution on the sub-parsec to parsec-scale environment of the AGN (Fabian et al., 2008; Ricci et al., 2017).

4.6 Chapter Summary

I presented a detailed study of the Type 1.2 Seyfert AGN ESO 323-G77 on the milliarcsecond scale in the mid-IR using MIDI and VISIR. I studied the geometry of the 300 − 400 K dust using a simple geometric model as well as the radiative transfer model *CAT3D-WIND* (Hönig and Kishimoto, 2017). The system axis of ESO 323-G77, from polarisation measurements and the NLR, is $174^\circ \pm 2^\circ$ (Schmid et al., 2003).

1. The geometric modelling of the interferometric data revealed that $\gtrsim 62\%$ of the flux is unresolved at all wavelengths and baselines. Among the remaining, resolved, fraction of the emission I discovered a dust structure with an axis ratio $\epsilon = 2.9 \pm 0.3$ elongated along PA = $155^\circ \pm 12^\circ$. Comparing the dust extension to the system axis in Figure 4.4, I conclude that this extension is in the polar direction.

2. I tested the dependence of the geometric model on the *uv* plane and showed that I could recover the PA reliably with an uncertainty of 12° for $\epsilon \geqslant 2$.

3. A model of ESO 323-G77 was created with the *CAT3D-WIND* model using its SED. Comparing the successful models to the interferometric data, the number of viable models is greatly narrowed down and the best fit model is described in Table 4.4.

I conclude that the geometric and *CAT3D-WIND* models agree within error and that both are a good description of the structure of the 300 − 400 K dust in ESO 323-G77. With the polar extension discovered in this chapter there are a total of eight AGN which have a sufficient *uv* coverage to constrain any extension. Six of these are polar extended and none have equatorial extension, making a strong case for the disk+wind model of AGN.

Chapter 5

The Near-IR Interferometric Study of ESO 323-G77

In Chapter 1, I explained how the dusty torus model is in contention with the mid-IR interferometric observations. In Chapter 4, further evidence was provided that the disk+wind model is the better description of the mid-IR interferometric observations of AGN. Central to the disk+wind model is a hot dust disk that can be seen in Type 1 AGN, but is hidden in Type 2 AGN such as Circinus. However, except for NGC 3783, no suitable observations are available yet to test if the hot dust disk is indeed present and even in that case, given the sparse data on NGC 3783, the observations are not conclusive (GRAVITY Collaboration et al., 2019). Here, I aim at testing the disk+wind hypothesis for the Type 1 AGN in ESO 323-G77.

The analysis in Chapter 4 was able to recover a strong elongation along the system axis at all wavelengths from $8-13\,\mu$m in ESO 323-G77. ESO 323-G77 is only the second Type 1 to reveal a clear polar extension. However, unlike in NGC 3783, the unresolved emission becomes more dominant at shorter wavelengths which is indicative of thermal emission from an unresolved hotter component. Indeed, ESO 323-G77, unlike NGC 3783, shows a near-IR bump that is stronger than the mid-IR emission (Kishimoto et al., 2011b). In the disk+wind picture, the dominant unresolved fraction would imply a stronger disk and weaker wind. Thus, it is the ideal object to test the disk+wind model. Here, I analyse near-IR interferometric observations from GRAVITY to test if such a hot disk is indeed present and attempt to constrain its size and direction.

5.1 Observations and Reduction

The full explanation behind the observation and reduction method can be found in Section 3.3. I will summarise the process here.

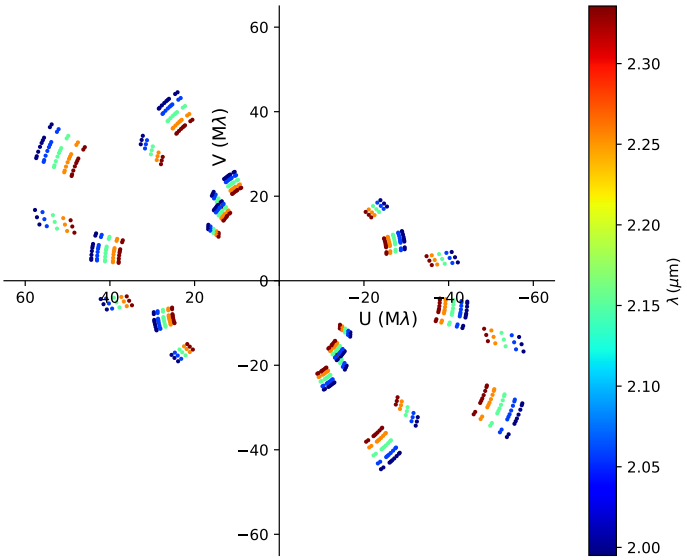

FIGURE 5.1: The GRAVITY *uv* plane for ESO 323-G77.

I successfully applied for and planned four GRAVITY observations of ESO 323-G77. Three of the GRAVITY observations for ESO 323-G77 were made in the ESO observing period p103 during 2019 as part of the observing run 0103.B-0096(A) (PI: J. Leftley). The observations dates themselves are in Table 5.1. Each observation block was structured RCAL-SCI-RCAL-CAL, however, the SCI component of the April and May block is split into three observations. The June block was instead split into six observations. When performing any analysis, the six June observations were reduced individually, paired together in time, and averaged into three observations. The averaging prevented them from having additional weight during any modelling. Each observation for April and May was 300 s long and the June observations were 160 s. In every case the CAL is HD 120271, the first RCAL is UCAC4 237-064201, and the second RCAL is NOMAD1 0480-0335664. The *uv* plane for the observations of ESO 323-G77 can be found in Figure 5.1.

The observations are initially reduced using the ESOREX GRAVITY pipeline. After the initial pipeline reduction, I utilise my own PYTHON scripts to convert the complex visibility per frame into the squared visibility and closure phase. When calculating the visibility squared only the 3% brightest frames, in terms of geometric flux, are used per baseline. The calculated visibility squared is calibrated using the red calibrators. The closure phase is found for each unique telescope triplet using the bispectrum method and calibrated by subtracting the average phase of the associated red calibrators. Unlike with the visibility squared frame selection, only pipeline flagged frames are ignored when calculating the closure phase.

5.2 Observational Results and Discussion

After reduction and calibration of the visibility squared and closure phase, I can already draw some conclusions. There is a clear drop in visibility squared of approximately 0.1 from the 20 Mλ to 60 Mλ baseline at all covered wavelengths except for the 1.99 μm bin. The shortest baseline has a lower visibility squared than the second shortest baseline in the May and June observations (see the red points in Figure 5.2). The lower squared visibility could suggest that the shortest baseline suffers an extra component of loss from an unknown source that was not mirrored in the calibrator. The suppressed first baseline is not present in the April observation which is at a similar PA to the June observation, this suggests it is not real structure. Similar losses are seen in other objects in GRAVITY Collaboration et al. (2019). However, I still include the shortest baseline in fitting because it is currently unclear if the lower visibility squared is truly artificial structure.

The first wavelength bin, 1.99 μm, is heavily suppressed in visibility and visibility squared by ~ 0.5. It also has a large, $\sim 10^{\circ}$, scattered closure phase. Both visibility and phase seem disordered; without the visibility selection, the visibility and visibility squared are negative. Because negative visibility is not physical, I do not consider results from the shortest wavelength to be reliable. The second bin (2.06 μm) also has squared visibilities that are ~ 0.1 lower than the latter three wavelength bins. By itself it can be considered reliable because the slightly suppressed visibilities show a similar structure to the latter bins and the scale of the squared visibilities is separately considered in fitting. As a precaution, I do not use the 2.06 μm bin when performing multi-wavelength fitting so as not to introduce erroneous structure.

The closure phase in each reliable bin shows structure. The phase for the 2.15 μm, 2.26 μm, and 2.34 μm wavelength bins is plotted in Figure 5.3 in purple. I find no phase for the larger triangles, as measured by the sum of the three baselines of the telescope triplet. The phase gradually increases to -1.5° for smaller triangles. A small change in phase could be interpreted

Date	Time	Int (s)
2019-04-23	03:04:24	300
2019-04-23	03:09:59	300
2019-04-23	03:25:07	300
2019-05-13	03:51:06	300
2019-05-13	04:00:33	300
2019-05-13	04:11:48	300
2019-06-20	23:38:04	160
2019-06-20	23:41:16	160
2019-06-20	23:47:47	160
2019-06-20	23:54:06	160
2019-06-21	00:00:40	160
2019-06-21	00:03:48	160

TABLE 5.1: The GRAVITY observations used in this chapter and their integration time.

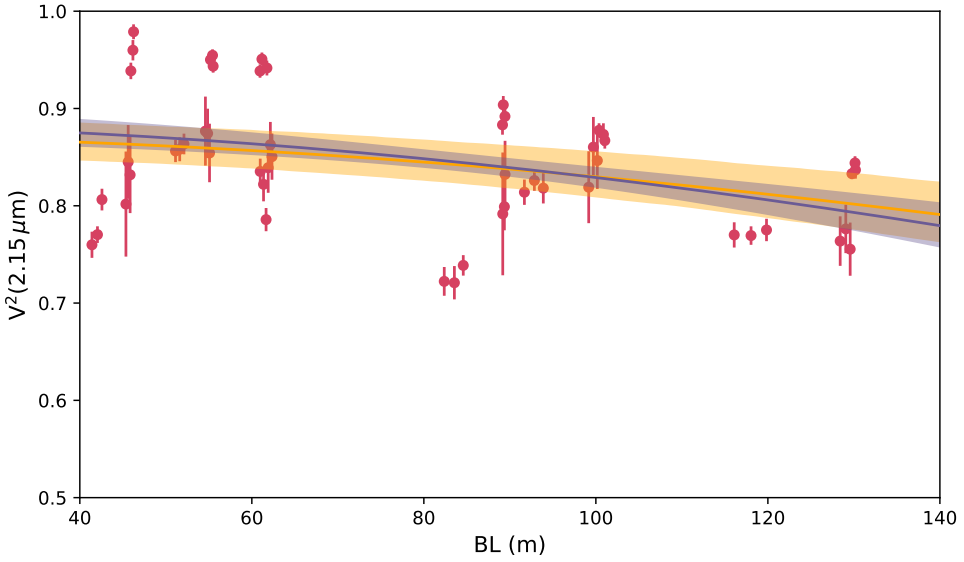

FIGURE 5.2: The visibility squared observations, at 2.15 μm, are in red. In purple is the best fit model to the observations with 1 σ error and in orange is the reverberation mapped radius with 1 σ error. I only show visibility squared from 0.5 to 1 for clarity.

as a small shift of photocentre at larger spacial scales. The component responsible for the phase would have to be resolved out for the higher spatial resolution triplets.

Over the last three wavelength bins (2.15 μm, 2.26 μm, and 2.34 μm), the visibility squared has a standard deviation of at most 0.05 at similar baseline lengths. There is no clear evidence that the variation is caused by PA dependent structure. Because there is no clear PA dependent structure, I make the assumption that the visibility squared in a single wavelength bin can be explained by a simple 1D Gaussian model. Additionally included in the model is a scale factor, this factor linearly scales the visibility squared so that the zero baseline value may be different from one due to either visibility loss or over-resolved structure. The model in Equation 4.1 becomes:

$$V^2(u,v,\lambda) \quad = \quad \left[F_1(u,v,\lambda,\Theta_y,\epsilon=1)\right]^2 - s_f, \tag{5.1}$$

where s_f is the scale factor. For fitting I use EMCEE and the same method employed in the geometric modelling of Chapter 4 except with three variables: Θ_y, s_f, and f. The reason for not including the point source in fitting is twofold: the visibility squared shows no evidence of a constant, although one is predicted due to contributions from the accretion disk, and it allows me to compare to the reverberation mapped radius, from Boulderstone et al. (in prep), using the method in GRAVITY Collaboration et al. (2019). When converting from Gaussian FWHM to ring size the point source contribution is folded in, I use a point source luminosity fraction of 0.15 instead of 0.2. A point source fraction of 0.15 is chosen because the point source fraction of 0.2 is a general value determined by Kishimoto et al. (2007) but a specific value for ESO 323-G77 was later determined by (Kishimoto et al., in prep).

Wavelength	Size (Light Days)
Reverberation	89^{11}_{18}
2.06 μm	91^{18}_{24}
2.15 μm	98^{15}_{18}
2.26 μm	117^{9}_{10}
2.34 μm	90^{10}_{11}
Average	100^{7}_{8}

TABLE 5.2: The size of the hot dust in ESO 323-G77 from a thin ring model fit to the visibility squared and the hot dust size from reverberation mapping (Boulderstone et al., in prep). The average is the mean of the visibility sizes.

From the fitting of the 2.15 μm bin, I find a FWHM of the Gaussian to be $0.42^{+0.06}_{-0.08}$ mas (the observations and model are plotted in Figure 5.2). Using an angular size for ESO 323-G77 of 0.311 pc mas^{-1}, this translates to a ring + point source radius of 98^{+15}_{-18} light days. The result is within 1 σ of the reverberation mapped radius of 89^{+11}_{-18} days. The 2.15 μm bin was chosen because the central wavelength matches the reverberation mapping wavelength. However, the wavelength range of GRAVITY is small enough that the assumption can be safely made that the regions probed by each wavelength are the same within the angular resolution of GRAVITY. Therefore, all the wavelength bins, except the 1.99 μm bin, were fit in the same manner to compare them (see Table 5.2). I find that the radial size agrees within 1 σ in all cases except for the 2.26 μm bin which is within 2 σ. There is a good agreement between both methods; although, the visibility size is always larger. As a point of interest, if the 2.15 μm bin is assumed to be the best candidate for matching the reverberation mapping radii and the disk of ESO 323-G77 is well described by a thin ring then a distance to ESO 323-G77 can be calculated by matching the two results. Comparing the sizes results in a distance of 58^{+15}_{-13} Mpc which is in agreement with the current luminosity distance in Table B.1 although the errors are large. The calculation is done naively and, furthermore, ignores the differences between the different distance measures in cosmology and the true geometry of the source. However, the cosmology effects are negligible at such low redshift.

5.3 Modelling

Simple models fit to the squared visibility gave me an overview of the dominant source structure; however, I proceeded to model the visibility and closure phase simultaneously. Fitting visibility and phase will allow me to extract more information from the observations. The modelling in this chapter was performed with PYTHON 3.7 and makes use of the packages: ASTROPY, GALARIO, and EMCEE. GALARIO allows me to perform Fourier transforms on images and derive complex visibility for a given set of *uv* points with little computational expense. Less

computational expense makes expensive fitting methods such as MCMC compatible with highly flexible models. For the MCMC method I use EMCEE with flat priors for all given variables.

Initially, I attempted to recreate the squared visibility and closure phase simultaneously using point sources. To compare different numbers of point sources, the Bayesian Information Criteria (BIC) is used. The BIC is defined as:

$$\mathrm{BIC} = \ln(n)k - 2\ln(L), \tag{5.2}$$

where n is the number of data points, k is the number of parameters, and L is the likelihood. Each point source had a ΔRA, ΔDec, and point source fraction (p_f). After the squared visibility is calculated, a scale factor (s_f) is subtracted in the same manner as Equation 5.1. The sum of all point source fractions is defined to be one. A single point source was fixed to the central pixel with a fixed fraction of 0.15, the value used for the accretion disk for the reverberation mapping comparison. All parameters are made relative to the central point source. The point source model contained 3(N_p-1) free parameters as well as s_f where N_p is the number of points. When calculating the BIC the number of free parameters does not include s_f because it is a non-physical component that is present in all models and only effects the visibility squared. The bounds for the free parameters are given in Table 5.3. When creating an image from the point source model, the model is shifted so the central image pixel is the photocentre. The bounds set for each parameter were as follows:

Parameter	Lower	Upper
ΔRA	-10 mas	10 mas
ΔDec	-10 mas	10 mas
p_f	0	0.85

TABLE 5.3: The bounds for each free parameter of the point source model.

The model sampled from 2 to 32 point sources, the initial walker positions were selected from a uniformly random distribution over the available parameter space. To prevent point source stacking, the bound is set that two point sources may not occupy the same pixel. The pixel size is 0.136 mas with an image size of 256x256 pixels. The squared visibility and closure phase are then calculated from the image and compared to the data.

The MCMC analysis of each N_p is run for 7000 iterations with 500 walkers. For the last 2000 iterations, or 1000000 samples, I calculate the BIC. All BICs from each N_p are compared and the best combination of values are taken. The lowest BIC parameter set are then set as the starting point for a final MCMC analysis to calculate the uncertainties of each parameter. I use the described method because the relatively sparse data coverage, as compared to other VLTI/GRAVITY observed AGN, requires an extremely large number of iterations to find the true coverage from a random starting position. There are also many "local minima" in the probability space preventing me from finding a good starting position with a minimiser. Furthermore, it is

too computationally expensive to calculate the BIC for every parameter combination. Therefore, the given method provided the best trade-off between accuracy and computational expense for the data.

Parameter	Lower	Upper
ΔRA	-10 mas	10 mas
ΔDec	-10 mas	10 mas
A_f	0	10
FWHM	10^{-4} mas	5 mas

TABLE 5.4: The bounds for each free parameter of the radially symmetric Gaussian model. A_f is the relative amplitude flux.

Utilising the same fitting method, I also employed a second set of models. The second set of models are composed of Gaussians instead of point sources. Both elongated and radially symmetric Gaussians were attempted. Both Gaussian models were compared to the point source model using the BIC. The radially symmetric Gaussian model has a central Gaussian with a fixed position and brightness, similar to the point source model; however, its FWHM was not fixed. Each non-fixed point has four free parameters: FWHM, ΔRA position, ΔDec position, and relative log amplitude flux (defined as the log of a Gaussian component's amplitude relative to the fixed point). Unlike the point source model, the fixed amplitude was not set to 0.15 because it is the integrated flux of the Gaussian that would need to be set to this value. The integration adds computational expense. To minimise computational expense, I instead set the log amplitude of the fixed Gaussian to 10 and set the stipulation that the fixed point was the highest in amplitude. Each log amplitude was then set relative to the fixed point and the image was normalised to a summed flux of one in linear space. The bounds are given in Table 5.4. The radially symmetric Gaussian model has $4N_G$-3 free parameters, where N_G is the number of Gaussians, when calculating the BIC.

The elongated Gaussian model was identical to the radially symmetric Gaussian model except that the FWHM parameter was replaced with the major axis FWHM and two extra free parameters were introduced which are the major-minor axis ratio and the PA of the major axis. The bounds are in Table 5.5. The major axis FWHM and the axis ratio were free parameters for the fixed Gaussian. The chosen setup gives the model $6N_G$-3 free parameters when calculating the BIC. Both Gaussian models sampled 2 to 16 Gaussians.

Parameter	Lower	Upper
ΔRA	-10 mas	10 mas
ΔDec	-10 mas	10 mas
A_f	0	10
$\text{FWHM}_{\text{major}}$	10^{-4} mas	5 mas
ϵ	0	1
PA	0°	180°

TABLE 5.5: The bounds for each free parameter of the elongated symmetric Gaussian model. A_f is the relative amplitude flux, $\text{FWHM}_{\text{major}}$ is the FWHM of the major axis, and ϵ is the axis ratio.

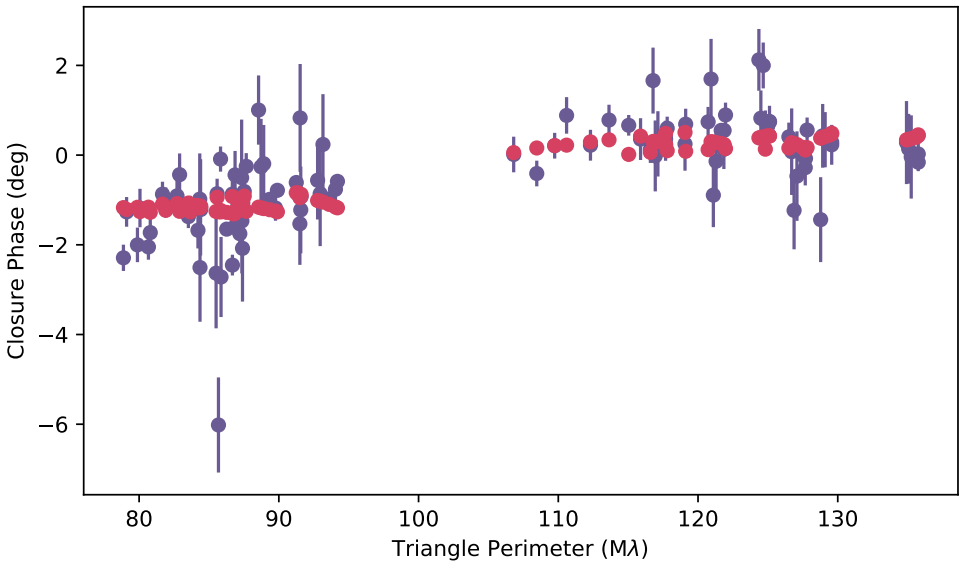

FIGURE 5.3: The closure phase for the 2.15 μm, 2.26 μm, and 2.34 μm wavelength bins are plotted in purple against baseline length in Mλ. The red depicts the best fitting model at sampled at the same *uv* locations.

5.4 Modelling Results and Discussion

Using the models and method discussed in Section 5.3, I attempt to explain the GRAVITY observations in the three longest wavelength bins simultaneously. Initially, the wavelength bins were modelled separately; however, all the models failed to constrain any reliable geometry. In a single wavelength bin, the data were too sparse for the relatively complex models, as compared to the one used in Chapter 4. Therefore, I make the assumption that the narrow range of wavelength covered by the GRAVITY fringe tracker probe the same hot dust component at different spatial scales, essentially allowing me to fill more of the *uv* plane. For simplicity, the modelling is performed in wavelength space.

I find that the best fit model uses 3 point source components (Table 5.6). The model, convolved with the beam size, is shown in Figure 5.4. The point source model provides a good description of the squared visibility (Figure 5.5) and the closure phase (Figure 5.3). However, the point source model does not reproduce the scatter of either observable. The scatter is on a larger scale than the error bars; however, the errors are derived from the inter-frame variation and the inter-observation variation may be larger. It is also possible the scatter is real and the model is too simplistic to reproduce it and only the overarching geometry is recovered. More complex models will need to be explored in future modelling. Due to the nature of the modelling, the physical interpretation of 3 point sources should be done with extreme caution. I find that two of the sources, one of which is the fixed component, are separated by 0.8 mas and responsible for 99% of the total flux. The separation is less than the FWHM of the calculated beam size in Figure 5.4. However, the given beam size denotes the separation at which the correlated flux of two point sources becomes zero, i.e. $\lambda/2B_{\mathrm{max}}$ where λ is the wavelength and B_{max} is the

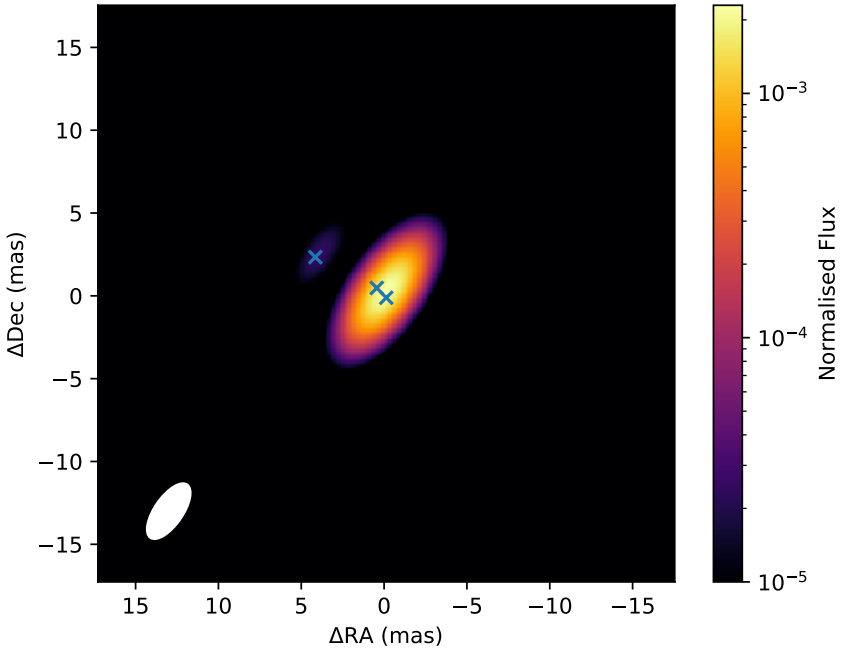

FIGURE 5.4: The three point source best fit model to the GRAVITY observations convolved with the beam size. The colourbar represents normalised flux in log scale. The beam is given in white and the crosses denote the point source locations.

maximum baseline length. In reality, partially resolved structure can be constrained on scales of half the beam size which is less than the separation of the points. The free component lies at 44° from the fixed component which is closer to an equatorial extension than polar. However, it is also in the direction of highest resolution (longest baseline). More data and a more rigorous statistical test would be required to determine if the direction was truly equatorial or an artefact of limited *uv* coverage. An extra observation was included in the original proposal and is due to be observed.

The remaining component is 4.2 mas away from the fixed component and is responsible for 1% of the flux. The faint component is essential for explaining the closure phase. It causes the small shift in photocentre required at lower spatial resolutions. It resides to the North-East of the group which is, temptingly, $\sim 90°$ from the mid-IR extension found in Chapter 4. However, it is on a larger scale than expected of the dusty disk and ESO 323-G77 is thought to be inclined at 60° from face on which makes interpretation more difficult. Therefore, it would be misleading to claim that the faint component is in anyway related to the dusty disk at this stage. While the separation is approaching the observable scale of MIDI, I do not consider this in conflict to the previous MIDI results.

In terms of spatial distance, the central point sources are separated by ~ 0.25 pc. The separation distance is remarkably close to the expected size of the hot dust from the *CAT3D-WIND* model given in Chapter 4. Upon further investigation, the reason for the size is the squared visibility.

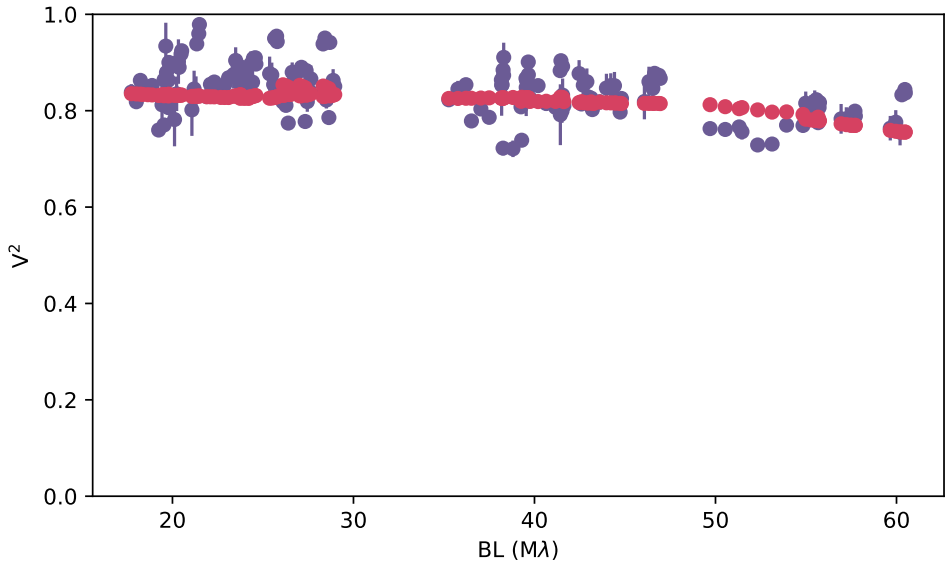

FIGURE 5.5: The visibility squared for the 2.15 μm, 2.26 μm, and 2.34 μm wavelength bins are plotted in purple against triangle perimeter in Mλ. The red depicts the best fitting model at sampled at the same *uv* locations.

The central separation is essentially what was measured when I compared the visibility squared to the reverberation mapped radius. With the limited *uv* coverage the two point sources would appear similar to a ring. The *CAT3D-WIND* model that was created in Chapter 4 can be used to create what would be seen by a near-IR interferometer in the same manner as was performed for the mid-IR. The *CAT3D-WIND* prediction is shown in Figure 5.6, it should be noted that this is given in visibility and not squared visibility. A visibility at a PA of 45°, to match the two central points, becomes a visibility squared at the longest baseline length of ~ 0.75. Therefore, the *CAT3D-WIND* model is consistent with the data. The central group does also contribute to the closure phase, however, the dominant component is the interplay between the group and the distant faint source.

The radially symmetric Gaussian model does reproduce the data, however, it is not a better fit than the point source model with the same number of components. Therefore, the BIC is larger for the radially symmetric Gaussian model when compared to the point source model. In the elongated Gaussian model, the axis ratio for each Gaussian component is unconstrained and it has a lower BIC than the point source and radially symmetric Gaussian models. Therefore, the point source model is the best descriptor based on the currently available data.

Component	p_f	ΔRA	ΔDec
1*	0.15	0	0
2	$0.839^{0.0008}_{0.0008}$	$-0.57^{0.06}_{0.06}$	$-0.59^{0.06}_{0.06}$
3	$0.01^{0.0003}_{0.0004}$	$3.71^{0.06}_{0.06}$	$1.9^{0.07}_{0.08}$

TABLE 5.6: The modelling result for the combination of the 2.15 μm, 2.26 μm, and 2.34 μm wavelength bins. *This component was fixed.

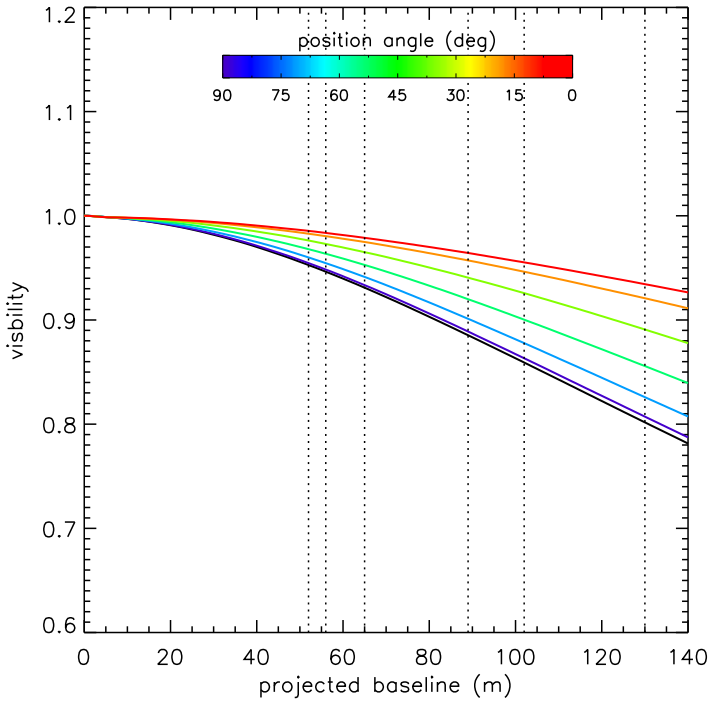

FIGURE 5.6: The 2.2 μm prediction of the visibility made by the *CAT3D-WIND* model created in Chapter 4.

I conclude that the central group of points represents structure on the scale of the putative sublimation radius and hot dust size predicted by the *CAT3D-WIND* in Chapter 4, although I cannot firmly conclude if it is the direction of the disk. The far point, at ~ 1.3 pc from the fixed component, could be a hot cloud blown out from the sublimation radius, a large cooler clump, or a more distant hot spot heated by some other means. In the case of the cooler clump, the faint component should be prominent in the L or M band with MATISSE. The data are currently too noisy and sparse to determine if the classical torus model or the dusty wind model is a better explanation of the observations. The addition of the expected new observation may allow me to distinguish between the two models.

Chapter 6

New Evidence for Radiative Pressure Driving

6.1 Introduction

This chapter is adapted from the published work Leftley et al. (2019). I am lead author of this work and led the reduction, analysis, and interpretation.

In Chapter 4 I report the tentative detection of evolution in the dust distribution with Eddington ratio. However, although the detection of such a relation is novel, the idea of a radiation pressure dependence on the dust structure is not. In radiation pressure driven models, such as the disk+wind model that features prominently in this thesis, it is not only expected but a core component.

6.1.1 Radiation pressure

Radiation pressure, specifically IR radiation emitted by the dust, was originally a way to explain how the geometrically thick classical dusty torus could be supported against collapsing into a thin disk (Pier and Krolik, 1992b). In modelling from Chan and Krolik (2016, 2017) it was found that, in the low Eddington ratio case of Seyfert AGN, the vertical support from the radiation is insufficient and the dust collapses into a thin disk but, nevertheless, a radial dusty wind is produced. Hydrodynamic models (e.g. Wada, 2015; Namekata and Umemura, 2016; Williamson et al., 2019) came to similar conclusions although the geometry of the disk and wind varies from model to model depending on the included model parameters and resolution of the simulation. Williamson et al. (2019) make the further point that the wind was highly sensitive to the anisotropy of the central radiation and to the Eddington ratio. The radiation pressure may be what launches the polar dust wind which will be studied in this chapter.

6.2 Eddington Ratio

Eddington ratio is the observable analogue to radiation pressure. So far it is known that the AGN is powered by accretion onto a compact object, possibly a supermassive black hole. One of the properties of accretion is that it relies on matter being able to fall down the gravitational potential well. As the energetic material radiates, the radiation carries momentum and pushes on the accreting matter. If the emission from the inflowing matter is enough, the inward force of gravity can no longer overcome the outward force from the radiation. The point in which these two balance is the Eddington limit.

The momentum carried by a photon of energy E=$h\nu$ is E/c. The pressure from radiation at a point r is therefore

$$\begin{aligned} P_r &= \frac{F}{c} \\ &= \frac{L}{4\pi r^2 c}. \end{aligned} \tag{6.1}$$

Where F is the flux and L is the luminosity. I make the assumption that the accretion material is fully ionised hydrogen in a spherical shell. The radiation mainly exerts force on the free electrons. Protons have a $(m_e/m_p)^2$ factor smaller scattering cross section than electrons (where m_e is the mass of an electron and m_p is the mass of a proton). As the electron is pushed it drags the proton (Hydrogen nucleus) with it through the electrostatic Coulomb force. The outward force on one proton and one electron is then:

$$F_r = \frac{\sigma_0 L}{4\pi r^2 c}. \tag{6.2}$$

Where σ_0 is the Thomson scattering cross section. The radiation pressure must then be balanced by gravity. The inward force from gravity is

$$F_g = \frac{G M_{\rm bh} m_p}{r^2}. \tag{6.3}$$

Where $M_{\rm bh}$ is the mass of the black hole. The mass of the electron is negligible and has been omitted. The Eddington luminosity is the luminosity required for the Eddington limit at a given mass:

$$\begin{aligned} F_g &= F_r \\ \frac{\sigma_0 L_{\rm Edd}}{4\pi r^2 c} &= \frac{G M_{\rm bh} m_p}{r^2} \\ L_{\rm Edd} &= \frac{4\pi c G M_{\rm bh} m_p}{\sigma_0} \\ &= 1.26x10^{31} \frac{M_{\rm bh}}{M_\odot} \,{\rm W}. \end{aligned} \tag{6.4}$$

Because the Eddington luminosity was derived under the assumption of spherical accretion, the Eddington limit can be overcome with a different accretion geometry, such as a disk, or anisotropic emission. The ratio of the bolometric luminosity of an AGN to its Eddington luminosity is the Eddington ratio.

In Section 6.3 I describe the observations used in this chapter and any reduction methodology specifics not covered in Chapter 3. In Section 6.4 I detail the modelling performed on the interferometric data. Next, in Section 6.5 I present the results of each object and our investigation into the relationship between Eddington ratio and dust distribution. In Section 6.6 I discuss the implications of the findings in Section 6.5 and possible avenues of future work. Finally, in Section 6.7 I summarise this chapter.

6.3 Observations and Reduction

This chapter is based on European Southern Observatory (ESO) observing programmes 71.B-0062, 078.B-0303, 083.B-0288, 083.B-0452, 084.B-0366, 086.B-0019, 086.B-0242, 087.B-0018, 087.B0401, 091.B-0025, 091.B-0647, 092.B-0718, 092.B-0738, 093.B-0287, 093.B-0647, 094.B-0918, 095.B-0376,0101.B-0411 and 290.B-5113 as well as the Spitzer programmes 86, 526, 3269, 3605, 30572, and 50588.

I analyse all yet unpublished MIDI data on 8 objects: Fairall 51, Fairall 49, Fairall 9, MCG-06-30-15, Mrk 509, NGC 2110, NGC 7213, and NGC 7674; which I supplement with archival and new spectrophotometric data obtained with the VLT-mounted Imager and Spectrometer for the mid-IR (VISIR; Lagage et al. 2004) as described in detail in the following.

6.3.1 MIDI

I use all publicly available MIDI data on the ESO archives for each object, including previously unpublished data. Observation dates and programme numbers are listed in Table B.2. All reduction is handled in as described in Section 3.1. I do not, however, use the structure function (SF) method for estimating the error from atmospheric variation because the SF, for all objects in this chapter, does not show useful structure. The lack of structure in the SF is due, in part,

to an insufficient number of calibrators observed during the night and possibly further influenced by the introduced variation from no-track calibrators (see Section 3.1.2.5). From the final product I extracted the correlated flux and compared it to the total flux from VISIR single dish spectrophotometry (see Section 6.3.2).

6.3.1.1 Non-detections

Many observations are of insufficient quality to use in fitting. I define an observation as bad if the 9μm atmospheric ozone feature is not clearly present in the uncalibrated correlated flux. However, a true non-detection, one not caused by weather or instrumental failure, can hold important information in interferometry. A low visibility means an object is highly resolved. I made two checks to identify true non-detections.

The first check is using the ESO Observatories Ambient Conditions Database to see if the observation coincided with adverse observing conditions. I also used the changes in the conversion factors of the calibrators (Burtscher et al., 2012) to confirm these events.

The second check is to look for correlations between PA, baseline length, and the non-detections. If the non-detections are true then they must either be a low emission period in the AGN or caused by the object being resolved to the interferometer. In the latter case the non-detections would be grouped either above a certain baseline length or at a particular PA if the extended component has an angular dependence. If, on the other hand, other observations with equal or larger baseline lengths at similar PAs have detections then the non-detection is not caused solely by the geometry of the source.

Most of the non-detections were shortly followed by successful no-track observations and, therefore, do not provide any useful upper limits. Fairall 49 is the only object where I have a true non-detection that was not followed by a no-track observation. However, the upper limit from the measurement provided no further constraint to Fairall 49, because the measured visibilities have very low uncertainties and are already lower than the limit from the non-detection. Therefore, the upper limit was not included in fitting because it is at a longer baseline length than the other two observations. The upper limit implies that the visibility does not increase after the 57 m observation which is already assumed by the simplistic model (see Section 6.4).

6.3.2 VISIR

The following section is based on the VISIR section from Leftley et al. (2019) and is important for understanding this work. The reduction was performed by Dr. Daniel Asmus.

Much the same as in Chapter 4, I supplement the MIDI photometry for all objects with the single-dish spectrophotometry from VISIR as total flux reference. Archival VISIR low spectral resolution N-band spectra are available for all objects except Fairall 51 (Fairall 9 and Fairall 49

in Jensen et al. 2017; MCG-06-30-15, Mrk 509, NGC 2110, NGC 7213 and NGC 7674 in Hönig et al. 2010). For Fairall 51, new spectra with VISIR were obtained after its upgrade (Käufl et al., 2015; Kerber et al., 2016) in October 2018 as part of ESO programme 0101.B-0411 (PI: D. Asmus) in low-resolution mode with standard chopping and parallel nodding, and an on-source exposure time of 5 min. The conditions were reasonably good (water vapour $\sim$ 2.5 mm, infrared sky surface temperature $\sim$ –93°C, optical seeing $\sim$ 0.8-1.0"). The data were reduced with the ESO pipeline and flux calibrated using the corresponding acquisition images. In particular, the spectra is scaled by the ratio of the synthetic photometry, derived from the acquisition filter transfer function, to the photometry of the acquisition image. The resulting spectra are shown in Figure 6.1.

In order to check for long-term variability of the AGN at the MIDI wavelengths and better constrain the total flux during the MIDI observations, two or more epochs of VISIR *imaging photometry* were obtained of all objects except Fairall 49 in 2015 and 2016 (ESO programme IDs 095.B-0376 and 096.B-0369; PI: D. Asmus) in the filters PAH1 (8.59 μm) and PAH2_2 (11.88 μm). Standard imaging mode with chopping and perpendicular nodding with a throw of 10" was used. The on-source exposure times were 7 and 10 min, respectively, and observations of the science targets were followed by mid-IR standard stars from the catalogue by Cohen et al. (1999), selected to be into a similar direction in the sky. The data reduction and flux measurements were performed with a custom made PYTHON pipeline (Asmus, in prep.).

The resulting fluxes and measured sizes of the nuclei are listed in Table 6.1, whereas the fluxes are averaged over all the epochs, and the FWHM values are the smallest measured for each filter.

The fluxes of the individual epochs are all consistent with no flux variations during the measurement epoch and also agree within the uncertainties of the historical values taken from Asmus et al. (2014), except for NGC 7213 and NGC 2110. In the case of NGC 7213, the flux level in both filters has decreased by $\sim$ 20% since the last measurement in 2009. Thus, I scale the VISIR LR spectrum accordingly to match the 2015 fluxes which are closer to the MIDI observations. Furthermore, NGC 2110 showed a flux increase by $\sim$ 20% over the whole *N*-band between 2007, when the VISIR LR spectrum was taken, to 2010. From 2010 to 2015, the flux levels seem to have remained constant. Therefore, I scale the VISIR LR spectrum 20% up to match the flux levels during the MIDI observations.

Finally, to check if the VISIR data are a good substitute for the MIDI spectrophotometry I compare all the MIDI total flux spectra for each object against its VISIR counterpart (Figure 6.1). I find good agreement between the spectrophotometries for all objects except Fairall 49 and NGC 7213. Both of these have a VISIR spectrophotometry consistently higher than the MIDI observations. The VISIR observations are within errors of the MIDI observations on both these objects but they are consistently above. For Fairall 49 I only have two observations, therefore, the difference is not significant. Furthermore, the one observation that was significantly lower does not agree with the contemporaneous correlated flux measurement. A comparison between the dimmer MIDI spectrophotometry and its correlated flux counterpart leads to visibilities of

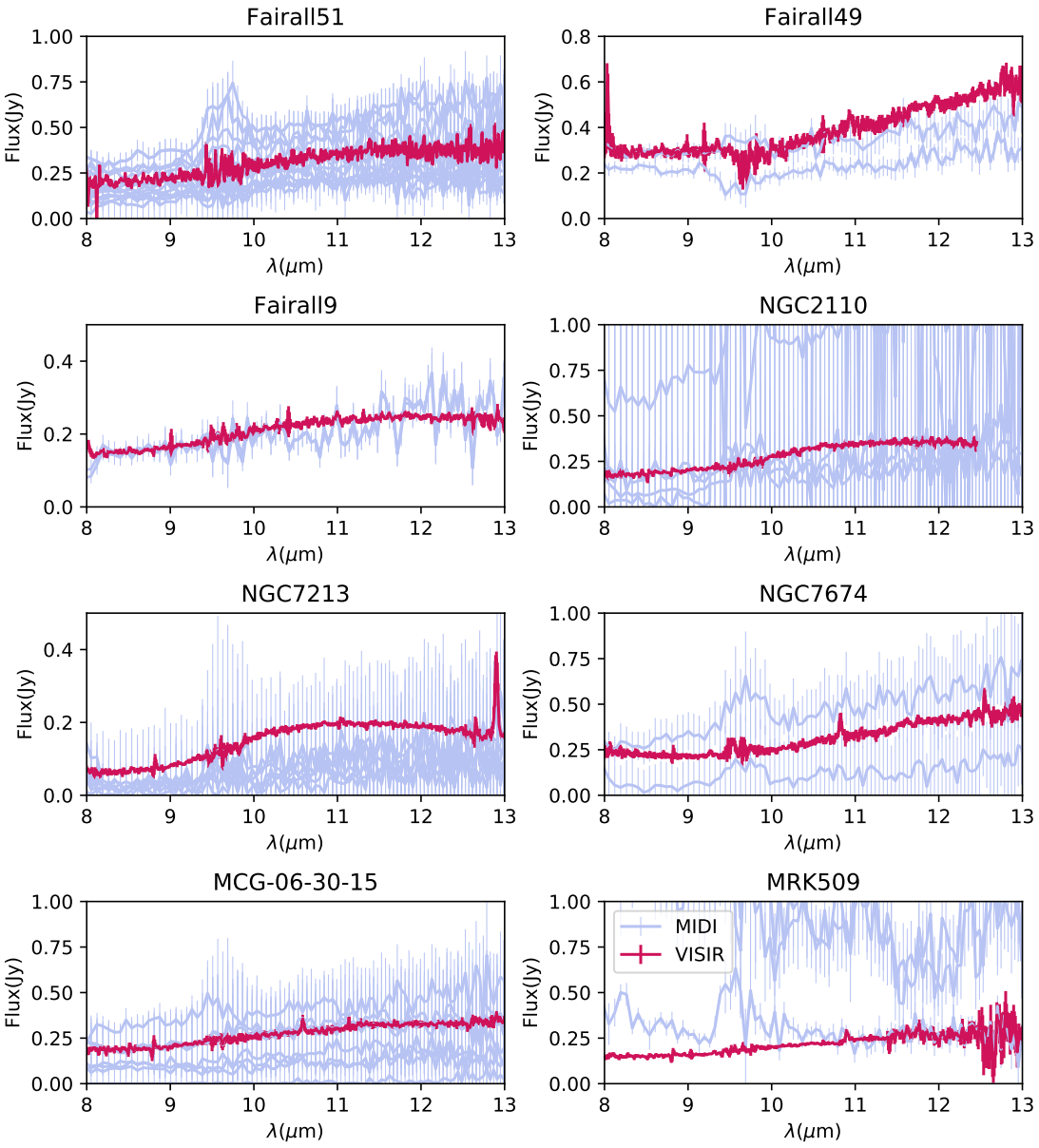

FIGURE 6.1: The comparison between the spectrophotometry from VISIR (in red) and MIDI (in light blue). Note that the VISIR spectra of NGC 7213 and NGC 2110 have been re-scaled as described in Section 6.3.2.

greater than 1. Further study of the spectrophotometry shows that the observation is suffering from poor sky subtraction. The remaining spectrophotometry agrees with the VISIR results. I will provide two interpretations of the geometry for NGC 7213 using both spectrophotometries as the zero baseline value.

Name	Dates	$F_\nu(8.6\,\mu\mathrm{m})$	$F_\nu(12\,\mu\mathrm{m})$	FWHM($8.6\,\mu$m)	FWHM($12\,\mu$m)
	[yy-mm-dd]	[mJy]	[mJy]	["]	["]
(1)	(2)	(3)	(4)	(5)	(6)
Fairall 9	15-07-07/15-08-01/15-08-29	195.7 ± 19.6	296.0 ± 29.6	0.26*	0.37*
Fairall 49	10-08-31*	$314.9^* \pm 31.5^*$	$523.5^* \pm 52.4^*$	0.55*	0.73*
Fairall 51	15-07-11/15-07-26/15-07-27/15-09-04	223.5 ± 22.3	361.2 ± 36.1	0.27	0.33
MCG-06-30-15	15-07-25/15-07-26	189.2 ± 18.9	334.0 ± 33.4	0.29	0.35*
Mrk 509	15-07-09/15-07-24/15-07-25	161.3 ± 16.1	255.1 ± 25.5	0.26	0.32
NGC 2110	15-11-08/15-12-30/16-02-14/16-02-15/16-02-27	201.8 ± 20.2	360.9 ± 36.1	0.28	0.34
NGC 7213	15-07-07/15-07-25	70.0 ± 7.2	197.0 ± 19.7	0.29	0.33*
NGC 7674	15-07-08/15-07-16	203.8 ± 20.4	395.2 ± 39.5	0.34*	0.40*

TABLE 6.1: VISIR photometry. Column descriptions: (2): Dates of the individual epochs during which always both filters, PAH1 and PAH2_2 were observed; (3) and (4): nuclear flux densities at $8.6\,\mu$m and $12\,\mu$m estimated from the filters PAH1 and PAH2_2, respectively through Gaussian fit photometry. The quoted uncertainties are dominated by the systematic uncertainties on the calibrator flux in all cases which is $\leq 10\%$; (5) and (6): the smallest FWHM values in the PAH1 and PAH2_2 filters, respectively, of all the epochs from Gaussian fitting. The major and minor axis are averaged. Values marked by a * are taken from the VISIR image collection of Asmus et al. (2014) if they provide better estimates than the new data. Fairall 49 is completely taken from the latter work and is listed here for convenience.

Object	Programme ID	Start Date	Mode
Fairall 49	86	2006-04-19	IRS Stare
Fairall 49	30572	2007-10-05	IRS Stare
Fairall 51	50588	2008-06-02	IRS Stare
Fairall 9	86	2003-12-17	IRS Stare
Fairall 9	30572	2007-06-13	IRS Stare
Fairall 9	526	2009-01-20	IRS Stare
MCG-06-30-15	86	2004-06-28	IRS Stare
MCG-06-30-15	3269	2005-02-15	IRS Map
MCG-06-30-15	30572	2007-07-29	IRS Stare
Mrk 509	86	2004-05-14	IRS Stare
Mrk 509	30572	2006-11-19	IRS Stare
NGC 2110	86	2004-03-22	IRS Stare
NGC 2110	30572	2007-11-04	IRS Stare
NGC 7213	86	2004-05-15	IRS Stare
NGC 7213	3269	2005-05-25	IRS Map
NGC 7213	30572	2007-06-13	IRS Stare
NGC 7674	3269	2004-12-10	IRS Map
NGC 7674	3605	2005-07-05	IRS Stare

TABLE 6.2: Spitzer/IRS observations used in SEDs.

6.3.3 SEDs

For each of the objects I attempt to create an infrared spectral energy distribution (SED). To match the angular resolution of VISIR I use archival ISAAC data (Moorwood et al., 1998) (see Table B.3). There was no ISAAC data available for NGC 2110 so NACO was used instead (Lenzen et al., 2003; Rousset et al., 2003). The reduction methodology is the same.

6.3.3.1 Spitzer

To cover the longer wavelengths I use archival level 2 Spitzer data (see Table 6.2). All observations of each AGN were collected and binned into 0.1 μm bins, the content of these bins were averaged. I then plot the Spitzer and ISAAC data along with the VISIR spectrophotometry in Figure 6.2. For the sake of clarity, I only plot the low resolution data. These SEDs allow for the relationship between SED features and interferometric visibilities to be explored (in Section 6.5.3).

6.4 Modelling

As an initial check for position angle dependence in the MIDI data I use the same method demonstrated for ESO 323-G77 in Chapter 4. To summarise the method, I compare the visibility at 12 μm $\pm$ 0.4 μm to the baseline length and separate the observations by PA into three groups

consisting of $0^\circ \leqslant \mathrm{PA} < 60^\circ$, $60^\circ \leqslant \mathrm{PA} < 120^\circ$, and $120^\circ \leqslant \mathrm{PA} < 180^\circ$. For all further discussion in this chapter I only use the visibilities at $12.0 \pm 0.4\,\mu$m. I only report at $12\,\mu$m to be consistent with Burtscher et al. (2013); López-Gonzaga et al. (2016) and because I am less effected by the no track mode error as well as other calibration losses. Fairall 49 is the only object to show a significant change in visibility with baseline length in the initial check, though I only have two observations from which to draw this conclusion. Since I do not find PA dependent structure in any objects I rotate the bins incrementally by 10° through 50° to rule out that the lack of structure was due to bin choice. I do not find a PA dependence in any objects, therefore, I can simplify the model for these AGN.

Because the objects show no clear variation in visibility with PA, at MIDI's level of accuracy, I fit a constant plus a radially symmetric Gaussian. The constant represents the fraction of the total flux that is unresolved to MIDI at all available baseline lengths. The fitting method is the same as detailed in Chapter 4 with two free variables, the FWHM of the Gaussian (θ) and the unresolved flux fraction (p_f). In most cases the FWHM of the extended component is unbound when fit.

In the cases where only a constant can be reliably fit the Gaussian can still give a lower bound for the radial size of the extended dust. For these objects I perform two fits to the data. In the second fit I additionally apply a non flat prior in the Θ direction where Θ is the FWHM of the Gaussian. The prior is linear and is defined as -0.15Θ. The linear prior makes smaller values for Θ more likely without affecting the result of the fit itself. After testing the prior against real data I find that any loss in accuracy caused by the introduced bias is far less than the derived error of the fit. The second fit provides the lower limit only, the point source fraction is still derived from the original flat prior fit.

6.4.1 SED modelling

The SED of an object can provide zeroth order information about the distribution of dust in the object, this is because the IR emission has a contribution from thermally emitting dust and the dust is heated by a central source. In the SED the dust emission manifests as two distinct bumps, the $3-5\,\mu$m bump and the $20\,\mu$m bump (Edelson and Malkan, 1986; Elvis et al., 1994; Mullaney et al., 2011). The bumps correspond to two dusty components, one warmer than the other. Therefore, the SED may be able to predict the unresolved fraction seen by the VLTI. predicting the unresolved fraction would be a huge advantage when finding candidates for observations. I hypothesise that a black body fit to the warm or hot dust bumps in the SED of an AGN will be able to predict the fraction of the $12\,\mu$m emission that the wind and disk, respectively, are responsible for. The wind and disk fraction would then translate into an unresolved source fraction and, therefore, a minimum visibility for future observations with, e.g., VLTI/MATISSE.

I fit two simple black bodies to the SED and compare the $12\,\mu$m emission fraction to the unresolved source fraction from MIDI.

Object	Θ (mas)	Θ_{up} (mas)	p_f
Fairall 51	$\geqslant 65$	330	$0.54^{0.01}_{0.01}$
Fairall 49	$38.28^{3.31}_{2.80}$	730	$0.51^{0.03}_{0.03}$
Fairall 9	$\geqslant 22$	370	$0.70^{0.05}_{0.05}$
MCG-06-30-15	$\geqslant 43$	350	$0.43^{0.02}_{0.02}$
NGC 2110	$\geqslant 21$	340	$0.53^{0.04}_{0.06}$
Mrk 509	$18.13^{6.83}_{4.02}$	320	$0.35^{0.16}_{0.21}$
NGC 7213	$\geqslant 20$	330	$0.63^{0.04}_{0.05}$
NGC 7674	$\geqslant 64$	400	$0.29^{0.04}_{0.04}$

TABLE 6.3: Modelling results. Θ is the FWHM of the extended Gaussian, p_f is the unresolved source fraction, and Θ_{up} is the upper limit of the FWHM estimated from the single-dish FWHM of the nucleus (Asmus et al., 2014, http://dc.g-vo.org/sasmirala)

.

6.5 Results

6.5.1 General results

I find that all of the studied sources are partially resolved to MIDI. However, only two show any clear, reliable change in visibility with baseline length, at MIDI's level of accuracy, when I perform the modelling. For the unconstrained objects I can only deduce lower limits to the angular sizes of the resolved dust as well as the unresolved source fraction.

Fairall 49 and Mrk 509 show an extended dust feature when fit with the combination of a Gaussian and an unresolved source. However, both objects have too scarce a sampling of the *uv* plane to say if the Gaussian and unresolved source model is an accurate descriptor of their geometry. The Gaussian and unresolved source model has well described all 25 previous AGN from literature. Of these 25 objects, 13 had both components, 7 had the extended component over-resolved and could only constrain the unresolved fraction, 4 only showed the extended component (marginally resolved), and 1 was unresolved (Burtscher et al., 2013; López-Gonzaga et al., 2016; Fernández-Ontiveros et al., 2018, 2019). Therefore, I take the model as a general description of AGN in the mid-IR.

6.5.2 Results for individual objects

The plotted results for each object can be found, with the *uv* plane and SED, in Figure 6.2. The probability distribution uses the flat prior for Θ and the model in the visibility plot shows the lower limit of the FWHM, as determined by the non flat prior, where the FWHM could not be constrained. Table 6.3 contains the results for the fitted model. The distances given are the NED, CMB, Hubble distance at the time of writing (H_0 = 67.8 km/sec/Mpc, Ωmatter = 0.308, Ωvacuum = 0.692).

Fairall 9 is at a distance of 206 Mpc. It hosts a Type 1.2 nucleus that has three observations which show no clear change in visibility with baseline length. Therefore, I tentatively report that Fairall 9's extended component is over-resolved and the unresolved source fraction is responsible for 68% of the flux.

Fairall 49 hosts a Type 2 nucleus and is at a distance of 88 Mpc. It has two MIDI observations, separated by one day, of high enough signal to noise to draw direct conclusions from. The $\sim 3\,\mathrm{M}\lambda$ baseline observation is unusually high when compared to the average MIDI single-dish spectrophotometry. At longer wavelengths it has a visibility of greater than 1. If I do not average the MIDI spectrophotometry and compare the unusually high observation to its contemporaneous spectrophotometry only I still get visibilities of greater than 1. However, when I compare the correlated flux to the VISIR spectrum, or the MIDI spectrophotometry of the second observation, I find that this observation gives sensible visibilities. Further inspection shows that the MIDI spectrophotometry may be suffering from poor sky subtraction. I therefore deem the interferometric observation reliable. When fit with the model, I constrain an extended component of 38 mas and unresolved source of 0.51. The non-detection, Section 6.3.1.1, implies that the visibility is unlikely to increase at longer baselines.

Fairall 51 has a Type 1 nucleus and is at a distance of 62 Mpc. It is partially resolved with an extended component that is larger than observable with MIDI. I conclude that Fairall 51 shows no change in visibility with baseline length or PA at MIDI's level of accuracy and available baselines. It has an unresolved fraction of 0.54 and the FWHM of the resolved component is between 65 mas and 330 mas. However, while Fairall 51 is fully consistent with an unresolved source the data suggests a bump in the visibility between $7\,\mathrm{M}\lambda$ and $10\,\mathrm{M}\lambda$ (Figure 6.2). The bump is well described by a simple dust ring around the unresolved source. Further observations will be necessary to conclude if the bump is real.

MCG-06-30-15 is host to a Type 1 nucleus at a distance of 38.3 Mpc. It shows partially resolved structure that has an unresolved fraction of 0.43, however, the extended structure of MCG-06-30-15 is over-resolved. The lower limit on the FWHM of the extended dust is 43 mas with an upper limit of 350 mas.

Mrk 509 hosts a Type 1.5 nucleus and is at a distance of 148 Mpc. It has three observations that show the object is partially resolved and suggests an extended dust component. The extended component has a FWHM of 18 mas, the unresolved fraction, however, is essentially unconstrained with an upper limit of 0.5.

NGC 2110 contains a Type 2 nucleus at a distance of 35.5 Mpc. It only has visibility measurements for a small range of baseline lengths. These points are mostly in agreement and show no angular dependent structure. Because of the small range of baselines I cannot say if I see baseline length dependent structure. Therefore, I cannot deduce the unresolved fraction or radial size. I find an upper limit of the unresolved source fraction of 0.6.

NGC 7213 hosts a Type 1.5 nucleus at a distance of 22.8 Mpc. It is partially resolved and shows an unresolved fraction of 0.63. The lower limit of the FWHM is 20 mas and the upper limit is 330 mas. However, in NGC 7213 I find that the MIDI spectrophotometry is much dimmer than the VISIR spectrophotometry. I compare the correlated flux data with the MIDI spectrophotometry and find that this gives unphysical, high visibilities of >1. Even using solely the brightest MIDI spectrum I still find the object is completely unresolved at all baseline lengths. Investigation into the MIDI spectrophotometry shows that it suffers from poor sky subtraction, possibly due to the strong, variable background described in Burtscher et al. (2012). Therefore, out of the two conclusions given for NGC 7213 I use the result derived using the VISIR spectrum.

NGC 7674 has a Type 2 nucleus and is at a distance of 122 Mpc. It has only two observations covering a large range of baselines. I can reliably say that it is partially resolved and it is likely that it has an over-resolved extended component and an unresolved fraction of ≈ 0.29. The lower limit for the extended component is 64 mas. When viewed with VISIR, the object shows an extended dust feature with a major axis FWHM of 400 mas (Asmus et al., 2016).

6.5.3 SED visibility fractions

When I fit a simplistic black body to the hot dust feature I find no significant correlation between the unresolved source fraction and the fraction of the flux that the hot dust is responsible for. I find that the hot dust in these objects is best explained by a temperature of either 750 K or 500 K. I also do not find a correlation within each of these temperatures. The null result could be due to small number statistics so I cannot rule out the intrinsic presence of a correlation.

As a further test I fit a black body to the cooler dust component, best fit by a temperature of ~ 150 K, and find no correlation between between the unresolved source fraction and the warm dust 12 μm flux contribution fraction.

6.5.4 Results on the correlation between extended flux fraction and Eddington ratio

In Chapter 4, I showed that the unresolved component was dominated by the hot dust in ESO 323-G77. When the source was compared to NGC 3783, it was thought that there could be an evolution of dust distribution with Eddington ratio. Here, I test the hypothesis further. For this chapter's 8 objects, I have the flux of the unresolved and resolved components and the flux values for 24 more objects are available in previous works (Burtscher et al., 2013; López-Gonzaga et al., 2016; Fernández-Ontiveros et al., 2018). I use the values for ESO 323-G77 from Chapter 4. As an initial check I compare the resolved and unresolved luminosities to a proxy for Eddington ratio. The proxy for Eddington ratio is the ratio of intrinsic X-ray luminosity collected from Asmus et al. (2015) and the black hole mass taken from various works in the literature (Onken and

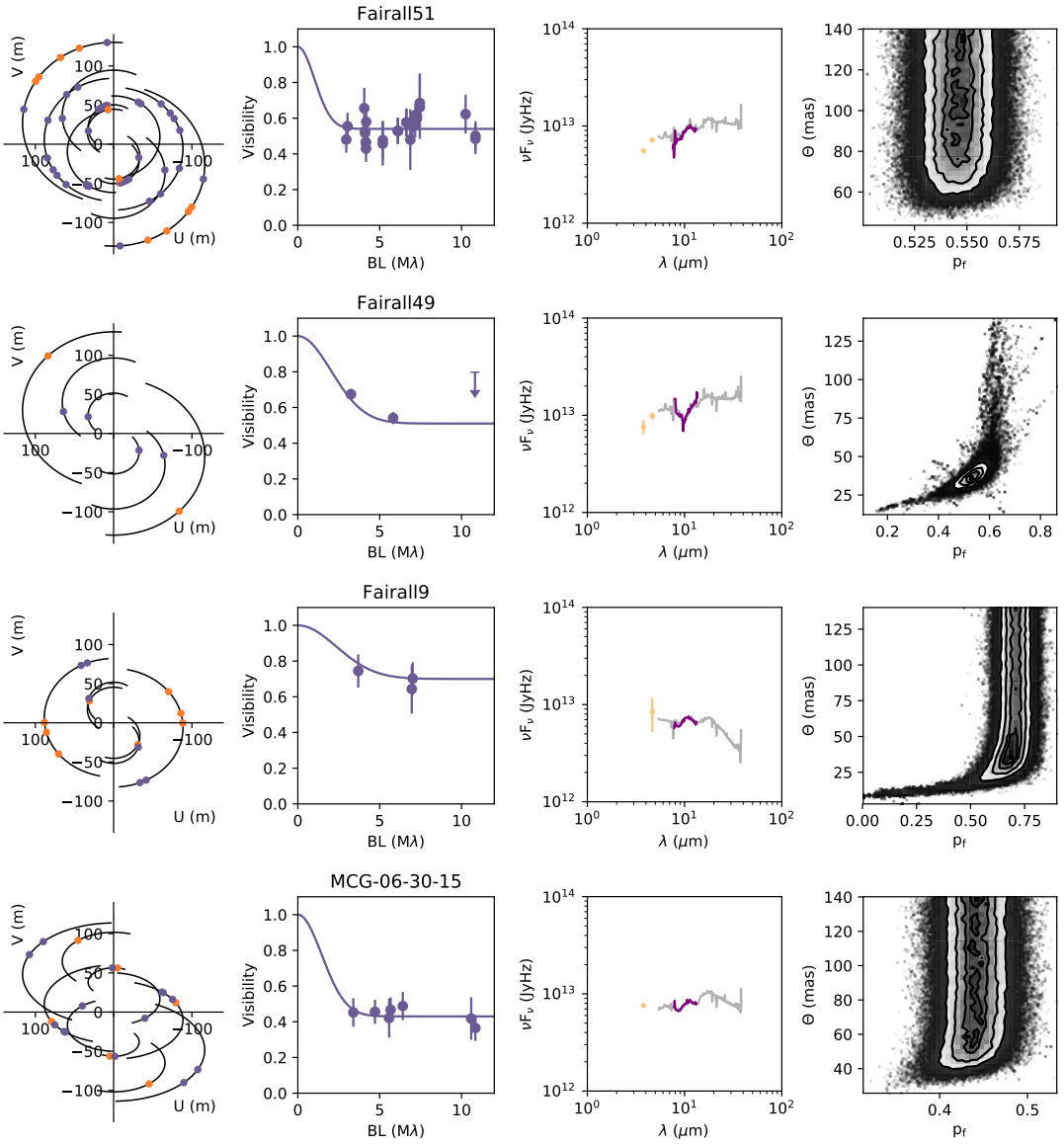

FIGURE 6.2: The subplots show, from left to right, the *uv* plane, the visibility measurements and best model fit, the SED, and the geometric model unresolved source fraction vs. extended component FWHM PDF. Each row shows the result for one object. In the *uv* plane, the purple points represent observations of high enough quality to be used directly in the analysis, the orange points are the excluded observations. The visibility plot depicts the visibility of each "good" observation vs. baseline length with the best fit geometric model overlaid. The SED contains data from ISAAC (pale orange), VISIR (purple), and Spitzer (grey).

Peterson, 2002; Greenhill et al., 2003; Lodato and Bertin, 2003; Peterson et al., 2004; Garcia-Rissmann et al., 2005; Denney et al., 2006; Gu et al., 2006; Wang and Zhang, 2007; Cappellari et al., 2009; Ho et al., 2009; Makarov et al., 2014) (see Table B.1 for a summary). To convert intrinsic X-ray luminosity to bolometric I use a conversion factor of 10 (Vasudevan et al., 2010).

The black hole mass is a major source of uncertainty in the Eddington ratio. I use maser emission and reverberation mapping where available, which have a typical uncertainty of <0.1 dex. However, the masses are primarily derived from stellar velocity distribution (SVD). For SVDs

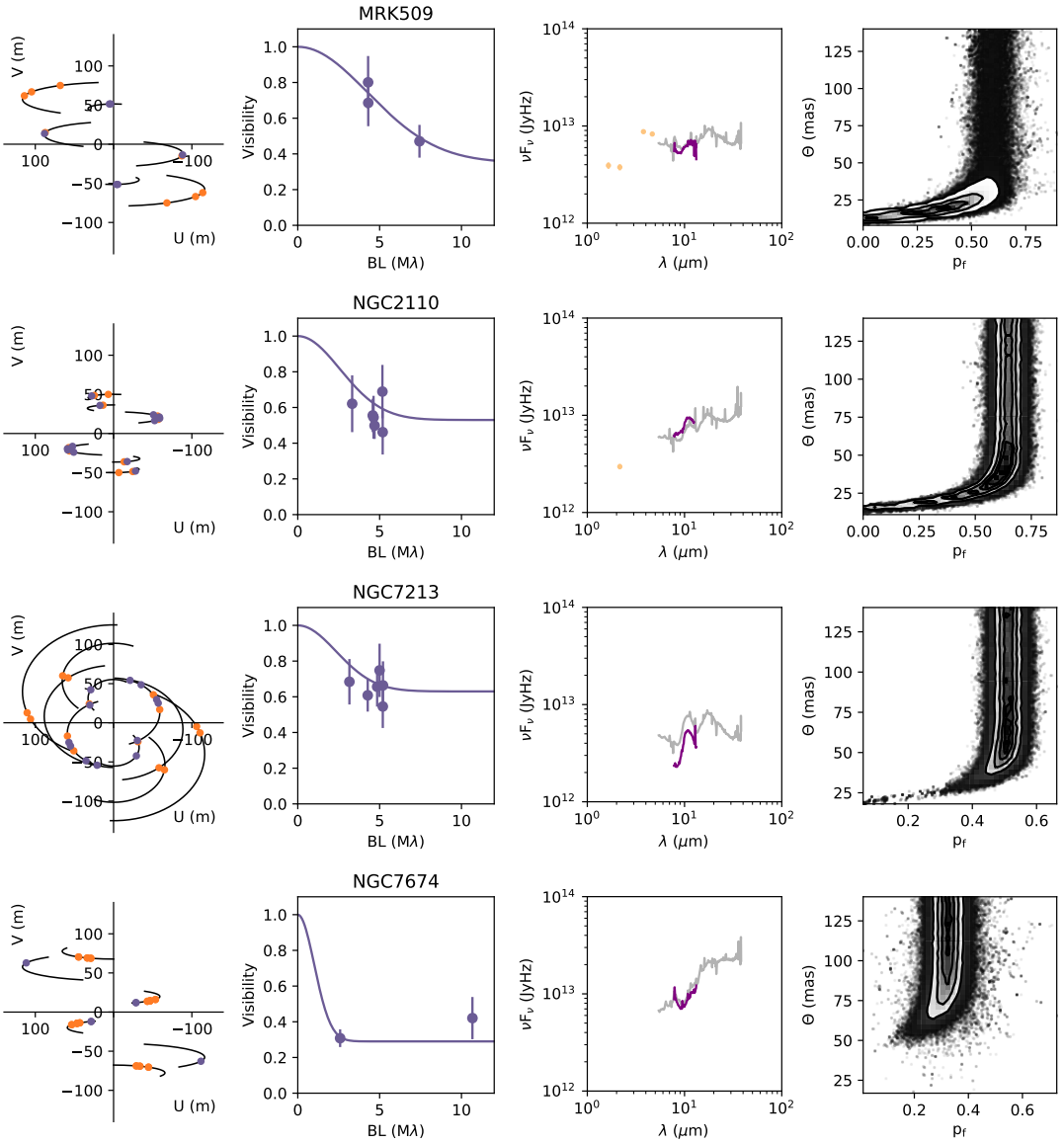

FIGURE 6.2: Cont.

I use the intrinsic M-σ scaling relation from Shankar et al. (2016) with a scatter of 0.25 dex. If none of these mass determinations are available, I use Hβ and [O III] which have uncertainties of $\geqslant$0.5 dex.

I found no correlation between the point source flux, or extended source flux, and Eddington ratio using the Spearman rank. However, I do find a tentative correlation between the ratio of resolved (F_{gs}) and unresolved (F_{pf}) flux with Eddington ratio for Type 2 AGN (Figure 6.3). In Type 1s I see a large scatter and no correlation (see Figure 6.4). Although the Type 1s are consistent with the correlation found in Type 2s, the Type 1s cover a smaller range of Eddington Ratios. If I take the Type 2 data without errors I get a z value (standard score) of 2.8 when testing the null hypothesis which, in this case, is that the data are uncorrelated. Equivalently, a z value of 2.8 is a p-value of 0.005 where p is the the two sided Spearman rank null hypothesis probability. As a more rigorous test of the correlation, I bootstrap, with replacement, the Spearman rank so as

to include the errors on the measurements and to reduce the effect of outliers on any correlation. Bootstrapping the Spearman rank will cause the correlation to be underestimated, I provide the p-value for both with and without bootstrapping.

Instead of just taking the 1σ errors on the objects in this chapter and the upper limit of NGC 2110 I can directly use their probability distributions from the MCMC Bayesian fitting which is a better representation of their true probability distributions. When I include the errors for all the objects the z value becomes 2.4 (p-value of 0.016). The Spearman rank correlation coefficient (ρ) using the errors is 0.65.

In these results I do not include NGC 1052 from Fernández-Ontiveros et al. (2019) due to their conclusion that the mid-IR photons do not arise from thermal emission. Non-thermal emission would make it unsuitable for a study of radiation pressure. However, the presence of silicate emission and nuclear obscuration suggests thermally emitting dust which could mean a very compact dust core is responsible for significant parts of the mid-IR emission. Therefore, I provide results with and without NGC 1052. With NGC 1052, the z value without errors becomes 3.3 and with bootstrapped errors 3.0 (p-value of 0.001 and 0.002 respectively) using an unresolved fraction of 0.96 from their Figure 3. The ρ, with errors included, becomes 0.71.

These results are highly suggestive of a positive correlation between the extended source flux fraction and the Eddington ratio. However, the correlation could, for example, be influenced by the resolution effect. Farther sources would, in theory, be less resolved because these sources would have more of their would-be "extended" emission included in the unresolved emission. Although, I would expect a resolution effect to cause the opposite correlation due to more distant objects generally being more powerful, ergo bright enough to detect with MIDI, and, therefore, likely to be higher Eddington ratio objects. Consequently, I compare the flux ratio to the distance (Figure 6.5) and X-ray luminosity (Figure 6.6). I find no significant correlation between either of these quantities and the flux ratio, reinforcing the idea that the correlation is truly between flux ratio and Eddington ratio. I discuss this further in the next section.

6.6 Discussion

6.6.1 The evolution of dust distribution with Eddington ratio

In Section 6.5.4, I presented the results of my comparison between Eddington ratio and the ratio between F_{gs} and F_{pf}. I found a possible correlation for Type 2s but not for Type 1s, this result can be explained by the orientation of Type 2 allowing for easier disentanglement of the resolved wind from the compact source. The prediction from Chapter 4 is that at higher Eddington ratios, more of the dust in the system would be located in a more compact disk. The compact disk could provide more fuel to the AGN explaining the higher Eddington ratio, and the larger unresolved source fraction.

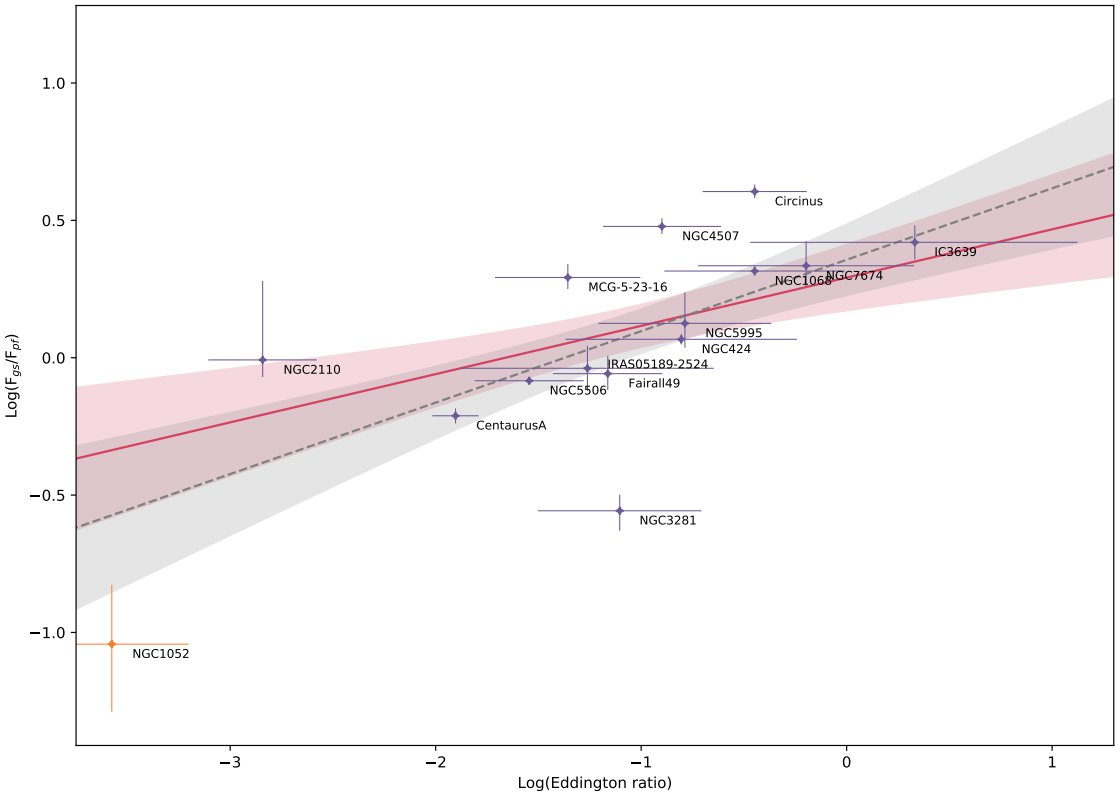

FIGURE 6.3: The of ratio extended source flux to unresolved source flux for Type 2 objects compared to their Eddington ratio. The purple points are the objects discussed in this chapter, the orange point is NGC 1052 from Fernández-Ontiveros et al. (2019). The red line overlaid is the linear best fit, with 1σ errors, to the purple points and the grey dashed line is the same but includes the orange point.

In this chapter, I find that the unresolved source fraction decreases with Eddington ratio which contradicts my prediction. A z value of 2.4 for the correlation, when using the MCMC Bayesian statistics directly, means that this correlation is uncertain but possible. The relatively low confidence value is mainly caused by two effects: the large black hole mass errors and the small number of objects. I cannot get better black hole masses due to no near-IR continuum reverberation mapping for Type 2s and the intrinsic scatter in SVD black hole masses. However, I will be able to increase the number of sources thanks to the introduction of MATISSE. With MATISSE a single snapshot analysis of an AGN will provide more data, 6 visibility measurements and 3 closure phases, than I have from MIDI on most of the current objects. An improved sensitivity, compared to MIDI, will also allow a greater number of viable targets. The improved capability should permit a survey of local Type 2s which would vastly improve the statistics.

I repeated the analysis to include a new object, NGC 1052. NGC 1052 was studied by Fernández-Ontiveros et al. (2019) and is an obscured LINER. It therefore provides an extra observation at low Eddington ratio. I find that the correlation statistics improve to a z of 3.0 using the Bayesian statistics directly, demonstrating the possible improvement in my statistics from the inclusion of a small number of new objects. I do not use NGC 1052 for the final conclusion, however, because it is not clear if the mid-IR emission in this object is from thermally emitting dust.

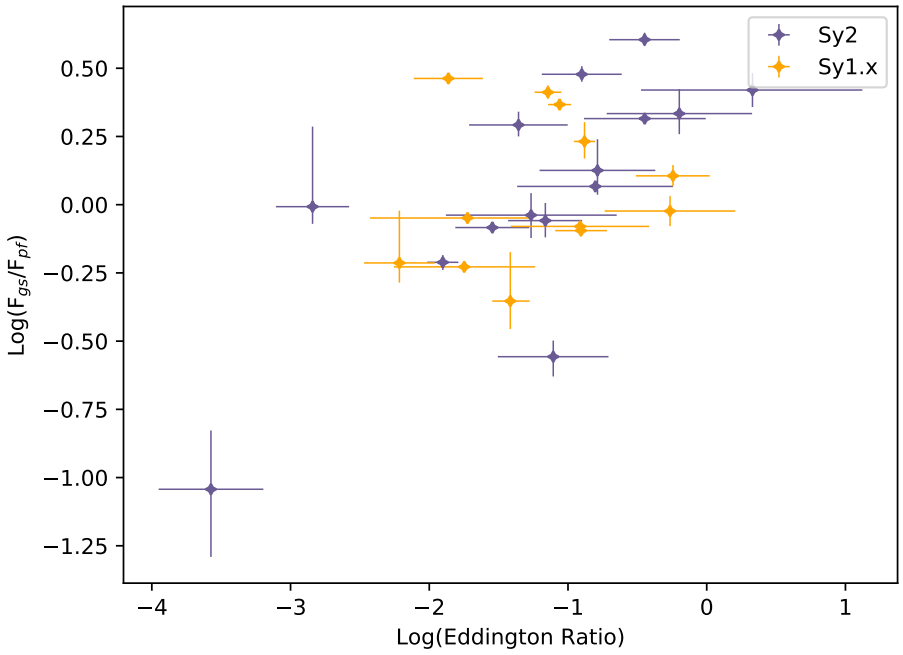

FIGURE 6.4: Flux ratio against Eddington ratio for all objects, including NGC 1052.

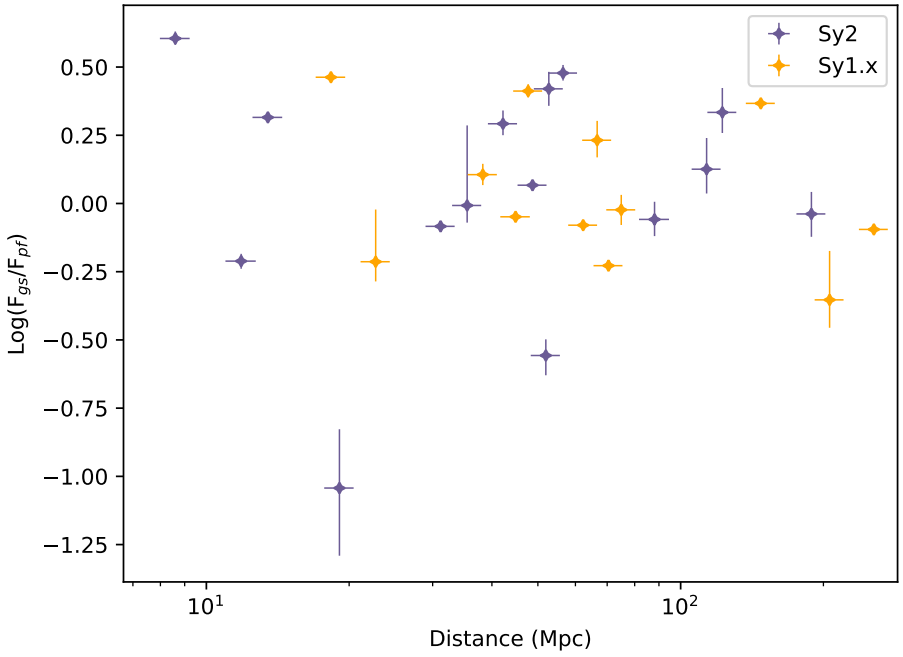

FIGURE 6.5: Flux ratio against distance for all objects, including NGC 1052.

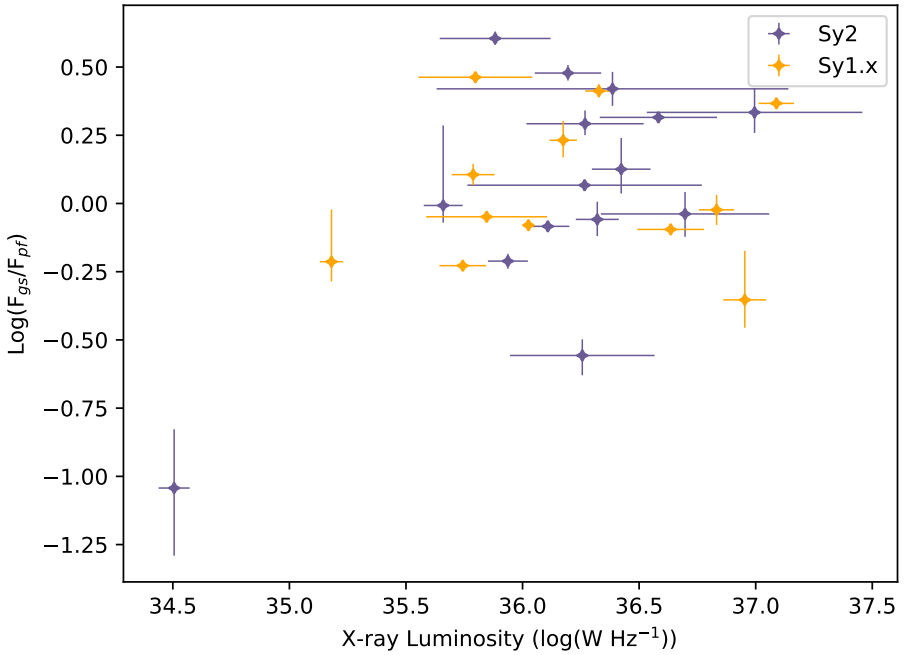

FIGURE 6.6: Flux ratio against X-ray luminosity for all objects, including NGC 1052.

Fernández-Ontiveros et al. (2019) report that the emission is likely synchrotron radiation from a compact jet as a thermally emitting dust structure would have to be unusually compact and the SED follows a broken power-law. The mid-IR emission does show a silicate emission feature, however, and there is an apparent source of nuclear obscuration which implies the presence of dust and dust emission.

In Meisenheimer et al. (2007), evidence was given that the unresolved source in Centaurus A is also dominated by synchrotron emission while the extended component is dust emission. Similar to NGC 1052, Centaurus A may be unsuitable for the correlation. Ergo, the z value without Centaurus A or NGC 1052 is 2.1 (p-value of 0.036). The result without Centaurus A is not significantly different to the result including it.

To explain the correlation between Eddington ratio and flux ratio I propose a different scenario to that in Chapter 4. In the radiation driven system of the dusty wind model the higher radiation pressure at higher Eddington ratios would blow more dust out of the disk into the wind. The explanation is further backed by radiation hydrodynamic modelling performed using the model in Williamson et al. (2019). The model showed that the bulk of the dust mass became less centrally concentrated at higher Eddington ratio. The outflows become stronger and brighter in the IR as Eddington ratio increases, shown in Figure 6.7 which was created using data from this model. Each line shows the fraction of IR dust emission interior to the radius r with a sublimation radius r_i for different Eddington ratios. The model starts from a disk and develops for a simulation time of 20 kyr. 20 kyr is enough time for the winds to develop but short enough that the disk is not depleted. Because the model is not a steady state solution it is not directly comparable to the

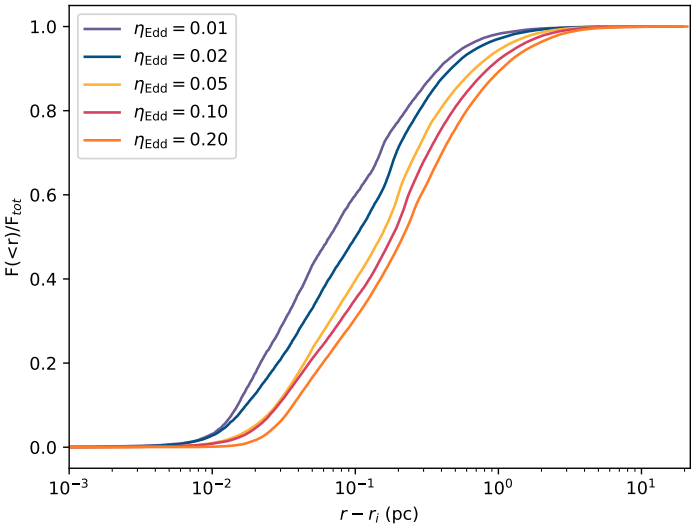

FIGURE 6.7: The fraction of flux interior to each radius, as a function of $r-r_i$, where r is the distance from the AGN engine, and r_i is the interior surface of the 'torus', for various Eddington ratios $\eta_{\rm Edd}$.

results, i.e. the winds may not fully develop before the disk depletes. However, if I do compare the model to the data, the model predicts a steeper gradient (see Figure 6.8) for a range of $r-r_i$ comparable to the scale of the disk. This could be explained by the wind not having time to develop as much at lower Eddington ratios.

6.6.2 MATISSE candidates

The coverage and phase information required to reconstruct an image of the dust structure in an AGN from the interferometric data was not available with MIDI. This is expected to change with the second generation instrumentation at the VLTI, and especially with the Multi-AperTure mid-Infrared SpectroScopic Experiment (MATISSE, Lopez et al., 2014). MATISSE will allow the reconstruction of mid-IR images on the same, or smaller, spacial scales as MIDI. MATISSE can access smaller spacial scales using the L and M band, whereas MIDI only had access to the N band.

The unresolved flux of the objects in this work make them viable targets for MATISSE. All the objects with less than 10 observations would benefit from a snapshot observation. However, I especially recommend Fairall 49, Mrk 509, and Fairall 51 due to their tentative partially resolved extended structure. In the case of Fairall 49 and Mrk 509, the extended structure is the dusty wind component. However, in Fairall 51 the extended structure is the tentative dust "ring".

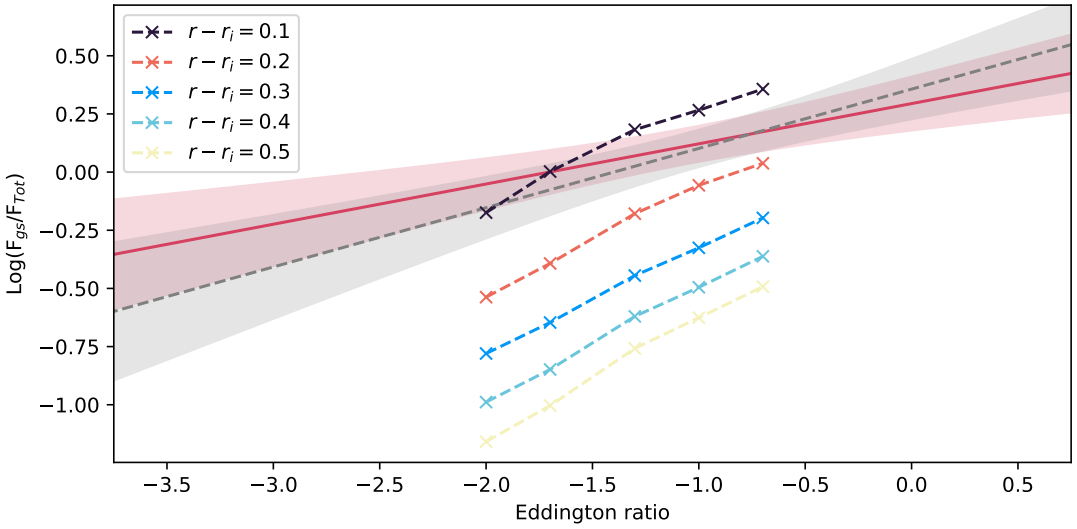

FIGURE 6.8: This plot shows the correlation from Figure 6.3 with the model from Figure 6.7 overlaid for different $r - r_i$.

6.7 Chapter Summary

I reduced and analysed the available MIDI data on 8 AGN. To each I fit a Gaussian and unresolved source model which is the PA independent version of the model used in Leftley et al. (2018). I find that:

1. All objects are partially resolved, showing visibilities of less than one.
2. Six objects have an unresolved source fraction that can be constrained by the available data. For Mrk 509 and NGC 2110 I derived an upper limit for the unresolved source fraction.
3. Two objects have a partially resolved component that can be constrained with the available data; Fairall 49 and Mrk 509. In the remaining objects the extended component appears over-resolved so I derive a lower limit for the FWHM.
4. Using the unresolved fraction for all objects, from this chapter and the literature, I find a tentative positive correlation between the ratio of extended and unresolved flux and Eddington ratio in Type 2s.

I conclude that the discovered relationship translates to more dust being ejected into the dusty wind at higher Eddington ratios which supports the idea that the wind is a radiation pressure driven outflow. I suggest a survey of Type 2s with VLTI/MATISSE to add more objects to the sample could improve the significance of the tentative correlation.

Chapter 7

The cold gas in NGC 3783

So far I have focused on the dust of local AGN. MIDI provided constraints on the geometry and affirmed that the dust is not in a simple torus but rather part of a complex radiation driven system. But where there is dust, there is gas and gas has the advantage of having narrow line emission from electron transitions which can provide precise kinematics of the material along the LoS from its Doppler shift. Kinematics adds a whole new layer of information when determining the structure of an AGN. By observing the kinematics of the gas, I can make inference into the kinematics of co-spatial dust; however, it is necessary to know which gas traces which dust. Different molecular lines trace different gas densities; the molecules targeted by the ALMA observations in this chapter are HCO+(4-3), HCN(4-3), and CO(3-2) which are thought to trace densities greater than that of the dusty wind (see Figure 7.1 and Hönig, 2019). It is more likely that the molecular lines actually trace the dusty disk instead. Therefore, with the molecular lines in this chapter I will likely trace the dusty material reservoir of the dust disk.

To observe the gas at high resolution, I use new ALMA data (PI: Dr Sebastian Hönig). These observations were of NGC 3783, a local Seyfert galaxy hosting a Type 1.5 AGN that is often considered to be archetypal (Figure 7.2). NGC 3783 was the first of only two Type 1 AGN to show a polar extension with MIDI; it also has an equatorial hot dust structure constrained with AMBER (Hönig et al., 2013; López-Gonzaga et al., 2016). Therefore, I can compare the known dust continuum geometry to the molecular gas of ALMA. Knowing the dust continuum emission geometry will allow me to test if the dense molecular gas traces the dust responsible for the bulk of the mid-IR emission or the dust disk as expected. The galaxy itself is a mostly face-on barred spiral galaxy with an inner ring and a pseudo outer ring. More details of NGC 3783 can be found in Table B.1.

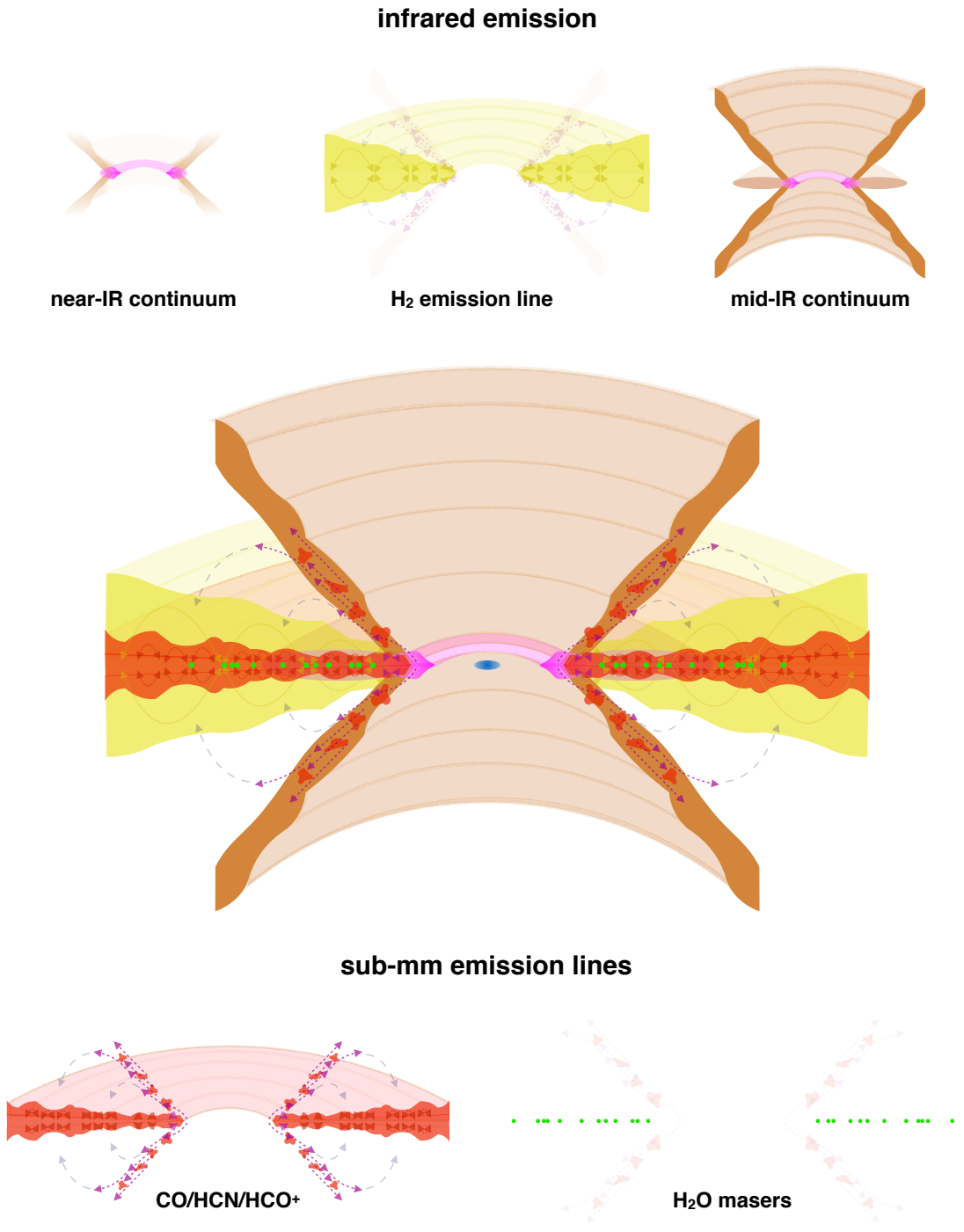

FIGURE 7.1: This figure is taken with permission from Hönig (2019). It depicts the dusty wind model and which component is traced by which molecular line or wavelength.

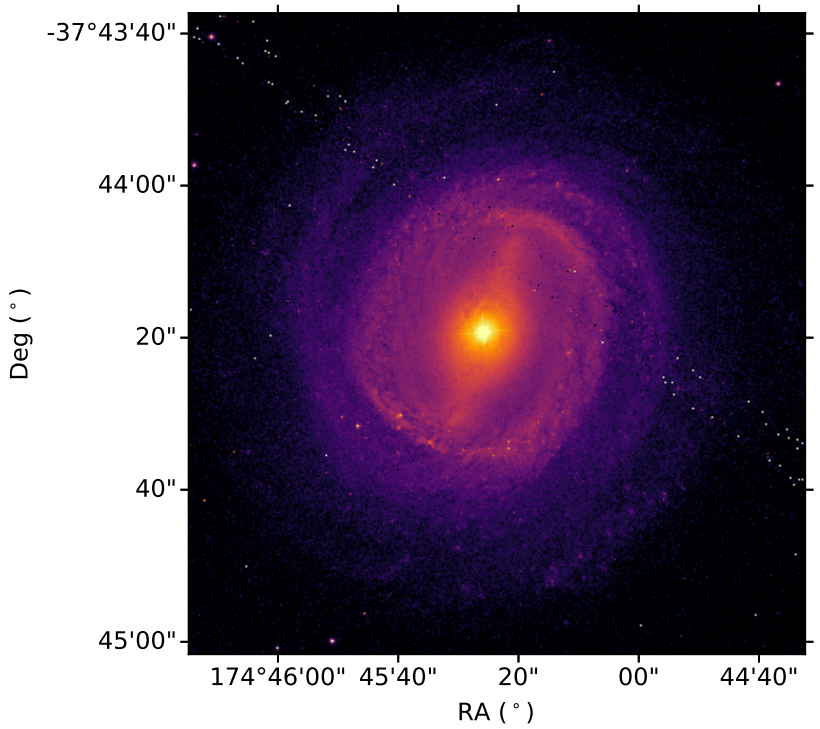

FIGURE 7.2: An HST image of NGC 3783 using the WFC3/UVIS detector. The data were downloaded from the HST Legacy Archive and was observed as part of the HST proposal 11661.

7.1 Observations and Reduction

At the time of writing, there are four observations of NGC 3783 in band 7 (see Table 7.1 for details). Band 7 is useful because it covers the frequency range of 275 – 373 GHz which contains the molecular transition lines HCO+(4-3), HCN(4-3), and CO(3-2) that are considered to be tracers for a range of gas densities. They have critical densities for collisional excitement of 10^6 cm^{-3}, 10^7 cm^{-3}, and 10^4 cm^{-3}, respectively (Shirley, 2015; Muraoka et al., 2016). Sampling these lines was the goal of the observations and the spectral windows were selected to include the frequencies of these lines. The observation time totalled 4.7 hrs, although the spectral windows differed slightly between observations (see Table 7.2 for details). While the observations were completed successfully, they did not reach the sensitivity requested in the proposal and future observations are planned to remedy this. The observations used in this chapter were done on 2015-12-01T11:11:20, 2015-12-01T12:17:03, 2017-11-09T10:28:00, and 2017-11-22T09:13:43 as part of programmes ADS/JAO.ALMA#2015.1.00555.S and ADS/JAO.ALMA#2017.1.00737.S. The 2015 observations have a maximum baseline length of 10 Mλ ($\sim$ 9 km) and the 2017 observations have a maximum length of 15 Mλ ($\sim$ 13 km). The details of the observations are in Table 7.1 and the spectral windows observed are in Table 7.2.

Project code	RA (Deg)	Dec (Deg)	Obs date	$\delta\Theta_{res}$ (")	FoV (")	$\delta\omega$ (kHz)	Int (s)
2015.1.00555.S	174.7571708	-37.7385	2015-11-21	0.029	0.51	7812	1216
2015.1.00555.S	174.7571708	-37.7385	2015-12-01	0.043	0.57	7812	1560
2017.1.00737.S	174.7571708	-37.7385	2017-11-09	0.021	0.76	7812	8491
2017.1.00737.S	174.7571708	-37.7385	2017-11-22	0.038	0.83	7812	5625

TABLE 7.1: ALMA observations used in this work, $\delta\Theta_{res}$ id the angular resolution, FoV is the maximum recoverable scale, $\delta\omega$ is the frequency resolution, and Int is the integration time.

Observation date	SPW1 (GHz)	SPW2 (GHz)	SPW3 (GHz)	SPW4 (GHz)
2015-11-21 13:44	338.73-339.67	341.18-342.11	350.62-351.56	352.83-353.76
2015-12-01 12:17	344.68-345.61	347.10-348.04	357.05-357.99	358.67-359.60
2017-11-09 10:28	338.73-339.67	341.21-342.14	350.62-351.56	352.83-353.76
2017-11-22 09:13	339.11-340.05	342.00-342.93	351.11-352.05	353.59-354.52

TABLE 7.2: The four spectral windows for each ALMA observation.

The reduction was performed using CASA and TCLEAN. The full method is available in Section 3.6; however, I will provide a summary here. I use CASA to reclaim the calibrated pipeline products. I passed the pipeline products to TCLEAN. TCLEAN is used to create a dirty image from the *uv* data which includes artefacts from uneven and incomplete sampling of the *uv* plane. The dirty image is produced using a weighting on the *uv* points, I used natural weighting for all observations in this chapter. A natural weighting uses the inverse of the squared standard deviation of each *uv* point to produce the weighting. I cleaned the dirty images in an attempt to remove the artefacts introduced into the images. The cleaning is done by masking true emission with user made masks, TCLEAN then attempts to deconvolve the dirty beam from the image and recover the true emission.

7.2 Results

While the results here use the natural weighting method for the reduction of the data to increase sensitivity, initially I utilised Briggs weighting which is more robust and provides a smaller PSF at the expense of sensitivity. However, with Briggs weighting all extended emission becomes invisible. Therefore, I fall back to the natural weighting in the following analysis.

The 2015-11-21 observation has high residuals after cleaning. There is no discernible line emission in this observation. Because the 2017-11-09 observation covers the same SPWs at higher signal to noise and higher angular resolution, the 2015-11-21 data provides no useful upper limits on detection. There is evidence for HCN emission in the 2017-11-09 observation, however, any extended emission from this line is confined to a small region (Figure 7.3) which has a low signal to noise. The average standard deviation of the continuum is 0.44 mJy beam^{-1} and the standard error on the HCN line emission in Figure 7.3 is 0.13 mJy beam^{-1}. Combining the 2015-11-21 and 2017-11-09 observations does not improve the signal to noise of this line. It is

likely that the lack of improvement was due to integration time of the 2015-11-21 observation. Using the ALMA sensitivity calculator, with a bandwidth of 10 km s^{-1} on the 12 m array, an integration time of 8491 s gives a sensitivity of 0.52 mJy. The same setup with an integration time of 9707 s gives a sensitivity of 0.49 mJy, this is not a significant improvement. No significant HCO+ emission is detected in any of the maps, the upper limit for 3σ detection of continuum subtracted flux density of HCO+ emission is 1 mJy ,beam^{-1} at a 10 MHz frequency bin width.

CO is present in the 2017-11-22 observation and it has a higher signal to noise than HCN and displays notable kinematics. The CO line emission can be seen in Figure 7.4. I use the redshift of 0.00973 from NED for defining the zero velocity for NGC 3783 and then produce a corresponding kinematic map for the CO line with a standard error of 0.1 mJy beam^{-1}. To measure the CO gas kinematics, I fit a Gaussian and constant to represent the line and continuum. Any Gaussian with an amplitude of zero, a sigma width of less than 0.01 GHz, or a sigma width of more than 0.1 GHz is regarded as having no line. The resulting map is in Figure 7.5 and displays some interesting structure. There are four seemingly distinct velocity components: the North-East blue (~ -25 km s^{-1}) component ~ 0.3" or a projected 69 pc (using the distance in Table B.1) from the centre, the South-East red (~ 25 km s^{-1}) component ~ 0.2" or 46 pc from the centre, the Western blue (~ -50 km s^{-1}) component ~ 0.1" or 23 pc from the centre, and the South-West blue-white (~ -10 km s^{-1}) component ~ 0.5" or 116 pc from the centre. For comparison to the host galaxy disk, the apparent (projected) maximum gas rotational velocity of the disk, as given by Hyperleda (Makarov et al., 2014), is 63 ± 2.2 km s^{-1} in NGC 3783. To determine if these are distinct components and what they may represent, I created a position-velocity (PV) diagram (Figure 7.6). The PV diagram depicts the intensity of emission for every velocity along a chosen line as a function of distance from the centre with the continuum subtracted. The line acts as a cut across the image, not an average across the image perpendicular to the line. The PV diagram allows me to determine how the velocity of the CO line changes as a function of distance from the AGN. The PA of the line chosen was 55° because this is close to the 45° equator of NGC 3783 as determined by polarisation (Smith et al., 2004) and cuts through all the supposed components.

Hönig et al. (2013) and López-Gonzaga et al. (2016) found that the dust emission in the nucleus of NGC 3783 is highly polar extended in the mid-IR, putting the bulk of the warm dust in the polar wind. CO is a warm ~ 1000 K gas tracer and there is a distinct lack of emission in the region North of the nucleus and a less definite lack in the South region. However, CO is also known to trace cold dense ~ 100 K dust and, therefore, may not trace the wind but the disk instead (Hönig, 2019; Williamson et al., 2019). Interestingly, one side of the cutoff is at a PA of $\sim -60°$ which is the PA of the mid-IR dusty extension from MIDI. The MIDI extension is thought to be the edge of one side of the cone which would agree with the idea that the outflowing material is significantly emitting in the North. Furthermore, there was a *CAT3D-WIND* model fitted to the SED and MIDI data of NGC 3783 in Hönig and Kishimoto (2017), which gives a half opening angle for the wind of 38° and an inclination of 30°. The *CAT3D-WIND* model gives a projected half opening angle of $\sim 57.4°$ which would place the other edge of the outflow

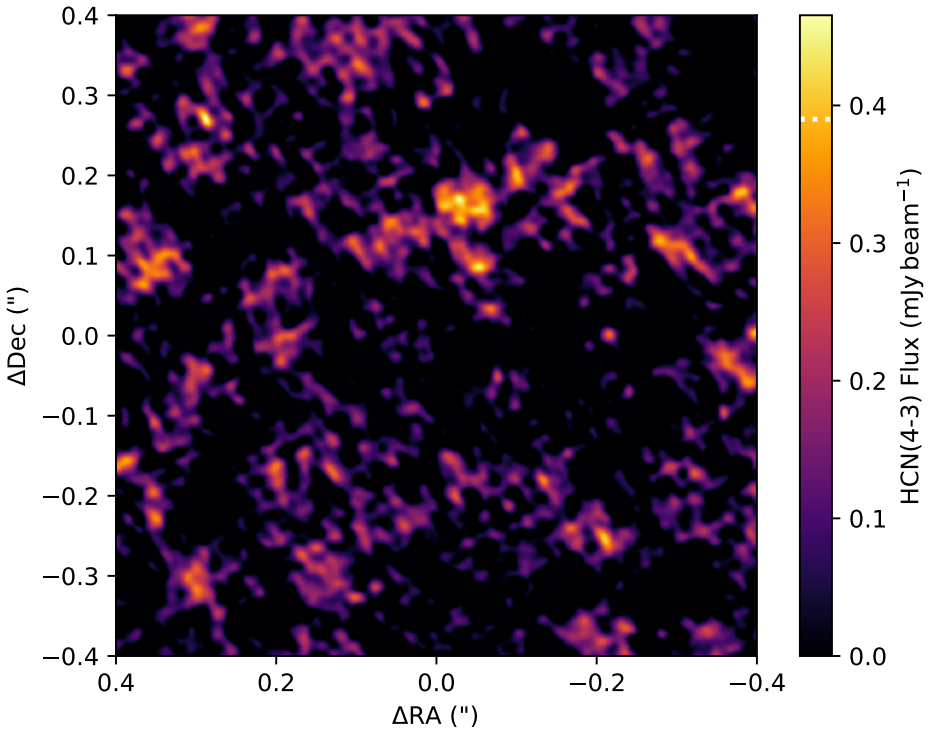

FIGURE 7.3: Average continuum subtracted HCN line flux density between 350.97 GHz, 351.02 GHz. The FWHM beam size is in white. The white dotted line on the colourbar is the 3σ level

cone at a PA of $\sim 54°$ when taken relative to the mid-IR axis. The modelled wind agrees very well with the other edge of the Northern empty region. The centre of the supposed outflow would be at a PA of $\sim 176°$ which is 41° off the polarisation system axis and 16° off the system axis as defined by the NLR (Fischer et al., 2013). The PA of the region is interesting as this would make the small scale outflow seen by ALMA closer to the outflow of the NLR instead of being perpendicular to the disk as determined by polarisation. To thoroughly test the hypothesis, I would need more integration time at similar baseline lengths of the CO(3-2) line to improve the signal to noise of this line. An improvement in the signal to noise will allow for a more robust cleaning of the continuum subtracted data. There are further observations accepted for NGC 3783 in an attempt to improve the signal to noise on the observed lines.

The PV diagram sheds some light on the nature of the unobscured gas. First, the two Eastern components are actually the same component. The curved structure between 0.1" and 0.4" on the PV diagram is continuous, suggesting a single structure, and reminiscent of a disk. A model PV diagram of the disk+wind scenario from Williamson et al. (2020) is shown in Figure 7.7 for comparison. The PV diagram is of a cut across the equator of the AGN similar to the PV diagram in Figure 7.6. The model is a hydrodynamic model that starts with a disk and applies radiation pressure. A wind develops and after a chosen time the simulation is frozen and the emission properties are determined. For more details see Williamson et al. (2019, 2020). In the model

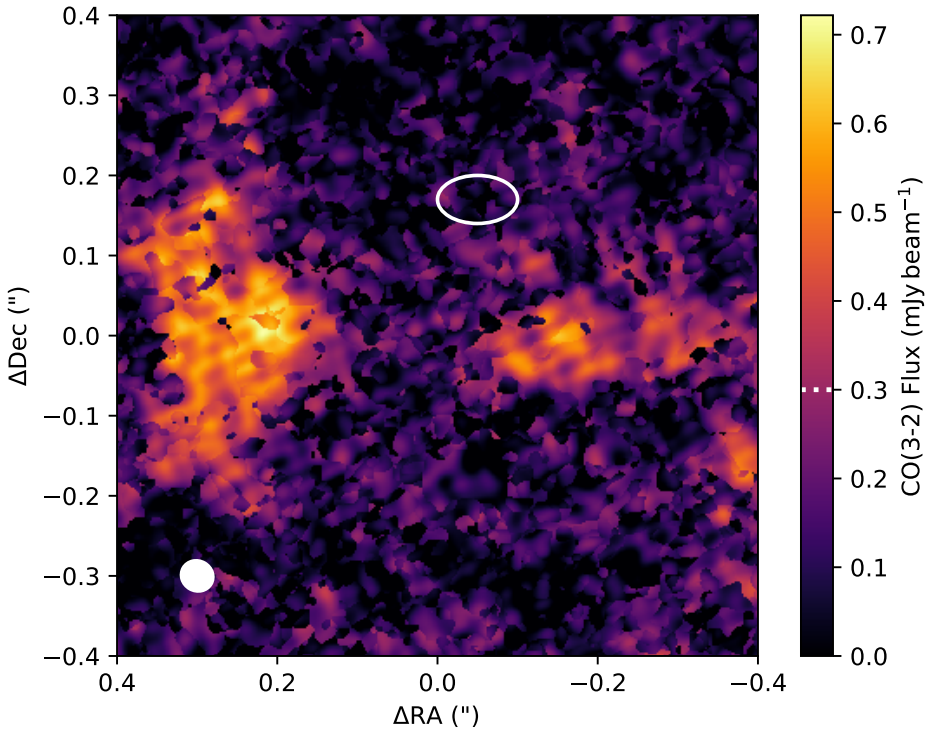

FIGURE 7.4: Average continuum subtracted CO line flux density over 100 MHz centred on the amplitude of the line. The FWHM beam size is in solid white. For comparison, the region of HCN emission is the white circle and the 3σ flux limit is the dotted white line in the colourbar.

PV diagrams the same curved structure can be seen, caused by the model disk. The appearance of two components in the observation is possibly caused by either an incorrect redshift, causing an offset on the zero velocity, or a peculiar motion of the structure. A redshift of ~ 0.00965 would give a zero velocity that would make the disk velocity go asymptotically toward zero at large radii from the black hole, although this is unlikely because the given redshift of 0.00973 for NGC 3783 is well constrained by the 21 cm line (Theureau et al., 1998).

In the West, the story is a little different. The middle structure present, between 0" and –0.2" (or a projected distance of 0 pc-46 pc) in ΔRA, has a constant velocity with distance. The constant velocity could be caused by looking down the outflow which would make the integrated velocity along the LoS less predictable. Any velocities would sum along the LoS which would cause any opposing gradients in velocity with position to cancel. An outflow against a disk for example. The last component, at $\Delta\text{RA} \leqslant -0.2$" or $\Delta\text{RA} \leqslant 46$ pc, seems to fall off in velocity like a disk which suggests that this detected molecular disk continues underneath the constant velocity component. I further studied the constant velocity component for evidence of multiple CO lines, which would be proof of two overlapping components, however, I found no evidence of two distinguishable lines. Furthermore, the single constant CO(3-2) line is not especially broad, or narrow, when compared to the other CO(3-2) emission. An alternative explanation is that the constant part is not part of the AGN and it is part of the host galaxy which is obscuring the

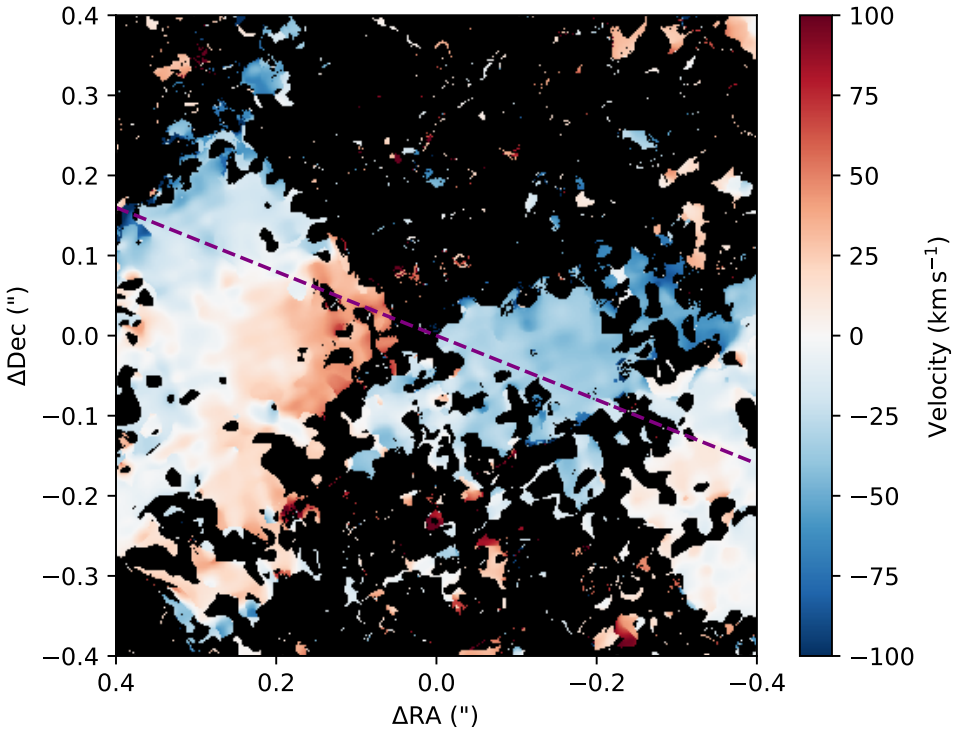

FIGURE 7.5: A velocity map of NGC 3783's CO line produced from band 7 data. Positive velocity is moving away from the observer. The purple line is the cut made to produce the PV diagram in Figure 7.6

emission from the disk component. It is unclear what the South-West structure is. If it is part of the disk then it does not agree with the zero velocity point set by the East side disk but rather the redshift determined zero velocity. The velocity offset would mean that it was not moving at the same velocity as the East side disk which is not consistent with being part of the same disk. Because of the discrepancy, and the lack of evidence that this component continues under the constant velocity component, I tentatively conclude that the South-West component may be contamination from the host galaxy in this explanation.

7.2.1 A molecular inflow?

The disk and outflow model I described agrees fairly well with the disk+wind model. To summarise: in the East there is a disk-like component, in the West there is a foreground component and possible contamination from the host galaxy. In the North and South there is no emission because the disk is only bright enough to be seen at the edges and the outflow does not emit CO(3-2).

The structure shown could also be explained by a molecular inflow. The two disk-like components in the East and West could instead be inflowing molecular gas. Inflows look similar

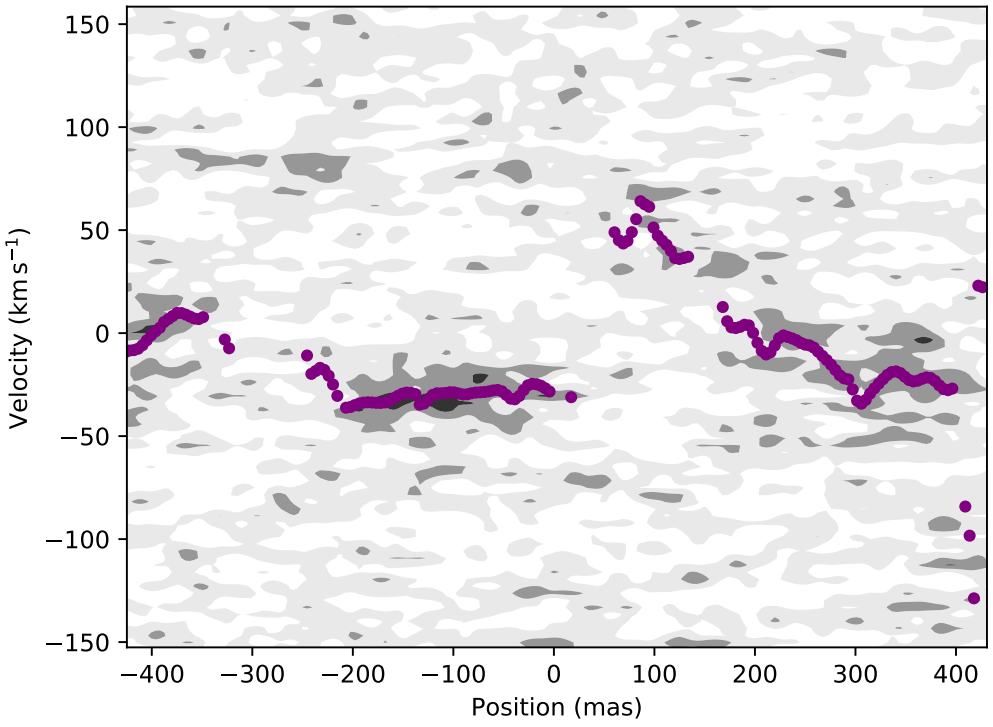

FIGURE 7.6: A PV diagram of NGC 3783's CO line along the purple line in Figure 7.5. The purple points are the velocity of the CO line as determined by a Gaussian fit. Positive velocity is moving away from the observer.

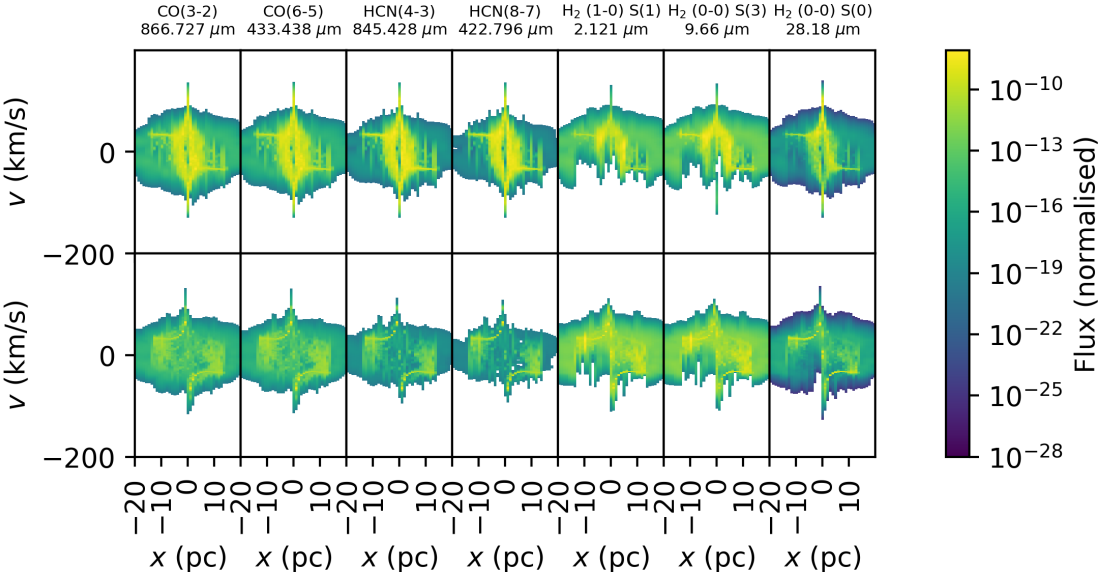

FIGURE 7.7: Figure from Williamson et al. (2020). A PV diagram created using a slit across the equator of a hydrodynamic disk+wind model inclined at 80°. The PV diagram is produced for a variety of line transitions. Each row contains a model with a different optical thickness. The details of the models can be found in the paper.

to disks in a PV diagram because they are both gravitationally bound material that increases in velocity towards the centre of gravity. An inflow would more naturally explain why the two components do not have the same zero velocity because they are not part of the same structure. The empty region would then be the area in which the outflow destroys the inflowing molecular gas leaving the region devoid of CO(3-2) emission. The alignment with the polar dust extension and *CAT3D-WIND* model support the existence of an outflow in the CO void region. Furthermore, Davies et al. (2007); Müller-Sánchez et al. (2011) show the H2 $1-0$ S(1) (2.12 μm), [Si VI] (1.96 μm), and Brγ (2.16 μm) kinematic maps. The [Si VI] and Brγ seem to trace a similar outflow structure, and Davies et al. (2007) reports that they both trace the ionised outflow of the AGN. Müller-Sánchez et al. (2011) also reports an outflow with the addition of rotational motion. Interestingly, the outflow has a PA of 0° which agrees well with the 176° PA of the *CAT3D-WIND* model outflow I gave previously and the empty region of the CO(3-2) emission. The constant component is still a foreground component in this interpretation.

7.2.2 The HCN emission

The detected HCN emission is uncharacteristically confined to a small region that does not coincide with the centre of the AGN or with any detectable CO emission. HCN observations of NGC 1068 have shown that the integrated flux ratio HCN(4–3)/CO(3–2) in AGN is 0.2 ± 0.04, i.e., the integrated CO(3-2) flux should be ~ 5 times brighter than the CO in the same region (Viti et al., 2014). Furthermore, HCN emission is usually bright in the centre of the AGN (e.g. Tacconi et al., 1994; Aalto et al., 2012; Davies et al., 2012; Audibert et al., 2019). In the ALMA band 7 observations, it is not. The lack of HCN(4-3) emission in the centre or the AGN could be due to the relatively low sensitivity, however, that does not explain why there is a non-central bright spot. The bright spot coincides with the outflow region and no CO emission which suggests it is a dense clump of gas that is too dense for CO emission. Either the clump is part of the outflow or it is foreground. It is not possible to distinguish between an outflowing clump and a foreground clump with such a small region of emission as compared to the beam size. If the clump is in the outflow, the illumination from the accretion disk could explain its brightness. If the clump is indeed dense it could prevent the destruction of the HCN molecules from the ionising radiation through self-shielding. The CO is less dense and therefore could have been destroyed by the ionising radiation, explaining the lack of CO emission. The new observations may shed some light on which scenario is more likely.

7.3 Chapter Conclusions and Summary

The ALMA observations show evidence of CO and HCN but not HCO+. However, CO is the only line with high enough signal to noise to gain insight into the geometry and kinematics of the gas. I conclude that the CO, which theoretically traces the dense dust of the disk, is consistent with an outflow+disk scenario. Both the supposed outflow and disk in the outflow+disk case

are consistent with the *CAT3D-WIND* model that was produced independently of these data. Alternatively, the CO(3-2) could be dominated by a molecular inflow, however, in this case the outflow is still fully consistent with the mid-IR polar extension and the *CAT3D-WIND* model.

Finally, I submit that to fully constrain the CO emitting structure, as well as the other emission lines present, I will need more observation time to increase the signal to noise. Currently the emission can only be constrained with natural weighting which causes a larger PSF than more robust methods such as Briggs weighting. Higher signal to noise data would allow for comprehensive kinematic modelling to distinguish between the two proposed scenarios for the CO emission. Further observations are scheduled for ALMA cycle 7.

Chapter 8

Conclusions

Throughout this work I have focused on the study of AGN with interferometry in an attempt to understand the inner parsec scale dust structure of these objects. Here I will summarise the primary findings of the previous chapters followed by my overarching conclusions.

8.1 The Polar Dust of ESO 323-G77 and its Implications

When studied with MIDI, ESO 323-G77 was conclusively shown to hold a polar dust structure fully consistent with the *CAT3D-WIND* model from Hönig and Kishimoto (2017). It was shown that an equatorial extension would be inconsistent with the MIDI observations. The polar extension was still present when accounting for the non-uniform sampling of the *uv* plane. The result made ESO 323-G77 the eighth AGN with sufficient *uv* plane sampling to constrain an extension and the eighth to not show evidence for an equatorial dusty torus. ESO 323-G77 was also the second Type 1 AGN to have its extended dust successfully constrained. The polar extension constrained in ESO 323-G77 is strong evidence for the polar dust model. The polar extensions discovered in the four Type 2 AGN can theoretically be explained through self-shielding and anisotropic illumination. However, in Type 1s a polar extension is not as easily achieved. It is also difficult to explain why all six extended objects, including ESO 323-G77, are $\sim 20°$ from the derived system axis rather than more scattered in terms of angle if anisotropic emission is the cause.

The polar dusty wind model can explain the offset polar extensions in both AGN types. The offset is caused by edge brightening effects in a hollow cone. In the case of a hollow cone that is comprised of clouds that thermally emit, the amount of flux seen by an observer will depend on the number of clouds along their LoS. Looking through the centre of the hollow cone will provide a smaller volume of clouds than looking though the edge, making it dimmer. Therefore, I conclude that the polar dust structure is both common in AGN and well explained by a dusty wind.

Furthermore, ESO 323-G77 shows a dominant contribution from the unresolved source at all wavelengths covered by MIDI. No polar extended object has ever shown a dominant unresolved source. The unresolved source was found to likely be from the Raleigh-Jeans tail of the hot dust component. The results from *CAT3D-WIND* also suggest that the hot component is very compact. Because ESO 323-G77 is considered to have a relatively high Eddington ratio (based on relatively narrow optical Hydrogen emission lines) when compared to typical Seyferts, this suggested that there could be a positive correlation between Eddington ratio and the fraction of the available dust in an AGN that is located in the disk. Evidence of the Eddington ratio effecting the dust distribution is a key point in the study of AGN. The distribution of dust in AGN, whether it is in the torus model or dusty wind model, is thought to depend on radiation pressure and Eddington ratio is an observable proxy of radiation pressure. Observational evidence suggests that sources are less obscured at higher Eddington ratios and that radiation pressure is the driver (Ricci et al., 2017). A correlation between the unresolved fraction and Eddington ratio would suggest a change in dust distribution with radiation pressure in AGN. Because it is the distribution of dust that is responsible for the amount of obscuration, such a correlation would be a completely independent confirmation of the dust covering factor, the fraction of inclinations over which an AGN appears obscured, having a dependency on radiation pressure.

8.2 The Sublimation Radius of ESO 323-G77

The GRAVITY observations of ESO 323-G77 were able to constrain some basic geometry of its hot dust. What I found is that the data can be explained by three point sources when one point source is fixed to the flux fraction expected from the accretion disk. Two of the point source components are separated on sub-parsec scales and are responsible for 99% of the flux. The central structure is consistent with the scale of the putative hot dust disk although I can not reliably confirm or deny if it is in the expected direction of the accretion disk without further modelling. In future work, I will first test if the direction of the two point sources is constrained by the visibility squared, the closure phase, or both. I can then create models with similar point source separations and a range of PAs and generate fake observations from them. By fitting these I can determine for what range of input PAs I can recover the real data determined PA. The fake observation generation is similar to what I performed in Chapter 4.

The agreement with reverberation mapping provides further proof that there is structure in the GRAVITY observations on the scale of the dust disk. During the comparison, the GRAVITY data always produced a larger sublimation radius than the reverberation mapping. While all but one result agreed within $1\,\sigma$, the average of the results only agrees within $2\,\sigma$. The difference is in agreement with the prediction made in Hönig et al. (2014). The angular size is expected to be larger than the time lag size even if the emission region is the same. The discrepancy is because the thin ring approximation is not a true representation of the hot dust, the ring does have a thickness. The thin ring will then give the average size of the brightness distribution. The

average size will be larger than the inner edge of the sublimation radius which the reverberation mapping is more sensitive to. The reverberation mapping also does not account for the hot disk having a thickness (Boulderstone, B., priv. comm.) which in reverberation mapping causes a smoothing effect in the IR light curve response. By modelling the light curve and visibility squared together, a true thick ring model can be found and the distance can be determined. There are also orientation effects which should not be discounted. The hot dust disk of ESO 323-G77 is thought to be inclined at $\sim 60^{\circ}$ from face on in the *CAT3D-WIND* model. If the *uv* plane is evenly sampled, the average size of the projected disk would be measured, i.e $0.5r(1+\cos(inc))$ where r is the ring radius and inc is the inclination. My *uv* plane is not evenly sampled however. Most of the observations are in the North-East (Figure 5.1). The *uv* sampling is in the direction of the equator from polarisation measurements, therefore, I am theoretically preferentially sampling the true radius size so this effect is reduced. It would be an improvement to model the visibility with a thin ring or thick ring model directly which I plan to do in future work.

8.3 Does the Distribution of Dust Depend on Radiation Pressure?

In Chapter 6, I showed, at a minimum of $2.1\,\sigma$ and a maximum of $3\,\sigma$ confidence level, that there is a possible relationship between dust distribution and Eddington ratio. It did, however, become apparent that there is actually an anti-correlation between Eddington ratio and the percentage of dust that is unresolved, unlike the prediction made in Chapter 4. The anti-correlation is more in line with predictions from hydrodynamic simulations (e.g. Wada, 2015; Namekata and Umemura, 2016; Williamson et al., 2019) and it agrees with the result from Asmus (2019) that finds the same relation in the subarcsecond dust with VISIR. It could also be further evidence for the dusty wind model. Because I compared the extended dust emission to the unresolved dust emission, the relationship with Eddington ratio tells me that more dust emission is on a larger scale with more radiation pressure; this is a model independent conclusion. In the dusty wind model the relationship is explainable and expected, it equates to more dust in the wind when compared to the disk. In the torus model the relationship is harder to explain, although a fountain torus model (Wada, 2012) where the torus is a dynamic radiation driven structure could offer another explanation.

Comparing the correlation to the one from Ricci et al. (2017) suggests that less dust in the wind leads to a higher covering factor of the central engine. The correlation of Chapter 6 suggests less of a wind is successfully launched at lower Eddington ratios. However, the dust could still be launched in a failed wind. At lower Eddington ratios, more dust could gather in these failed winds and provide a greater covering fraction. The failed wind would still be unresolved to the interferometer and increase the point source fraction as seen in the correlation from Chapter 6.

To confirm or disprove the relation, more objects at low Eddington ratios must be observed with MATISSE. With the additional constraints, the relation may provide a valuable real world test

for simulations. For example, the slope of the relation may be a measure of how easily material is liberated from the unresolved region.

8.4 The Missing Dust

Out of the 9 MIDI observed objects presented in this work, only 3 showed any evidence of partially resolved structure. The remaining 6 had an unresolved component and an over-resolved component. Burtscher et al. (2013) also report that 6 of their 23 AGN are in the same over-resolved + unresolved regime as well as IC 3639 from Fernández-Ontiveros et al. (2018). Cen A, NGC 3281, NGC 4593, NGC 5506, and NGC 7674 are extended to VISIR. Under the assumption that the subarcsecond dust of VISIR is connected to the mas dust of MIDI, 8 of 33 AGN studied with MIDI have the bulk of the extended emitting structure between the scales of the shortest VLTI baseline, maximum spatial scale probed of ~ 60 mas at 12 μm, and the mirror size of the VLT, resolution of 370 mas at 12 μm. An opportunity is presented for 30 m class telescopes in the mid-IR, such as the Mid-infrared ELT Imager and Spectrograph (METIS; Brandl et al., 2012) at the ELT, to fill the gap. The dust emission, in the mid-IR, for these objects must be between 370 mas and 60 mas which makes them interesting candidates for imaging. The 30 m class telescopes should observe the missing dust in these objects. However, the missing dust objects are not the only interesting targets.

Sources that show extended dust on both scales would also be interesting targets because this may allow the connection of the mas dust extensions of MIDI and the subarcsecond dust of VISIR. If shown to be the case, the dusty wind could provide an avenue of feedback from the AGN to the galaxy in the form of energy and dusty material. One particular object of interest would be ESO 323-G77. ESO 323-G77 is the only object to show equatorial dust in VISIR and polar dust with MIDI. It is possible that something is happening between these scales that is responsible for the discrepancy.

The ELT is not due to start operations before 2025. In the mean time, instead of a larger telescope, a shorter wavelength could be used. The problem is observing continuum at a shorter wavelength observes hotter, thus more compact in AGN, dust. A solution is to use a near-IR IFU such as NIRSpec on JWST or ERIS on the VLT. A near-IR IFU will allow the study of molecular hydrogen lines, specifically H_2(S(1-0)), which are predicted to trace the warm dusty outflow in hydrodynamic simulations (Williamson, D. in prep). The H_2(S(1-0)) line would allow not only for the study of the warm dust in the spacial scales between MIDI and VISIR but also for the study of its kinematics. The H_2(S(1-0)) line is produced at 1000 K - 2000 K which is much hotter than the dust but the dust and associated gas temperature are not equal and this gas temperature should coincide with the warm dusty wind (Williamson et al., 2019).

8.5 The Molecular Disk of NGC 3783

NGC 3783 is a Type 1 AGN which was observed with ALMA band 7. I managed to constrain extended CO(3-2) emission and conclude that there is evidence of an outflow and a disk-like structure that matches well with disk+wind model as described by the *CAT3D-WIND* model. The ALMA observation agrees with the idea that the dusty gas in an AGN resides in an equatorial reservoir, however, it is not clear with the current data if the reservoir takes the form of a disk with a scale height, a molecular inflow, or a torus. With the currently available data, the disk-like CO emission is neither proof for or against the disk+wind model by itself. The outflow, however, does support the dusty wind model. The polar dust extension direction, determined by MIDI, and the *CAT3D-WIND* model agree well with the [Si VI], Brγ, and the CO(3-2) absence region.

The disk explanation is preferred by previous observations of AGN with ALMA CO (e.g. Gallimore et al., 2016; Combes et al., 2019). However, the sharp cutoff of the CO(3-2) backs up the molecular inflow and ionised outflow explanation. It is interesting to note that if the molecular inflow explanation is true, then the polar dust and ionised gas outflow agrees more with the direction of the NLR than the system axis as defined by polarisation. The polarisation is equatorially scattered in NGC 3783 which means it defined the direction of the disk and not necessarily the outflow. The equatorial scattering is consistent with the predicted size of the BLR (Smith et al., 2002, 2005). The wind originates from the dusty disk however. While the accretion disk, BLR, and dusty disk should all be aligned, it is not impossible for the system to be warped such as may be present in Circinus (Tristram et al., 2014).

Another explanation for the empty region is that it is not an outflow destroying the molecular gas but obscuration from the host galaxy. The PA of the empty region is not dissimilar to the host PA of 163° (Hyperleda, Makarov et al., 2014). However, host obscuration does not innately explain the apparent conical shape of the empty region or the constant velocity component. Furthermore, NGC 3783 appears mostly face on in HST images (see Figure 7.2). Therefore, I conclude that the outflow scenario is more likely.

8.6 The General Structure of AGN Dust

The main conclusion of this work is that the classical dusty torus is not an adequate explanation of the inner dusty structure of an AGN. In reality these objects appear to be a dynamic and complex system. The warm dust appears to be both located in the polar direction and effected by radiation pressure, the gas seems to form an equatorial structure consistent with a disk, and the hot dust is on a scale consistent with the hot dust disk and sublimation radius. These pieces of evidence support the disk+wind model; although, this does not mean it is the only explanation.

What I can say without model dependency is that the material reservoir for AGN is equatorial, more dust, and therefore gas, is driven further from the central engine at higher radiation pressures, and this driven material is located in the polar region which is most likely an outflow.

The main challenge of future work will be attempting to distinguish between true structure and the apparent distribution of dusty gas clouds. In a radiation driven clumpy system, high resolution data will have to be handled with care.

Appendix A

Figures

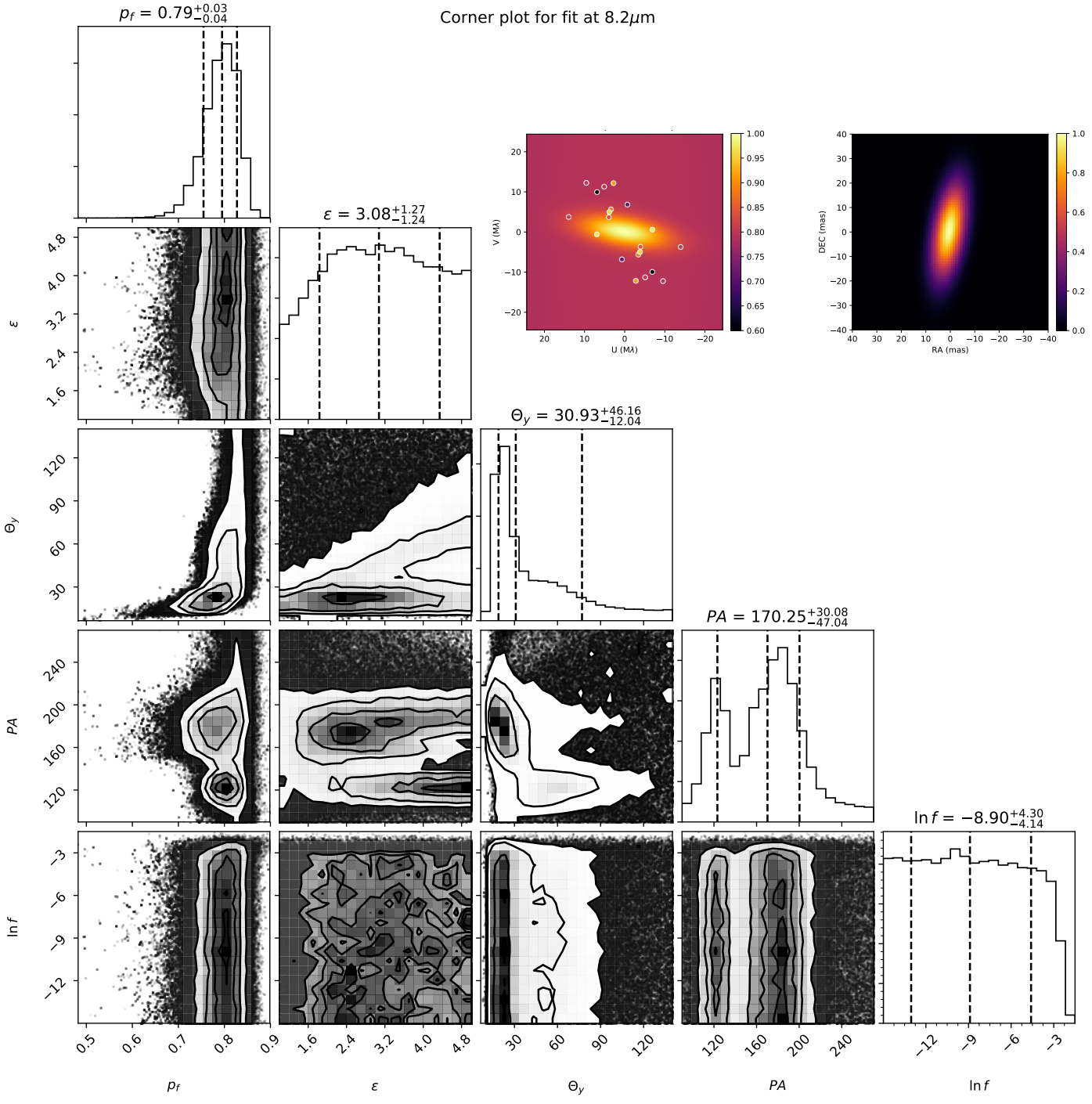

FIGURE A.1: Corner plot (Foreman-Mackey, 2016) of the Probability Density Function (PDF) of each parameter, the fitted Fourier space visibility distribution, and the reconstructed brightness distribution for the 8.2 μm geometric model fit.

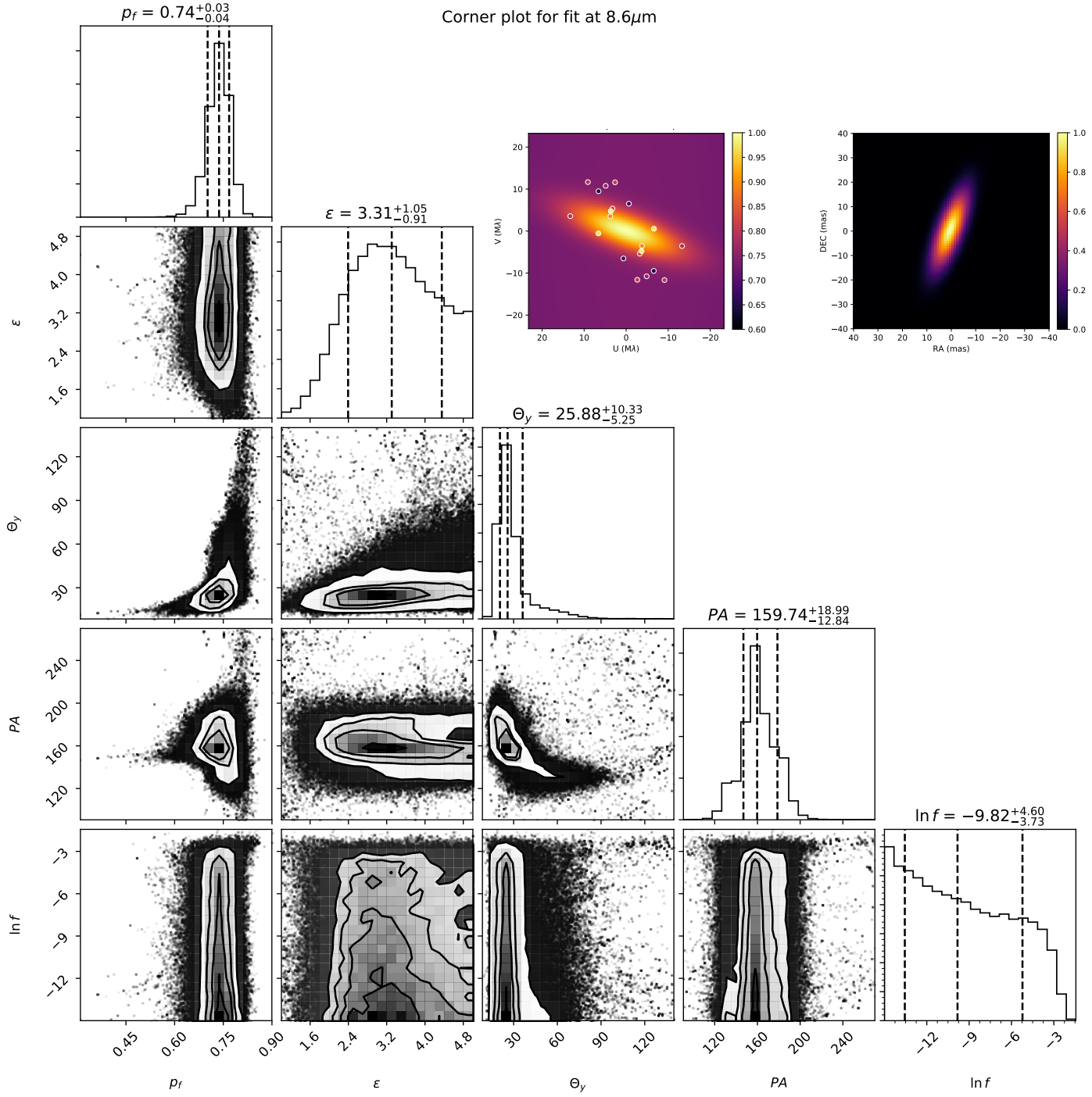

FIGURE A.2: The same as figure A.1 for the 8.6 μm geometric model fit.

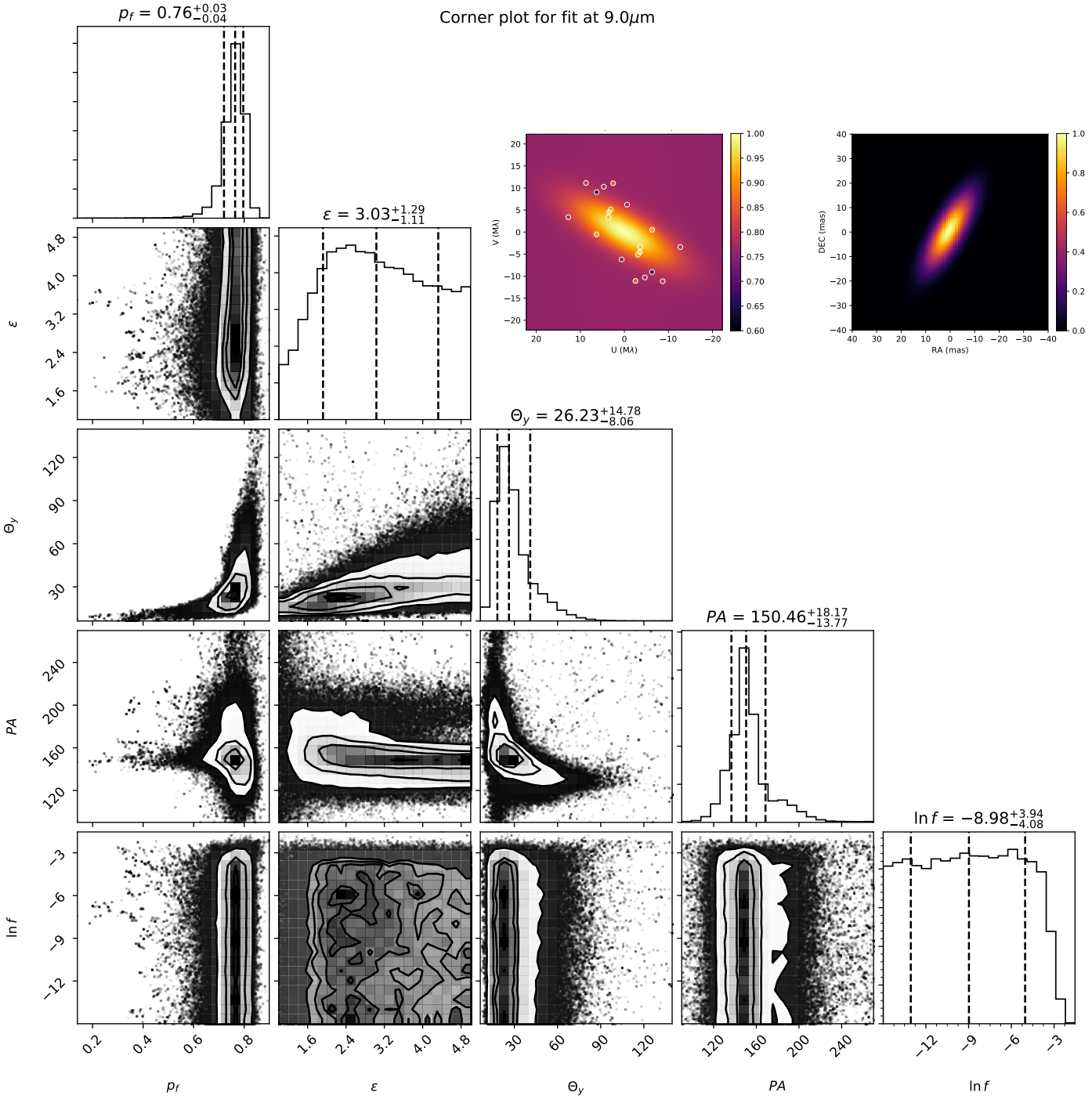

FIGURE A.3: The corner plot for the 9.0 μm geometric model fit and the model result displayed in both Fourier and real space.

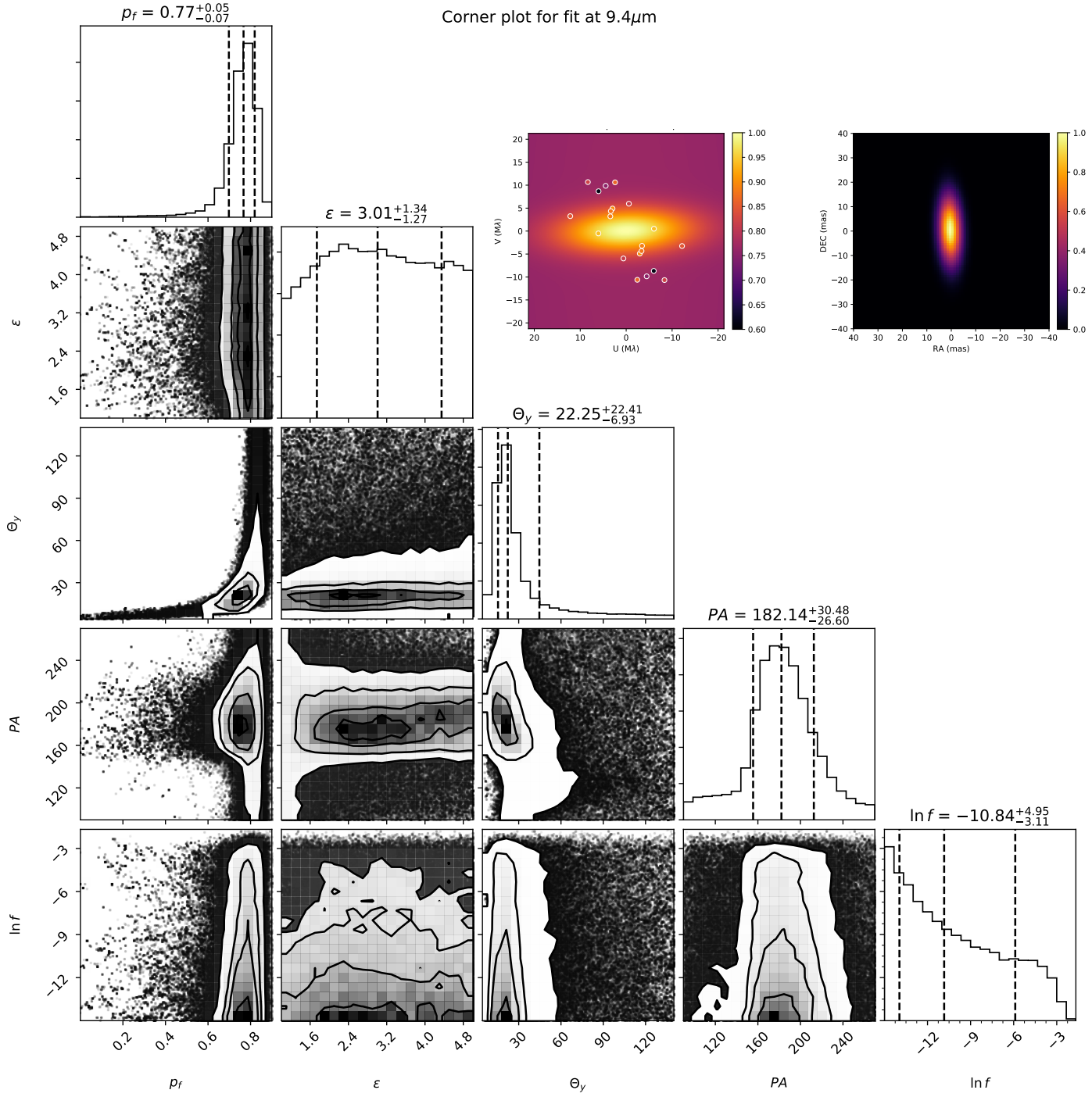

FIGURE A.4: Same as figure A.1, but for the 9.4 μm geometric model fit.

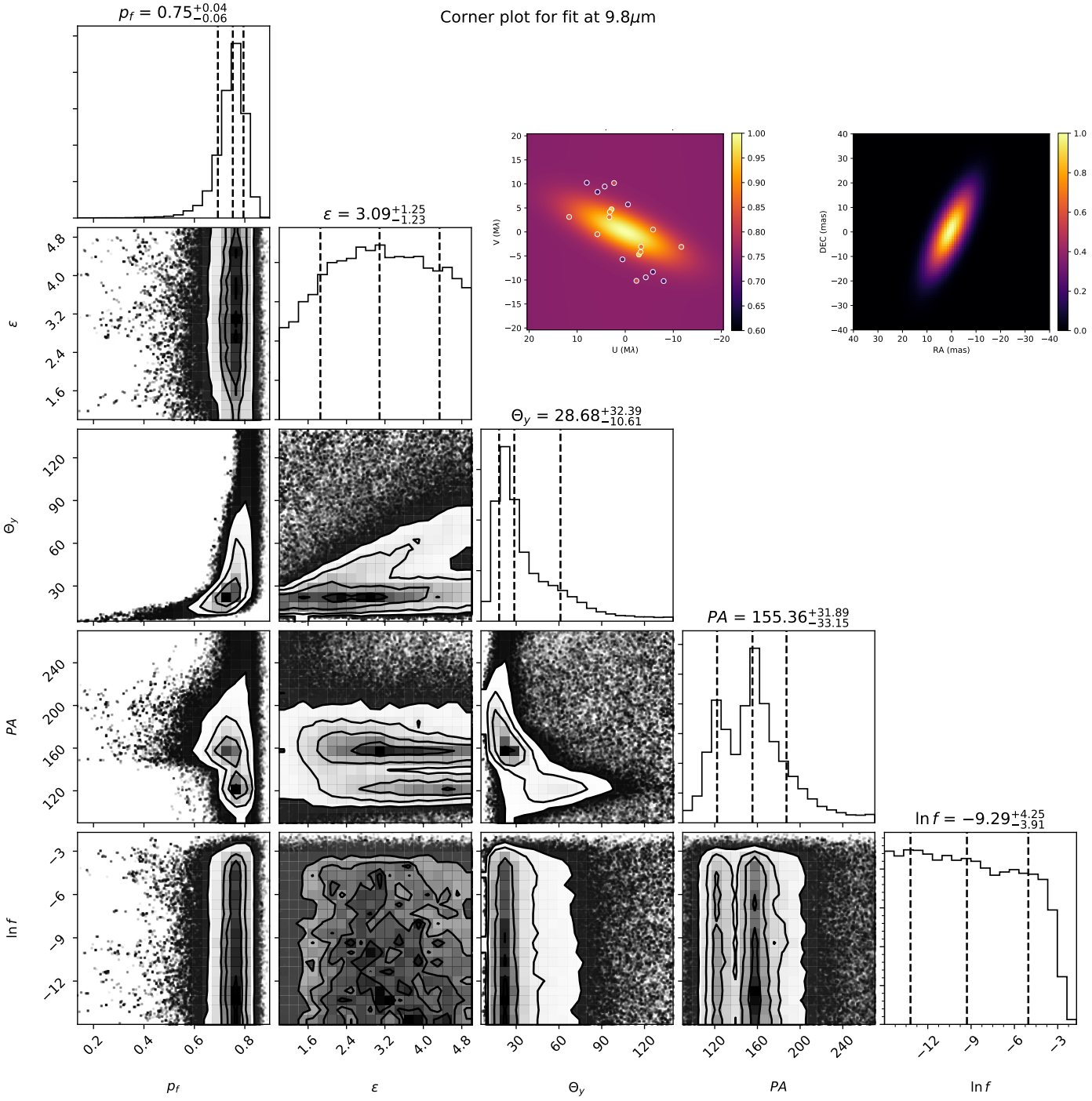

FIGURE A.5: The same as figure A.1 for the 9.8 μm geometric model fit.

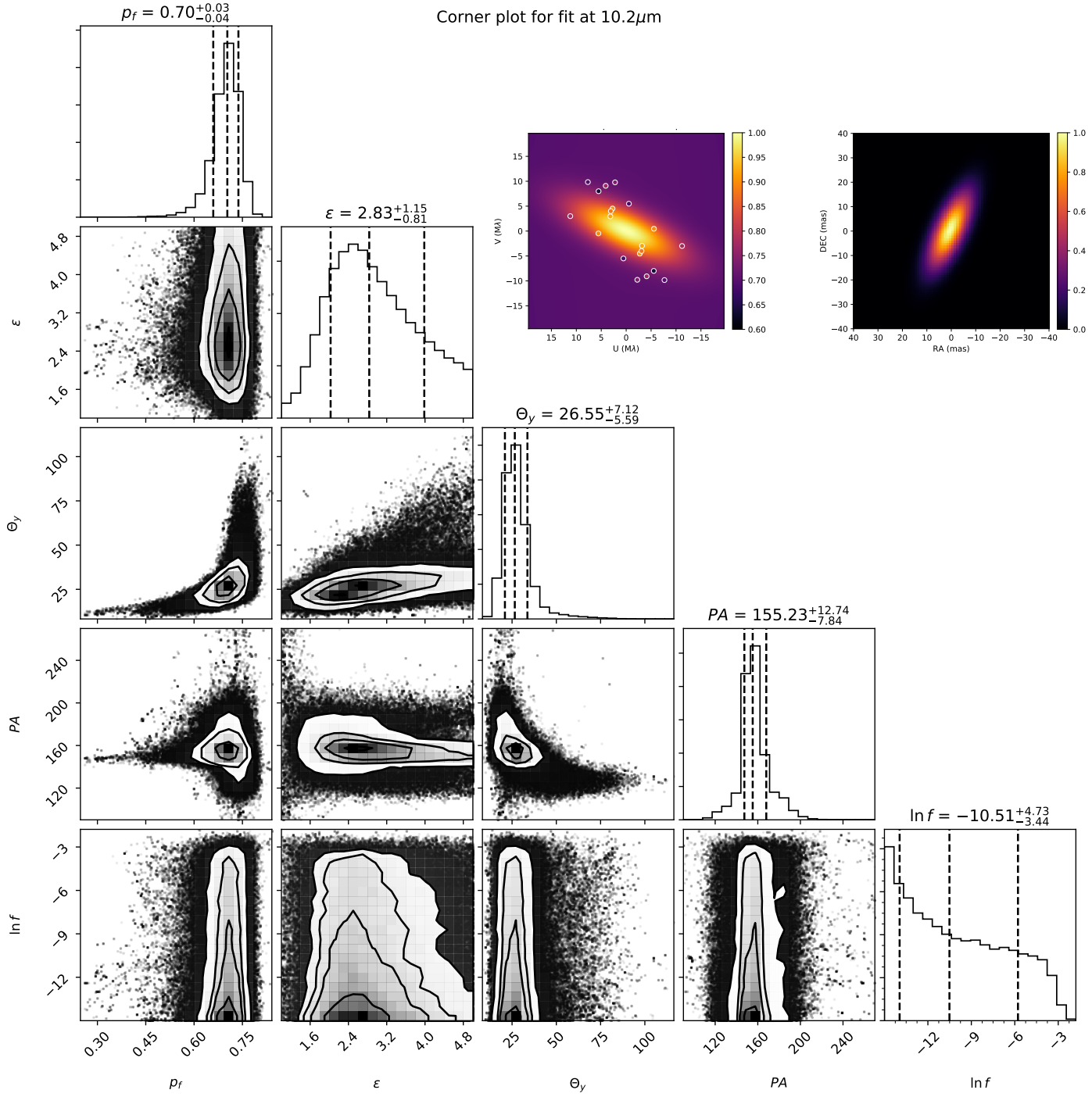

FIGURE A.6: The same as figure A.1 for the 10.2 μm geometric model fit.

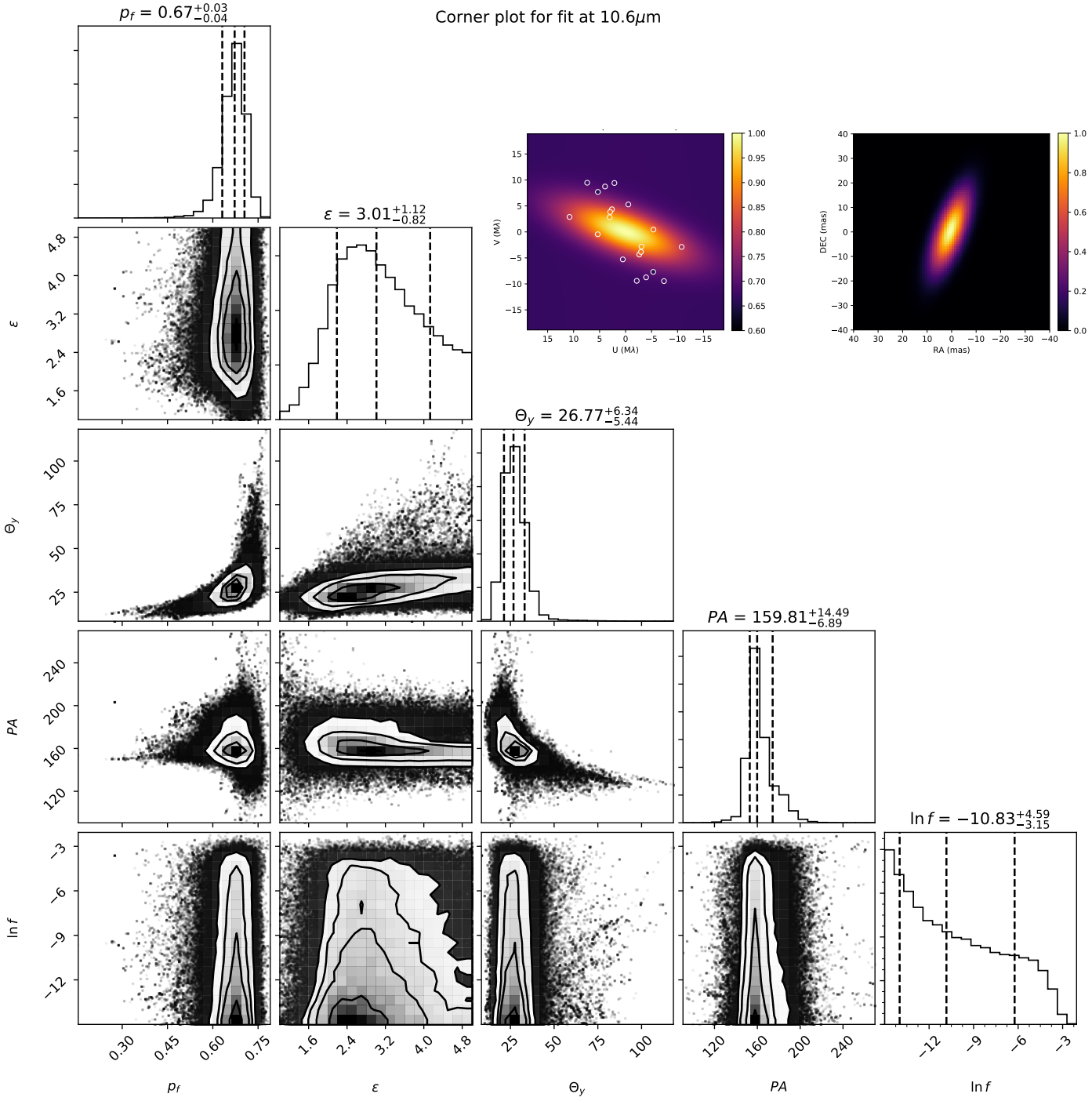

FIGURE A.7: Same as figure A.1, but for the 10.6 μm geometric model fit.

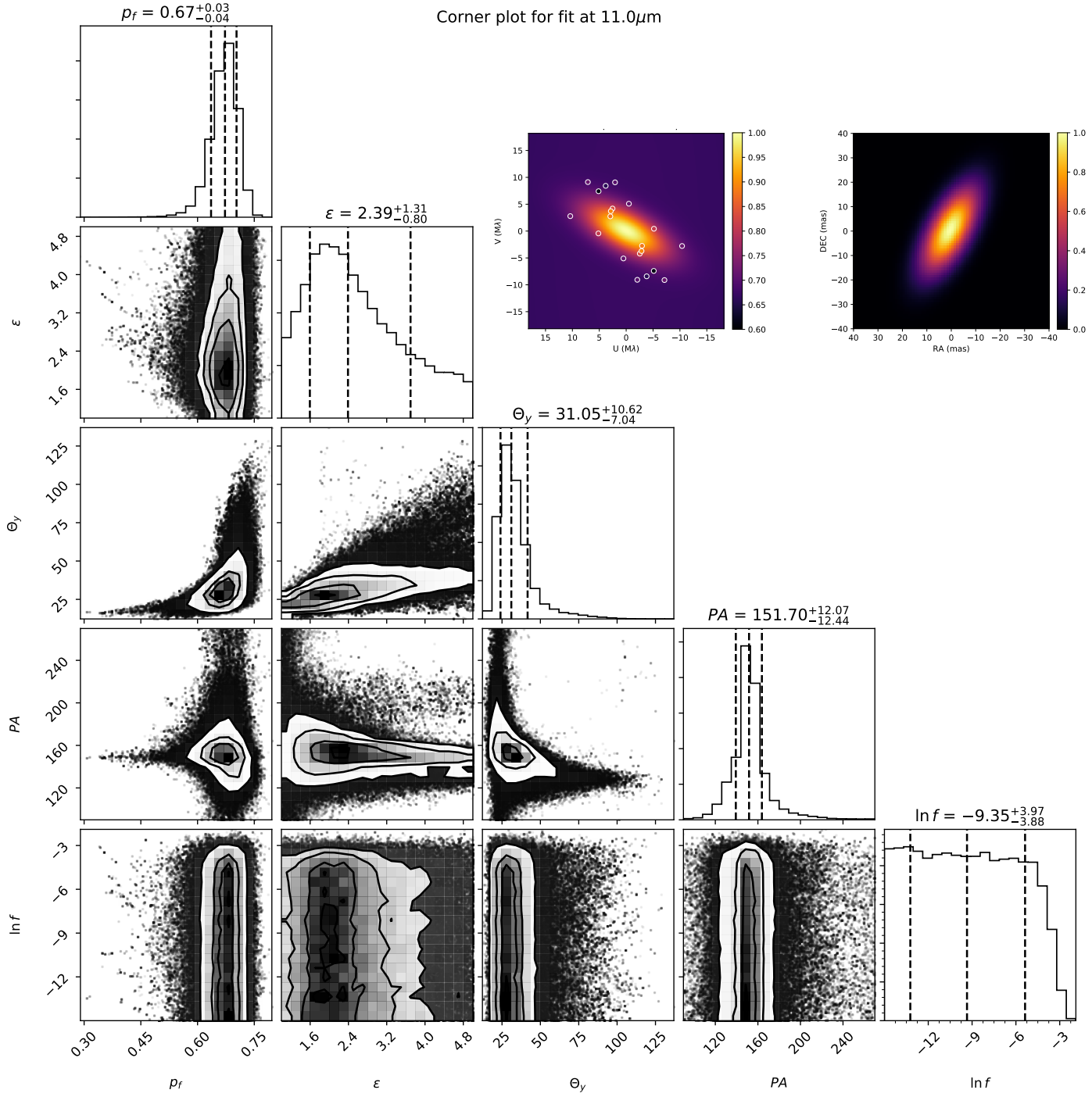

FIGURE A.8: The same as figure A.1 for the 11 μm geometric model fit.

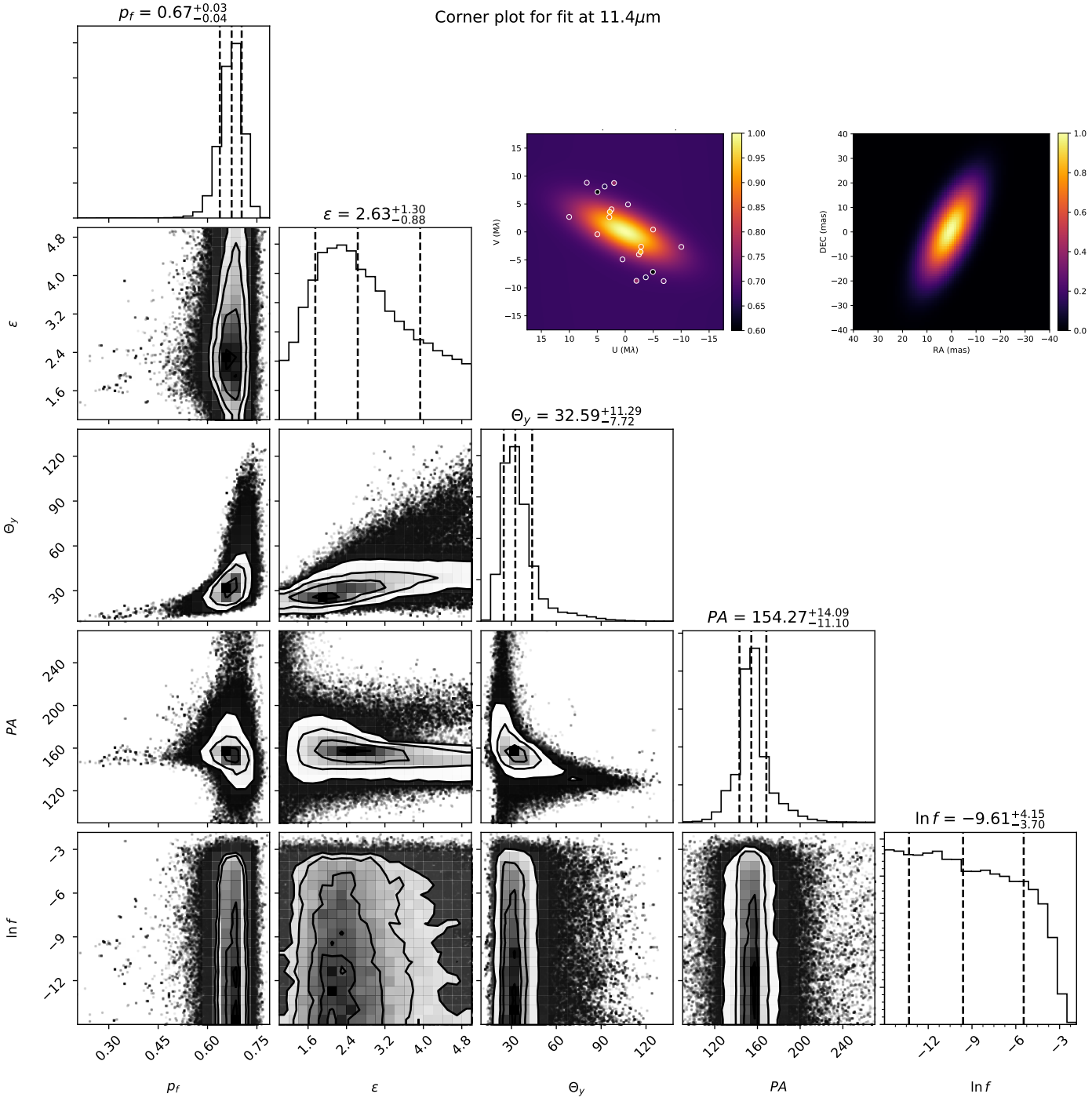

FIGURE A.9: The same as figure A.1 for the 11.4 μm geometric model fit.

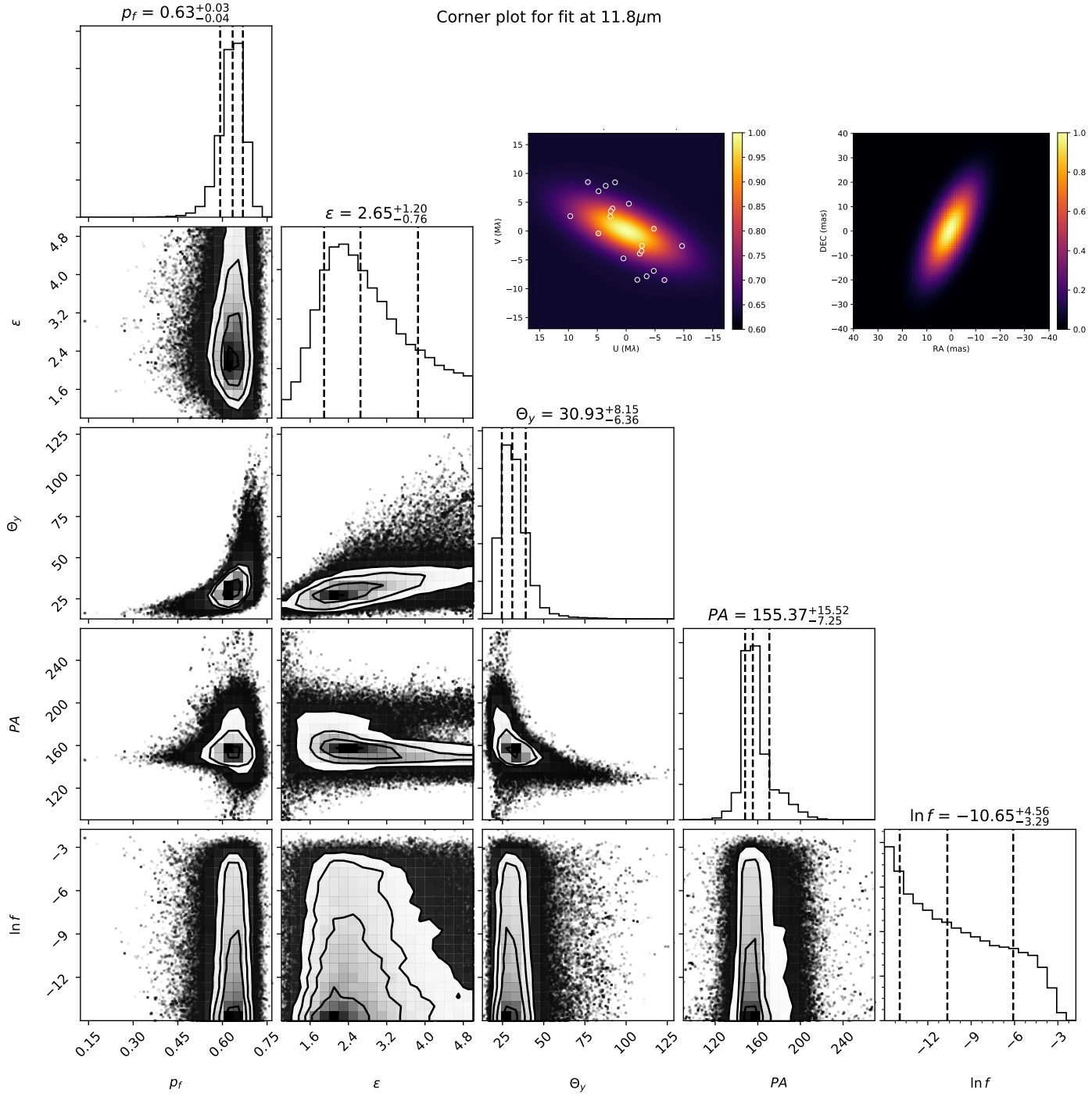

FIGURE A.10: Same as figure A.1, but for the 11.8 μm geometric model fit.

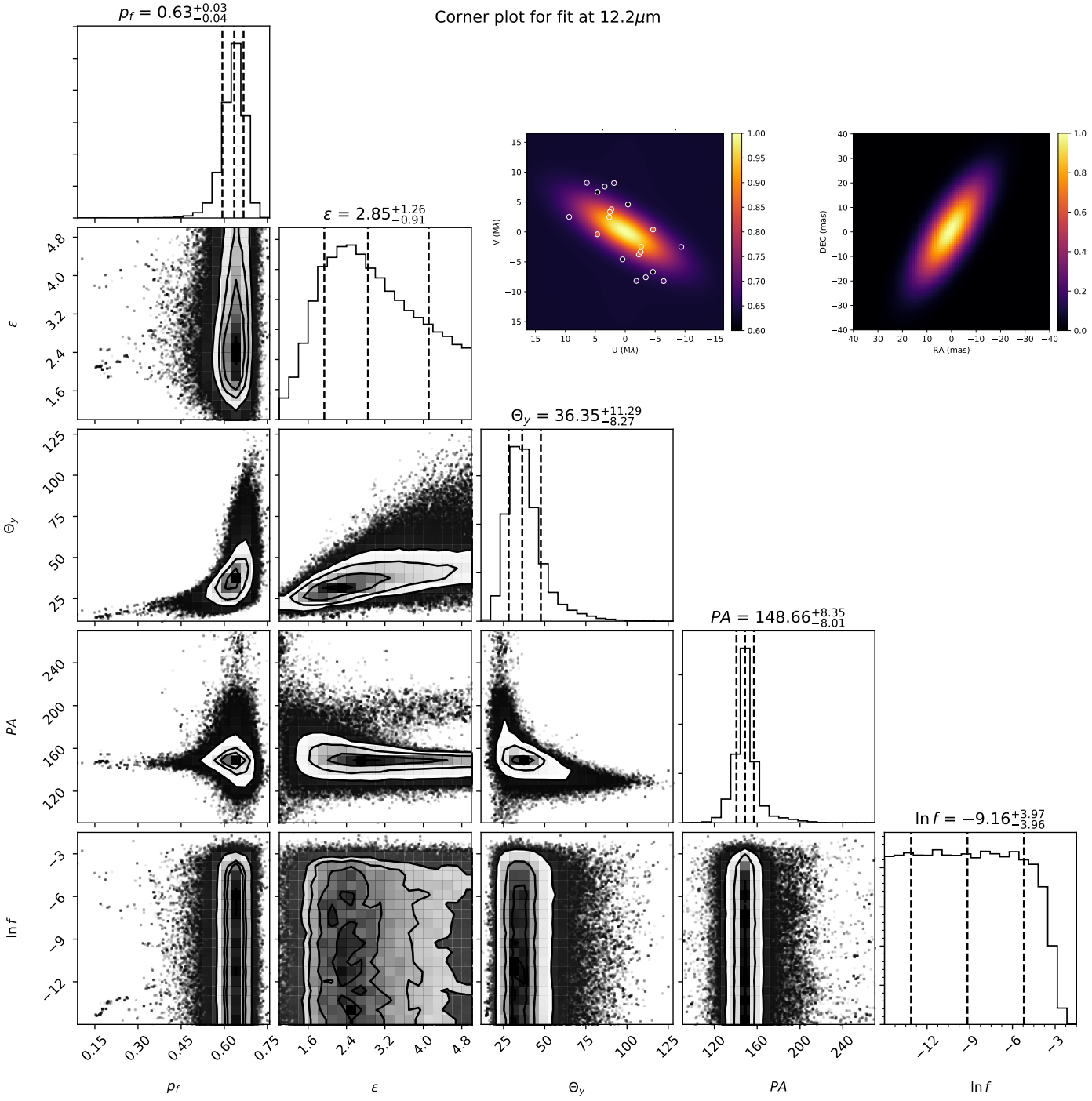

FIGURE A.11: The same as figure A.1 for the 12.2 μm geometric model fit.

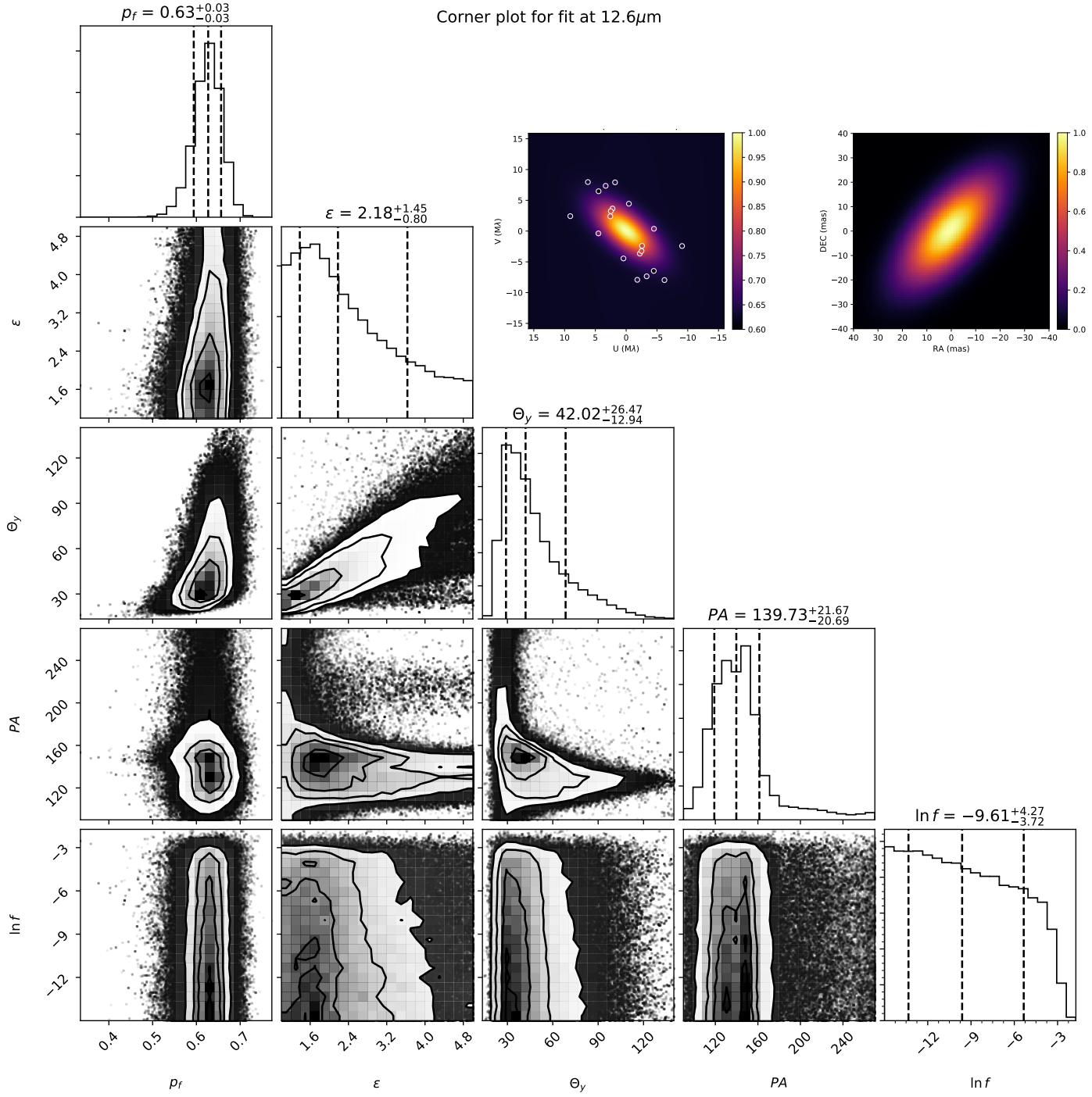

FIGURE A.12: The same as figure A.1 for the 12.6 μm geometric model fit.

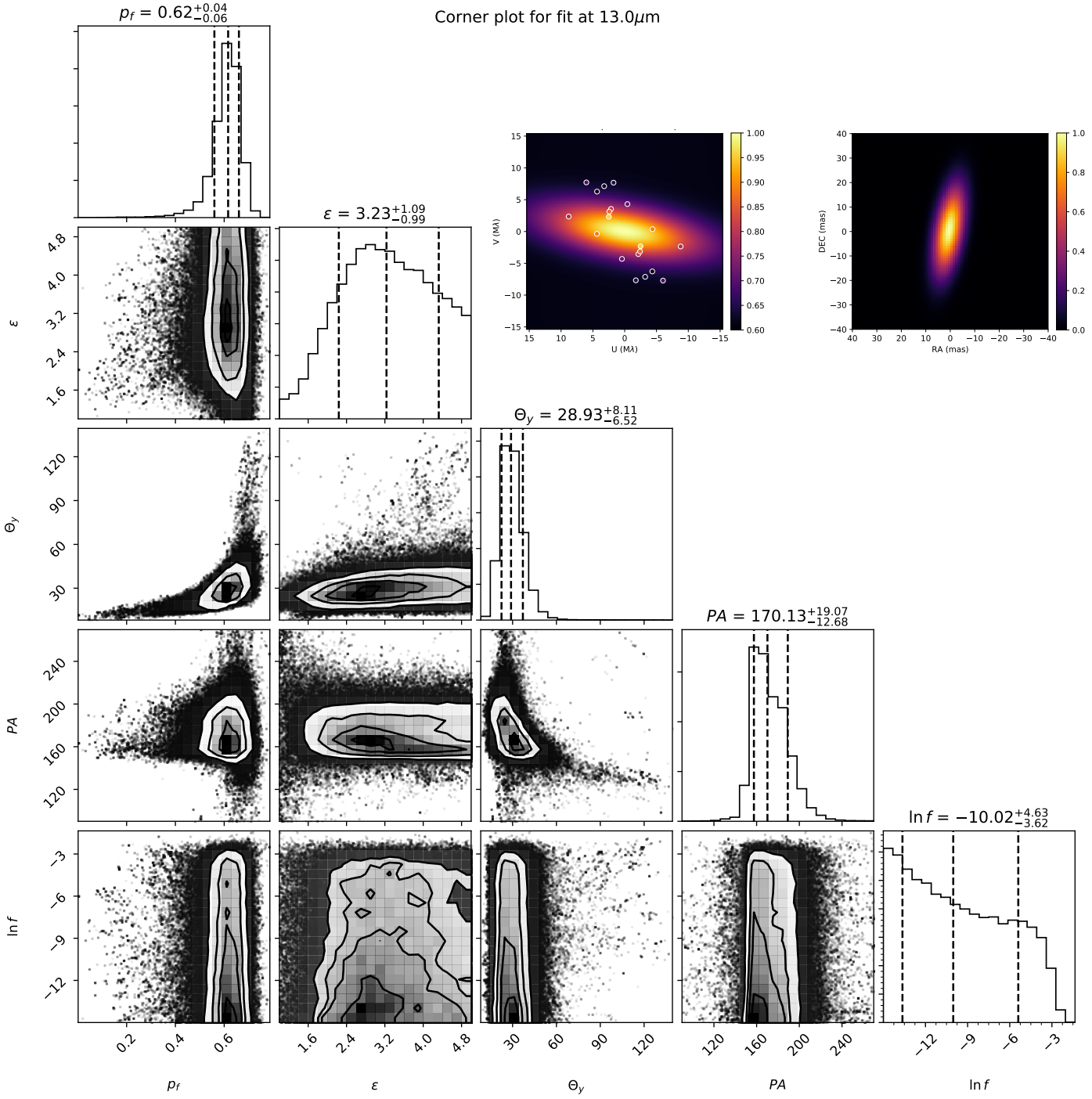

FIGURE A.13: Same as figure A.1, but for the 13 μm geometric model fit.

Appendix B

Tables

Table B.1: Summary table of AGN featured in this work

Object	Type	Ref[a]	D[b] (Mpc)	$L^{c}_{12\,\mu m}$ ($\log(W\,Hz^{-1})$)	$L^{d}_{2-10\,Kev}$ ($\log(W\,Hz^{-1})$)	M_{BH} ($\log(M_{\odot})$)	Ref[e]	N_H[f] ($\log(cm^{-1})$)	F^{g}_{gs} (Jy)	F^{h}_{pf} (Jy)	Ref[i]
NGC 424	2	α	48.7 ± 3.4	$36.66^{0.019}_{0.019}$	36.3 ± 0.5	$6.97^{0.25}_{0.25}$	1	$\geqslant 25$	$0.35^{0.01}_{0.01}$	$0.3^{0.01}_{0.01}$	Lo
NGC 1068	2	β	13.5 ± 1.0	$36.94^{0.017}_{0.018}$	36.6 ± 0.25	$6.93^{0.36}_{0.36}$	2	$\geqslant 25$	$10.81^{0.19}_{0.19}$	$5.23^{0.19}_{0.19}$	Lo
NGC 3783	1.5	α	47.7 ± 3.4	$36.67^{0.024}_{0.025}$	36.33 ± 0.059	$7.37^{0.077}_{0.076}$	3	$\geqslant 20.9$	$0.49^{0.01}_{0.01}$	$0.19^{0.01}_{0.01}$	Lo
Circinus	2	α	8.6 ± 0.6	$36.4^{0.024}_{0.025}$	35.9 ± 0.24	$6.23^{0.09}_{0.09}$	4	24.7 ± 0.17	$8.08^{0.11}_{0.11}$	$2.01^{0.11}_{0.11}$	Lo
NGC 5506	2	α	31.1 ± 2.2	$36.48^{0.012}_{0.012}$	36.11 ± 0.092	$7.55^{0.25}_{0.25}$	5	22.4 ± 0.1	$0.47^{0.01}_{0.01}$	$0.57^{0.01}_{0.01}$	Lo
MCG-5-23-16	2	α	42.1 ± 3.0	$36.5^{0.043}_{0.047}$	36.3 ± 0.25	$7.53^{0.25}_{0.25}$	5	22.1 ± 0.07	$0.39^{0.01}_{0.01}$	$0.2^{0.02}_{0.02}$	Lo
NGC 4507	2	α	56.5 ± 4.0	$36.79^{0.028}_{0.03}$	36.2 ± 0.14	$7^{0.25}_{0.25}$	6	23.7 ± 0.19	$0.48^{0.01}_{0.01}$	$0.16^{0.01}_{0.01}$	Lo
1Zw1	1	β	255.1 ± 17.9	$37.91^{0.34}_{0.301}$	36.6 ± 0.14	$7.44^{0.12}_{0.12}$	7	21 ± 0.45	$0.11^{0.13}_{0.03}$	$0.31^{0.03}_{0.13}$	Bu
NGC 1365	1.8	α	22.7 ± 1.6	$35.66^{0.014}_{0.015}$	35.3 ± 0.17	$7.1^{0.25}_{0.25}$	5	23.2 ± 0.45	--	$0.3^{0.01}_{0.01}$	Bu
IRAS 05189-2524	2	α	189 ± 13.2	$37.69^{0.074}_{0.089}$	36.7 ± 0.36	$7.86^{0.5}_{0.5}$	8	22.8 ± 0.02	$0.22^{0.03}_{0.03}$	$0.24^{0.03}_{0.03}$	Bu
H 0557-385	1.2	α	151 ± 10.9	$37.45^{0.094}_{0.09}$	36.8 ± 0.19	--	--	22.8 ± 0.78	$0.13^{0.03}_{0.02}$	$0.28^{0.02}_{0.03}$	Bu
IRAS 09149-6206	1	α	256 ± 17.9	$37.96^{0.066}_{0.078}$	37.0 ± 0.25	--	--	21.7 ± 0.45	$0.13^{0.02}_{0.02}$	$0.34^{0.02}_{0.02}$	Bu
Mrk 1239	1n	α	93 ± 6.6	$37.17^{0.037}_{0.04}$	36.3 ± 0.25	$8.48^{0.25}_{0.25}$	5	23.5 ± 0.45	--	$0.57^{0.05}_{0.05}$	Bu
NGC 3281	2	α	52 ± 3.7	$36.41^{0.06}_{0.07}$	36.3 ± 0.3	$7.26^{0.25}_{0.25}$	9	24.3 ± 0.45	$0.07^{0.01}_{0.01}$	$0.25^{0.01}_{0.01}$	Bu
NGC 4151	1.5	α	18.3 ± 1.3	$36.01^{0.015}_{0.016}$	35.8 ± 0.24	$7.56^{0.051}_{0.047}$	10	22.7 ± 0.19	$0.87^{0.01}_{0.01}$	$0.3^{0.01}_{0.01}$	Bu
3C273	1	α	705 ± 49.4	$38.68^{0.051}_{0.058}$	38.8 ± 0.1	$8.84^{0.077}_{0.113}$	10	$\geqslant 19.7$	--	$0.32^{0.04}_{0.04}$	Bu
NGC 4593	1	α	45 ± 3.2	$36.18^{0.1}_{0.13}$	35.8 ± 0.26	$6.88^{0.84}_{0.104}$	11	20.4 ± 0.45	$0.12^{0.03}_{0.03}$	$0.13^{0.01}_{0.01}$	Bu
Centaurus A	2	γ	12 ± 0.9	$35.79^{0.026}_{0.028}$	35.94 ± 0.086	$7.74^{0.073}_{0.073}$	12	23.1 ± 0.45	$0.56^{0.03}_{0.03}$	$0.91^{0.03}_{0.03}$	Bu
IRAS 13349+2438	1n	α	480 ± 33.6	$38.54^{0.017}_{0.018}$	36.89 ± 0.075	--	--	21.6 ± 0.45	--	$0.5^{0.02}_{0.02}$	Bu
IC 4329A	1.2	α	75 ± 5.3	$37.28^{0.051}_{0.058}$	36.83 ± 0.076	$7^{0.463}_{0.463}$	10	21.5 ± 0.42	$0.55^{0.05}_{0.05}$	$0.58^{0.05}_{0.05}$	Bu
NGC 5995	2	δ	113 ± 8.0	$37.1^{0.084}_{0.11}$	36.4 ± 0.13	$7.11^{0.4}_{0.4}$	13	22 ± 0.45	$0.18^{0.03}_{0.02}$	$0.15^{0.02}_{0.03}$	Bu

Object	Type	Ref[a]	D[b] (Mpc)	$L^{c}_{12\,\mu m}$ ($\log(W\,Hz^{-1})$)	$L^{d}_{2-10\,Kev}$ ($\log(W\,Hz^{-1})$)	M_{BH} ($\log(M_{\odot})$)	Ref[e]	N_H[f] ($\log(cm^{-1})$)	F^{g}_{gs} (Jy)	F^{h}_{pf} (Jy)	Ref[i]
NGC 7469	1.5	α	67 ± 4.7	$36.92^{0.061}_{0.071}$	36.17 ± 0.059	$6.96^{0.048}_{0.05}$	10	$\geqslant 24.4$	$0.39^{0.03}_{0.03}$	$0.23^{0.03}_{0.03}$	Bu
Mrk 509	1.5	α	148 ± 10.4	$37.24^{0.2}_{0.61}$	37.09 ± 0.076	$8.05^{0.035}_{0.035}$	10	$\geqslant 20.7$	$0.28^{0.058}_{0.076}$	$0.14^{0.07}_{0.09}$	Th
Fairall 49	2	α	88 ± 6.4	$37.07^{0.043}_{0.048}$	36.32 ± 0.092	$7.38^{0.25}_{0.25}$	14	22.2 ± 0.45	$0.26^{0.02}_{0.02}$	$0.26^{0.02}_{0.02}$	Th
Fairall 51	1	ϵ	62 ± 4.4	$36.64^{0.013}_{0.014}$	36.03 ± 0.025	$6.84^{0.5}_{0.5}$	13	22.4 ± 0.12	$0.18^{0.004}_{0.004}$	$0.21^{0.004}_{0.004}$	Th
MCG-06-30-15	1	ϵ	38.3 ± 2.7	$36.16^{0.036}_{0.04}$	35.79 ± 0.092	$5.93^{0.25}_{0.25}$	9	20.2 ± 0.45	$0.19^{0.01}_{0.01}$	$0.14^{0.009}_{0.009}$	Th
NGC 2110	2	α	35.5 ± 2.5	$36.13^{0.15}_{0.23}$	35.66 ± 0.084	$8.4^{0.25}_{0.25}$	5	22.5 ± 0.06	$0.2^{0.05}_{0.05}$	$0.16^{0.05}_{0.05}$	Th
NGC 7213	1.5	ζ	22.8 ± 1.6	$35.46^{0.061}_{0.061}$	35.18 ± 0.05	$7.3^{0.25}_{0.25}$	5	20.3 ± 0.45	$0.07^{0.01}_{0.007}$	$0.12^{0.008}_{0.01}$	Th
NGC 7674	2	α	122 ± 8.6	$37.27^{0.069}_{0.082}$	37.0 ± 0.46	$7.09^{0.25}_{0.25}$	5	$\geqslant 24.4$	$0.3^{0.02}_{0.02}$	$0.13^{0.02}_{0.02}$	Th
ESO 323-G77	1.2	α	70 ± 5.0	$36.74^{0.13}_{0.19}$	35.7 ± 0.1	$7.39^{0.5}_{0.5}$	13	23.6 ± 0.45	$0.14^{0.036}_{0.035}$	$0.23^{0.06}_{0.06}$	Le
Fairall 9	1.2	α	206 ± 14.4	$37.55^{0.06}_{0.07}$	36.95 ± 0.092	$8.3^{0.078}_{0.116}$	10	$\geqslant 20.5$	$0.08^{0.01}_{0.01}$	$0.19^{0.01}_{0.01}$	Th
IC 3639	2	α	52.7 ± 3.7	$36.42^{0.16}_{0.26}$	36.4 ± 0.75	$5.96^{0.25}_{0.25}$	9	$\geqslant 25$	$0.24^{0.02}_{0.02}$	$0.09^{0.009}_{0.009}$	F8
NGC 1052	3b	α	19.1 ± 1.4	$35.13^{0.48}_{0.11}$	34.51 ± 0.067	$7.98^{0.37}_{0.37}$	15	23 ± 0.45	$0.005^{0.01}_{0.001}$	$0.118^{0.01}_{0.01}$	F9

Table B.1: The Luminosities and black hole masses used in this work. a) Reference for given AGN activity type: α) Véron-Cetty and Véron (2006), β) Osterbrock and Martel (1993), γ) Krimm et al. (2013), δ) Panessa and Bassani (2002), ϵ) Bennert et al. (2006), ζ) Veron-Cetty and Veron (1998); b) Hubble Distances (CMB) from NED; c) Total 12 μm Luminosity values derived fluxes provided by Asmus et al. (2014); d) Absorption corrected X-ray Luminosity derived from Asmus et al. (2015); e) Reference for black hole mass: 1) Gu et al. (2006), 2) Lodato and Bertin (2003), 3) Onken and Peterson (2002), 4) Greenhill et al. (2003), 5) Makarov et al. (2014), 6) Cid Fernandes et al. (2004), 7) Vestergaard and Peterson (2006), 8) Wang and Zhang (2007), 9) Garcia-Rissmann et al. (2005), 10) Peterson et al. (2004), 11) Denney et al. (2006), 12) Cappellari et al. (2009), 13) Wang and Zhang (2007), 14) Koss et al. (2017) ,15) Ho et al. (2009); f) N_H values from Asmus et al. (2015); g) extended component flux; h) unresolved source flux; i) Reference for extended and unresolved fluxes: Lo) López-Gonzaga et al. (2016), Bu Burtscher et al. (2013), Th) This work, Le) Leftley et al. (2018), F8) Fernández-Ontiveros et al. (2018), F9) Fernández-Ontiveros et al. (2019)

Table B.2: List of MIDI Observations

Date	Time	Notes	No Track	Programme	#Files	PA (deg)	BL (m)
Fairall 51							
2010-10-19	00:04:05		n	086.B-0019(B)	2	63	73.3
2010-10-20	00:09:14	Poor tracking[ab], included	n	086.B-0019(C)	1	119	82.4
2013-06-21	01:50:34	Off centre target	n	091.B-0025(K)	3	20.0	130.2
2013-06-21	02:44:46	Fringe tracking failed[a]	n	091.B-0025(K)	2	32.0	130.0
2013-06-23	01:54:23	Fringe tracking failed[ab]	n	091.B-0025(H)	1	9	44.6
2013-08-19	04:35:40	Fringe tracking failed[ab]	n	091.B-0647(A)	1	146	62.3
2013-08-19	04:51:42		y	091.B-0647(A)	1	150	62.2
2014-05-16	03:00:53		y	093.B-0287(A)	2	4	130.2
2014-05-16	04:10:22		y	093.B-0287(A)	2	32	86.1
2014-05-16	04:56:02		y	093.B-0287(A)	2	43	87.3
2014-05-16	06:51:08		y	093.B-0287(A)	3	70	89.4
2014-05-16	09:14:33		y	093.B-0287(A)	2	102	86.4
2014-05-16	10:02:03		y	093.B-0287(A)	3	113	83.9
2014-08-07	00:58:34	Poor fringe tracking[ac]	n	093.B-0287(E)	1	48	128.5
2014-08-07	01:13:28	Insufficient number of central fringes	y	093.B-0287(E)	2	51	128.0
2014-08-07	02:38:41		y	093.B-0287(E)	3	69	123.0
2014-08-08	00:24:57		y	093.B-0287(E)	3	14	49.8
2014-08-08	05:41:38		y	093.B-0287(E)	2	130	79.6
2014-08-08	23:52:17	Low S/N, short exposure time	n	093.B-0287(E)	2	9	50.1
2014-08-09	00:05:43		y	093.B-0647(A)	2	11	50.0
2014-08-09	00:54:40		y	093.B-0647(A)	2	19	49.3

Date	Time	Notes	No Track	Programme	#Files	PA (deg)	BL (m)
2014-08-09	01:24:55		y	093.B-0647(A)	1	24	48.7
2014-08-09	05:33:02		y	093.B-0647(A)	2	62	36.5
Fairall 49							
2009-08-03	05:30:13	Very high S/N	n	083.B-0288(A)	2	57	38.9
2009-08-04	05:29:50	Very high S/N	n	083.B-0288(C)	2	67	69.9
2013-06-21	03:18:09	No fringes[a], seeing of 1.89	n	091.B-0025(K)	1	40	129.9
Fairall 9							
2013-12-16	00:38:44	No fringes, seeing of 1	y	092.B-0738(D)	1	42	47.6
2013-12-17	00:54:48	OPD>100μm	y	092.B-0738(C)	1	88	89.8
2013-12-17	01:33:03	OPD>100μm	y	092.B-0738(C)	1	87	98.0
2013-12-17	03:06:08	OPD>100μm	y	092.B-0738(C)	1	81	119.5
2014-08-08	04:42:40		n	093.B-0287(E)	2	84	23.7
2014-08-08	05:05:15		y	093.B-0287(E)	2	84	29.5
2014-08-09	10:36:28		y	093.B-0647(A)	2	44	45.4
MCG-06-30-15							
2010-03-01	03:49:58	Poor fringe tracking[a]	n	084.B-0366(A)	1	175	56.6
2010-03-01	04:35:22		n	084.B-0366(A)	4	2	56.6
2010-03-02	06:46:10	Insufficient number of central fringes[ad]	n	084.B-0366(C)	2	27	102.3
2010-03-03	03:48:11		n	084.B-0366(B)	1	79	40.7
2014-05-15	04:46:12	Failure in fringe tracking[a], partial tracking only	n	093.B-0287(A)	1	99	80.3
2014-05-15	05:08:16		y	093.B-0287(A)	2	102	76.9
2014-05-15	06:03:23		y	093.B-0287(A)	1	113	66.9
2014-05-16	00:57:54		y	093.B-0287(A)	2	45	127.1
2014-05-16	02:06:01		y	093.B-0287(A)	2	56	130.2

Date	Time	Notes	No Track	Programme	#Files	PA (deg)	BL (m)
2014-05-16	05:53:57		y	093.B-0287(A)	4	111	68.0
Mrk 509							
2014-08-07	01:40:17	Insufficient number of central fringes	y	093.B-0287(E)	2	42	101.3
2014-08-07	03:33:21	Insufficient number of central fringes	y	093.B-0287(E)	2	57	124.3
2014-08-07	04:29:20	Insufficient number of central fringes	y	093.B-0287(E)	2	61	129.6
2014-08-08	01:28:26		y	093.B-0287(E)	2	4	51.6
2014-08-08	01:39:32		n	093.B-0287(E)	1	6	51.7
2014-08-08	03:55:01	Suppressed 12 micron emission[ac]	n	093.B-0287(E)	1	80	88.6
2014-08-08	04:12:05		y	093.B-0287(E)	2	80	89.2
NGC 2110							
2013-12-14	02:36:09		y	092.B-0738(B)	2	107	55.0
2013-12-14	03:28:23	Insufficient number of central fringes	y	092.B-0738(B)	1	107	60.1
2013-12-14	04:07:39		y	092.B-0738(B)	2	108	62.0
2013-12-14	04:56:54		y	092.B-0738(B)	2	109	62.2
2013-12-14	05:36:26	Insufficient number of central fringes	y	092.B-0738(B)	1	111	60.6
2013-12-15	02:27:37	Insufficient number of central fringes/high background[b]	y	092.B-0738(A)	2	7	50.4
2013-12-15	04:54:22	Insufficient number of central fringes/high background[b]	y	092.B-0738(A)	2	26	54.4
2013-12-15	05:36:05	High background[b]	y	092.B-0738(A)	1	30	55.6
2013-12-16	02:14:24	High background[b]	y	092.B-0738(D)	1	20	38.6
2013-12-16	02:44:45	Insufficient number of central fringes/high background[b]	y	092.B-0738(D)	4	26	39.9
2014-11-05	09:01:36		y	094.B-0918(B)	3	115	56.3
NGC 7213							
2013-08-18	04:45:11	Insufficient fringes, too faint to track	n	091.B-0647(A)	1	106	61.3
2013-08-18	05:28:56		y	091.B-0647(A)	1	114	62.3

Date	Time	Notes	No Track	Programme	#Files	PA (deg)	BL (m)
2013-08-18	06:30:12	No fringes	y	091.B-0647(A)	2	125	62.2
2013-08-18	08:01:22		y	091.B-0647(A)	2	144	60.0
2013-08-18	09:03:47		y	091.B-0647(A)	2	159	58.2
2013-08-19	05:50:13		y	091.B-0647(A)	2	119	62.5
2013-10-20	02:37:37	Low S/N , spike in seeing from clouds	y	092.B-0718(D)	1	47	88.5
2013-12-15	01:07:59	Insufficient number of central fringes/high background[b]	y	092.B-0738(A)	1	52	39.4
2014-08-09	02:38:57	Insufficient number of central fringes	y	093.B-0647(A)	2	45	81.6
2014-08-09	06:34:44		y	093.B-0647(A)	3	35	51.3
2014-08-09	08:10:11	No fringes	y	093.B-0647(A)	1	87	106.2
2014-08-09	09:47:50		y	093.B-0647(A)	3	53	37.8
2014-11-03	02:08:41	Insufficient number of central fringes	y	094.B-0918(C)	2	83	111.2
NGC 7674							
2013-08-19	07:23:06	Insufficient number of central fringes	y	091.B-0647(A)	2	106	55.9
2013-08-19	08:14:06	Insufficient number of central fringes	y	091.B-0647(A)	3	107	48.8
2013-08-19	09:46:12		y	091.B-0647(A)	4	112	31.0
2013-10-20	00:13:28	Insufficient fringes[ab], very faint	n	092.B-0718(D)	3	23	74.6
2013-10-20	00:31:26	Insufficient number of central fringes	y	092.B-0718(D)	2	26	76.9
2013-10-20	01:19:37	Insufficient number of central fringes	y	092.B-0718(D)	3	32	83.4
2014-08-09	08:57:45		y	093.B-0647(A)	2	60	128.0

Table B.2: a) Due to short coherence time (<4ms), b) high atmospheric dust, c) clouds, d) high wind (pointing limited)

Table B.3: List of ISAAC Observations

Object	Date	Time	Programme	Band
Fairall 51	2013-06-26	08:15:25.8863	290.B-5113(A)	L
Fairall 51	2013-06-26	08:16:51.9090	290.B-5113(A)	L
Fairall 51	2013-06-26	08:18:51.3442	290.B-5113(A)	M
Fairall 51	2013-06-26	08:20:18.0000	290.B-5113(A)	M
Fairall 49	2013-06-26	07:49:39.6196	290.B-5113(A)	L
Fairall 49	2013-06-26	07:51:08.0927	290.B-5113(A)	L
Fairall 49	2013-06-26	07:53:09.7430	290.B-5113(A)	M
Fairall 49	2013-06-26	07:54:34.9486	290.B-5113(A)	M
Fairall 9	2010-10-07	02:45:49.1390	086.B-0242(B)	M
Fairall 9	2010-10-07	02:47:16.1162	086.B-0242(B)	M
Fairall 9	2010-10-15	02:18:14.8860	086.B-0242(B)	M
Fairall 9	2010-10-15	02:19:41.1381	086.B-0242(B)	M
Fairall 9	2010-10-22	03:46:13.8033	086.B-0242(B)	M
Fairall 9	2010-10-22	03:47:38.1333	086.B-0242(B)	M
Fairall 9	2010-10-27	01:56:13.4726	086.B-0242(B)	M
Fairall 9	2010-10-27	01:57:38.9651	086.B-0242(B)	M
Fairall 9	2010-11-10	00:14:07.9850	086.B-0242(B)	M
Fairall 9	2010-11-10	00:15:33.5360	086.B-0242(B)	M
Fairall 9	2010-11-11	00:01:09.7147	086.B-0242(B)	M
Fairall 9	2010-11-11	00:02:34.0413	086.B-0242(B)	M
Fairall 9	2010-11-22	01:02:22.1393	086.B-0242(B)	M
Fairall 9	2010-11-22	01:03:48.2911	086.B-0242(B)	M
Fairall 9	2010-11-26	01:13:47.6723	086.B-0242(B)	M
Fairall 9	2010-11-26	01:15:13.2734	086.B-0242(B)	M
Fairall 9	2010-12-07	00:31:34.9685	086.B-0242(B)	M
Fairall 9	2010-12-07	00:33:01.7285	086.B-0242(B)	M
Fairall 9	2010-12-13	00:56:50.4999	086.B-0242(B)	M
Fairall 9	2010-12-13	00:58:14.5939	086.B-0242(B)	M
Fairall 9	2011-01-09	01:16:23.4416	086.B-0242(B)	M
Fairall 9	2011-01-09	01:17:47.7227	086.B-0242(B)	M
Fairall 9	2011-07-14	06:41:46.3601	087.B-0018(B)	M
Fairall 9	2011-07-14	06:43:12.1778	087.B-0018(B)	M
Fairall 9	2011-07-20	09:45:08.6944	087.B-0018(B)	M
Fairall 9	2011-07-20	09:46:33.2340	087.B-0018(B)	M
Fairall 9	2011-07-21	07:52:47.3671	087.B-0018(B)	M
Fairall 9	2011-07-21	07:54:11.5805	087.B-0018(B)	M
Fairall 9	2011-07-21	08:13:06.3934	087.B-0018(B)	M
Fairall 9	2011-07-21	08:14:33.8256	087.B-0018(B)	M

Object	Date	Time	Programme	Band
Fairall 9	2011-08-18	09:17:22.2906	087.B-0018(B)	M
Fairall 9	2011-09-04	09:29:24.9498	087.B-0018(B)	M
Fairall 9	2011-09-04	09:30:49.2816	087.B-0018(B)	M
Fairall 9	2011-09-12	09:35:55.6440	087.B-0018(B)	M
Fairall 9	2011-09-12	09:37:22.9466	087.B-0018(B)	M
Fairall 9	2011-09-15	06:54:45.6165	087.B-0018(B)	M
Fairall 9	2011-09-15	06:56:11.3908	087.B-0018(B)	M
MCG-6-30-15	2013-07-04	01:51:18.5046	290.B-5113(A)	L
MCG-6-30-15	2013-07-04	01:52:44.5524	290.B-5113(A)	L
Mrk 509	2003-04-21	08:11:01.1533	71.B-0062(A)	H
Mrk 509	2003-04-21	08:17:14.8658	71.B-0062(A)	H
Mrk 509	2003-04-21	08:19:52.8216	71.B-0062(A)	Ks
Mrk 509	2003-04-21	08:26:10.1533	71.B-0062(A)	Ks
Mrk 509	2011-08-02	04:02:48.1658	087.B-0018(B)	M
Mrk 509	2011-08-02	04:04:12.1794	087.B-0018(B)	M
Mrk 509	2011-09-13	23:28:42.6615	087.B-0018(B)	M
Mrk 509	2011-09-13	23:30:05.9334	087.B-0018(B)	M
Mrk 509	2011-09-23	23:45:18.2757	087.B-0018(B)	M
Mrk 509	2011-09-23	23:46:42.7027	087.B-0018(B)	M
Mrk 509	2011-09-23	23:50:22.2386	087.B-0018(B)	M
Mrk 509	2011-09-23	23:51:54.4285	087.B-0018(B)	M
Mrk 509	2011-09-24	23:20:24.1184	087.B-0018(B)	M
Mrk 509	2011-09-24	23:21:50.9830	087.B-0018(B)	M
Mrk 509	2013-07-03	05:26:37.4303	290.B-5113(A)	L
Mrk 509	2013-07-03	05:28:02.8710	290.B-5113(A)	L
Mrk 509	2013-07-03	05:30:03.3439	290.B-5113(A)	M
Mrk 509	2013-07-03	05:31:28.8123	290.B-5113(A)	M
Mrk 509	2013-07-03	05:32:47.8805	290.B-5113(A)	M
Mrk 509	2013-07-03	05:34:14.6913	290.B-5113(A)	M
NGC 2110	2006-11-19	08:18:03.5029	078.B-0303(B)	Ks
NGC 2110	2007-01-03	02:51:45.8785	078.B-0303(B)	Ks
NGC 2110	2007-01-03	02:52:35.9237	078.B-0303(B)	Ks
NGC 2110	2007-01-03	02:53:29.9559	078.B-0303(B)	Ks
NGC 2110	2007-01-03	02:54:20.6548	078.B-0303(B)	Ks
NGC 2110	2007-01-03	02:55:09.8860	078.B-0303(B)	Ks
NGC 2110	2007-01-03	02:56:00.0158	078.B-0303(B)	Ks
NGC 2110	2007-01-03	03:22:05.0696	078.B-0303(B)	Ks
NGC 2110	2007-01-03	03:23:34.4361	078.B-0303(B)	Ks
NGC 2110	2007-01-03	03:25:02.9489	078.B-0303(B)	Ks

Bibliography

S. Aalto, S. Garcia-Burillo, S. Muller, J. M. Winters, P. van der Werf, C. Henkel, F. Costagliola, and R. Neri. Detection of HCN, HCO+, and HNC in the Mrk 231 molecular outflow. Dense molecular gas in the AGN wind. *Astronomy and Astrophysics*, 537:A44, January 2012. ISSN 0004-6361.

Milton Abramowitz and Irene A Stegun. *Handbook of mathematical functions: with formulas, graphs, and mathematical tables*. Dover Publications, New York, 1970. ISBN 978-0-486-61272-0. OCLC: 18003605.

R. Antonucci. Unified models for active galactic nuclei and quasars. *Annual Review of Astronomy and Astrophysics*, 31:473–521, 1993.

R. R. J. Antonucci and J. S. Miller. Spectropolarimetry and the nature of NGC 1068. *The Astrophysical Journal*, 297:621–632, October 1985. ISSN 0004-637X.

K. A. Arnaud, G. Branduardi-Raymont, J. L. Culhane, A. C. Fabian, C. Hazard, T. A. McGlynn, R. A. Shafer, A. F. Tennant, and M. J. Ward. EXOSAT observations of a strong soft X-ray excess in MKN 841. *Monthly Notices of the Royal Astronomical Society*, 217:105–113, November 1985. ISSN 0035-8711.

Robin Arsenault, Jaime Alonso, Henri Bonnet, Joar Brynnel, Bernard Delabre, Robert Donaldson, Christophe Dupuy, Enrico Fedrigo, Jacopo Farinato, Norbert N. Hubin, L. Ivanescu, Markus E. Kasper, J. Paufique, S. Rossi, Sebastien Tordo, Stefan Stroebele, Jean-Luis Lizon, Pierre Gigan, Francoise Delplancke, A. Silber, Marco Quattri, and Roland Reiss. MACAO-VLTI: an adaptive optics system for the ESO Interferometer. In *Adaptive Optical System Technologies II*, volume 4839, pages 174–185. International Society for Optics and Photonics, February 2003.

D. Asmus. New evidence for the ubiquity of prominent polar dust emission in AGN on tens of parsec scales. *Monthly Notices of the Royal Astronomical Society*, 489:2177–2188, October 2019. ISSN 0035-8711.

D. Asmus, P. Gandhi, S. F. Hönig, A. Smette, and W. J. Duschl. The subarcsecond mid-infrared view of local active galactic nuclei - II. The mid-infrared-X-ray correlation. *Monthly Notices of the Royal Astronomical Society*, 454(1):766, November 2015.

D. Asmus, S. F. Hönig, and P. Gandhi. The Subarcsecond Mid-infrared View of Local Active Galactic Nuclei. III. Polar Dust Emission. *The Astrophysical Journal*, 822(2):109, 2016. ISSN 0004-637X.

D. Asmus, S. F. Hönig, P. Gandhi, A. Smette, and W. J. Duschl. The subarcsecond mid-infrared view of local active galactic nuclei - I. The N- and Q-band imaging atlas. *Monthly Notices of the Royal Astronomical Society*, 439:1648–1679, April 2014.

Astropy Collaboration, Thomas P. Robitaille, Erik J. Tollerud, Perry Greenfield, Michael Droettboom, Erik Bray, Tom Aldcroft, Matt Davis, Adam Ginsburg, Adrian M. Price-Whelan, Wolfgang E. Kerzendorf, Alexander Conley, Neil Crighton, Kyle Barbary, Demitri Muna, Henry Ferguson, Frédéric Grollier, Madhura M. Parikh, Prasanth H. Nair, Hans M. Unther, Christoph Deil, Julien Woillez, Simon Conseil, Roban Kramer, James E. H. Turner, Leo Singer, Ryan Fox, Benjamin A. Weaver, Victor Zabalza, Zachary I. Edwards, K. Azalee Bostroem, D. J. Burke, Andrew R. Casey, Steven M. Crawford, Nadia Dencheva, Justin Ely, Tim Jenness, Kathleen Labrie, Pey Lian Lim, Francesco Pierfederici, Andrew Pontzen, Andy Ptak, Brian Refsdal, Mathieu Servillat, and Ole Streicher. Astropy: A community Python package for astronomy. *Astronomy and Astrophysics*, 558:A33, October 2013. ISSN 0004-6361.

A. Audibert, F. Combes, S. García-Burillo, L. Hunt, A. Eckart, S. Aalto, V. Casasola, F. Boone, M. Krips, S. Viti, S. Muller, K. Dasyra, P. van der Werf, and S. Martín. ALMA captures feeding and feedback from the active galactic nucleus in NGC 613. *Astronomy and Astrophysics*, 632:A33, December 2019. ISSN 0004-6361.

Richard Barvainis. Hot dust and the near-infrared bump in the continuum spectra of quasars and active galactic nuclei. *The Astrophysical Journal*, 320:537–544, September 1987. ISSN 0004-637X.

D. Batcheldor, A. Robinson, D. J. Axon, S. Young, S. Quinn, J. E. Smith, J. Hough, and D. M. Alexander. NICMOS Polarimetry of "Polar-scattered" Seyfert 1 Galaxies. *The Astrophysical Journal*, 738(1):90, 2011. ISSN 0004-637X.

Jacques Maurice Beckers, Daniel Enard, Michel Faucherre, Fritz Merkle, G. P. Di Benedetto, R. Braun, R. Foy, Reinhard Genzel, Laurent Koechlin, and Gerd Weigelt. VLT interferometer: proposed implementation. In *Advanced Technology Optical Telescopes IV*, volume 1236, pages 108–124. International Society for Optics and Photonics, July 1990.

T. Beckert and W. J. Duschl. The dynamical state of a thick cloudy torus around an AGN. *Astronomy and Astrophysics*, 426:445–454, November 2004. ISSN 0004-6361.

N. Bennert, B. Jungwiert, S. Komossa, M. Haas, and R. Chini. Size and properties of the narrow-line region in Seyfert-1 galaxies from spatially-resolved optical spectroscopy. *Astronomy and Astrophysics*, 459(1):55, November 2006.

Stefano Bianchi, Roberto Maiolino, and Guido Risaliti. AGN Obscuration and the Unified Model. *Advances in Astronomy*, 2012:782030, 2012.

Larry Bradley, Brigitta Sipocz, Thomas Robitaille, Erik Tollerud, Zé Vinícius, Christoph Deil, Kyle Barbary, Hans Moritz Günther, Mihai Cara, Ivo Busko, Simon Conseil, Michael Droettboom, Azalee Bostroem, E. M. Bray, Lars Andersen Bratholm, Tom Wilson, Matt Craig, Geert Barentsen, Sergio Pascual, Axel Donath, Johnny Greco, Gabriel Perren, P. L. Lim, and Wolfgang Kerzendorf. astropy/photutils: v0.6, January 2019.

Bernhard R. Brandl, Rainer Lenzen, Eric Pantin, Alistair Glasse, Joris Blommaert, Michael Meyer, Manuel Guedel, Lars Venema, Frank Molster, Remko Stuik, Eva Schmalzl, Jeff Meisner, Emeric Le Floc'h, Wolfgang Brandner, Stefan Hippler, Ignas Snellen, and Klaus Pontoppidan. METIS: the thermal infrared instrument for the E-ELT. In *Ground-based and Airborne Instrumentation for Astronomy IV*, volume 8446, page 84461M. International Society for Optics and Photonics, September 2012.

L. Burtscher, W. Jaffe, D. Raban, K. Meisenheimer, K. R. W. Tristram, and H. Röttgering. Dust Emission from a Parsec-Scale Structure in the Seyfert 1 Nucleus of NGC 4151. *The Astrophysical Journal Letters*, 705:L53–L57, November 2009. ISSN 0004-637X.

L. Burtscher, K. Meisenheimer, K. R. W. Tristram, W. Jaffe, S. F. Hönig, R. I. Davies, M. Kishimoto, J.-U. Pott, H. Röttgering, M. Schartmann, G. Weigelt, and S. Wolf. A diversity of dusty AGN tori - Data release for the VLTI/MIDI AGN Large Program and first results for 23 galaxies. *Astronomy & Astrophysics*, 558:A149, October 2013. ISSN 0004-6361, 1432-0746.

Leonard Burtscher, Konrad R. W. Tristram, Walter J. Jaffe, and Klaus Meisenheimer. Observing faint targets with MIDI at the VLTI: the MIDI AGN large programme experience. In *Optical and Infrared Interferometry III*, volume 8445, page 84451G. International Society for Optics and Photonics, September 2012.

Michele Cappellari, N. Neumayer, J. Reunanen, P. P. van der Werf, P. T. de Zeeuw, and H.-W. Rix. The mass of the black hole in Centaurus A from SINFONI AO-assisted integral-field observations of stellar kinematics. *Monthly Notices of the Royal Astronomical Society*, 394 (2):660, April 2009.

Chi-Ho Chan and Julian H. Krolik. RADIATION-DRIVEN OUTFLOWS FROM AND RADIATIVE SUPPORT IN DUSTY TORI OF ACTIVE GALACTIC NUCLEI. *The Astrophysical Journal*, 825(1):67, June 2016. ISSN 0004-637X.

Chi-Ho Chan and Julian H. Krolik. Geometrically Thick Obscuration by Radiation-driven Outflow from Magnetized Tori of Active Galactic Nuclei. *The Astrophysical Journal*, 843(1):58, July 2017. ISSN 0004-637X.

R. Cid Fernandes, Q. Gu, J. Melnick, E. Terlevich, R. Terlevich, D. Kunth, R. Rodrigues Lacerda, and B. Joguet. The star formation history of Seyfert 2 nuclei. *Monthly Notices of the Royal Astronomical Society*, 355(1):273, November 2004.

Michele Cirasuolo. Extremely Large Telescope(s). In *The Very Large Telescope in 2030*, page 16, July 2019. Conference Name: The Very Large Telescope in 2030.

J. Clavel, W. Wamsteker, and I. S. Glass. Hot dust on the outskirts of the broad-line region in Fairall 9. *The Astrophysical Journal*, 337:236–250, February 1989. ISSN 0004-637X.

Martin Cohen, Russell G. Walker, Brian Carter, Peter Hammersley, Mark Kidger, Kunio Noguchi, Martin Cohen, Russell G. Walker, Brian Carter, Peter Hammersley, Mark Kidger, and Kunio Noguchi. Spectral Irradiance Calibration in the Infrared. X. A Self-Consistent Radiometric All-Sky Network of Absolutely Calibrated Stellar Spectra, Spectral Irradiance Calibration in the Infrared. X. A Self-Consistent Radiometric All-Sky Network of Absolutely Calibrated Stellar Spectra. *The Astronomical Journal, The Astronomical Journal*, 117, 117: 1864, 1864, April 1999.

M. M. Colavita, P. L. Wizinowich, R. L. Akeson, S. Ragland, J. M. Woillez, R. Millan-Gabet, E. Serabyn, M. Abajian, D. S. Acton, E. Appleby, J. W. Beletic, C. A. Beichman, J. Bell, B. C. Berkey, J. Berlin, A. F. Boden, A. J. Booth, R. Boutell, F. H. Chaffee, D. Chan, J. Chin, J. Chock, R. Cohen, A. Cooper, S. L. Crawford, M. J. Creech-Eakman, W. Dahl, G. Eychaner, J. L. Fanson, C. Felizardo, J. I. Garcia-Gathright, J. T. Gathright, G. Hardy, H. Henderson, J. S. Herstein, M. Hess, E. E. Hovland, M. A. Hrynevych, E. Johansson, R. L. Johnson, J. Kelley, R. Kendrick, C. D. Koresko, P. Kurpis, D. Le Mignant, H. A. Lewis, E. R. Ligon, W. Lupton, D. McBride, D. W. Medeiros, B. P. Mennesson, J. D. Moore, D. Morrison, C. Nance, C. Neyman, A. Niessner, C. G. Paine, D. L. Palmer, T. Panteleeva, M. Papin, B. Parvin, L. Reder, A. Rudeen, T. Saloga, A. Sargent, M. Shao, B. Smith, R. F. Smythe, P. Stomski, K. R. Summers, M. R. Swain, P. Swanson, R. Thompson, K. Tsubota, A. Tumminello, C. Tyau, G. T. van Belle, G. Vasisht, J. Vause, F. Vescelus, J. Walker, J. K. Wallace, U. Wehmeier, and E. Wetherell. The Keck Interferometer. *Publications of the Astronomical Society of the Pacific*, 125(932):1226, October 2013. ISSN 1538-3873.

F. Combes, S. García-Burillo, A. Audibert, L. Hunt, A. Eckart, S. Aalto, V. Casasola, F. Boone, M. Krips, S. Viti, K. Sakamoto, S. Muller, K. Dasyra, P. van der Werf, and S. Martin. ALMA observations of molecular tori around massive black holes. *Astronomy & Astrophysics*, 623: A79, March 2019. ISSN 0004-6361, 1432-0746.

R. Davies, D. Mark, and A. Sternberg. Dense molecular gas around AGN: HCN/CO in NGC 3227. *Astronomy and Astrophysics*, 537:A133, January 2012. ISSN 0004-6361.

R. I. Davies, F. Müller Sánchez, R. Genzel, L. J. Tacconi, E. K. S. Hicks, S. Friedrich, and A. Sternberg. A Close Look at Star Formation around Active Galactic Nuclei. *The Astrophysical Journal*, 671:1388–1412, December 2007. ISSN 0004-637X.

Kelly D. Denney, Misty C. Bentz, Bradley M. Peterson, Richard W. Pogge, Edward M. Cackett, Matthias Dietrich, Jeffrey K. J. Fogel, Himel Ghosh, Keith D. Horne, Charles Kuehn, Takeo Minezaki, Christopher A. Onken, Vladimir I. Pronik, Douglas O. Richstone, Sergey G. Sergeev, Marianne Vestergaard, Matthew G. Walker, and Yuzuru Yoshii. The Mass of the

Black Hole in the Seyfert 1 Galaxy NGC 4593 from Reverberation Mapping. *The Astrophysical Journal*, 653(1):152–158, December 2006. ISSN 0004-637X.

Mark Durré and Jeremy Mould. The AGN Ionization Cones of NGC 5728. I. Excitation and Nuclear Structure. *The Astrophysical Journal*, 867(2):149, November 2018. ISSN 0004-637X. Publisher: American Astronomical Society.

R. A. Edelson and M. A. Malkan. Spectral Energy Distributions of Active Galactic Nuclei between 0.1 and 100 Microns. *The Astrophysical Journal*, 308:59, September 1986. ISSN 0004-637X.

Martin Elvis, Belinda J. Wilkes, Jonathan C. McDowell, Richard F. Green, Jill Bechtold, S. P. Willner, M. S. Oey, Elisha Polomski, and Roc Cutri. Atlas of Quasar Energy Distributions. *The Astrophysical Journal Supplement Series*, 95:1, November 1994.

A. C. Fabian, R. V. Vasudevan, and P. Gandhi. The effect of radiation pressure on dusty absorbing gas around active galactic nuclei. *Monthly Notices of the Royal Astronomical Society*, 385 (1):L43, March 2008.

Edward Arthur Fath. The spectra of some spiral nebulae and globular star clusters. *Lick Observatory Bulletin*, 149:71, 1909.

J. A. Fernández-Ontiveros, N. López-Gonzaga, M. A. Prieto, J. A. Acosta-Pulido, E. Lopez-Rodriguez, D. Asmus, and K. R. W. Tristram. A compact jet at the infrared heart of the prototypical low-luminosity AGN in NGC 1052. *Monthly Notices of the Royal Astronomical Society*, 485(4):5377, June 2019.

J. A. Fernández-Ontiveros, K. R. W. Tristram, S. Hönig, P. Gandhi, and G. Weigelt. Embedded AGN and star formation in the central 80 pc of IC 3639. *Astronomy and Astrophysics*, 611: A46, March 2018.

T. C. Fischer, D. M. Crenshaw, S. B. Kraemer, and H. R. Schmitt. Determining Inclinations of Active Galactic Nuclei via their Narrow-line Region Kinematics. I. Observational Results. *The Astrophysical Journal Supplement Series*, 209:1, November 2013. ISSN 0067-0049.

Daniel Foreman-Mackey. corner.py: Scatterplot matrices in Python. *The Journal of Open Source Software*, 1(2):1864–1889, June 2016.

Daniel Foreman-Mackey, David W. Hogg, Dustin Lang, and Jonathan Goodman. emcee: The MCMC Hammer. *Publications of the Astronomical Society of the Pacific*, 125:306, March 2013. ISSN 0004-6280.

Matteo Fossati, Michele Fumagalli, Alessandro Boselli, Giuseppe Gavazzi, Ming Sun, and David J. Wilman. MUSE sneaks a peek at extreme ram-pressure stripping events - II. The physical properties of the gas tail of ESO137-001. *Monthly Notices of the Royal Astronomical Society*, 455:2028–2041, January 2016. ISSN 0035-8711.

J. Frank, A. King, and D. Raine. Accretion power in astrophysics. *Camb. Astrophys. Ser.*, 21, 1992.

D. L. Fried. Probability of getting a lucky short-exposure image through turbulence. *Journal of the Optical Society of America (1917-1983)*, 68:1651–1658, December 1978. ISSN 0030-3941.

Jack F. Gallimore, Moshe Elitzur, Roberto Maiolino, Alessandro Marconi, Christopher P. O'Dea, Dieter Lutz, Stefi A. Baum, Robert Nikutta, C. M. V. Impellizzeri, Richard Davies, Amy E. Kimball, and Eleonora Sani. HIGH-VELOCITY BIPOLAR MOLECULAR EMISSION FROM AN AGN TORUS. *The Astrophysical Journal*, 829(1):L7, September 2016. ISSN 2041-8205.

P. Gandhi, H. Horst, A. Smette, S. Hönig, A. Comastri, R. Gilli, C. Vignali, and W. Duschl. Resolving the mid-infrared cores of local Seyferts. *Astronomy & Astrophysics*, 502(2):457–472, August 2009. ISSN 0004-6361, 1432-0746.

A. Garcia-Rissmann, L. R. Vega, N. V. Asari, R. Cid Fernandes, H. Schmitt, R. M. González Delgado, and T. Storchi-Bergmann. An atlas of calcium triplet spectra of active galaxies. *Monthly Notices of the Royal Astronomical Society*, 359(2):765, May 2005.

S. García-Burillo, F. Combes, A. Usero, S. Aalto, M. Krips, S. Viti, A. Alonso-Herrero, L. K. Hunt, E. Schinnerer, A. J. Baker, F. Boone, V. Casasola, L. Colina, F. Costagliola, A. Eckart, A. Fuente, C. Henkel, A. Labiano, S. Martín, I. Márquez, S. Muller, P. Planesas, C. Ramos Almeida, M. Spaans, L. J. Tacconi, and P. P. van der Werf. Molecular line emission in NGC 1068 imaged with ALMA. I. An AGN-driven outflow in the dense molecular gas. *Astronomy and Astrophysics*, 567:A125, July 2014. ISSN 0004-6361.

I. M. George and A. C. Fabian. X-ray reflection from cold matter in active galactic nuclei and X-ray binaries. *Monthly Notices of the Royal Astronomical Society*, 249:352–367, March 1991. ISSN 0035-8711.

I. S. Glass. Infrared variability of the Seyfert galaxy NGC 3783. *Monthly Notices of the Royal Astronomical Society*, 256:23P–27P, May 1992. ISSN 0035-8711.

Jonathan Goodman and Jonathan Weare. Ensemble samplers with affine invariance. *Communications in Applied Mathematics and Computational Science*, 5(1):65–80, January 2010. ISSN 2157-5452.

GRAVITY Collaboration. An Image of the Dust Sublimation Region in the Nucleus of NGC 1068. *The Messenger*, 178:24–26, December 2019. ISSN 0722-6691.

GRAVITY Collaboration, R. Abuter, M. Accardo, A. Amorim, N. Anugu, G. Ávila, N. Azouaoui, M. Benisty, J. P. Berger, N. Blind, H. Bonnet, P. Bourget, W. Brandner, R. Brast, A. Buron, L. Burtscher, F. Cassaing, F. Chapron, É. Choquet, Y. Clénet, C. Collin, V. Coudé Du Foresto, W. de Wit, P. T. de Zeeuw, C. Deen, F. Delplancke-Ströbele, R. Dembet, F. Derie,

J. Dexter, G. Duvert, M. Ebert, A. Eckart, F. Eisenhauer, M. Esselborn, P. Fédou, G. Finger, P. Garcia, C. E. Garcia Dabo, R. Garcia Lopez, E. Gendron, R. Genzel, S. Gillessen, F. Gonte, P. Gordo, M. Grould, U. Grözinger, S. Guieu, P. Haguenauer, O. Hans, X. Haubois, M. Haug, F. Haussmann, Th. Henning, S. Hippler, M. Horrobin, A. Huber, Z. Hubert, N. Hubin, C. A. Hummel, G. Jakob, A. Janssen, L. Jochum, L. Jocou, A. Kaufer, S. Kellner, S. Kendrew, L. Kern, P. Kervella, M. Kiekebusch, R. Klein, Y. Kok, J. Kolb, M. Kulas, S. Lacour, V. Lapeyrère, B. Lazareff, J.-B. Le Bouquin, P. Lèna, R. Lenzen, S. Lévêque, M. Lippa, Y. Magnard, L. Mehrgan, M. Mellein, A. Mérand, J. Moreno-Ventas, T. Moulin, E. Müller, F. Müller, U. Neumann, S. Oberti, T. Ott, L. Pallanca, J. Panduro, L. Pasquini, T. Paumard, I. Percheron, K. Perraut, G. Perrin, A. Pflüger, O. Pfuhl, T. Phan Duc, P. M. Plewa, D. Popovic, S. Rabien, A. Ramírez, J. Ramos, C. Rau, M. Riquelme, R.-R. Rohloff, G. Rousset, J. Sanchez-Bermudez, S. Scheithauer, M. Schöller, N. Schuhler, J. Spyromilio, C. Straubmeier, E. Sturm, M. Suarez, K. R. W. Tristram, N. Ventura, F. Vincent, I. Waisberg, I. Wank, J. Weber, E. Wieprecht, M. Wiest, E. Wiezorrek, M. Wittkowski, J. Woillez, B. Wolff, S. Yazici, D. Ziegler, and G. Zins. First light for GRAVITY: Phase referencing optical interferometry for the Very Large Telescope Interferometer. *Astronomy and Astrophysics*, 602:A94, June 2017. ISSN 0004-6361.

GRAVITY Collaboration, R. Abuter, A. Amorim, N. Anugu, M. Bauböck, M. Benisty, J. P. Berger, N. Blind, H. Bonnet, W. Brandner, A. Buron, C. Collin, F. Chapron, Y. Clénet, V. Coudé Du Foresto, P. T. de Zeeuw, C. Deen, F. Delplancke-Ströbele, R. Dembet, J. Dexter, G. Duvert, A. Eckart, F. Eisenhauer, G. Finger, N. M. Förster Schreiber, P. Fédou, P. Garcia, R. Garcia Lopez, F. Gao, E. Gendron, R. Genzel, S. Gillessen, P. Gordo, M. Habibi, X. Haubois, M. Haug, F. Haußmann, Th. Henning, S. Hippler, M. Horrobin, Z. Hubert, N. Hubin, A. Jimenez Rosales, L. Jochum, K. Jocou, A. Kaufer, S. Kellner, S. Kendrew, P. Kervella, Y. Kok, M. Kulas, S. Lacour, V. Lapeyrère, B. Lazareff, J.-B. Le Bouquin, P. Léna, M. Lippa, R. Lenzen, A. Mérand, E. Müler, U. Neumann, T. Ott, L. Palanca, T. Paumard, L. Pasquini, K. Perraut, G. Perrin, O. Pfuhl, P. M. Plewa, S. Rabien, A. Ramírez, J. Ramos, C. Rau, G. Rodríguez-Coira, R.-R. Rohloff, G. Rousset, J. Sanchez-Bermudez, S. Scheithauer, M. Schöller, N. Schuler, J. Spyromilio, O. Straub, C. Straubmeier, E. Sturm, L. J. Tacconi, K. R. W. Tristram, F. Vincent, S. von Fellenberg, I. Wank, I. Waisberg, F. Widmann, E. Wieprecht, M. Wiest, E. Wiezorrek, J. Woillez, S. Yazici, D. Ziegler, and G. Zins. Detection of the gravitational redshift in the orbit of the star S2 near the Galactic centre massive black hole. *Astronomy and Astrophysics*, 615:L15, July 2018a. ISSN 0004-6361.

GRAVITY Collaboration, J. Dexter, J. Shangguan, S. Hönig, M. Kishimoto, D. Lutz, H. Netzer, R. Davies, E. Sturm, O. Pfuhl, A. Amorim, M. Bauböck, W. Brandner, Y. Clénet, P. T. de Zeeuw, A. Eckart, F. Eisenhauer, N. M. Förster Schreiber, F. Gao, P. J. V. Garcia, R. Genzel, S. Gillessen, D. Gratadour, A. Jiménez-Rosales, S. Lacour, F. Millour, T. Ott, T. Paumard, K. Perraut, G. Perrin, B. M. Peterson, P. O. Petrucci, M. A. Prieto, D. Rouan, M. Schartmann, T. Shimizu, A. Sternberg, O. Straub, C. Straubmeier, L. J. Tacconi, K. Tristram, P. Vermot, I. Waisberg, F. Widmann, and J. Woillez. The resolved size and structure of hot dust in the immediate vicinity of AGN. *arXiv e-prints*, 1910:arXiv:1910.00593, October 2019.

Gravity Collaboration, O. Pfuhl, R. Davies, J. Dexter, H. Netzer, S. Hönig, D. Lutz, M. Schartmann, E. Sturm, A. Amorim, W. Brandner, Y. Clénet, P. T. de Zeeuw, A. Eckart, F. Eisenhauer, N. M. Förster Schreiber, F. Gao, P. J. V. Garcia, R. Genzel, S. Gillessen, D. Gratadour, M. Kishimoto, S. Lacour, F. Millour, T. Ott, T. Paumard, K. Perraut, G. Perrin, B. M. Peterson, P. O. Petrucci, M. A. Prieto, D. Rouan, J. Shangguan, T. Shimizu, A. Sternberg, O. Straub, C. Straubmeier, L. J. Tacconi, K. R. W. Tristram, P. Vermot, I. Waisberg, F. Widmann, and J. Woillez. An image of the dust sublimation region in the nucleus of NGC 1068. *Astronomy and Astrophysics*, 634:A1, February 2020. ISSN 0004-6361.

GRAVITY Collaboration, E. Sturm, J. Dexter, O. Pfuhl, M. R. Stock, R. I. Davies, D. Lutz, Y. Clénet, A. Eckart, F. Eisenhauer, R. Genzel, D. Gratadour, S. F. Hönig, M. Kishimoto, S. Lacour, F. Millour, H. Netzer, G. Perrin, B. M. Peterson, P. O. Petrucci, D. Rouan, I. Waisberg, J. Woillez, A. Amorim, W. Brandner, N. M. Förster Schreiber, P. J. V. Garcia, S. Gillessen, T. Ott, T. Paumard, K. Perraut, S. Scheithauer, C. Straubmeier, L. J. Tacconi, and F. Widmann. Spatially resolved rotation of the broad-line region of a quasar at sub-parsec scale. *Nature*, 563:657–660, November 2018b. ISSN 0028-0836.

L. J. Greenhill, R. S. Booth, S. P. Ellingsen, J. R. Herrnstein, D. L. Jauncey, P. M. McCulloch, J. M. Moran, R. P. Norris, J. E. Reynolds, and A. K. Tzioumis. A Warped Accretion Disk and Wide-Angle Outflow in the Inner Parsec of the Circinus Galaxy. *The Astrophysical Journal*, 590(1):162, June 2003.

Q. Gu, J. Melnick, R. Cid Fernandes, D. Kunth, E. Terlevich, and R. Terlevich. Emission-line properties of Seyfert 2 nuclei. *Monthly Notices of the Royal Astronomical Society*, 366(2): 480, February 2006.

T. M. Heckman. An optical and radio survey of the nuclei of bright galaxies - Activity in normal galactic nuclei. *Astronomy and Astrophysics*, 87:152–164, July 1980. ISSN 0004-6361.

Ryan C. Hickox and David M. Alexander. Obscured Active Galactic Nuclei. *Annual Review of Astronomy and Astrophysics*, 56:625–671, September 2018. ISSN 0066-4146.

Luis C. Ho, Jenny E. Greene, Alexei V. Filippenko, and Wallace L. W. Sargent. A SEARCH FOR "DWARF" SEYFERT NUCLEI. VII. A CATALOG OF CENTRAL STELLAR VELOCITY DISPERSIONS OF NEARBY GALAXIES. *The Astrophysical Journal Supplement Series*, 183(1):1–16, June 2009. ISSN 0067-0049.

S. F. Hönig, M. Kishimoto, R. Antonucci, A. Marconi, M. A. Prieto, K. Tristram, and G. Weigelt. Parsec-scale Dust Emission from the Polar Region in the Type 2 Nucleus of NGC 424. *The Astrophysical Journal*, 755(2):149, 2012. ISSN 0004-637X.

S. F. Hönig, M. Kishimoto, P. Gandhi, A. Smette, D. Asmus, W. Duschl, M. Polletta, and G. Weigelt. The dusty heart of nearby active galaxies. I. High-spatial resolution mid-IR spectro-photometry of Seyfert galaxies. *Astronomy and Astrophysics*, 515:A23, June 2010.

Sebastian F. Hönig. Redefining the Torus: A Unifying View of AGNs in the Infrared and Submillimeter. *The Astrophysical Journal*, 884:171, October 2019. ISSN 0004-637X.

Sebastian F. Hönig and Makoto Kishimoto. Dusty Winds in Active Galactic Nuclei: Reconciling Observations with Models. *The Astrophysical Journal Letters*, 838(2):L20, 2017. ISSN 2041-8205.

Sebastian F. Hönig, Makoto Kishimoto, Konrad RW Tristram, M. Almudena Prieto, Poshak Gandhi, Daniel Asmus, Robert Antonucci, Leonard Burtscher, Wolfgang J. Duschl, and Gerd Weigelt. Dust in the polar region as a major contributor to the infrared emission of active galactic nuclei. *The Astrophysical Journal*, 771(2):87, 2013.

Sebastian F. Hönig, Darach Watson, Makoto Kishimoto, and Jens Hjorth. A dust-parallax distance of 19 megaparsecs to the supermassive black hole in NGC 4151. *Nature*, 515(7528): 528–530, November 2014. ISSN 0028-0836.

Walter J. Jaffe. Coherent fringe tracking and visibility estimation for MIDI. In *New Frontiers in Stellar Interferometry*, volume 5491, pages 715–725. International Society for Optics and Photonics, October 2004.

J. J. Jensen, S. F. Hönig, S. Rakshit, A. Alonso-Herrero, D. Asmus, P. Gandhi, M. Kishimoto, A. Smette, and K. R. W. Tristram. PAH features within few hundred parsecs of active galactic nuclei. *Monthly Notices of the Royal Astronomical Society*, 470(3):3071–3094, September 2017. ISSN 0035-8711.

W. C. Keel. Spectroscopic evidence for activity in the nuclei of normal spiral galaxies. *The Astrophysical Journal*, 269:466–486, June 1983. ISSN 0004-637X.

Florian Kerber, Hans Ulrich Käufl, Konrad Tristram, Daniel Asmus, Pedro Baksai, Nicola Di Lieto, Danuta Dobrzycka, Philippe Duhoux, Gert Finger, Christian Hummel, Derek Ives, Gerd Jakob, Lars Lundin, Dimitri Mawet, Leander Mehrgan, Eric Pantin, Miguel Riquelme, Joel Sanchez, Stefan Sandrock, Ralf Siebenmorgen, Jörg Stegmeier, Alain Smette, Julian Taylor, Mario van den Ancker, Guillermo Valdes, Lars Venema, Florian Kerber, Hans Ulrich Käufl, Konrad Tristram, Daniel Asmus, Pedro Baksai, Nicola Di Lieto, Danuta Dobrzycka, Philippe Duhoux, Gert Finger, Christian Hummel, Derek Ives, Gerd Jakob, Lars Lundin, Dimitri Mawet, Leander Mehrgan, Eric Pantin, Miguel Riquelme, Joel Sanchez, Stefan Sandrock, Ralf Siebenmorgen, Jörg Stegmeier, Alain Smette, Julian Taylor, Mario van den Ancker, Guillermo Valdes, and Lars Venema. VISIR upgrade overview: all's well that ends well, VISIR upgrade overview: all's well that ends well. *Society of Photo-Optical Instrumentation Engineers (SPIE) Conference Series, Society of Photo-Optical Instrumentation Engineers (SPIE) Conference Series*, 9908, 9908:99080D, 99080D, August 2016.

E. Ye Khachikian and D. W. Weedman. An atlas of Seyfert galaxies. *The Astrophysical Journal*, 192:581, September 1974.

M. Kishimoto, S. F. Hönig, R. Antonucci, R. Barvainis, T. Kotani, K. R. W. Tristram, G. Weigelt, and K. Levin. The innermost dusty structure in active galactic nuclei as probed by the Keck interferometer. *Astronomy and Astrophysics*, 527:A121, March 2011a.

M. Kishimoto, S. F. Hönig, R. Antonucci, T. Kotani, R. Barvainis, K. R. W. Tristram, and G. Weigelt. Exploring the inner region of type 1 AGNs with the Keck interferometer. *Astronomy & Astrophysics*, 507(3):L57–L60, December 2009. ISSN 0004-6361, 1432-0746.

M. Kishimoto, S. F. Hönig, R. Antonucci, F. Millour, K. R. W. Tristram, and G. Weigelt. Mapping the radial structure of AGN tori. *Astronomy \& Astrophysics*, 536:A78, December 2011b. ISSN 0004-6361, 1432-0746.

M. Kishimoto, S. F. Hönig, T. Beckert, and G. Weigelt. The innermost region of AGN tori: implications from the HST/NICMOS type 1 point sources and near-IR reverberation. *Astronomy and Astrophysics*, 476(2):713, December 2007.

Michael Koss, Benny Trakhtenbrot, Claudio Ricci, Isabella Lamperti, Kyuseok Oh, Simon Berney, Kevin Schawinski, Mislav Baloković, Linda Baronchelli, D. Michael Crenshaw, Travis Fischer, Neil Gehrels, Fiona Harrison, Yasuhiro Hashimoto, Drew Hogg, Kohei Ichikawa, Nicola Masetti, Richard Mushotzky, Lia Sartori, Daniel Stern, Ezequiel Treister, Yoshihiro Ueda, Sylvain Veilleux, and Lisa Winter. BAT AGN Spectroscopic Survey. I. Spectral Measurements, Derived Quantities, and AGN Demographics. *The Astrophysical Journal*, 850(1):74, November 2017.

H. A. Krimm, S. T. Holland, R. H. D. Corbet, A. B. Pearlman, P. Romano, J. A. Kennea, J. S. Bloom, S. D. Barthelmy, W. H. Baumgartner, J. R. Cummings, N. Gehrels, A. Y. Lien, C. B. Markwardt, D. M. Palmer, T. Sakamoto, M. Stamatikos, and T. N. Ukwatta. The Swift/BAT Hard X-Ray Transient Monitor. *The Astrophysical Journal Supplement Series*, 209(1):14, November 2013.

Jerome Kristian. Quasars as Events in the Nuclei of Galaxies: the Evidence from Direct Photographs. *The Astrophysical Journal Letters*, 179:L61, January 1973. ISSN 0004-637X.

Julian H. Krolik. Active galactic nuclei : from the central black hole to the galactic environment. *Princeton University Press*, 1999.

Julian H. Krolik and Mitchell C. Begelman. Molecular tori in Seyfert galaxies - Feeding the monster and hiding it. *The Astrophysical Journal*, 329:702–711, June 1988. ISSN 0004-637X.

H. U. Käufl, F. Kerber, D. Asmus, P. Baksai, N. Di Lieto, P. Duhoux, S. Heikamp, C. Hummel, D. Ives, G. Jakob, J.-P. Kirchbauer, L. Mehrgan, Y. Momany, E. Pantin, E. Pozna, M. Riquelme, S. Sandrock, R. Siebenmorgen, A. Smette, J. Stegmeier, J. Taylor, K. Tristram, G. Valdes, M. van den Ancker, U. Weilenmann, B. Wolff, H. U. Käufl, F. Kerber, D. Asmus, P. Baksai, N. Di Lieto, P. Duhoux, S. Heikamp, C. Hummel, D. Ives, G. Jakob, J.-P. Kirchbauer, L. Mehrgan, Y. Momany, E. Pantin, E. Pozna, M. Riquelme, S. Sandrock,

R. Siebenmorgen, A. Smette, J. Stegmeier, J. Taylor, K. Tristram, G. Valdes, M. van den Ancker, U. Weilenmann, and B. Wolff. The Return of the Mid-infrared to the VLT: News from the VISIR Upgrade, The Return of the Mid-infrared to the VLT: News from the VISIR Upgrade. *The Messenger, The Messenger*, 159, 159:15, 15, March 2015.

S. Lacour, R. Dembet, R. Abuter, P. Fédou, G. Perrin, É Choquet, O. Pfuhl, F. Eisenhauer, J. Woillez, F. Cassaing, E. Wieprecht, T. Ott, E. Wiezorrek, K. R. W. Tristram, B. Wolff, A. Ramírez, X. Haubois, K. Perraut, C. Straubmeier, W. Brandner, and A. Amorim. The GRAVITY fringe tracker. *Astronomy and Astrophysics*, 624:A99, April 2019.

P. O. Lagage, J. W. Pel, M. Authier, J. Belorgey, A. Claret, C. Doucet, D. Dubreuil, G. Durand, E. Elswijk, P. Girardot, H. U. Käufl, G. Kroes, M. Lortholary, Y. Lussignol, M. Marchesi, E. Pantin, R. Peletier, J.-F. Pirard, J. Pragt, Y. Rio, T. Schoenmaker, R. Siebenmorgen, A. Silber, A. Smette, M. Sterzik, C. Veyssiere, P. O. Lagage, J. W. Pel, M. Authier, J. Belorgey, A. Claret, C. Doucet, D. Dubreuil, G. Durand, E. Elswijk, P. Girardot, H. U. Käufl, G. Kroes, M. Lortholary, Y. Lussignol, M. Marchesi, E. Pantin, R. Peletier, J.-F. Pirard, J. Pragt, Y. Rio, T. Schoenmaker, R. Siebenmorgen, A. Silber, A. Smette, M. Sterzik, and C. Veyssiere. Successful Commissioning of VISIR: The Mid-Infrared VLT Instrument, Successful Commissioning of VISIR: The Mid-Infrared VLT Instrument. *The Messenger, The Messenger*, 117, 117:12, 12, September 2004.

James H. Leftley, Sebastian F. Hönig, Daniel Asmus, Konrad R. W. Tristram, Poshak Gandhi, Makoto Kishimoto, Marta Venanzi, and David J. Williamson. Parsec-scale Dusty Winds in Active Galactic Nuclei: Evidence for Radiation Pressure Driving. *The Astrophysical Journal*, 886:55, November 2019. ISSN 0004-637X.

James H. Leftley, Konrad R. W. Tristram, Sebastian F. Hönig, Makoto Kishimoto, Daniel Asmus, and Poshak Gandhi. New Evidence for the Dusty Wind Model: Polar Dust and a Hot Core in the Type-1 Seyfert ESO 323-G77. *The Astrophysical Journal*, 862(1):17, 2018. ISSN 0004-637X.

Ch Leinert, U. Graser, F. Przygodda, L. B. F. M. Waters, G. Perrin, W. Jaffe, B. Lopez, E. J. Bakker, A. Böhm, O. Chesneau, W. D. Cotton, S. Damstra, J. de Jong, A. W. Glazenborg-Kluttig, B. Grimm, H. Hanenburg, W. Laun, R. Lenzen, S. Ligori, R. J. Mathar, J. Meisner, S. Morel, W. Morr, U. Neumann, J.-W. Pel, P. Schuller, R.-R. Rohloff, B. Stecklum, C. Storz, O. von der Lühe, and K. Wagner. MIDI – the 10 μm instrument on the VLTI. *Astrophysics and Space Science*, 286(1-2):73–83, August 2003. ISSN 0004-640X, 1572-946X.

Rainer Lenzen, Markus Hartung, Wolfgang Brandner, Gert Finger, Norbert N. Hubin, Francois Lacombe, Anne-Marie Lagrange, Matthew D. Lehnert, Alan F. M. Moorwood, and David Mouillet. NAOS-CONICA first on-sky results in a variety of observing modes. In *Instrument Design and Performance for Optical/Infrared Ground-based Telescopes*, volume 4841, pages 944–952. International Society for Optics and Photonics, March 2003.

E. P. T. Liang and K. A. Thompson. Models of unsaturated Compton disks around supermassive black holes. *Monthly Notices of the Royal Astronomical Society*, 189:421–432, November 1979. ISSN 0035-8711.

G. Lodato and G. Bertin. Non-Keplerian rotation in the nucleus of NGC 1068: Evidence for a massive accretion disk? *Astronomy and Astrophysics*, 398:517, February 2003.

B. Lopez, S. Lagarde, W. Jaffe, R. Petrov, M. Schöller, P. Antonelli, U. Beckmann, P. Berio, F. Bettonvil, A. Glindemann, J.-C. Gonzalez, U. Graser, K.-H. Hofmann, F. Millour, S. Robbe-Dubois, L. Venema, S. Wolf, T. Henning, T. Lanz, G. Weigelt, T. Agocs, C. Bailet, Y. Bresson, P. Bristow, M. Dugué, M. Heininger, G. Kroes, W. Laun, M. Lehmitz, U. Neumann, J.-C. Augereau, G. Avila, J. Behrend, G. van Belle, J.-P. Berger, R. van Boekel, S. Bonhomme, P. Bourget, R. Brast, J.-M. Clausse, C. Connot, R. Conzelmann, P. Cruzalèbes, G. Csepany, W. Danchi, M. Delbo, F. Delplancke, C. Dominik, A. van Duin, E. Elswijk, Y. Fantei, G. Finger, A. Gabasch, J. Gay, P. Girard, V. Girault, P. Gitton, A. Glazenborg, F. Gonté, F. Guitton, S. Guniat, M. De Haan, P. Haguenauer, H. Hanenburg, M. Hogerheijde, R. ter Horst, J. Hron, Y. Hugues, C. Hummel, J. Idserda, D. Ives, G. Jakob, A. Jasko, P. Jolley, S. Kiraly, R. Köhler, J. Kragt, T. Kroener, S. Kuindersma, L. Labadie, C. Leinert, R. Le Poole, J.-L. Lizon, C. Lucuix, A. Marcotto, F. Martinache, G. Martinot-Lagarde, R. Mathar, A. Matter, N. Mauclert, L. Mehrgan, A. Meilland, K. Meisenheimer, J. Meisner, M. Mellein, S. Menardi, J.-L. Menut, A. Merand, S. Morel, L. Mosoni, R. Navarro, E. Nussbaum, S. Ottogalli, R. Palsa, J. Panduro, E. Pantin, T. Parra, I. Percheron, T. P. Duc, J.-U. Pott, E. Pozna, F. Przygodda, Y. Rabbia, A. Richichi, F. Rigal, R. Roelfsema, G. Rupprecht, D. Schertl, C. Schmidt, N. Schuhler, M. Schuil, A. Spang, J. Stegmeier, L. Thiam, N. Tromp, F. Vakili, M. Vannier, K. Wagner, and J. Woillez. An Overview of the MATISSE Instrument — Science, Concept and Current Status. *The Messenger*, 157:5–12, September 2014. ISSN 0722-6691.

N. López-Gonzaga, L. Burtscher, K. R. W. Tristram, K. Meisenheimer, and M. Schartmann. Mid-infrared interferometry of 23 AGN tori: On the significance of polar-elongated emission. *Astronomy & Astrophysics*, 591:A47, July 2016. ISSN 0004-6361, 1432-0746.

N. López-Gonzaga, W. Jaffe, L. Burtscher, K. R. W. Tristram, and K. Meisenheimer. Revealing the large nuclear dust structures in NGC 1068 with MIDI/VLTI. *Astronomy and Astrophysics*, 565:A71, May 2014.

Dmitry Makarov, Philippe Prugniel, Nataliya Terekhova, Hélène Courtois, and Isabelle Vauglin. HyperLEDA. III. The catalogue of extragalactic distances. *Astronomy & Astrophysics*, 570: A13, October 2014. ISSN 0004-6361, 1432-0746.

A.P. Marschern. Jets in Active Galactic Nuclei. In Tomaso Belloni, editor, *The Jet Paradigm: From Microquasars to Quasars*, Lecture Notes in Physics, pages 173–201. Springer, Berlin, Heidelberg, 2010. ISBN 978-3-540-76937-8.

J. P. McMullin, B. Waters, D. Schiebel, W. Young, and K. Golap. CASA Architecture and Applications. In *Astronomical Data Analysis Software and Systems XVI*, volume 376, page 127. ASP Conference Series, October 2007.

K. Meisenheimer, K. R. W. Tristram, W. Jaffe, F. Israel, N. Neumayer, D. Raban, H. Röttgering, W. D. Cotton, U. Graser, Th Henning, Ch Leinert, B. Lopez, G. Perrin, and A. Prieto. Resolving the innermost parsec of Centaurus A at mid-infrared wavelengths. In *Astronomy and Astrophysics*, volume 471, page 453. ASP Conference Series, August 2007.

A. A. Michelson and E. W. Morley. On the relative motion of the Earth and the luminiferous ether. *American Journal of Science*, Series 3 Vol. 34(203):333–345, November 1887. ISSN 0002-9599, 1945-452X.

Florentin Millour, Eric Tatulli, Alain E. Chelli, Gilles Duvert, Gerard Zins, B. Acke, and Fabien Malbet. Data reduction for the AMBER instrument. In *New Frontiers in Stellar Interferometry*, volume 5491, pages 1222–1230. International Society for Optics and Photonics, October 2004.

Florentin Millour, Bruno Valat, Romain G. Petrov, and Martin Vannier. "Advanced" data reduction for the AMBER instrument. In *Optical and Infrared Interferometry*, volume 7013, page 701349. International Society for Optics and Photonics, July 2008.

A. Moorwood, J.-G. Cuby, P. Biereichel, J. Brynnel, B. Delabre, N. Devillard, A. van Dijsseldonk, G. Finger, H. Gemperlein, R. Gilmozzi, T. Herlin, G. Huster, J. Knudstrup, C. Lidman, J.-L. Lizon, H. Mehrgan, M. Meyer, G. Nicolini, M. Petr, J. Spyromilio, and J. Stegmeier. ISAAC sees first light at the VLT. *The Messenger*, 94:7, December 1998.

John S. Mulchaey, Andrew S. Wilson, and Zlatan Tsvetanov. An Emission-Line Imaging Survey of Early-Type Seyfert Galaxies. I. The Observations. *The Astrophysical Journal Supplement Series*, 102:309, February 1996. ISSN 0067-0049.

J. R. Mullaney, D. M. Alexander, A. D. Goulding, and R. C. Hickox. Defining the intrinsic AGN infrared spectral energy distribution and measuring its contribution to the infrared output of composite galaxies. *Monthly Notices of the Royal Astronomical Society*, 414(2):1082, June 2011.

Kazuyuki Muraoka, Miho Takeda, Kazuki Yanagitani, Hiroyuki Kaneko, Kouichiro Nakanishi, Nario Kuno, Kazuo Sorai, Tomoka Tosaki, and Kotaro Kohno. CO(J = 3-2) on-the-fly mapping of the nearby spiral galaxies NGC 628 and NGC 7793: Spatially resolved CO(J = 3-2) star-formation law. *Publications of the Astronomical Society of Japan*, 68:18, April 2016. ISSN 0004-6264.

F. Müller-Sánchez, M. A. Prieto, E. K. S. Hicks, H. Vives-Arias, R. I. Davies, M. Malkan, L. J. Tacconi, and R. Genzel. OUTFLOWS FROM ACTIVE GALACTIC NUCLEI: KINEMATICS OF THE NARROW-LINE AND CORONAL-LINE REGIONS IN SEYFERT GALAXIES,. *The Astrophysical Journal*, 739(2):69, September 2011. ISSN 0004-637X. Publisher: IOP Publishing.

Daisuke Namekata and Masayuki Umemura. Sub-parsec-scale dynamics of a dusty gas disc exposed to anisotropic AGN radiation with frequency-dependent radiative transfer. *Monthly Notices of the Royal Astronomical Society*, 460(1):980–1018, July 2016. ISSN 0035-8711.

Christopher A. Onken and Bradley M. Peterson. The Mass of the Central Black Hole in the Seyfert Galaxy NGC 3783. *The Astrophysical Journal*, 572(2):746–752, June 2002. ISSN 0004-637X.

D. E. Osterbrock. The spectrum of III ZW 77 : an unusual, high-ionization Seyfert 1 galaxy. *The Astrophysical Journal*, 246:696, June 1981.

D. E. Osterbrock and R. W. Pogge. The spectra of narrow-line Seyfert 1 galaxies. *The Astrophysical Journal*, 297:166–176, October 1985. ISSN 0004-637X.

Donald E. Osterbrock and Andre Martel. Spectroscopic study of the CfA sample of Seyfert galaxies. *The Astrophysical Journal*, 414:552–562, September 1993. ISSN 0004-637X.

F. Panessa and L. Bassani. Unabsorbed Seyfert 2 galaxies. *Astronomy and Astrophysics*, 394: 435, November 2002.

B. M. Peterson, L. Ferrarese, K. M. Gilbert, S. Kaspi, M. A. Malkan, D. Maoz, D. Merritt, H. Netzer, C. A. Onken, R. W. Pogge, M. Vestergaard, and A. Wandel. Central Masses and Broad-Line Region Sizes of Active Galactic Nuclei. II. A Homogeneous Analysis of a Large Reverberation-Mapping Database. *The Astrophysical Journal*, 613(2):682, October 2004. ISSN 0004-637X.

Bradley M. Peterson. An Introduction to Active Galactic Nuclei. *An introduction to active galactic nuclei*, February 1997.

R. G. Petrov, F. Malbet, G. Weigelt, P. Antonelli, U. Beckmann, Y. Bresson, A. Chelli, M. Dugué, G. Duvert, S. Gennari, L. Glück, P. Kern, S. Lagarde, E. Le Coarer, F. Lisi, F. Millour, K. Perraut, P. Puget, F. Rantakyrö, S. Robbe-Dubois, A. Roussel, P. Salinari, E. Tatulli, G. Zins, M. Accardo, B. Acke, K. Agabi, E. Altariba, B. Arezki, E. Aristidi, C. Baffa, J. Behrend, T. Blöcker, S. Bonhomme, S. Busoni, F. Cassaing, J.-M. Clausse, J. Colin, C. Connot, A. Delboulbé, A. Domiciano de Souza, T. Driebe, P. Feautrier, D. Ferruzzi, T. Forveille, E. Fossat, R. Foy, D. Fraix-Burnet, A. Gallardo, E. Giani, C. Gil, A. Glentzlin, M. Heiden, M. Heininger, O. Hernandez Utrera, K.-H. Hofmann, D. Kamm, M. Kiekebusch, S. Kraus, D. Le Contel, J.-M. Le Contel, T. Lesourd, B. Lopez, M. Lopez, Y. Magnard, A. Marconi, G. Mars, G. Martinot-Lagarde, P. Mathias, P. Mège, J.-L. Monin, D. Mouillet, D. Mourard, E. Nussbaum, K. Ohnaka, J. Pacheco, C. Perrier, Y. Rabbia, S. Rebattu, F. Reynaud, A. Richichi, A. Robini, M. Sacchettini, D. Schertl, M. Schöller, W. Solscheid, A. Spang, P. Stee, P. Stefanini, M. Tallon, I. Tallon-Bosc, D. Tasso, L. Testi, F. Vakili, O. von der Lühe, J.-C. Valtier, M. Vannier, and N. Ventura. AMBER, the near-infrared spectro-interferometric three-telescope VLTI instrument. *Astronomy & Astrophysics*, 464(1):1–12, March 2007. ISSN 0004-6361, 1432-0746.

Edward A. Pier and Julian H. Krolik. Infrared spectra of obscuring dust tori around active galactic nuclei. I - Calculational method and basic trends. *The Astrophysical Journal*, 401: 99–109, December 1992a. ISSN 0004-637X.

Edward A. Pier and Julian H. Krolik. Radiation-Pressure–supported Obscuring Tori around Active Galactic Nuclei. *The Astrophysical Journal*, 399:L23, November 1992b. ISSN 0004-637X.

Edward A. Pier and Julian H. Krolik. Infrared Spectra of Obscuring Dust Tori around Active Galactic Nuclei. II. Comparison with Observations. *The Astrophysical Journal*, 418:673, December 1993. ISSN 0004-637X.

David Raban, Walter Jaffe, Huub Röttgering, Klaus Meisenheimer, and Konrad R. W. Tristram. Resolving the obscuring torus in NGC 1068 with the power of infrared interferometry: revealing the inner funnel of dust. *Monthly Notices of the Royal Astronomical Society*, 394: 1325–1337, April 2009. ISSN 0035-8711.

Claudio Ricci, Benny Trakhtenbrot, Michael J. Koss, Yoshihiro Ueda, Kevin Schawinski, Kyuseok Oh, Isabella Lamperti, Richard Mushotzky, Ezequiel Treister, Luis C. Ho, Anna Weigel, Franz E. Bauer, Stephane Paltani, Andrew C. Fabian, Yanxia Xie, and Neil Gehrels. The close environments of accreting massive black holes are shaped by radiative feedback. *Nature*, 549(7673):488, September 2017.

G. Risaliti, M. Elvis, G. Fabbiano, A. Baldi, and A. Zezas. Rapid Compton-thick/Compton-thin Transitions in the Seyfert 2 Galaxy NGC 1365. *The Astrophysical Journal Letters*, 623: L93–L96, April 2005. ISSN 0004-637X.

Gerard Rousset, Francois Lacombe, Pascal Puget, Norbert N. Hubin, Eric Gendron, Thierry Fusco, Robin Arsenault, Julien Charton, Philippe Feautrier, Pierre Gigan, Pierre Y. Kern, Anne-Marie Lagrange, Pierre-Yves Madec, David Mouillet, Didier Rabaud, Patrick Rabou, Eric Stadler, and Gerard Zins. NAOS–the first AO system of the VLT: on-sky performance. In *Adaptive Optical System Technologies II*, volume 4839, pages 140–149. International Society for Optics and Photonics, February 2003.

E. E. Salpeter. Accretion of Interstellar Matter by Massive Objects. *The Astrophysical Journal*, 140:796–800, August 1964. ISSN 0004-637X.

M. Schartmann, K. Meisenheimer, M. Camenzind, S. Wolf, and Th Henning. Towards a physical model of dust tori in Active Galactic Nuclei. Radiative transfer calculations for a hydrostatic torus model. *Astronomy and Astrophysics*, 437(3):861, July 2005.

M. Schartmann, K. Meisenheimer, M. Camenzind, S. Wolf, K. R. W. Tristram, and T. Henning. Three-dimensional radiative transfer models of clumpy tori in Seyfert galaxies. *Astronomy and Astrophysics*, 482(1):67, April 2008.

H. M. Schmid, I. Appenzeller, and U. Burch. Spectropolarimetry of the borderline Seyfert 1 galaxy ESO 323-G077. *Astronomy and Astrophysics*, 404:505 – 511, June 2003.

Maarten Schmidt. Quasistellar Objects. *Annual Review of Astronomy and Astrophysics*, 7:527, 1969. ISSN 0066-4146.

Carl K. Seyfert. Nuclear Emission in Spiral Nebulae. *The Astrophysical Journal*, 97:28, January 1943.

Francesco Shankar, Mariangela Bernardi, Ravi K. Sheth, Laura Ferrarese, Alister W. Graham, Giulia Savorgnan, Viola Allevato, Alessandro Marconi, Ronald Läsker, and Andrea Lapi. Selection bias in dynamically measured supermassive black hole samples: its consequences and the quest for the most fundamental relation. *Monthly Notices of the Royal Astronomical Society*, 460(3):3119, August 2016.

Yancy L. Shirley. The Critical Density and the Effective Excitation Density of Commonly Observed Molecular Dense Gas Tracers. *Publications of the Astronomical Society of the Pacific*, 127:299, March 2015. ISSN 0004-6280.

J. E. Smith, A. Robinson, D. M. Alexander, S. Young, D. J. Axon, and Elizabeth A. Corbett. Seyferts on the edge: polar scattering and orientation-dependent polarization in Seyfert 1 nuclei. *Monthly Notices of the Royal Astronomical Society*, 350:140–160, May 2004. ISSN 0035-8711.

J. E. Smith, A. Robinson, S. Young, D. J. Axon, and Elizabeth A. Corbett. Equatorial scattering and the structure of the broad-line region in Seyfert nuclei: evidence for a rotating disc. *Monthly Notices of the Royal Astronomical Society*, 359:846–864, May 2005. ISSN 0035-8711.

J. E. Smith, S. Young, A. Robinson, E. A. Corbett, M. E. Giannuzzo, D. J. Axon, and J. H. Hough. A spectropolarimetric atlas of Seyfert 1 galaxies. *Monthly Notices of the Royal Astronomical Society*, 335:773–798, September 2002. ISSN 0035-8711.

Marko Stalevski, Daniel Asmus, and Konrad R. W. Tristram. Dissecting the active galactic nucleus in Circinus - I. Peculiar mid-IR morphology explained by a dusty hollow cone. *Monthly Notices of the Royal Astronomical Society*, 472(4):3854, December 2017.

Marko Stalevski, Konrad R. W. Tristram, and Daniel Asmus. Dissecting the active galactic nucleus in Circinus - II. A thin dusty disc and a polar outflow on parsec scales. *Monthly Notices of the Royal Astronomical Society*, 484(3):3334, April 2019.

M. Swain, G. Vasisht, R. Akeson, J. Monnier, R. Millan-Gabet, E. Serabyn, M. Creech-Eakman, G. van Belle, J. Beletic, C. Beichman, A. Boden, A. Booth, M. Colavita, J. Gathright, M. Hrynevych, C. Koresko, D. Le Mignant, R. Ligon, B. Mennesson, C. Neyman, A. Sargent, M. Shao, R. Thompson, S. Unwin, and P. Wizinowich. Interferometer Observations of Subparsec-Scale Infrared Emission in the Nucleus of NGC 4151. *The Astrophysical Journal Letters*, 596(2):L163, 2003. ISSN 1538-4357.

L. J. Tacconi, R. Genzel, M. Blietz, M. Cameron, A. I. Harris, and S. Madden. The nature of the dense obscuring material in the nucleus of NGC 1068. *The Astrophysical Journal Letters*, 426:77–80, May 1994. ISSN 0004-637X.

E. Tatulli, F. Millour, A. Chelli, G. Duvert, B. Acke, O. Hernandez Utrera, K.-H. Hofmann, S. Kraus, F. Malbet, P. Mège, R. G. Petrov, M. Vannier, G. Zins, P. Antonelli, U. Beckmann, Y. Bresson, M. Dugué, S. Gennari, L. Glück, P. Kern, S. Lagarde, E. Le Coarer, F. Lisi, K. Perraut, P. Puget, F. Rantakyrö, S. Robbe-Dubois, A. Roussel, G. Weigelt, M. Accardo, K. Agabi, E. Altariba, B. Arezki, E. Aristidi, C. Baffa, J. Behrend, T. Blöcker, S. Bonhomme, S. Busoni, F. Cassaing, J.-M. Clausse, J. Colin, C. Connot, A. Delboulbé, A. Domiciano de Souza, T. Driebe, P. Feautrier, D. Ferruzzi, T. Forveille, E. Fossat, R. Foy, D. Fraix-Burnet, A. Gallardo, E. Giani, C. Gil, A. Glentzlin, M. Heiden, M. Heininger, D. Kamm, M. Kiekebusch, D. Le Contel, J.-M. Le Contel, T. Lesourd, B. Lopez, M. Lopez, Y. Magnard, A. Marconi, G. Mars, G. Martinot-Lagarde, P. Mathias, J.-L. Monin, D. Mouillet, D. Mourard, E. Nussbaum, K. Ohnaka, J. Pacheco, C. Perrier, Y. Rabbia, S. Rebattu, F. Reynaud, A. Richichi, A. Robini, M. Sacchettini, D. Schertl, M. Schöller, W. Solscheid, A. Spang, P. Stee, P. Stefanini, M. Tallon, I. Tallon-Bosc, D. Tasso, L. Testi, F. Vakili, O. von der Lühe, J.-C. Valtier, and N. Ventura. Interferometric data reduction with AMBER/VLTI. Principle, estimators, and illustration. *Astronomy and Astrophysics*, 464:29–42, March 2007. ISSN 0004-6361.

G. Theureau, L. Bottinelli, N. Coudreau-Durand, L. Gouguenheim, N. Hallet, M. Loulergue, G. Paturel, and P. Teerikorpi. Kinematics of the local universe. VII. New 21-cm line measurements of 2112 galaxies. *Astronomy and Astrophysics Supplement Series*, 130:333–339, June 1998. ISSN 0365-0138.

Adam D. Thomas, Michael A. Dopita, Prajval Shastri, Rebecca Davies, Elise Hampton, Lisa Kewley, Julie Banfield, Brent Groves, Bethan L. James, Chichuan Jin, Stéphanie Juneau, Preeti Kharb, Lalitha Sairam, Julia Scharwächter, P. Shalima, M. N. Sundar, Ralph Sutherland, and Ingyin Zaw. Probing the Physics of Narrow-line Regions in Active Galaxies. IV. Full Data Release of the Siding Spring Southern Seyfert Spectroscopic Snapshot Survey (S7). *The Astrophysical Journal Supplement Series*, 232(1):11, 2017. ISSN 0067-0049.

K. R. W. Tristram. Mid-infrared interferometry of nearby Active Galactic Nuclei. *Ph.D. Thesis*, July 2007.

K. R. W. Tristram, K. Meisenheimer, W. Jaffe, M. Schartmann, H.-W. Rix, Ch. Leinert, S. Morel, M. Wittkowski, H. Röttgering, G. Perrin, B. Lopez, D. Raban, W. D. Cotton, U. Graser, F. Paresce, and Th. Henning. Resolving the complex structure of the dust torus in the active nucleus of the Circinus galaxy. *Astronomy and Astrophysics*, 474:837–850, November 2007. ISSN 0004-6361.

Konrad R. W. Tristram, Leonard Burtscher, Walter Jaffe, Klaus Meisenheimer, Sebastian F. Hönig, Makoto Kishimoto, Marc Schartmann, and Gerd Weigelt. The dusty torus in the Circinus galaxy: a dense disk and the torus funnel. *Astronomy & Astrophysics*, 563:A82, March 2014. ISSN 0004-6361, 1432-0746.

R. V. Vasudevan, A. C. Fabian, P. Gandhi, L. M. Winter, and R. F. Mushotzky. The power output of local obscured and unobscured AGN: crossing the absorption barrier with Swift/BAT and IRAS. *Monthly Notices of the Royal Astronomical Society*, 402(2):1081–1098, February 2010. ISSN 0035-8711.

M. P. Veron-Cetty and P. Veron. VizieR Online Data Catalog: Quasars and Active Galactic Nuclei (8th Ed.) (Veron+ 1998). *VizieR Online Data Catalog*, page VII/207, March 1998.

Marianne Vestergaard and Bradley M. Peterson. Determining Central Black Hole Masses in Distant Active Galaxies and Quasars. II. Improved Optical and UV Scaling Relationships. *The Astrophysical Journal*, 641(2):689, April 2006.

S. Viti, S. García-Burillo, A. Fuente, L. K. Hunt, A. Usero, C. Henkel, A. Eckart, S. Martin, M. Spaans, S. Muller, F. Combes, M. Krips, E. Schinnerer, V. Casasola, F. Costagliola, I. Marquez, P. Planesas, P. P. van der Werf, S. Aalto, A. J. Baker, F. Boone, and L. J. Tacconi. Molecular line emission in NGC 1068 imaged with ALMA. II. The chemistry of the dense molecular gas. *Astronomy and Astrophysics*, 570:A28, October 2014. ISSN 0004-6361.

B. Vollmer and T. Beckert. Turbulent viscosity in clumpy accretion disks. Application to the Galaxy. *Astronomy and Astrophysics*, 382:872–887, February 2002. ISSN 0004-6361.

B. Vollmer, M. Schartmann, L. Burtscher, F. Marin, S. Hönig, R. Davies, and R. Goosmann. Thick turbulent gas disks with magnetocentrifugal winds in active galactic nuclei. Model infrared emission and optical polarization. *Astronomy and Astrophysics*, 615:A164, August 2018.

M.-P. Véron-Cetty and P. Véron. A catalogue of quasars and active nuclei: 11th edition. *Astronomy and Astrophysics*, 412:399–403, December 2003. ISSN 0004-6361.

M.-P. Véron-Cetty and P. Véron. A catalogue of quasars and active nuclei: 12th edition. *Astronomy and Astrophysics*, 455(2):773, August 2006.

Keiichi Wada. Radiation-driven Fountain and Origin of Torus around Active Galactic Nuclei. *The Astrophysical Journal*, 758(1):66, October 2012.

Keiichi Wada. OBSCURING FRACTION OF ACTIVE GALACTIC NUCLEI: IMPLICATIONS FROM RADIATION-DRIVEN FOUNTAIN MODELS. *The Astrophysical Journal*, 812(1):82, October 2015. ISSN 0004-637X.

Jian-Min Wang and En-Peng Zhang. The Unified Model of Active Galactic Nuclei. II. Evolutionary Connection. *The Astrophysical Journal*, 660(2):1072, May 2007.

G. Weigelt, K.-H. Hofmann, M. Kishimoto, S. Hönig, D. Schertl, A. Marconi, F. Millour, R. Petrov, D. Fraix-Burnet, F. Malbet, K. Tristram, and M. Vannier. VLTI/AMBER observations of the Seyfert nucleus of NGC 3783. *Astronomy & Astrophysics*, 541:L9, 2012. ISSN 0004-6361, 1432-0746.

David Williamson, Sebastian Hönig, and Marta Venanzi. 3D Radiation Hydrodynamics of a Dynamical Torus. *The Astrophysical Journal*, 876(2):137, May 2019.

David Williamson, Sebastian Hönig, and Marta Venanzi. Radiation hydrodynamics models of Active Galactic Nuclei: Beyond the central parsec. *arXiv e-prints*, 2006:arXiv:2006.00918, June 2020.

A. S. Wilson and E. J. M. Colbert. The difference between radio-loud and radio-quiet active galaxies. *The Astrophysical Journal*, 438:62–71, January 1995. ISSN 0004-637X.

H. Winkler. Variability studies of Seyfert galaxies - II. Spectroscopy. *Monthly Notices of the Royal Astronomical Society*, 257:677, August 1992. ISSN 0035-8711.

L. Woltjer. Emission Nuclei in Galaxies. *The Astrophysical Journal*, 130:38, July 1959. ISSN 0004-637X.

Thomas Young. The Bakerian Lecture: Experiments and Calculations Relative to Physical Optics. *Philosophical Transactions of the Royal Society of London*, 94:1–16, 1804. ISSN 0261-0523.